

DEVELOPMENT AND VALIDATION OF ALLUVIAL RISK IDENTIFICATION METHODOLOGIES THROUGH THE INTEGRATED USE OF REMOTE SENSING FROM SATELLITE AND HYDRAULIC MODELING WITH PARTICULAR REFERENCE TO POST- EVENT ANALYSIS AND NOWCASTING PHASES

Ph.D. in Environmental and Hydraulic engineering – XXXII cycle

Ph.D. candidate

Eng. Vincenzo Scotti

Supervisor

Prof. Francesco Cioffi

Academic year: 2018/2019



SAPIENZA
UNIVERSITÀ DI ROMA

e-geos
AN ASI / TELESPAZIO COMPANY

Summary

1	PREFACE.....	7
2	INTRODUCTION	12
2.1	FLOODING RISK ASSESSMENT FROM SATELLITE	13
2.1.1	REMOTE SENSING FROM SATELLITE FOR THE RETRIEVAL OF SOIL MOISTURE.....	17
2.1.2	REMOTE SENSING FROM SATELLITE FOR THE SUBSIDENCE PHENOMENA ASSESSMENT	20
2.1.3	REMOTE SENSING FROM SATELLITE FOR THE DETECTION OF FLOODING EXTENSION	23
2.1.4	REMOTE SENSING FROM SATELLITE FOR THE PRECIPITATION ESTIMATION.....	26
2.2	OTHER TECHNIQUES IN FLOODING RISK ASSESSMENT	27
2.2.1	HYDRAULIC MODELLING IN FLOOD RISK ASSESSMENT.....	28
2.2.2	FLOODING RISK ASSESSMENT USING SOCIAL MEDIA MARKER.....	29
2.2.3	ARTIFICIAL INTELLIGENCE ALGORITHMS IN THE NOWCASTING PHASE OF FLOOD RISK ASSESSMENT.....	31
2.3	AIM OF THE THESIS.....	35
3	APPLICATION TO CASE STUDIES OF THE REMOTE SENSING FOR FLOODING RISK ANALYSIS	37
3.1	ANALYSIS OF THE SUBSIDENCE IN THE COASTAL AREA AND HYDRAULIC RISK IN MAZZOCCHIO AREA (LT)	38
3.2	INTEGRATION OF SATELLITE INFORMATION (SAR) WITH HYDRAULIC MODELING: CASE STUDY OF THE STRYMON BASIN	52
3.3	RECONSTRUCTION OF FLOODING MAP IN INSTRUMENTED AREA (CASE STUDY: HARVEY HURRICANE, HOUSTON).....	59
3.4	RECONSTRUCTION OF FLOODING MAP IN A NON-INSTRUMENTED AREA, CASE STUDY OF THE DIAMREY TYPHOON IN QUANG NGAI (VIETNAM).....	73
3.5	ANALYSIS OF PRECIPITATION DATASET ALWAYS AVAILABLE AS INPUT OF HYDRAULIC MODELING IN A NOT INSTRUMENTED AREA	77
4	THE TWO-DIMENSIONAL MODEL FHM 2D	89
4.1	THE NECESSITY OF A MORE ACCURATE HYDRAULIC MODEL	89
4.2	GOVERNING EQUATIONS	94
4.3	NUMERICAL MODEL	95
4.4	TIME INTEGRATION	96
4.5	DISCRETIZATION OF NUMERICAL FLUXES	99
4.6	SOURCE TERM DISCRETIZATION.....	105
4.7	NUMERICAL TESTS.....	110
4.8	APPLICATION FHM-2D TO A REAL CASE STUDY.....	124
5	FLOOD RISK ASSESSMENT IN NOWCASTING PHASE.....	133
5.1	THE NOWCASTING PHASE	133

5.2	A REAL TIME FLOOD SURROGATE MODEL	133
5.3	PRELIMINARY RESULTS	139
5.4	CONCLUSIONS AND ONGOING DEVELOPMENTS	142
6	SUMMARY AND PERSPECTIVES	144
6.1	SUMMARY	144
7	REFERENCES.....	150

Figure 1 - Typology of sensors system onboard the satellite	13
Figure 2 - Satellite Radar Systems available now and into the future (from Tapete, D., & Cigna, F. (2019)).	15
Figure 3 - Example of soil moisture detection with ERS SAR satellite	19
Figure 5 - flooding detection from SAR satellite.....	24
Figure 6 - Social marker posted during hurricane Harvey in Houston that allows to localize the area affected to flood	30
Figure 7 - Feed forward artificial neural network structure using a sigmoid activation function.....	34
Figure 8 - On the left in red the area of interest of Mazzocchio is highlighted, while on the right the Mazzocchio's basin ground elevation.....	39
Figure 9 - Examples of applications of satellite interferometry.	40
Figure 10 - PS-InSAR technique.	41
Figure 11 - Results of interferometric measurements (PS-InSAR) obtained from Sentinel-1 represented on Google Earth. In red it was delineated the boundary of Mazzocchio basin (Aoi).	42
Figure 12 - Example of a historical series of movement of a PS.....	43
Figure 13 - IDW interpolation of interferometric data - a) Vertical displacement velocity [mm / year]; b) Subsidence from January 2018 compared to October 2014.....	44
Figure 14 - Identification of 16 targets in map of subsidence of January 2018.	45
Figure 15 - Subsidence trend for the 16 selected targets (2014-2018 period).....	46
Figure 16 - Examples of photographs for the 10 and 12 targets that allowed to view the presence or absence of subsidence.	47
Figure 17 - Location ant typologies of wells presents in Aoi	48
Figure 18 - Results of the correlation between PCA and Target (individual data of each target in the image on the left. Correlation map in the image on the right).	49
Figure 19 - Precipitation and subsidence trends inherent to the 16 selected targets.....	50
Figure 20 - SPI index values and subsidence trend inherent to the 16 selected targets.	50
Figure 21 - Subsidence - Drought Correlation (SPI elaborated by the pluviometric data of the Pontinia station).....	51
Figure 22 - Location map. In yellow was represented the SAR subset processed image; in black the Serres basin, and at least the meteo-stations (polygons) 1: Lithotopos, 2: Koimissi Serron, 3: Achladochori, water level telemetry stations (polygons) 4: Trimeristis, 5: Nigrita, 6: Aggitis.....	53
Figure 23 - Water/non-water. Binary images water/non-water from October 2014 to March 2015.	57
Figure 24 - Flooding maps obtained from Hydraulic modelling.....	58
Figure 25 - Flooding hazard maps of Harvey Hurricane of a) 28/08/2017, b) 30/08/2017 and c) 31/08/2018	62
Figure 26 - Location of social media marker in Houston and b) example of photo used for the validation of hydraulic modelling (obtained from E2mC).....	63
Figure 27 - Land cover by supervised classification algorithm on Copernicus images.....	64
Figure 28 - Rainfall amount (right) and runoff rate dR/dP for different values of k (left)	66
Figure 29 - Flooding map obtained from hydraulic modelling ($k=0.1$).....	67
Figure 30 - Correspondence between the flooding areas obtained by hydraulic simulation and SAR satellite	68
Figure 31 - Location of measurement stations of the levels considered and hydrometric levels detected during the extreme event.	69
Figure 32 - Temporal trend of the floods in Houston during Hurricane Harvey from 26/08 to 31/08. Red symbols indicate the locations where the water level exceeds the top of the bank, the yellow where the level is near the top of the bank and the green when the water flows inside the bank.....	70
Figure 33 - Social media marker referred at the same day of the flooding maps (28/08/2017) used for the validation of the results.....	71

Figure 34 - Track of Diamrey Typhoon	74
Figure 35 - Result of the hydraulic modeling is shown on the left and the result of the Change Detection technique applied to Sentinel images 1 on the right.	75
Figure 36 - Zoom showing the occlusions presents on DEM used as input of hydraulic modelling for the rebuild of post event flooding map	76
Figure 37 - Validation of hydraulic modeling results with pictures of the Aol	76
Figure 38 - Number of gauge stations used in different databases in operation over time (Sun et al. 2018)	78
Figure 39 - GPM Costellation, Hou et al.(2014).....	80
Figure 40 - Comparison between the amount of rain detected on the ground with that from satellite (TRMM); the rainfall from rain gauges are averaged for the stations, indicated in green square, in the figure on the left.	85
Figure 41 - a) DEM used for the tests; b) computational mesh with breaklines (visible as pink lines).	90
Figure 42 - Flow hydrograph used how input for the analysis	91
Figure 43 - Hydraulic simulation results for the depth and velocity at the mesh size 5x5 vs 10x10, 100x100 and 500x500.	92
Figure 44 - Momentum numerical fluxes through the face of the cells	100
Figure 49 - Shallow domain.....	105
Figure 46 - Schematization of Infiltration variables definition in the Green Ampt method variables used in FHM-2D.....	109
Figure 47 - Oscillating lake: well-balanced scheme. First-order scheme (times crosses). Second order scheme (plus crosses). Initial solution and bottom topography (solid and dotted lines).	111
Figure 48 - Oscillating lake with drag: well-balanced scheme. In a) is shown the analytical solution and bottom topography (black line).obtained in (Sampson et al., 2004); in b) the first-order scheme (times crosses) (light blue line) and in c) the second order scheme (plus crosses) obtained from FHM-2D (green line).	114
Figure 49 – Dam break test: a) analytical solution; b) with first order estension; and c) with second order estension.....	116
Figure 50 - $Z(x)$, $h(x, t) + Z(x)$ transcritical flow without shock. In a is represented the analytical solution; in b that obtained from first order and in c that from second order extension.	117
Figure 51 - $Z(x)$, $h(x, t) + Z(x)$ Transcritical flow with shock. In a is represented the analytical solution; in b that obtained from first order and in c that from second order extension.	117
Figure 52 - $Z(x)$, $h(x, t) + Z(x)$ subcritical flow. In a is represented the analytical solution; in b that obtained from first order and in c that from second order extension.	118
Figure 53 - Elliptical hump used for the test case. The lowest contour level is at 0.01 and the bump has height 0.8.....	119
Figure 54 - Bump test results in 2D	119
Figure 55 - Detailed topography of the catchment (from Cea et al, 2010).....	120
Figure 56 - Velocity fields computed at time $t = 20$ s in runoff test with slope	121
Figure 57 – Outlet hyetograph obtained from FHM-2D using the first and second order of accuracy for differents number of cell computation 348x192 and 256x128.	121
Figure 58 - Outlet hyetograph obtained in Cea et al, 2010 used for the comparison with the FHM-2D results.	122
Figure 59 - The bottom setting of numerical examples. The figure illustrates the case of urban draining with obstacles like houses.	122
Figure 60 - Outlet discharge as a function of time obtained from (Chertock et al., 2015). On x-axis was reported the time in seconds and in y-axes the discharge.	123
Figure 61 - Outlet discharge as a function of time obtained with FHM-2D: figure a, b, c, d are referred at first order of accuracy and respectively at 100, 200, 400 and 800 m of computational grid size; e, f, g, h are	

<i>referred at second order of accuracy and respectively at 100, 200, 400 and 800 m of computational grid size.</i>	123
Figure 62 - Area of Interest: Saint Lucia Island.....	124
Figure 63 - Tracks of nearly 150 years of tropical cyclones weave across the globe	125
Figure 64 - Rain gauge stations presents in Saint Lucia island and status of completeness of rainfall data in SLUMET and WRMA stations.....	127
Figure 65 - In yellow are shown the 12 extreme climatic events simulated and the sources where it were founded the social marker used for the validation of results.....	127
Figure 66 - DEM of Saint Lucia island rebuilt for the simulation and zoom of urban area where is possible to see the good accuracy in the reproduction of the elements (houses, rivers, etc.)	128
Figure 67 - FHM-2D result of Tomas hurricane	129
Figure 68 - FHM-2D result of Tomas hurricane and zoom on three urban areas present on the island of Saint Lucia.....	130
Figure 69 - FHM-2D result of Tomas hurricane and map showing the damage that emerged during the extreme flooding event.....	131
Figure 70 - zoom of a part of the island flooding in the CHARIM map and in the hydraulic model map..	131
Figure 71 - social markers used in the validation of the results obtained by FHM-2D.....	132
Figure 72 - face recognition technique.....	135
Figure 73 - Hyetograph of a rainfall with 10 years return period	137
Figure 74 - Input and output features of matrix	138
Figure 75 - Operative frameworks of the algorithm	138
Figure 76 - The eight eigen-values derived from PCA transformation of training dataset	139
Figure 77 - cost of the validation dataset as a function of the number of epochs (left) and accuracy of the validation dataset as a function of the number of epochs (right).....	140
Figure 78 - Results obtained from the algorithm for a) 10 years, b) 20 year and c) 50 year of return time.	141
Figure 79 - Flag classification classification obtained from the flow depth and velocity relationship.....	142

1 PREFACE

Flood risk assessment, as essential part of flood risk management, is a useful tool for the indication of economic damages and for the identification of the most vulnerable cities worldwide. In most cases, cities with a high concentration of people and goods are vulnerable to floods (Kubal et al., 2009). As a consequence there is a need to assess the flooding risk in all its entirety.

Risk is the outcome of the interaction between a hazard phenomenon and the elements at risk within the community (e.g. people, buildings and infrastructure) that are vulnerable to such an impact (Jacks et al., 2010). In risk assessment, one has to consider the probabilities of hazardous events affecting the community and the consequent harm to the community. Probability is a concept and skill that most people have problems understanding, as many cannot handle statistical concepts or effectively factor probabilities into their decision-making (*"PWS Guidelines on Communicating Forecast Uncertainty" (PWS-18)*, WMO/TD No. 1422).

The flooding risk assessment consists on different phases: prevention, forecasting, real time monitoring and finally post-event.

In the prevention phase, all the actions that allow to reduce the risk of flooding for the most sensitive areas are implemented. These actions are different and the mains are intended to: a) introduce advance flood warning and pre-planning can significantly reduce the impact of flooding; b) modify homes and business to help the population to withstand the floods; c) Construct buildings above flood levels; d) tackle climate change; e) protect wetlands and introduce trees strategically; f) restore rivers to their natural courses; g) introduce water storage areas; h) put up more flood barriers; and at least l) improve soil conditions. All these phenomena are investigated through post event flooding maps. However, because of the ongoing climate change these flooding maps based on past extreme events are obsolete. In fact, the return period (intended as an average time or an estimated average time between events such as floods) of such floods is completely different from the ones happened in the past and therefore there is a need to update these maps.

The forecasting and nowcasting phases (the term forecast is referred to a very short time, generally from zero to six hours) are very important from the point of view of effective warnings and response in order to reduce the disaster risk. The forecast phase generally is based on four components: Observational Data and Monitoring Systems, Numerical Weather Prediction, Conceptual Models and Situational Awareness. For all of these components higher temporal and spatial resolution of the data (temperature, humidity pressure and wind data) are required to lead to a better weather diagnosis. These analyses allow to plan a better warning response. To date both these two phases are fundamental for the civil protection in providing information to

the citizens (from e.g. media, governance institutions, etc.), understanding the hazard and, at least, in the emergency response plans. Especially the nowcasting phase, that is characterized by short times, requires a wide range of tools that allow to evaluate the hazard immediately. However, in some cases it is not possible to give these technologies to the civil protection and therefore, sometimes they entrust themselves to the experiences of the operators or/and to their knowledge based on the experiences of past extreme events.

The monitoring phase, instead, is managed by collecting information on the territory thanks to the ground-based systems linked to the local databases available or through the rescue teams. The ground stations (i.e. sensors measuring precipitation and / or water levels at relevant sites in local waterways) often are not available or capable to monitor well the extreme event. In fact, it is of extreme importance for this phase that the spatial disposition of the stations is such as to cover the whole area of interest. Because of this usually does not happen, the local rescue emergency team are employed, hence, exposing them at risk.

Finally, the post-event phase deals with the using of flooding maps obtained with numerical models and / or via photographic evidence of the damages happened. These maps, as mentioned above, usually are obsolete considering the ongoing climate change and, often, do not make possible to localize all the area affected by the flood. Moreover, often these maps are implemented with hydraulic modelling using old input data (Digital Elevation Model, land cover, etc.) that do not represent the real status of the environment at the time of the extreme event of interest. Finally, usually these tools are validated considering maps based on past extreme events. As a consequence, this methodology is not useful for the reconstruction of post event maps with high accuracy, because of the land and climatic changes lead to consider new flooding areas that were safety in the past. Regarding the post event analysis with photographic evidences, the goodness of the maps depends directly from the area considered for the analysis. In fact, if the zone is in a developed city it is simple to find pictures that show the situation and that allow to rebuild a flooding map, while it is very difficult if the area is in a developing country.

In flood risk assessment, satellite remote sensing constitutes a very useful tool in all above described phases. In fact, through the satellites it is possible to have, with regard to the prevention phase, a record of the floods that occurred in the past and the consequent location of the areas most exposed to the risk of flooding. For the forecast phase, information on the distribution and intensity of the rains that is about to fall can be obtained. In the monitoring phase, the satellites allow to follow the evolution of the extreme event and detect the flooding. Finally, in the post-event phase, satellites allow to a rebuilding of the flood maps and to the identification of flooded areas and to a consequently better organization of the securing of the areas most at risk.

Remote sensing from satellite, therefore, for all the phases of flooding risk assessment, allows obtaining important information in the detection of soil moisture, subsidence, precipitation and the extent of flooding.

Satellite technology is an excellent solution for obtaining information for flooding risk assessment for several reasons: a) allows analysis on a much larger scale compared to those made with ground instruments; b) involves less risk for rescue teams in action during floods; c) some sensors, such as radar, allows to get information in correspondence with any atmospheric configuration and during the night; finally d) in the near future satellites will be launched capable of providing ever better spatial resolutions and revisit time.

At the same time, this technology also has some rather important limitations that lead us to integrate it with other existing techniques. Some of the most important limits are: a) of an instrumental nature (i.e. the radar is not able to capture flooding in the urban area); b) the spatial and temporal resolution not always able to capture the peak of flood during the extreme event; and finally c) that not all satellite missions are free and / or accessible;

For this reason the satellite instrument alone is not sufficient and must necessarily be associated with other existing and compatible technologies for flooding risk assessment.

Specifically, in this thesis we explore the possibility to improve flood risk assessment by the integration of hydraulic models with satellite data with reference at the two phases of post-event analysis and nowcasting.

Regarding the post event, the aim was to understand if the remote sensing from satellite, considering its limitation, is a useful tool for the reconstruction of very accurate flooding maps that can perform the flooding risk assessment. Furthermore, also the possibility to integrate this technology with other available tools (social media marker and hydraulic modelling) was explored. Drawbacks arose about open source shallow water model (HEC-RAS) used in the case studies have suggested to develop a new 2D hydraulic model, that has been used in the carrying out of nowcasting phase.

Concerning the nowcasting phase, the possibility to integrate data of precipitation measured by radar with real time flood forecast model was explored. A flood model, following an artificial intelligence approach, was carried out. Such model was trained by a number of simulations carried out by the 2D hydraulic model.

The development of the thesis has seen three main moments:

- 1) Analysis of the capabilities of remote sensing in flooding risk assessment by applying it to real cases and other available tools (hydraulic modeling and social media markers);
- 2) Application to the post-event phases in which it was first rebuilt the extreme event of Hurricane Harvey in Houston and then an assessment of the need to build more flexible numerical models than the one used for the simulations was done;
- 3) Application to the analysis of flooding risk assessment in the nowcasting phase through the construction of a real time artificial intelligence model.

In the first point, first of all was studied how remote sensing from satellite was used in the evaluation of flooding risk assessment for: detection of soil moisture and subsidence phenomenon; flood detection; and finally for estimating precipitation. For each of these applications the sensors and missions currently in orbit that are mostly used for these purposes have been presented. Such applications have been reported as case studies. Finally, other existing tools were investigated, such as hydraulic modeling and social media markers, useful for the flooding risk assessment.

In the second point, instead, considering the applications developed in point 1, in particular that of the reconstruction of the flooding emerged in Greece (river Strymon) and in Vietnam (Quang Ngai), remote sensing techniques from satellite with hydraulic modeling and social media markers were integrated. The numerical code used in these simulations was HEC-RAS 5.0.3. This hydraulic model was considered because suggested by FEMA and because of its excellent results in terms of robustness. The peculiarity of this hydraulic model is that it exploits the subgrid approach (Casulli et al., 2008). This method allows using large meshes to perform hydraulic simulations in large areas with reasonable computational times. The Hurricane Harvey, occurred in Houston, was adopted as a test case. In this study the technique of remote sensing from satellite was integrated with hydraulic modeling and social media markers. This methodology allowed us to reconstruct, using the information obtained from ground stations, extremely accurate flood maps for all days of the extreme flood event. Subsequently, tests were carried out on the robustness of the HEC-RAS code on a portion of the urban area of Houston. These analysis, conducted in correspondence of complex geometries (such as buildings, roads, slope changes, etc.), have allowed us to understand the goodness of the approach to the subgrid in returning the results of depth and velocity of the flow to the different spatial resolutions of the computational grid. The results of the tests led to the creation of a new numerical code that was able to overcome the limitations found in HEC-RAS and, in general, those that afflict the various models present in the literature. The model created was first of all object of a bench marking test and then of an application to a real case study. Twelve extreme events occurred in correspondence of Saint Lucia Island were simulated and the results were validated with social media collected by the local population.

Finally, the third and final point allowed us to explore the possibility of overcoming the main limitation in the application of hydraulic models in the nowcasting phase. In fact, the numerical codes for simulations require much longer times than those useful for the nowcasting phase (a few seconds). For this reason, an approach based on artificial intelligence has been used that allows, for a given atmospheric configurations that occurs, to obtain in a short time flooding maps based on past events similar to the extreme event that is coming. The surrogate model, in this thesis, has been trained with the simulated maps for the extreme events happened on Saint Lucia in past.

2 INTRODUCTION

There are very few places on earth where flooding is not a concern. In fact, any zone where heavy rain happened is vulnerable to flooding. A flooding occurs when water inundates land that is normally dry. This phenomenon can happen in a multitude of ways: heavy rainfall, a rapid melting of snow or ice, storm surge, presence of beaver dam in a particular position of a river; a breaking of a dam or a levee; and for subsidence phenomena, especially in a coastal area.

Most flooding take hours or several days to develop, giving residents and civil protection to prepare or evacuate. Others generate quickly and with little warning and are called flash floodings. This typology of events is extremely dangerous, in fact, can instantly turning a babbling brook or even a dry wash into rushing rapids that sweep everything in their path downstream.

Climate change is increasing the risk of flooding worldwide, particularly in coastal and low-lying areas, because of its role in extreme weather events and sea level rising.

Flooding cause more than 40 billion of dollars in damage worldwide annually, according to the Organization for Economic Cooperation and Development (OECD, 2016). Casualties have increased in recent decades to more than 100 people a year. When flooding waters recede, affected areas are often blanketed with silt and mud. The water and landscape can be contaminated with hazardous materials such as sharp debris, pesticides, fuel, and untreated sewage. Residents of flooding areas can be left without power and clean drinking water, leading to outbreaks of deadly waterborne diseases like typhoid, hepatitis A, and cholera.

Because of the importance of the flooding issue, it is necessary to use strong monitoring technologies that allow to follow the extreme event and provide all the information for mitigate and assess the flooding risk.

As mentioned above, the flooding risk assessment consists on different phases: prevention; forecasting; real time monitoring and finally post-event.

Several technologies for each of those phases, useful for the flooding risk assessment, have been reported in literature. Among such technologies, remote sensing from satellite is one of the most useful thanks to its ability to be used in all the phases. A wide range of information are provided by this technology: the analyses of soil moisture; subsidence phenomena; detection of the extension of inundation; estimation of precipitation intensity and monitoring of distribution. Hence, remote sensing from satellite is gaining, recently, considerable and increasing interest. Despite its advantages, there are some shortcomings that required to be overcome and for this reasons other technologies should be investigated and combined to it.

2.1 FLOODING RISK ASSESSMENT FROM SATELLITE

Remote sensing from satellite is defined as the science and art of obtaining information about an object, area or phenomena through the analysis of data acquired by a device that is not in contact with the object, area, or phenomena under investigation.

The sensors are divided into active and passive, the former receiving a back scattering fraction of their previously emitted signal, while the latter only pick up the electromagnetic waves naturally spread by the target (Figure 1).

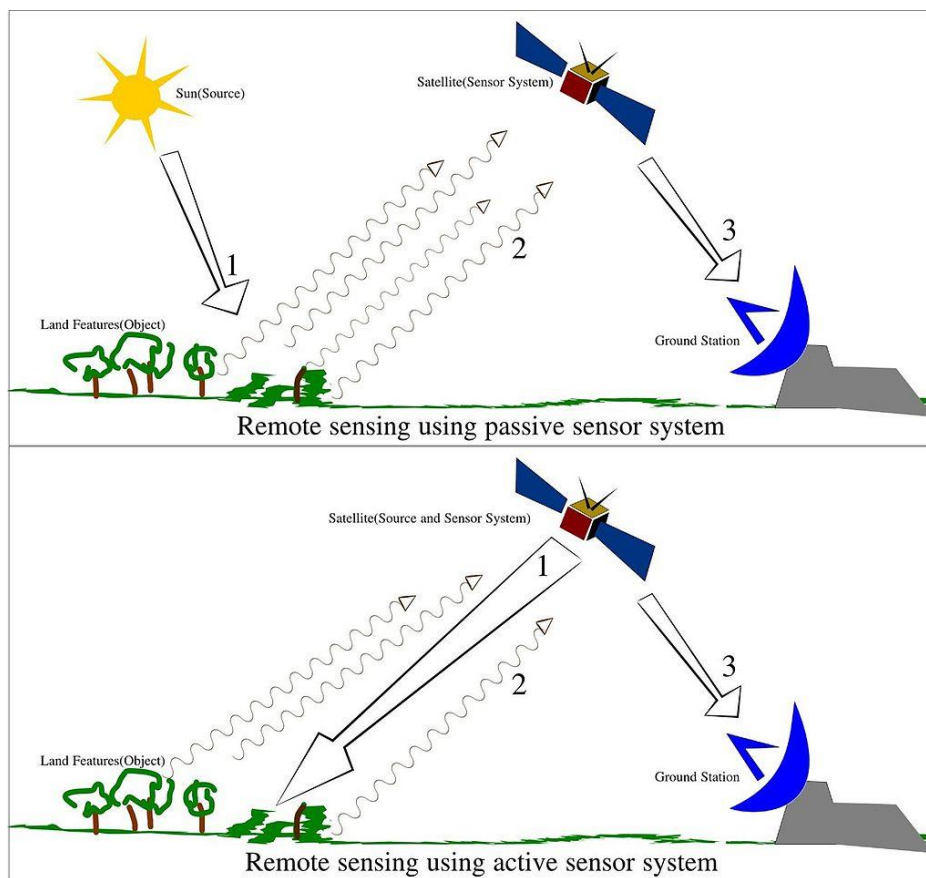


Figure 1 - Typology of sensors system onboard the satellite

For the purpose of flooding risk monitoring, depending on the scale on which the analysis is performed, a variety of satellite data is used. In order to carry out effective monitoring, several conditions must be met: 1. data should be collected at the appropriate frequency depending on the mode (preventive/ operational); 2. the data should be adequately detailed to provide information on the state of the water and the status of the flooding embankments. Data from meteorological systems is useful to forecast precipitation and its intensity. Very high-resolution satellite images (VHRS) and high-resolution satellite images (HRS) can be used to monitor flooding embankments and their condition, and to monitor flooding plains. This applies to both radar and optical data. Radar data is weather independent and generally considered to be better suited for

water detection (Pluto-Kossakowska et al. 2017), while optical data is easier for photointerpretation and acts as a compaction of measurements from radar data.

The active sensors most used in remote sensing are the SAR (*Synthetic Aperture Radar*) with radar sensors (*RAdio Detection And Ranging*), which allow to detect an object and establish its distance from the sensor itself through radio waves. These waves can have wavelengths (λ) with values between microwaves and radio waves (with λ between 1 mm and 1 m and frequencies ranging from 0.3 to 30 GHz). The wavelengths are chosen according to the target to be analyzed and to the platform that supports the sensor, for example in the case of satellite RADAR the choice to use the typical frequencies of the microwave field depends on the fact that they have a transmissivity 100% in the atmosphere and therefore there is no signal loss, despite the presence of interference.

A RADAR device consists of four parts: a transmitter, a receiver, an antenna and a recorder. The ability of a RADAR sensor to observe an object depends on many factors including the intensity of the emitted signal, the sensor-target distance, the λ of the incident signal and finally the reflectivity of the object itself. This last parameter depends in turn on numerous factors both inherent to the characteristics of the RADAR such as: frequency, signal polarization and acquisition geometry; both intrinsic properties of the target such as: roughness, humidity, size and electrical properties of the object. The roughness of the surface of the object determines the amount of backscattered energy that will return to the sensor, the more it will be wrinkled the brighter it will be during acquisition. On the contrary smooth surfaces will appear black, due to the type of reflection of the waves, which in this case will be of specular type, without the possibility of returning to the receiver. A surface is considered smooth if the roughness on it is lower than the λ of the signal. The angular reflection instead depends on the presence of walls perpendicular to the ground, such as buildings, and has the effect of amplifying the backscattered signal as one or more signal reflections occur, this phenomenon typically occurs in densely populated areas. The humidity of the target is a very important parameter because, by virtue of the electrical properties of the water, it determines its greater or lesser capacity to allow itself to be penetrated by the incident signal. An object rich in water will be more reflective than one that is devoid of it, this property depends on the dielectric constant of the material and is particularly important in the case of vegetation as its properties vary considerably during the year. The RADAR sensors can operate with different bands and each one provides different information on the investigated targets. The most used bands are those that do not interfere with the atmosphere, i.e. that guarantee an atmospheric transmissivity close to 100%, in particular the most common sensors exploit the microwave portion corresponding to the X, C and L bands.

All satellites equipped with radar sensors (SAR - Synthetic Aperture Radar) orbit the earth on a near-polar orbit at an altitude ranging from 500 to 800 km above the earth's surface, depending on the satellite platform

hosting the SAR sensor. The angle between true north-south and the satellite orbit varies slightly, depending on the satellite but, in general lies in the range of 10 degrees.

Figure 2 shows all the SAR satellites distinguished by the typology of radar band.

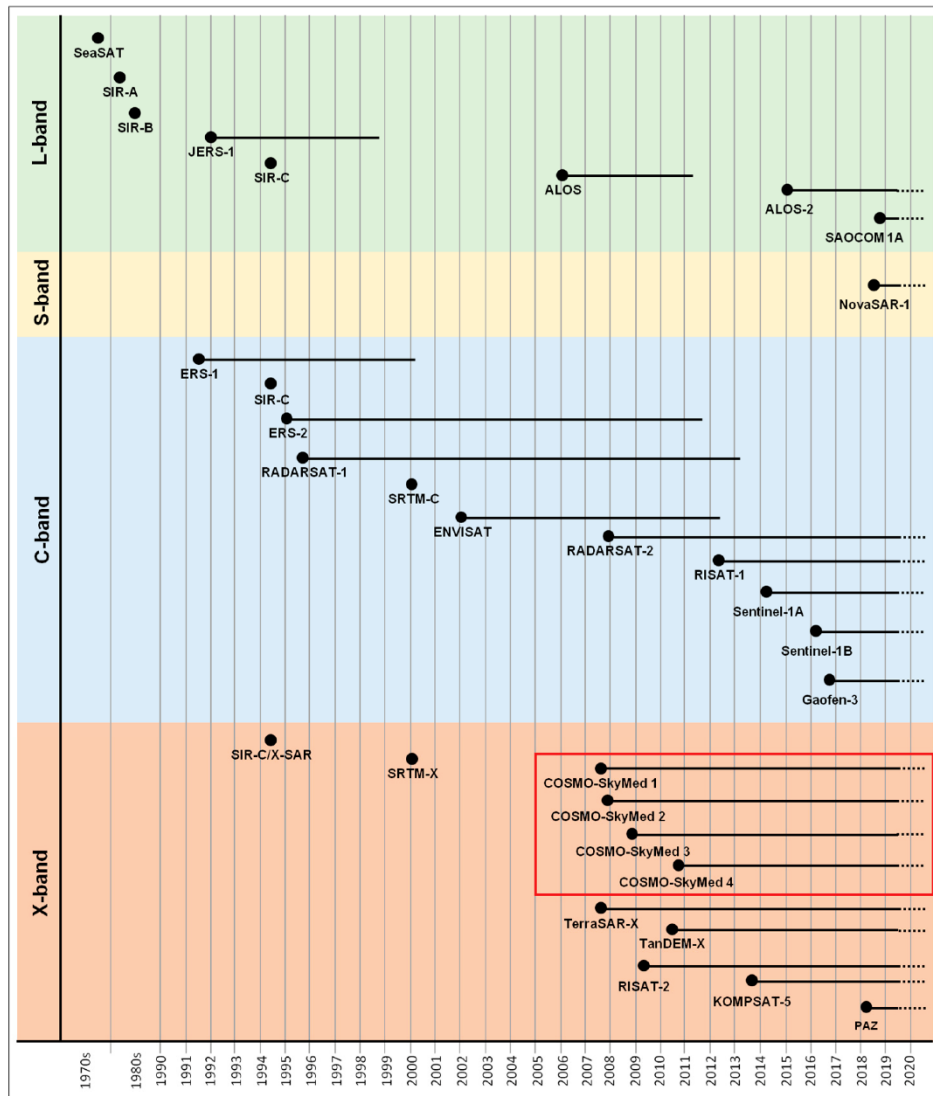


Figure 2 - Satellite Radar Systems available now and into the future (from Tapete, D., & Cigna, F. (2019)).

Satellite sensors are mounted on their platforms with the direction of transmission at 90° to the flight direction. The earlier satellites (ERS-1, ERS-2, Radarsat-1 and Envisat) were all right looking satellites, meaning that microwave beam transmits and receives on the right side only of the satellite, relative to its orbital path, i.e. the system cannot rotate. Newer satellites (Radarsat-2, TerraSAR-X and COSMO-SkyMed) have both right-looking and left-looking capabilities, thus they can ‘look’ to the right or the left of the craft, but not both directions simultaneously. The angle at which the sensor is pointed toward the earth’s surface is referred to as the off nadir, or look, angle.

Optical satellite remote sensing systems are characterized by a variety of technical parameters, including very important spatial and spectral resolution. Both of these parameters are crucial for monitoring the condition of embankments and forecasting the occurrence of floodings. For preventive monitoring this is a sufficient revisit time, but the possibilities of the usage of satellite optical systems are limited by the weather conditions and cloud cover.

Optical data, due to frequent cloudiness occurring in the period of increased flooding hazard, is less common for operational use in monitoring damage to levees (Weintrit et al., 2018). It is possible to use such data only in cloudless conditions or in the presence of slight cloud cover. This means that the identification of damage to flooding embankments with the use of optical data can be carried out as quasi-continuous monitoring, conducted in order to detect damages early. Examples of optical data with very high spatial resolution (IKONOS, QuickBird) being used to identify damage to flooding embankments are shown in the literature – these cover, for example, damage to the sod in the main body of the embankment and on the embankment slopes (Hossain et al. 2004). Optical data is much more frequently used to assess the state of damage after a flooding event or to determine the extent of flooding, or for flooding risk assessment (Stancalie et al. 2007; Ho et al. 2010; Skakun 2012; Shaker et al. 2012; Asare-Kyei et al. 2015; Byun et al. 2015; Hu et al. 2015; Malinowski et al. 2015).

The progress of satellite systems in the assessment of flooding risk open the way for a greater use of such techniques in the study, analysis and forecast of flooding events. In fact, remote sensing allows the monitoring of ongoing phenomena, which otherwise will be difficult to assess on a large scale, by means of change detection techniques (Singh A., 1989). The goal of change detection is to discern those areas on digital images that depict change in the feature of interest between two or more image dates. The reliability of the change detection process may be strongly influenced by various environmental factors that might change between image dates (Mishra et al., 2017).

There are different information that is possible to obtain with remote sensing useful for flooding risk assessment, beyond what has already mentioned before, as: analyses of land use/cover changes for understanding the complex relationships between human activities and their environmental impacts; to provide land use/cover information such as the degradation level of forests (Franci et al., 2015; Hayes & Sader, 2001) and wetlands; the evaluation of water resources (Frazier & Page, 2000); the urbanization rate (Maktav et al., 2005; Dewan & Yamaguchi 2009; Bagan & Yamagata, 2012); the intensity of agricultural activities (Akbari et al., 2006) and other man-induced changes (Khan 2000).

Their spatial resolution makes these images suitable for analyses on regional scale that allow to have a complete scenario of what are happens in the area of interest. It is important to underlain again that is not possible with the instrument locate in situ.

Both the type of sensors present onboard the satellite, optical or radar, allow to do flooding risk assessment.

In the following sections it is reported how the remote sensing from satellite is exploited in the investigation of different elements that should be considered in the flooding risk assessment. Particular interest is given to the satellite missions and sensors used for this purpose.

2.1.1 REMOTE SENSING FROM SATELLITE FOR THE RETRIEVAL OF SOIL MOISTURE

As far as soil moisture is concerned, knowing this measure in the pre-event and monitoring phases would make it possible to assess the soil saturation rate and thus to obtain a better estimate of the flooding risk of the area involved from alluvial event. In fact, an extremely humid or saturated soil, decreasing its infiltration capacity, tends to favor the development of a superficial inundations and therefore to increase the flooding risk.

Soil moisture is traditionally measured in situ to obtain accurate information on the point level with high temporal resolution, but these measurements have limited spatial coverage (Dorigo et al., 2011). A good solution to solve this issue is represented by remote sensing from satellite.

Many satellite active and passive microwave sensors launched since the 1970s have been widely used to estimate regional and global surface soil moisture, including the Soil Moisture Active Passive (SMAP) (Entekhabi et al., 2010, Reichle et al., 2016), Scanning Multichannel Microwave Radiometer (SMMR) (Paloscia et al., 2001), Advanced Scatterometer (ASCAT) (Lindell and Long, 2016), Soil Moisture and Ocean Salinity Sensor (SMOS) (Kerr et al., 2012, Wigneron et al., 2017), Fengyun Satellites (FY) (Parinussa et al., 2014, Song and Jia, 2016), Advanced Microwave Scanning Radiometer on the Earth Observing System (AMSR-E) (Du et al., 2016, Njoku et al., 2003) and Advanced Microwave Scanning Radiometer 2 (AMSR2) (Parinussa et al., 2015) on board on Aqua satellite.

The production of soil surface moisture maps, up to 5 cm deep, with remote sensing can be carried out thanks to optical or SAR image processing.

For the optical data, the activity consists in the calibration of inversion models that use the electromagnetic information collected in the thermal and reflectance bands. The techniques for estimate surface soil moisture with data acquired in the visible band and in the NIR, VNIR, SWIR and thermal bands (TIR) are based on reflectance and emittance measurements (Sadeghi et al., 1984), and were partially revealed effective (Sommer et al, 1998). The methods most frequently founded in the literature refer to: multispectral indices of humidity / drought based on reflectance bands, surface energy balance, thermal inertia and apparent thermal inertia, and behavioral model radiative soil-vegetation (method of the triangle T_s / Fr).

Several study, in order to improve the retrieve of soil moisture, suggest the use of multiple microwave bands or brightness temperature observations of multiple satellite. This allow to overcome the main limits that afflict this technique, as the revisit time (days) and the spatial resolution (km) that are not always good for the monitoring of soil moisture. In (Zhang K. et al, 2019) it is underlined how (Njoku and Li, 1999) using satellite microwave radiometer data from multiple bands of AMSR; (Piles et al., 2016) used the triangle inversion technique to enhance soil moisture retrieval through synergies of SMOS microwave observations and Spinning Enhanced Visible and InfraRed Imager (SEVIRI) optical and infrared data onboard the Meteosat Second Generation (MSG) satellite; (Liu et al. 2012) developed a method to combine passive and active microwave products to improve the estimation of soil moisture; (Rodríguez-Fernandez et al., 2015) and (Kolassa et al., 2016) adopted artificial neural network methods to combine observations from active and passive satellite microwaves to retrieve soil moisture; (Aires et al., 2012) compared synergistic multi-wavelength remote sensing to a posteriori combination of retrieved products; (Kolassa et al., 2017) further investigated the assimilation of soil moisture retrieved from active and passive satellites into a land surface model. There is also the European Space Agency (ESA) Climate Change Initiative (CCI) project (Dorigo et al., 2015; Enenkel et al., 2016), that merges a long-term record of global soil moisture from SMOS, AMSR-E, and AMSR2 (Yao et al., 2017), and a record based on the SMOS and AMSR-E (Van der Schalie et al., 2018).

All these studies, have revealed the effectiveness of synergistically using observations from multiple satellites or multiple sensors to improve the retrieval of soil moisture. However, in literature, this challenge is still open. In fact, it is rare to retrieve studies on the merge of soil moisture data obtained from different sensors.

As mentioned before, one of the main limits of passive sensors measure is the poor spatial resolution (more than 40 km). Active sensors, instead, particularly the Synthetic Aperture Radar (SAR) have a spatial resolution better than 50 m and have been widely used in recent years.

The soil moisture retrieval with SAR sensors is based on the interpretation of backscattering signal (see Wagner et al., 1999). Despite the good spatial resolution, the SAR technique present some important limitations in the retrieve of soil moisture. In fact, as reported in (Zribi et al., 2006), in case of presence of bare soil the backscattered radar signal depends strongly on soil moisture and surface roughness (Ulaby et al. 1986); in case of sparse vegetation, the return signal depends both on the vegetation backscattering characteristics and on the attenuation it introduces to backscattering from the soil (Ulaby et al. 1982, Prevot et al. 1993); in case of dense vegetation, such as in forests, the soil contribution, in the C band, is generally very weak, particularly at high incidence angles (Ulaby et al. 1986, Fung 1994). (Zribi et al., 2006) describe in his paper, that many models have been developed to understand the physics of the interaction between radar signal and surface or vegetation parameters. For bare soils, different theoretical and empirical approaches have been developed (Fung et al. 1992, Oh et al. 1992, Dubois et al. 1995, Wang et al. 1997, Shi et al. 1997, Zribi and Dechambre 2003). Among these, the 'linear approach' linking surface soil moisture to

calibrated and validated SAR radar measurements (ERS, SIRC, RADARSAT, and so on) is widely used (Cognard et al. 1995, Quesney et al. 2000, Le Hegarat-Masclé et al. 2002, Zribi et al. 2005).

W. Wagner et al. (1999), in their paper, report how ERS (*European Remote Sensing*) technology is an excellent instrument that can provide the soil moisture of a given area with a good precision. ERS technology is part of the SAR (*Synthetic aperture radar*) systems. The fundamental principle on which the SAR systems are based is that of emitting electromagnetic radiation (in the microwave region, in particular, for ERS, in the C band with a frequency of 5.3 GHz) in the direction of the Earth's surface and recording the amount and the return time of the diffusion energy (backscattering). These sensors allow images to be acquired regardless of sunlight and clouds. The two SAR ERS-1 and 2 satellites, whose launch took place respectively in July 1991 and in April 1995 by the ESA (European Space Agency) of which the ASI (Italian Space Agency) is part, have the same characteristics: helio-synchronous orbit, circular, with inclination of 98.5°, rotation around the Earth every 100 minutes at a height of 785 km. The two satellites are able to acquire images at every point on the surface of the Earth every 17 days in ascending and descending orbit, so that the entire coverage of the Earth is obtained in 35 days, with a ground resolution of approximately 25 meters.

Wagner et al. employed an algorithm for a series of 6 years data, also proposing a qualitative comparison between the results obtained using as input the data deriving from satellite with those obtained from direct instrumentation. The article shows how the data obtained from the ERS scatterometer very well approximate those obtained on land, thus demonstrating the soundness of the technique for estimating soil moisture.

The figure 3 shows an application of phase-retrieved soil moisture, applied across agricultural fields (De Zan et al, 2014). Here, the differential phase (in degrees) between two SAR images clearly shows delineation along field boundaries, associated with differing moisture states.

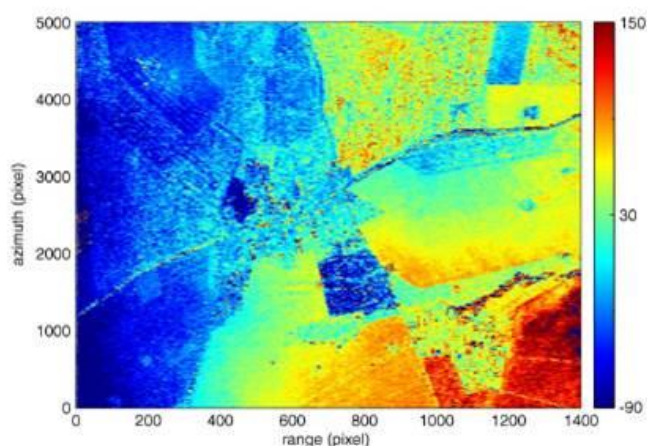


Figure 3 - Example of soil moisture detection with ERS SAR satellite

Another interesting approach in which ERS technology is used is found in the article proposed by (Scipal K. Et al, 2008) which compares the results of soil moisture obtained from inputs provided by the satellite with

those of the date ERA INTERIM base. The ERA interim global atmospheric numerical modeling dataset is processed by the European Center for Medium-Range Weather Forecasts (ECMWF).

The comparison shows that the two technologies give very similar results, thus underlining the great flexibility of ERS technology.

The *Advanced spatial resolution Advanced Synthetic Aperture Radar (ASAR)* radar sensor on board the ENVISAT satellite owned by the European Space Agency (ESA) is operating in C band (5.33 GHz), which resumes with incidence angles between 15 ° and 45 ° with a temporal frequency of 35 days. Potentially it allows to have images on the ground with high spatial resolution (up to 12.5 m) and thanks to the possibility of acquiring images in Alternating Polarization modes, and therefore in double polarization, this sensor is today a promising and potential humidity monitoring tool on large spatial areas. The Advanced Synthetic Aperture Radar (ASAR) on board the ENVISAT satellite is an active radar sensor operating in the microwave frequencies (5.33 GHz). The antenna consists of a transmitter and a receiver (monostatic radar), and resumes in look side mode, ie from the side with respect to the direction of flight, with angles of inclination with respect to the vertical for the sensor between 15 ° and 45 ° . The radar estimates the backscattering coefficient σ_0 of the soil, from which the dielectric constant ϵ directly connected to soil moisture is derived (Topp et al., 1980). The soil moisture is then derived from the dielectric constant of the soil. The dielectric constant was estimated using the physically based model with proven validity Integral Equation Model by (Fung et al., 1992). Once the dielectric constant ϵ is obtained, the soil moisture θ has been estimated by (Topp et al., 1980).

Other SAR satellites widely used for this type of application are Sentinel 1, RADARSAT-2, ALOS PALSAR and SAOCOM. All the missions have on board sensors operating in L band with frequency 0.39 - 1.55 GHz. Given their ability to operate a different mode of acquisitions, they are able to provide a good spatial resolution, of the order of the meter, and for these reasons their use is becoming more and more frequent in the study of soil moisture. The limit that characterizes the products deriving from these missions, except for the Sentinel product, is that the images are not free.

2.1.2 REMOTE SENSING FROM SATELLITE FOR THE SUBSIDENCE PHENOMENA ASSESSMENT

Subsidence is a process of slow lowering of the ground level (mm-cm / year) to a local or regional scale, which can be produced both from natural and/or anthropic causes. Like soil moisture, the phenomenon of subsidence is also very studied through the use of remote sensing, in particular through the Interferometric technique.

The main natural phenomena responsible for causing subsidence are: tectonic movements (Watts, 1982; Dokka, 2006), volcanic activity (Branney, 1995; Takada & Fukushima, 2013) and all the processes related to

land consolidation (Tovey & Paul, 2002; Van Asselen, 2011). A common characteristic of the majority of natural causes of subsidence is that the areas involved are very extensive (regional scale) and the rates of soil sinking are very low, therefore they do not involve immediate risk situations and the effects are observed after several years.

On the contrary, anthropic causes, which are usually associated with the construction of buildings and infrastructures (Stramondo et al, 2008; Manunta et al, 2008) and the extraction of fluids from the underground (Stramondo et al, 2007; Tomas et al, 2005; Klemm et al, 2010), involve consolidation processes on a local scale which can be much faster.

Interferometry is the study of the amplitude and phase difference obtained by comparing two SAR images inherent to the same scene, but which were taken at a different time and therefore with slightly different viewing angles. The image obtained by this comparison is called an interferogram. Interferograms are maps of relative ground-surface change that are constructed from InSAR data to help scientists to understand how tectonic or human activities, such as groundwater pumping and hydrocarbon production, can cause the land surface to uplift or subside. Interferograms require 2 images taken at intervals in time to determine if there has been any shift in land surface levels. If the ground has moved away from (subsidence) or towards (uplift) the satellite between the times of the two SAR images, a slightly different portion of the wavelength is reflected back to the satellite resulting in a measurable phase shift that is proportional to displacement. The map of phase shifts, or interferogram, is depicted with a repeating color scale that shows relative displacement between the first and the second acquisitions. The direction of displacement - subsidence or uplift - is indicated by sequence of the color progression of the fringe(s) toward the center of a deforming feature (Figure 4).

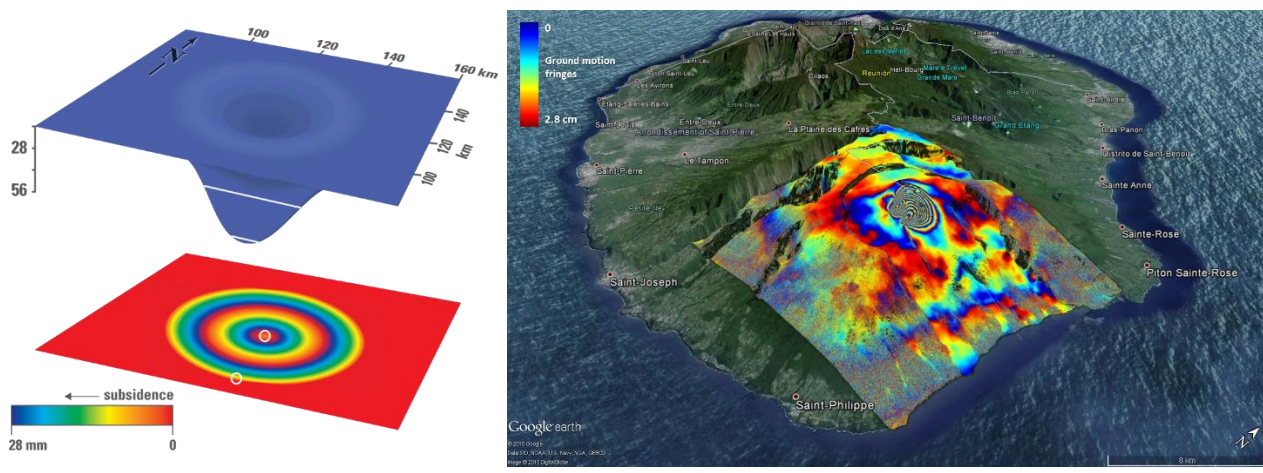


Figure 4 - left the Interferogram interpretation (left) and the SAR interferogram processed right) by TRE ALTAMIRA capturing the deformation occurred in the volcano Piton de la Fournaise (Reunion Island) in May 2015

This analysis is very useful for monitoring any type of land surface variation (Massonet & Feigl, 1998; Rosen et al, 2000), such as the effect of earthquakes, landslides and subsidence on the pre-existing topography.

Interferometric Synthetic Aperture Radar (InSAR), also referred to as SAR Interferometry, is the measurement of signal phase change, or interference, over time. When a point on the ground moves, the distance between the sensor and the point on the ground also changes and so the phase value recorded by a SAR sensor flying along a fixed orbit will be affected, too.

There are two different ways of acquiring InSAR images: single pass or dual pass. The first involves the presence of two antennas on board the satellite and the two acquisitions to be compared take place at the same time, with a minimal variation of the position. The second one involves the use of a single antenna and therefore the acquisition of the two SAR images to be compared takes place at different times. In the latter case the two orbits can undergo slight variations in space (from a few meters to hundreds of meters). To describe these imperfections of the orbit two parameters are used: the spatial baseline which is the distance between the two satellites at the time of acquisition and the temporal baseline, which instead describes the time interval between the two.

When a pair of images is subjected to interferometric analysis with a view to identifying movement and, thereafter, quantifying that movement, the process is referred to as *Differential InSAR (DInSAR)*. Since change detection is now the goal, topographic effects are compensated for by using a Digital Elevation Model (DEM) of the area of interest, creating what is referred to as a differential interferogram (the word “differential” here refers to the subtraction of the topographic phase contribution from the SAR interferogram).

The DInSAR analysis was born at the Milan Polytechnic at the end of the 1990s and allows the measurement of extremely slow ground movements, in the order of mm / year. The SAR differential interferometry is particularly suitable for the study of ground deformation phenomena because it has numerous advantages, including: acquisition 24 hours a day in any weather condition and in any corner of the planet (even the least accessible areas), possibility to quickly analyze very large areas, the continuous implementation of ever-increasing technologies and new data belonging to different space agencies.

The two major limitations of this technique are: the inability to measure displacements greater than half a wavelength between adjacent resolution cells (using microwaves the measurable variability must be in the order of mm or cm) and the impossibility to measure the absolute displacements if not along the direction of the line of sight (LOS) and therefore the descending component of the displacement cannot be detected while all the intermediate displacements are detected as projections along the LOS.

The most advanced techniques using differential interferometry are called A-DInSAR (Advanced Differential Synthetic Aperture RADAR Interferometry) and include: PS (Ferretti et al, 2001), SBAS (Berardino et al, 2002), SqueeSAR (Ferretti et al, 2011), SPN (Arnaud et al, 2003), CPT (Blanco-Sanchez et al, 2008), MT-UnSAR (Hooper, 2008) and ISBAS (Sowter et al, 2013). There are numerous studies that highlight the effectiveness of these interferometric techniques in the applications to the study of subsidence (Tomas et al, 2005;

Strasmondo et al, 2007; Manunta et al, 2008; Sousa et al, 2010; Tomas et al, 2010; Teatini et al, 2012; Raspini et al, 2014) arguing that: the areas to be monitored are often the urbanized ones and that therefore the density of the permanent reflectors is sufficiently high in most cases, the subsidence is vertical and therefore the fact is important of not being able to measure the displacement N-S.

Moreover, thanks to these types of analysis it is possible to obtain a lot of different information, such as analyzing subsidence in vegetated areas (Tosi et al, 2016) combining HD images in X-band (studied with PS) and L-band images capable of penetrating the vegetation (studied with the SBAS), or to combine interferometric analysis and geological and geomorphological information to highlight the different deformative behaviors of the units present in the area studied (Conesa-García et al, 2016).

2.1.3 REMOTE SENSING FROM SATELLITE FOR THE DETECTION OF FLOODING EXTENSION

Active and passive sensors, operating in visible, infrared, thermal and microwave portions of the electromagnetic spectrum provide cost-effective and vital information on the flooding impacted areas (Anusha & Bharathi, 2019; Sanyal and Lu, 2004). With advancement in the technology over recent years, there is an increase in the availability of during and post event satellite products to the users both in terms of quality and quantity. ALOS PALSAR, RADARSAT-1/2, TerraSAR-X, ENVISAT ASAR, Sentinel-1A/1B etc., are prime examples for active sensors. AVHRR/3, SeaWiFS, MODIS (Chen and Zhang, 2004), Landsat, AWiFS, Sentinel-2A/2B etc., are few passive sensors.

A further application that is mostly carried out using SAR sensors is the extraction of the extension of flooding. The SAR, given the characteristics of the sensor, allows to obtain information about the flooding during an extreme event (Figure 5). This fact, which is impossible to achieve with optical sensors, since that they cannot be used when there is an important cloud cover or during the night, leads them to be considered the main sensors to be exploited for the detection of flooding extensions. The SAR systems operate in the micro-wave band, which are long waves and have the capability to penetrate through clouds, to some degree of vegetation, rain showers, fog and snow (Anusha & Bharathi, 2019). Also, SAR frequent revisits make it ideal for flooding monitoring. The radar, however, gives information, as in the case of humidity estimation, only in a suburban environment. In fact, the presence of buildings, dense vegetation, shadows and rough terrain do not allow the sensor to detect and delineate the flooding.

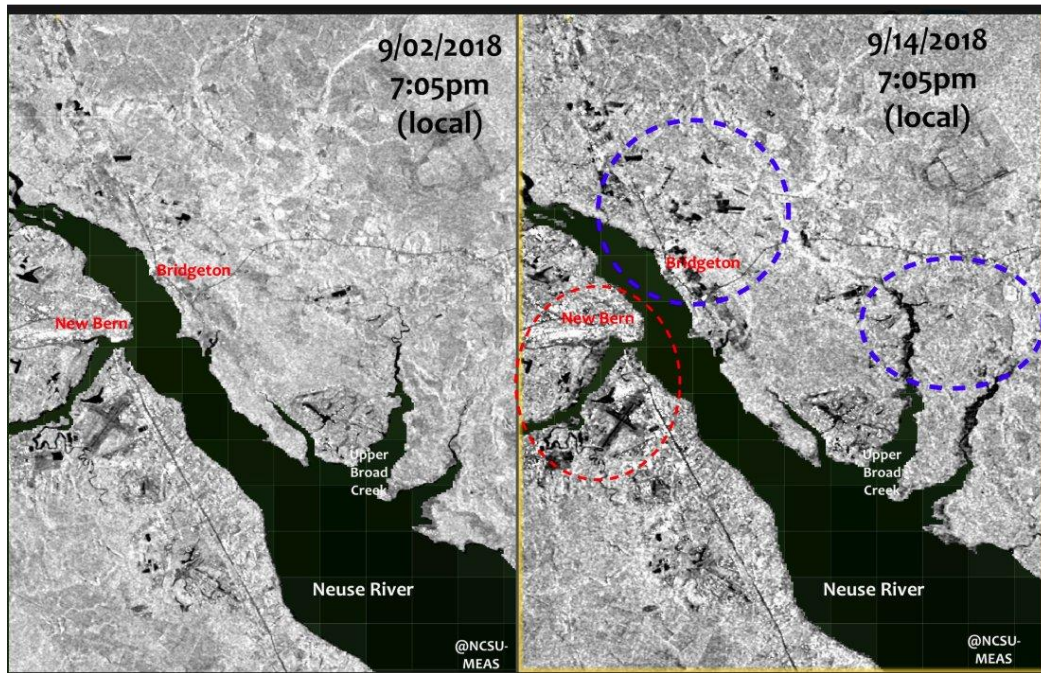


Figure 5 - flooding detection from SAR satellite

Active sensors transmit a signal and receive the backscatter characteristics of different surface features (Anusha & Bharathi, 2019; Martinis and Rieke, 2015). The strength of the radar backscatter depends on multiple factors, notably surface roughness, dielectric properties, and local topography in relation to the radar look angle (Klemas, 2014). The smooth open water surface acts as a specular reflector of the radar pulse, which scatters the radar energy away from the sensor (Anusha & Bharathi, 2019; Martinis and Rieke, 2015), resulting in minimal signal returned to the satellite. As a result, the stagnant water pixels appear dark in radar data which is in contrast with non-water areas. This makes water pixel differentiation and detection easy in the radar data. Due to its good capability to distinguish water with other land surfaces, SAR data is more suitable for flooding detection. Various methods have been proposed in literature to delineate the flooding waters and the most used is the change detection method.

From the simple observation of any SAR image, it is possible to clearly distinguish the sea area from the earth zones. The response on the sea, due to the action of the wind, is spatially constant, similar to an equally distributed background noise. The response on earth varies greatly from area to area, based on the morphological characteristics of the corresponding surfaces. The channels and areas flooded in these images appear black due to the smooth surface of the water.

The scenes that must be used for the analyses are interferometric pairs, that is, that do not have a difference between the phase values of the radar signal between the two on the same area. This fact is very important, in fact it indicates the possibility of measuring the phase variations of the SAR signal coming from the same target on the ground for each image.

As mentioned before, one of the most used technique that is applied to this type of images is the "change detection" (CD). This technique is the process of identifying changes in an object or a phenomenon that occur in a particular time interval. A fundamental assumption of this type of analysis carried out with remote sensing data is that a change in the coverage of the ground or of the surface observed by a sensor corresponds to a change in the radiometric spectral response, and that this spectral change is significantly more significant than the changes due to other factors, such as atmospheric conditions at the time of acquisition, or soil moisture or even differences in the conditions for acquiring remote sensing data. Precisely in order to take this fact into account, images must be chosen that do not have an important temporal distance, even if in any case one is always tied to what is the availability of these in the archive.

The most used SAR satellites for this application refer to those working in the X band. The most found in literature are referred to Cosmo-Skymed constellation, Sentinel 1, Terrasar-X and Radarsat-2 missions.

The optical sensor, given the high resolutions that are in any case provided by the last missions launched in orbit (Sentinel 2, Landsat, Quickbird, Black-sky, etc.) and their excellent revisit time, are increasingly taken into consideration for those events persistent over time. In fact, if the water persists over an area the time that the cloud cover vanishes it is possible to deduce and define, in any type of area, the flooding.

To extrapolate the areas flooded by the optical image an index that use the spectral reflectance signature can be used. The Normalized Difference Water Index (NDWI) (Mc Feeters S.K.,1996), Modification Of Normalized Difference Water Index (MNDWI) (Ko et al., 2015), Normalized Difference Moisture Index (NDMI) (Zhang, K. et al., 2016), Water Ratio Index (WRI) (Feyisa G.L. et al., 2014) and Automated Water Extraction Index (AWEI) (Mukherjee, N. R. et al., 2016) are among the best known,. In Table 1 the formula of these indexes are shown.

Index	Formula
Normalized Difference water Index (NDWI)	$NDWI = \frac{GREEN - NIR}{GREEN + NIR}$
Modification Of Normalized Difference Water Index (MNDWI)	$MNDWI = \frac{GREEN - SWIR2}{GREEN + SWIR2}$
Normalized Difference Moisture Index (NDMI)	$NDMI = \frac{RED - NIR}{RED + NIR}$
Automated Water Extraction Index(AWEI)	$AWEI = 4 * (GREEN - SWIR2) - (0.25 * NIR + 2.75 * SWIR1)$
Water Ratio Index(WRI)	$WRI = \frac{GREEN + RED}{NIR + SWIR2}$

Table 1 - Indexes formula used for the flooding detection in optical images

A very useful approach, when the data is available, is to integrate the information obtained both from the SAR and from the optician in order to be able to overcome the previously explained limits that afflict the two technologies. An example is that, if there are no important cloud coverings in the optic, it is possible to

integrate the information extracted from the SAR so as to define the floodings also in the urban area, one of the most important areas for emergency planning.

2.1.4 REMOTE SENSING FROM SATELLITE FOR THE PRECIPITATION ESTIMATION

A final fundamental application of satellite sensing for the assessment of flooding risk is that of estimating precipitation. This information is fundamental because it would allow us to have data that can be used both in the early warning and nowcasting phases. In fact, for the forecast the data obtainable from satellite could be the basis for the forecast weather models (forecasts up to 15 days) and for the nowcasting, because they allow to estimate the precipitation amount that could happen in a specific area of interest.

Measurements of precipitation can be made using rain gauge stations, ground radar, or remote sensing technology. Rain gauge stations are traditional point measurements and have higher accuracy but it is difficult to obtain such precipitation measurements over oceanic and high-altitude areas where only sparse rain gauge stations are available.

The development of satellite remote sensing has provided several advantages, including its broad spatial coverage, automatic data acquisition and long-term continuity but the signals themselves are affected by the atmospheric and surface characteristics, which will lead to retrieval uncertainties (Zeng et al., 2018; Tang et al., 2012). However, remote sensing is an important method for retrieving high spatial and temporal resolution rainfall measurements over complex terrains and mountainous areas, where rain gauge stations are very limited or unavailable.

The satellite retrieval methodologies fall primarily into three categories, which are the visible and infrared (VIS/IR) methods, microwave (MW) methods and multi-sensor methods.

The VIS precipitation retrieval method mainly operates the empirical relationship between cloud brightness and rainfall because precipitation is considered to occur under highly bright clouds, which can be associated with cloud types, cloud areas and cloud growth rates (Zeng et al., 2018; Barrett, E.C et al., 1981; Kidd et al., 1999; Levizzani et al., 2001).

IR imagery is associated with cloud top temperatures and cloud growth rates can be obtained via the thermal emissions during both night and day; generally, heavier rainfall tends to be associated with larger, taller clouds with colder cloud tops (Kidd et al., 1999). Many researchers have developed different methods to retrieve precipitation based on VIS/IR data from geosynchronous earth orbit (GEO) and low-earth orbit (LEO) satellites, including the 3-hourly and monthly mean rainfalls (Levizzani et al., 2001; Atlas et al., 1981; Behrangi et al., 2009; Kühnlein et al., 2014; Stenz et al., 2015).

MW sensors can detect rain clouds directly and can provide information about the atmospheric constituents and hydro-meteorological profiles, which are more directly related to the ground precipitation rate (Joyce et al., 2003; Kidd et al., 2003; Welheit et al., 1977 and 2003; Sephens et al., 2008).

However, precipitation is not always associated with clouds and the VIS/IR methods cannot detect information below clouds (Kalinga et al., 2010). Meanwhile, MW instruments are restricted to polar-orbiting platforms, meaning that they obtain only a small amount of data and have the disadvantages of low spatial and temporal resolutions (Pan et al., 2010).

The idea of combining VIS/IR and MW observations to retrieve precipitation from multiple satellite sensors was proposed to compensate for the weaknesses of the two methods (Boushaki et al., 2008). Many products were developed by blending the MW and IR data, such as CMORPH (Climate Prediction Center's morphing technique), PERSIANN (Precipitation Estimation from Remotely Sensed Information using Artificial Neural Networks), TRMM (Tropical Rainfall Measuring Mission), GPM (Global Precipitation Measurement), and at least GSMaP (Global Satellite Mapping of Precipitation).

These products, also if they combine different methods, in correspondence of heavy rainfall, produce an underestimation of peak of precipitation. This issue is due to several motivations, i.e. instrumental limits, morphology of the area of interest, atmospheric conditions, presence of high humidity, etc. In literature there are a lot of studies with the goal to quantify the underestimation but this issue is still open. In fact, due to the limits that afflict this technology, to date it is not possible to identify a parameter that allow the correction of the precipitation value estimate from remote sensing.

2.2 OTHER TECHNIQUES IN FLOODING RISK ASSESSMENT

As widely reported in the previous section, remote sensing exhibits some limitations (mainly spatial and temporal resolution and instrumental limits). The need to overcome its disadvantages as well as the exigence of having very accurate information in the all phases of the flood risk assessment, are leading to the attempt to integrate this technique with other well-known techniques (i.e. hydraulic modelling in the prevention and post event phases) and/or other innovative tools (i.e social media marker for the monitoring and post event phases). In detail, hydraulic modelling and social media marker as supporting techniques for the post event investigation and machine learning for the nowcasting phase are described.

2.2.1 HYDRAULIC MODELLING IN FLOOD RISK ASSESSMENT

Modelling, in conjunction with hydrological analysis, allows determination of flooding extents, levels, depths, velocities, and overland flood routing. Modelling may also be used to determine scour, sediment and pollution dispersal. All these parameters are important in order to assess a flooding risk in the area of interest.

Effective flooding management requires flooding inundation mapping, probabilistic estimates of potential damage and risks in flooding zones, and the design of a master plan for flooding risk mitigation (Pinos & Timbe, 2019).

Hydrodynamic–numeric models compute flooding by solving the hydrodynamic equations of motion for given geometric and hydraulic boundaries and initial conditions (Fohringer J. et al., 2015).

Usually, hydraulic modeling flooding maps are mainly obtained by 2-D flooding simulations, (see, for example, Proust et al., 2010; Costabile & Macchione, 2012), even if there are some applications with 3D models (Orton et al. 2018).

In general, computation time depends on the spatial resolution (Falter et al., 2013) and on the complexity level of the numerical algorithms for integrating model equations (Horritt and Bates, 2002; Vacondio et al., 2014).

The two-dimensional approach is preferred when the flooding must be simulated on a large scale (more than 10000 km²) (Hunter et al., 2008; Mignot et al., 2006). The information extractable from this numerical method refers to the depth, velocity and the extension of the flooding. These are the fundamental quantities required for damage evaluation (Grigg, N. S., & Helweg, O. J., 1975). Another approach that is widely found in the literature refers to 1D + 2D models, in which the river is discretized in one dimension while the surrounding environment in two-dimensional (Mazzoleni et al., 2013; Leandro et al., 2009). Generally, flooding hazard assessments by hydraulic models are affected by several sources of uncertainties which have significant consequences on the flooding maps accuracy. In particular, uncertainty could arise from scarcity of the hydrological data or knowledge of hydraulic parameters necessary to model calibration and validation, from a low spatial resolution assumed to limit the time consuming, especially in the case of flow simulation in urban areas where the motion resistances depend on the complex interaction of the flow with the structure (Di Baldassarre & Montanari, 2009; Bales & Wagner, 2009; Di Baldassarre et al., 2010; Grimaldi et al., 2013; Domeneghetti et al., 2013; Dottori et al., 2013; Jung and Merwade, 2015, Ferrari et al. 2019). Very accurate hydraulic simulations require the use of computational cell sizes of the same order of accuracy of the Digital Terrain Model (DTM). If the latter has very high spatial resolution, e.g. LiDAR, simulations are extremely time consuming.

To reduce the computation time, especially in the case of modeling a flooding in urban areas and in very large areas, some hydraulic models use an approach called subgrid (see, eg, the reviews by Balzano, 1998; Bates and Hervouet, 1999; 2009). Shallow water equations that include subgrid models for bottom elevation were proposed in the past by Bates and Hervouet (1999), Casulli (2009), Defina (2000), Viero et al. (2014).

Such subgrid approaches were applied to model effects such as overland flow over irregular topography (Defina, 2000), roughness and topographic effects based on LiDAR data (Casas et al., 2010), additional friction due to emerging vegetation (Mason et al., 2003), inundation of urban areas (McMillan and Brasington, 2007; Sanders et al., 2008; Yu and Lane, 2006), river hydraulics over large areas and data sparse areas (Neal et al., 2015; 2012), and coupled hydrological-hydrodynamic simulations in low-land catchments (Viero et al., 2014).

Furthermore, 2D hydraulic models for flooding simulations have to be able to manage wet and dry conditions, shock from super critical to subcritical flows and the direct application of the rainfall.

2D hydraulic models able to capture this shock have been proposed by Alcrudo & Garcia-Navarro (1993), Anastasiou & Chan (1997), Mingham & Causon (1998), Toro (2000), Liand et al. (2004), Vacondio et al. (2014). Such studies have shown that most of the schemes provide good results in particular flow conditions, for example on regular discontinuous flows. Different performances were obtained in the case of irregularity of the topography or in the presence of dry areas (Sinagra et al., 2012).

(Pinos & Timbe, 2019) in their paper reported that there is a wide range of 2D packages developed by commercial organizations, government agencies, research groups, and universities (e.g. HEC-RAS in Brunner (2016), Iber in Bladé et al. (2014b), TUFLOW in Syme (2001), TELEMAC in Hervouet (2000), MSN_Flooding in Hartnett and Nash (2017), rapid floodings preading method-explicit diffusion wave with acceleration term (RFSM-EDA) in Jamieson et al. (2012), and the Wolf software in Archambeau et al. (2002)). Merwade et al. (2008) claimed that the numerical solution schemes of models are the most important source of uncertainty. Furthermore, hydraulic models are sensitive to the description of geometry, the value of model parameters, and the representation of hydraulic structures such as bridges, culverts, and embankments.

2.2.2 FLOODING RISK ASSESSMENT USING SOCIAL MEDIA MARKER

Social media markers (e.g. Twitter, Facebook, Telegram etc.) are a rather recent source of information, potentially very useful in the flooding risk assessment and in the management of flooding emergency. In fact, the citizens, with their smartphone, examples are shown in figure 6, can provide detailed real-time descriptions on the type of flooding and the damage that is taking place. Moreover, these “posts”, allow the identification of position and the time to which a particular flooding event refers. Thus, social media can potentially provide timely and reliable information as to the extent of damages during and immediately after natural disasters.



Figure 6 - Social marker posted during hurricane Harvey in Houston that allows to localize the area affected to flood

A very interesting application of social media useful for the flooding risk assessment is for the build a rapid flooding map (Fohringer et al., 2015). The flooding map was created using only the photo information filtered by Twitter and Flickr. The images obtained from the social network have been selected through keywords, for the period of interest of the extreme event considered and for the geolocation of the seats. In other studies (Li Z. et al., 2018; Wang R. Q. et al., 2018; De Brujin et al., 2018; Li J. et al., 2017; Rosser J. F. et al., 2017; Smith L. et al., 2015; Poser K. et al., 2010) it has been shown how the use of social media, from the point of view of qualitative information, is potentially a good way for the creation of flooding maps data for emergency response. However, while social media data may be used to fill the gaps in remote sensing data, they struggle to provide information on flooding in urban areas or covered by vegetation as described above.

However, these references also demonstrate that flooding maps obtained using only social media data give rise to overestimations in terms of extension of inundation. Sources of errors include the differences between the place where the photo is taken and the location of the tweet posted online, the photo-interpretation of the perspective with which the photo is taken that can involve significant estimation errors from the point of view of the depth and the horizontal extension of the flooding. In order to improve the interpretation of depth, often the estimate is made by comparing the parameters of a DEM with what is seen in the photograph. This technique is widely used when you want to make flooding maps quickly and you tend to combine a higher resolution DEM LiDAR with the photographs you have available. (Mandlburger et al., 2009) showed that by combining high resolution DEM and social media it is possible to obtain alluvial risk maps with acceptable vertical precisions.

In each case, an issue still not completely solved for a generalized use of social markers concerns the selection of the photographs which are appropriate and useful for drafting flooding hazard maps. This requires the necessity to filter the huge amount of information from the social media. Recently, several approaches have been pursued so far: (1) filtering by keywords or by geographic queries (Rogstadius et al., 2013) or Joseph et al., 2014), (2) filtering by crowdsourcing (Howe, 2006), (3) automatic filtering utilizing machine learning and natural language processing (Sakaki et al., 2010); Yin et al., 2012) and (4) interactive visual spatiotemporal analysis/geovisual analytics (MacEachren et al., 2011); Morstatter et al., 2013). None of such approaches has resulted completely satisfying, and often a further rather empirical post-processing phase by the direct observation of the photographs from the operator is typically applied.

2.2.3 ARTIFICIAL INTELLIGENCE ALGORITHMS IN THE NOWCASTING PHASE OF FLOOD RISK ASSESSMENT

As previously reported, the main goal of the hydraulic modeling, based on the numerical integration of fluid motion equations, is to provide flooding maps that can allow to obtain information at different times about the inundation extension, and flow depth and velocity. Generally hydraulic simulations with a reasonable spatial scale resolution require computational times that are too long to provide flooding maps in real time as it is necessary in the nowcasting phase, or in applications that require a large number of model runs, e.g. in sensitivity, scenario and optimization analyses (Christelis et al. (2016). In order to reduce the computational time needed to calculate flooding maps produced by heavy rainfall events, different strategies have been already proposed. In detail, continuous researches and developments were conducted to reduce the computation time, focusing mainly on 2D model enhancement methods (Chen et al. 2012b). Among the different approaches, grid coarsening methods (Hartnack et al., 2009) have shown that a 2D multicell solver may reduce the model runtimes up to 10 times. This multicell solver combines a coarse hydraulic computation grid with a fine grid that contains topographical data. Instead, (Chen et al. 2012a) introduced a Building Coverage Ratio and a Conveyance Reduction Factor combined in a 2D Urban Inundation Model (UIM) to take into account building structures within a coarse grid. They then developed a multi-layered approach to add flow diversion or blockage effect due to the presence of the buildings in their previous method (Chen et al. 2012b). Some other recent studies show promising developments in the cellular automata approach for urban hydroinformatics (Dottori & Todini 2011, 2012; Ghimire et al. 2011). Such approaches are emerging in urban flooding applications but still require to be tested on large areas and real-life case studies (Ghimire et al. 2011).

Other modelling speeding-up strategies, reported in the literature, focus on parallel processing and hardware advances (Heronin et al., 2013). In detail, Lamb et al. (2011) developed a 2D diffusive wave code that uses fast graphic processing units (GPU) usually dedicated to games and advanced computer graphics. They showed that the use of such enhanced hardware appears very promising for fast 2D flood simulations

achieving a 114 speed-up factor with their accelerated GPU code compared to the conventional central processing unit (CPU) code. Vacondio et al, (2014, 2017) in his study showed the potentiality of the GPU-accelerated 2D SWE numerical code PARFLOOD. This model solves the conservative form of the 2- D shallow water equations on a finite volume scheme. Moreover, in order to reduce the computational time, the Jacobian matrix estimation procedure has been parallelized. This methodology allowed to take advantage of the computational capability of modern high-performance computing (HPC) clusters, which are usually equipped with many GPUs.

Alternative approaches to those above cited are based on surrogate models, also known as a meta-model or reduced-order models (ROM), that are empirical approximated models that mimics the physically based relationship, formalized by the hydraulic model, between the input and the output data. Meta-models and surrogate modeling are often used as synonyms (Ratto et al., 2012; Razavi et al., 2012a). The aim of surrogate models is to emulate and replace the complex simulation calculated by an hydraulic model, that requires high computational resources, with one obtained by a simplified and fast-to-run model (Castelletti et al., 2012; Yazdi and Salehi Neyshabouri, 2014). In the past, different well-known approximating approaches were used for flooding applications, such as kriging, polynomial functions, genetic algorithms, fuzzy logic, artificial neural networks (ANN), radial basis functions (RBF), k-nearest neighbor (K-NN), gaussian emulator machines, support vector machines (SVM), smoothing splines, ANOVA models, etc. (Campolo 2003; Chau et al. 2005; Lin et al. 2009; Cheng et al. 2010; Solomatine & Ostfeld 2008). As already mentioned, Christelis et al. (2016) reported that the surrogate models are often used in applications that require a large number of model runs, e.g. in sensitivity, scenario and optimization analyses. In flood management applications, several surrogate models have been exploited for reservoir operations (Castro-Gama et al., 2014; Tsoukalas and Makropoulos, 2015), water resources management (Tsoukalas et al., 2016), and for reducing the complexity in hydraulic simulations (Gama et al., 2014; Meert et al., 2016; Wolfs et al., 2015).

An extensive review of meta-modeling techniques has been carried out by Santana-Quintero et al. (2010) and Ratto et al. (2012).

The use of machine learning, in particular artificial neural network as surrogate model, as clearly shown by the literature, appears to be very promising for this purpose. Among all the techniques present in the literature, neural network techniques are useful for time series modeling and forecasting because they do not require detailed prior knowledge of the underlying physical processes. Razavi et al., 2012 in his review on surrogate modeling shows that the ANN approach, compared to other existing machine learning models, presents the ability to predict multiple outputs simultaneously, making it the most appropriate for the real time applications.

In this thesis the Artificial Neural Network (ANN) was employed for building a machine learning model. In detail, the Time Delay Neural Network (TDNN) algorithm was chosen thanks to its ability to significantly reduce the computational costs.

ANN is an efficient mathematical modeling system that, through an efficient parallel processing, has the ability to mimic the biological neural network using inter-connecting the neuron units. Determination of the optimal structure of ANNs for a particular problem is probably the most important step in the design of ANN-based surrogates. ANN structural parameters/decisions include number of hidden layers, number of neurons in each hidden layer, and the type of transfer functions.

Among all ML methods, ANNs, as the most popular learning algorithms, are known to be versatile and efficient in modeling the complex flooding processes with a high fault tolerance and accurate approximation (Abbot et al., 2014). In comparison to the traditional statistical models, the ANN approach has been used for prediction with greater accuracy (Li et al., 2012). The ANN algorithms are the most popular in modeling the flooding prediction since the first usages in 1990s (Wu et al., 2010). ANNs are considered as the reliable data-driven tools for constructing the black box models to model the complex and non-linear relationship of rainfall and flooding (Sulaiman et al., 2017), as well as river flow and discharge forecasting (Kar et al., 2010).

There are two methods to train an artificial neural network: supervised and unsupervised (Kotsiantis, 2007).

Data sets for training machine learning algorithms may be continuous, categorical, or binary. When instances within the data set are provided with known labels (i.e. the correct outputs) the training process is known as a “supervised” process (Kotsiantis, 2007). When the labels are unknown, the process is called “unsupervised” (Kotsiantis, 2007).

Algorithms designed to undertake unsupervised learning, generally work with clustering techniques such as Bayesian techniques (Neal, 1995). Clustering techniques are methods that identify similarities between data instances. Such instances are given to membership of “clusters” with the aim to identify unknown but potentially useful classifications of data. Moreover, these have been used in a large number of problems, such as road sign recognition (Prieto and Allen, 2009), water resources (Kalteh et al., 2008) and text detection with character recognition (Coates et al., 2011). In general, unsupervised learning is based on the modeling of the underlying or hidden structure or distribution of the data to learn more about the data. Unsupervised learning is usually used when only the input data are available without the corresponding output variables.

Supervised learning requires a set of training data that is pre-processed such that, along with each instance of data, there is an included expected output for the artificial neural network. The most common model for supervised-learning neural network architecture is a feed forward network (see Figure 7). This is an arrangement of different layers of “nodes”, most commonly an input layer, a “hidden” layer, and an output

layer. Each layer within this arrangement has connections to the outputs of nodes of the previous layer, and each of these connections have an associated weight (Lippman, 1987).

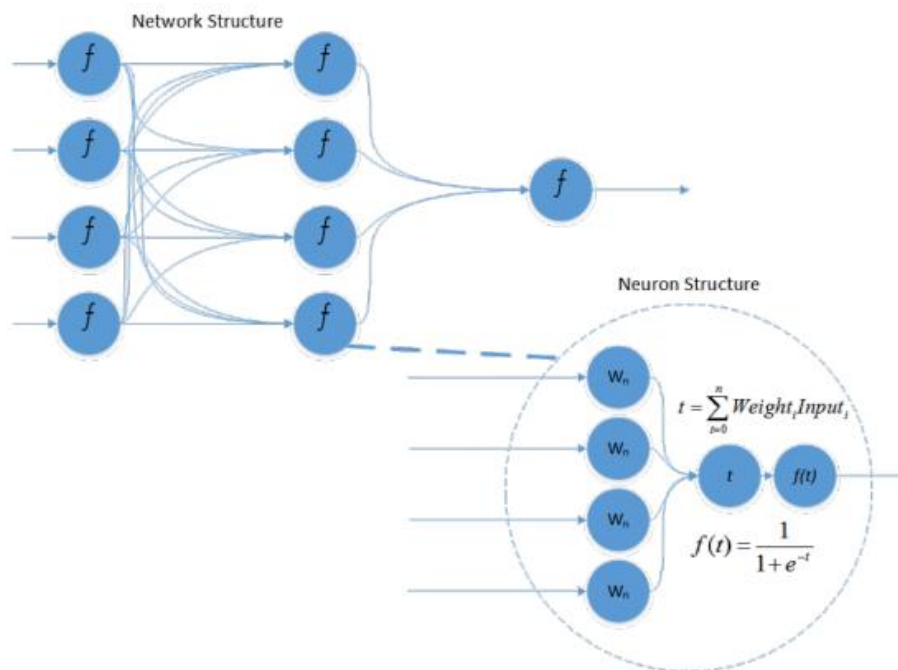


Figure 7 - Feed forward artificial neural network structure using a sigmoid activation function

Data then enter into the network at the “input” points and proceed through the network node by node. At each connection, data are multiplied by the value of the weight attached to that connection. In general, supervised learning is a simply process of learning algorithm from the training dataset. Supervised learning is used where input variables and an output variable are available, and an algorithm to learn the mapping function from the input to the output can be used. The aim of this approach is the approximation of the mapping function to predict the output variables for the data when a new input is available for that.

ANNs offer the potential for a more flexible, less assumption-dependent approach to modelling flooding processes, and they have already been demonstrated to work successfully as substitutes for rainfall-runoff models (Minns and Hall, 1996; Smith and Eli, 1995; Abrahart and Kneale, 1997; Khondker et al., 1998). Most of the studies in the literature reported the use of feedforward multi-layer perceptron trained with backpropagation (BPNNs) (Rumelhart et al., 1986). However, there are many other ANN algorithms and architectures that still have to be investigated (Shepherd, 1997). Time Delay Neural Networks (TDNNs), which are used in speech recognition (Waibel, 1989), are gained considerable attention thanks to their ability to significantly reduce the computational costs. They provide one type of network that could especially benefit the flow forecasting because these networks can potentially find the temporal relationship between inputs. TDNNs are designed to detect temporal relationships in a succession of inputs, independent of the absolute time (they seeks relationships between inputs in their position relative to each other, rather than their

position in the data set). This technique has already been exploited for both the forecast and nowcasting phases of flooding risk assessment (Kneale et al., 2001; Debbarma et al., 2019; Wu et al., 2019; Wan et al., 2019; Kim et al., 2019).

2.3 AIM OF THE THESIS

The main advantages of the remote sensing from satellite are its ability to give information of huge areas (including areas that are difficult to be reached from other technologies) and to be a useful tool in all the phases of flooding risk assessment. As a consequence, this technique is raising an increasing interest and hence several missions will be launched in the space in the next few years.

On this bases, **Chapter 3** analyses the capability of remote sensing to be helpful in the post-event flooding risk assessment by applying it to a real case. In detail, the coastal area of Mazzocchio (LT) was selected and SAR images were analysed using the PS technique to evaluate the subsidence phenomenon. After that, in order to overcome some limitations emerged during the study, other techniques were integrated with remote sensing from satellite and applied, even in this case, to rebuild post event flooding maps. For this purpose, remote sensing was combined with hydraulic modelling to determine the flood extension of the Strymon river after an extreme alluvial event by using SAR images. However, because of the lack of validation of the obtained results in this case study, also social media marker were considered and the combination of all of these techniques (remote sensing from satellite, hydraulic modelling and social media marker) was applied to rebuild two different real case studies, namely, Harvey hurricane and Diamrey Typhoon. Such events happened in the instrumented area of Houston and in the instrumented area of Quang Ngai (Vietnam), respectively. For the Harvey Hurricane, precipitation data from gauge stations were also considered and compared to those of remote sensing satellite, reanalyses and radar to understand which dataset could be used as input of the hydraulic modelling in not instrumented areas.

In **Chapter 4** some analyses have been performed to highlight the limitations exhibited from HEC-RAS software (used for three of the case studies reported in Chapter 2) in the rebuilding of the post event flooding maps. Therefore, a finite volume calculation code for the integration of motion equations mediated along the depth was developed. Such code was also validated though benchmarking tests and a real-case study.

Finally, **Chapter 5** describes the development of a surrogate model with the aim to overcome some shortcoming of the hydraulic modelling, mainly the long computational times. Such computational costs, in fact, are the main responsible for its failure in the nowcasting phase. The developed model was trained using radar real time weather maps as inputs and inundation maps (obtained as previously described in chapter 3) as outputs and through the machine learning approach. The accuracy of the model was then evaluated

comparing the outputs obtained from the trained surrogate model with those came from the inundation maps.

3 APPLICATION TO CASE STUDIES OF THE REMOTE SENSING FOR FLOODING RISK ANALYSIS

In this chapter, analyses of the capability of remote sensing to be helpful in the post-event flooding risk assessment were carried out by applying it to a real case. The analysis was conducted with reference to the possibility given by remote sensing to detect relevant variables affecting the flooding risk as subsidence, flooding area extension, spatial and temporal distribution of rainfall fields.

In the first application, the subsidence phenomena in the coastal area of Mazzocchio (LT) was studied. This area presents some depressions below the sea level and a dense network of channels. The analysis was implemented using SAR images through the PS technique. The main goal of this application was to understand if the remote sensing is a useful technique for the detection and monitoring of subsidence phenomenon.

After that, other techniques were integrated with remote sensing from satellite and applied to rebuild post event flooding maps.

For this purpose, remote sensing was combined with hydraulic modelling to determine the flood extension of the Strymon river after an extreme alluvial event by using SAR images. This case study revealed that the combination of hydraulic modelling with only the remote sensing results is not exhaustive to build a post event flooding map with high accuracy.

For this reason, also social media marker were considered and were combined with remote sensing from satellite and hydraulic modelling to rebuild two different real case studies, namely, Harvey hurricane and Diamrey Typhoon.

The choice of these two extreme events was not casual. In fact, Harvey hurricane happened in an instrumented area of Houston, while Diamrey typhoon in a not instrumented area of Quang Ngai (Vietnam).

In the first case it was investigated first of all if the integration of remote sensing, hydraulic modelling and social media marker allowed to rebuild a post event flooding map with high accuracy. In this case, social media markers were applied for the validation of depth results obtained with hydraulic modelling. Compared to the first case it was possible to have more information (i.e. from ground stations measurement) also from the social media marker, which enabled to understand the godness of the accuracy of the flooding map.

In the second case study, taking into account that Quang Ngai is a totally un-instrumented area from the point of view of the rain gauge stations and not provided with an accurate DEM (Digital Elevation Model), the importance of the accuracy of input data was investigated to obtain post event flooding maps with good

accuracy. For this study, both precipitation from satellite and DEM with low resolution (30 meters) were used.

After this study, an analysis was carried out on the precipitation datasets available in the literature - specifically deriving from satellite, reanalysis and ground radar - to understand if and which of them can be useful as input of hydraulic modeling in ungauged areas. A comparison was also made between the rainfall data measured by the ground-based measurement stations and those from the satellite, specifically from the TRMM using precipitation data of Harvey hurricane in Houston.

The different applications carried out are described in the following sections.

3.1 ANALYSIS OF THE SUBSIDENCE IN THE COASTAL AREA AND HYDRAULIC RISK IN MAZZOCCHIO AREA (LT)

The main goal of the analysis was to understand if remote sensing is a tool able to localize and quantify the phenomenon of subsidence, and also to understand the triggers that led this phenomenon to the area of interest.

Soil lowering phenomena, generally referred to as subsidence, represent the last stage and the surface result of a series of processes that take place underground. The main causes are due to natural and anthropic phenomena; the former are of geological origin, while the latter are linked to the superficial use of the soil. The subsidence involves most of the coastal and alluvial plains and is triggered or accelerated by the extraction and reclamation activities carried out by man. This induced subsidence can compromise human works and activities, often involving considerable material damage as well as modifying the physical-mechanical characteristics of the land involved and the surrounding environmental conditions, in a mostly irreversible manner. In particular, it increases the hydraulic risk in coastal areas, especially in areas with levels slightly above or below sea level, with frequent flooding in urban and agricultural areas; advances the salt intrusion inducing the rising of saline water through the subsoil; it makes the franc of "reclamation" jump and raise the ground water levels, modifying the characteristics of the subsoil and compromising also the cultivations; reduces system efficiency and surface water management in coastal reclamation areas; accentuates eustatism.

The monitoring of surface movements of the soil plays a fundamental role. Until the end of the last century, geometric leveling was the only method of height measurement that allowed the correct measurement of the extent of subsidence. Unfortunately, the national altimetric networks are very often inadequate for monitoring subsidence that requires millimetric precision. Since the 2000s, GPS and the SAR interferometric technique have been used through images acquired from satellite platforms. The continuous development

of the SAR interferometric technique, and the launch of new satellites ever more efficient, allowed to obtain more precise measurements, limiting in fact the use of geometric leveling and GPS. The use of interferometry allows us to study phenomena that affect very large areas with millimeter precision (up to 1 mm of precision), allowing us to reach places that are difficult to access by humans. Furthermore, this technique is less expensive than other monitoring techniques, such as airplane and / or drone operations. There are many case studies concerning the phenomenon of anthropic subsidence in coastal areas, among which the most important and documented, based on satellite interferometry, are the United States (New Orleans), Japan (Tokyo), Indonesia (Jakarta) and Italy (coastal strip of the Upper Adriatic, in particular Venice and Ravenna).

For the analysis of the subsidence phenomenon it was chosen one of the most sensitive and depressed areas of the Pontine Plain, Mazzocchio (Figure 8). This area was chosen because:

- 1) inside there is a complex hydraulic system susceptible to the sea level;
- 2) it has a particular morphology, in fact there is a depression below the sea level;
- 3) there is a geology and a hydrogeology that presents a poor surface drainage.

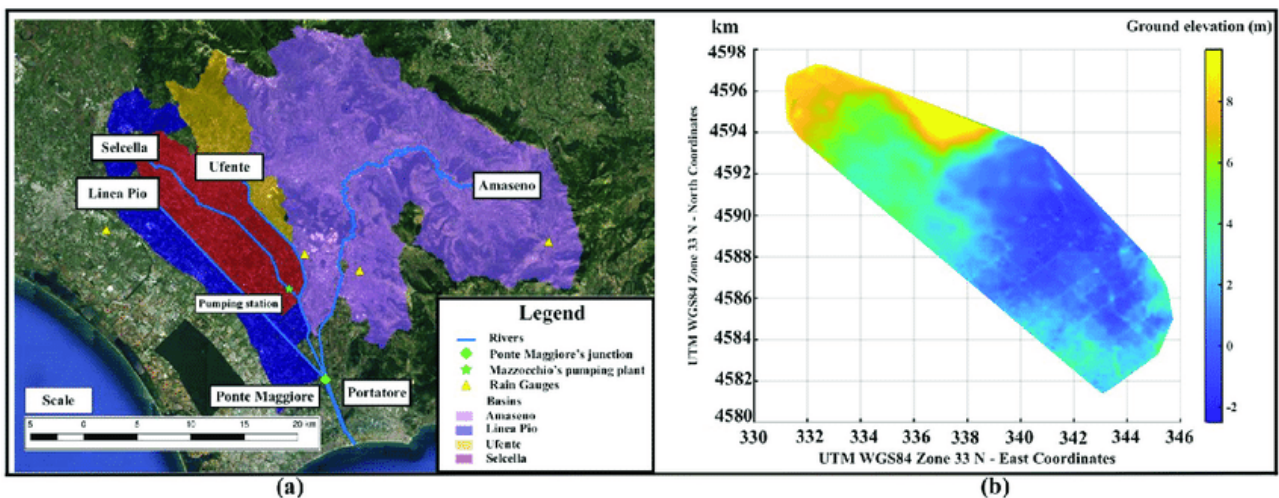


Figure 8 - On the left in red the area of interest of Mazzocchio is highlighted, while on the right the Mazzocchio's basin ground elevation.

The sea level is extremely important for the hydraulic management of the study area. In correspondence of extreme alluvial events, increasingly violent and frequent in recent years, when there is a high tide there is a reversing of the flow direction in the various rivers towards the hinterland. This phenomenon involves an increase in the hydrometric level of the various rivers present, causing suffering for the various depressed areas in the catchment area of interest and above all in Mazzocchio.

In order to drain the flow of surface water, at Mazzocchio, six water pumps have been installed.

The design of these hydraulic works was based on past hydrological considerations which, given the climate changes taking place, are totally different from today.

The area of interest, moreover, presents a condition of poor water drainage for three reasons: the completely flat morphology; the hydrogeological composition; and the presence of many springs.

The Pontine Plain, from the hydrogeological point of view, in fact, presents an extensive aquifer system characterized by a complex water circulation that is based on several levels, with different circulation modes. Starting from the top, we can recognize a thickness varying between 40-50 m (locally thicknesses of 100 m can be reached) of predominantly limno-marsh sediments consisting of alternations of silts and clays, with lenses of peat, clay, travertine and sand that not favor the infiltration of surface water.

The satellite images that have been used refer to those of the Sentinel-1 mission. This satellite mounts a Synthetic Aperture Radar (SAR) instrument on board.

The technique used for the implementation of the images refers to SAR interferometry. This is the study of the amplitude and phase difference of the retro-diffuse signal obtained by comparing SAR images, inherent to the same scene, taken at successive moments and therefore with slightly different viewing angles. The map of phase differences between two SAR images is called interferogram and this is "translated" into a displacement map. This type of analysis is very useful for monitoring any type of change in the earth's surface, such as the effect of earthquakes, landslides, subsidence, etc. (Figure 9).

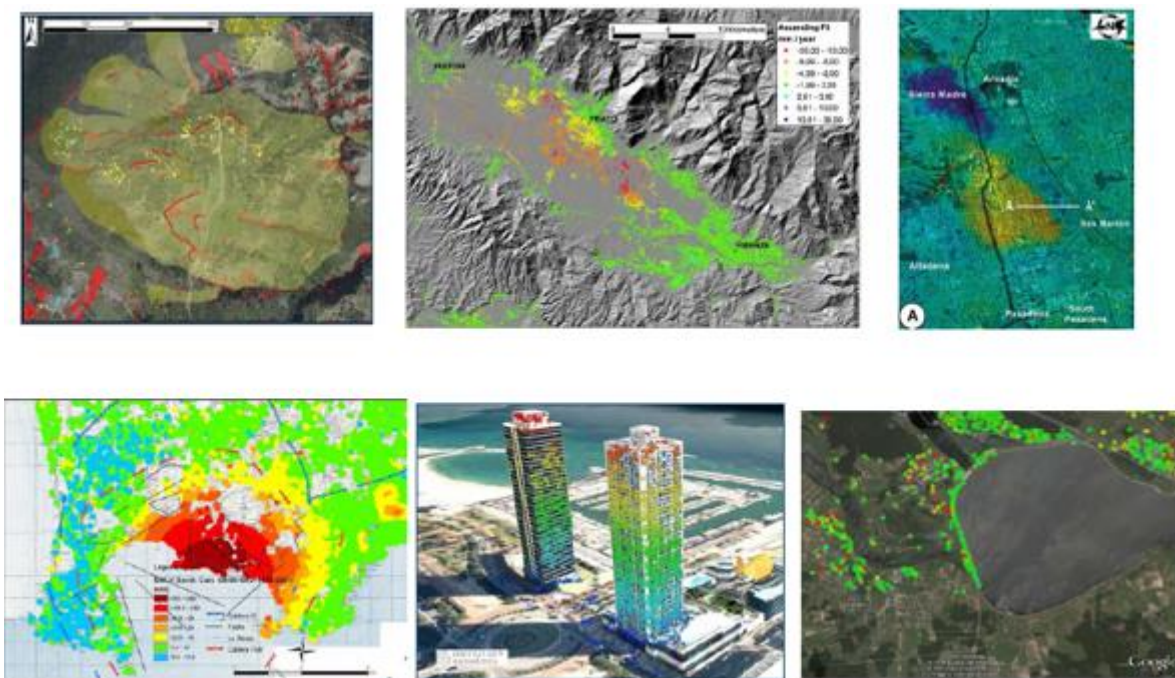


Figure 9- Examples of applications of satellite interferometry.

The techniques developed following the first promising interferometric results include a multi-image analysis to overcome the limitations of interferometry and to obtain quantitative and punctual measurements. We have said that the SAR image carries with it information on the phase and wave amplitude where the amplitude provides information on the reflectivity of the target, while the phase contains information on the sensor-target distance. These two types of information are fundamental for the Persistent Scatterers (PS) technique, ie the interferometric detection technique used in this study. The amplitude allows the identification of the PS, while the phase allows to estimate the displacement. The PS are targets with electromagnetic characteristics unchanged in all the acquired images. In general, they are points present on the ground (scatterers) visible in all images acquired during the observation period and which maintain a sufficient stability over time (permanent).

In this study, the RADAR satellite interferometric detection technique used is that of the PS-InSAR and represents an extremely effective tool for monitoring with millimeter accuracy based on the use of satellite RADAR image time series over the same area. This technique provides that the sensor sends an electromagnetic pulse towards the earth's surface and the elements on the ground reflect the signal, returning a portion to the satellite (retro-diffusion). By measuring the time elapsed between sending the signal and receiving the retro-spread signal, the system is able to determine the distance between the sensor and the target. Therefore, if the object is in an area affected by phenomena of surface deformation, the sensor detects, between one image and another, a change in distance and therefore the movement of the PS (Figure 10).

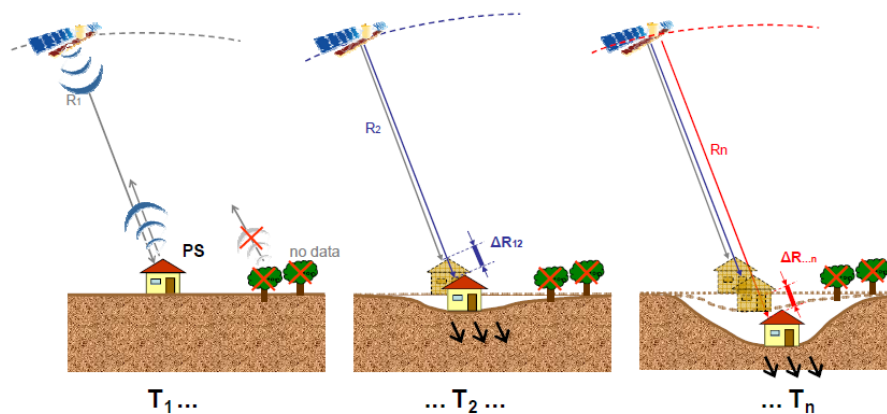


Figure 10 - PS-InSAR technique.

This technology allows to obtain a mill metric precision in the estimation of the displacement measurements on the ground allowing to carry out a subsidence monitoring with a high precision at any scale. The PS approach is practically immune to the effects of spatial decorrelation (PSs are much smaller targets than the resolution cell) and temporal (they are stable over time, in fact they maintain the same "electromagnetic signature" in all images to respect the geometry acquisition and climatic conditions, thus preserving the phase information over time).

Typically, the PS are artificial or natural elements already present in the soil whose electromagnetic characteristics do not change significantly from acquisition to acquisition. To perform accurate estimates of atmospheric disturbances it is necessary that the spatial density of the PS is sufficiently high ($> 5-10$ PS / km²) and use a data set of at least 25-30 images.

For the analysis, 178 images from Sentinel-1 were used, therefore a robust dataset, which allowed to analyze, for the area of Mazzocchio, the evolution of land displacement in a period from October 2014 to January 2018 .

Figure 11 shows the results of PS-InSAR analysis referred to Latina Province in which these local points (PS) are depicted on which the subsidence phenomenon.

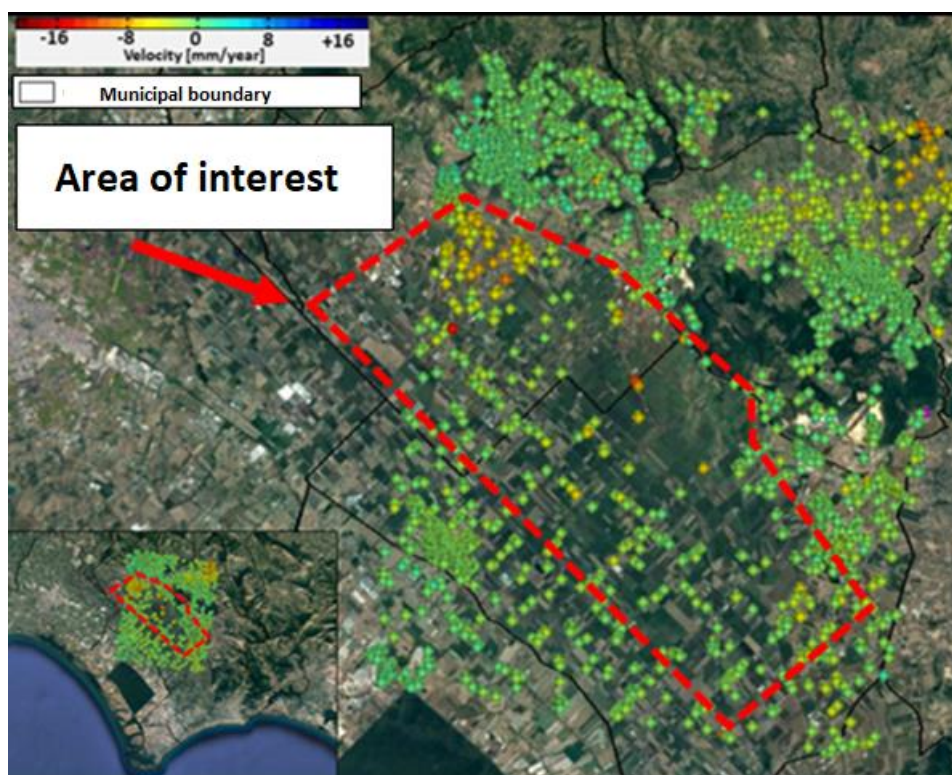


Figure 11 - Results of interferometric measurements (PS-InSAR) obtained from Sentinel-1 represented on Google Earth.
In red it was delineated the boundary of Mazzocchio basin (AoI).

In the figure with the colors yellow, orange and red the velocity of lowering of the ground is highlighted, in correspondence with the green there are substantially stable points (velocity values between -1 and 1 mm / year) and finally with various shades of blue the velocity inherent the raising of the land.

Note also that the distribution of PS is not homogeneous, i.e. in some areas there is a cloud with a greater density of points while in others the density is smaller. This is due to the presence, in the study area, of less urbanized areas and therefore with less target (PS) useful for the analysis. For these areas a geological and geotechnical study was conducted to understand the phenomenon of subsidence.

The main information extrapolated for each PS is:

- the location of the target on the ground, i.e. its spatial coordinates (latitude / north, longitude / east and altitude).
- the average annual velocity of displacement, expressed in mm / year, calculated in the interval of acquisition of the images processed in relation to the reference point;
- the time series of historical movements (Figure 12).

While the PS position is generally known with a precision of a few meters, the average velocity and time series of the ground displacements can be estimated with millimeter precision on the single point.

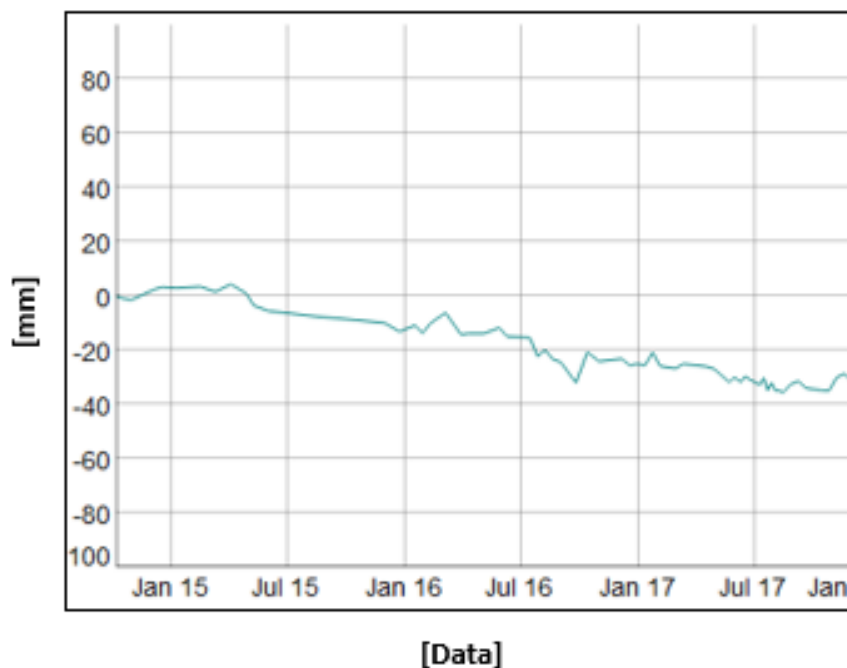


Figure 12 - Example of a historical series of movement of a PS.

Starting from these PSs, interpolation maps have been created that describe the evolution of subsidence in the area of interest. In this way it was much easier to identify those areas where the subsidence rate is more important. It has been applied for analysis the IDW interpolation algorithm (Inverse Distance Weighted) available as a plugin within QGIS. This method ensures a linear extrapolation of speed values in areas of the map that do not have PS. Inverse distance weighting (IDW) is a type of deterministic method for multivariate interpolation with a series of known scattered points. The values assigned to unknown points are calculated with a weighted average of the values available in the known points. The IDW interpolation suffers from an unfortunate artifact, the bulls eye effect. This issue describes concentric areas of the same value around known data points. The effect gets worse as the data points become more isolated.

IDW suffers from this problem more than other interpolation methods (e.g., Kriging), but to a large extent nearly any interpolation method will give unreliable results if the points are sparse and clustered. Conversely,

IDW gets good results with a range of methods if the points, as in our case study, are dense and uniformly spaced. Figure 13 shows the result of IDW applied in Mazzocchio basin.

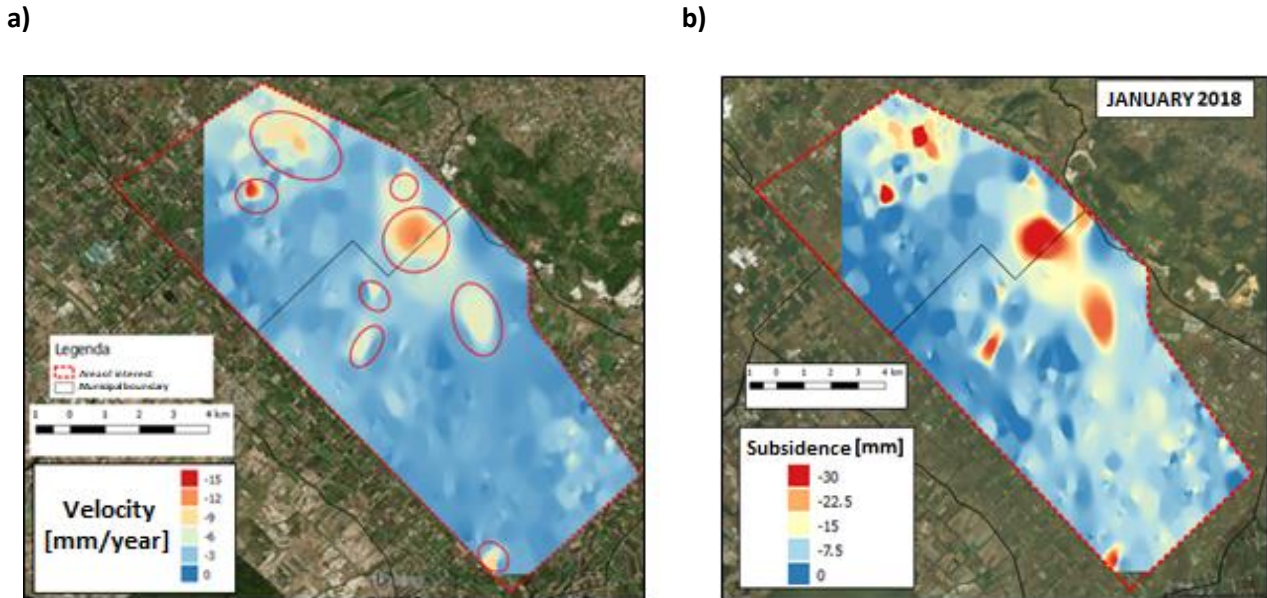


Figure 13 - IDW interpolation of interferometric data - a) Vertical displacement velocity [mm / year]; b) Subsidence from January 2018 compared to October 2014.

Figure 13 a shows that the phenomenon of subsidence in some areas was relatively faster than in others. This could lead to the hypothesis that we are dealing with subsidence caused by human activities rather than natural causes, remembering that this event occurs relatively quickly.

The purpose of this step was to identify the territorial areas in which the subsidence rate is more "critical", so as to concentrate mainly on them and obtain exemplary cases, which could explain the causes of subsidence.

IDW interpolation has also allowed the creation of a second supplementary map, visible in Figure 13b, corresponding to the actual dropouts [mm] of the study area. The color scale chosen in such a way as to better highlight the territorial areas that have suffered a significant lowering. It was decided to set the interval from 0 to -30 mm to display only the territorial areas that have suffered a negative movement or a sinking. Figure 13 b shows the territorial situation corresponding to the acquisition of January 2018 compared to that of October 2014. It is noted that in some areas there has been a decrease equal to and greater than 30 mm of the land underline the importance of the phenomenon in this area.

Using these subsidence maps it was possible to focus on some areas that have undergone significant subsidence and select a 16 PS to be used as exemplary cases for in-depth studies (Figure 14).

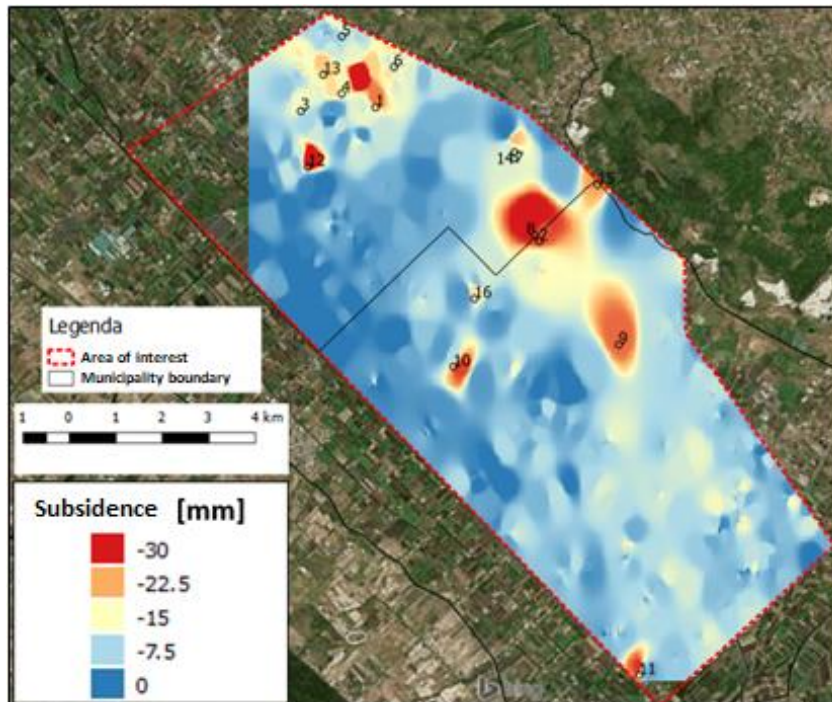


Figure 14 - Identification of 16 targets in map of subsidence of January 2018.

Once these 16 targets of interest were identified, it was possible to carry out various analyses:

1. For each target, see the subsidence trend in all satellite images used for the InSAR analysis;
2. Photographic analysis;
3. Existence of a correlation between the locations of the target with the presence of wells;
4. Existence of a correlation between the locations of the target with land use;
5. Spatial correlation through the technique of principal component analysis (PCA);
6. Comparison between precipitation and subsidence trends;
7. Spatial correlation between subsidence and drought through the evaluation of the SPI index.

The different points in the previous list will be discussed below.

As anticipated, the data acquired, for each PS, range from October 2014 to January 2018 with an average acquisition of 2 surveys per month. Figure 15 shows the absence of data in a few months (November 2014, July 2015, September 2015, October 2015 and November 2015) due to the fact that the images, for those months, were not available on the ESA geoportal. For the realization of the diagram and to have a clearer representation of the phenomenon, an average of the target values was realized based on the number of acquisitions made for each month, so as to report a single indicative value for each single target. Having said this preliminary phase, it can be seen how, at the end of 2014 until the middle of 2015, the performance of

some targets is positive. This behavior can be translated as the approach of the target to the ground towards the sensor placed on the satellite. Positive values can be interpreted as a phenomenon of groundwater recharge which induces a mill metric elevation of the soil. With regard to the actual phenomena of subsidence (negative lowering) it can be noted that this event is clearly more marked in the summer periods of each year, becoming more and more evident as time passes. In the summer of 2017 a strong subsidence was found which, for some targets, reached 40 mm. The trend of subsidence, after this "critical" period of 2017, has undergone a slight reduction reaching the month of January 2018 at a value that is not entirely negligible. This suggests that the phenomenon is more irreversible, that is, that the soil is unable to return to the same altitude in which it was previously.

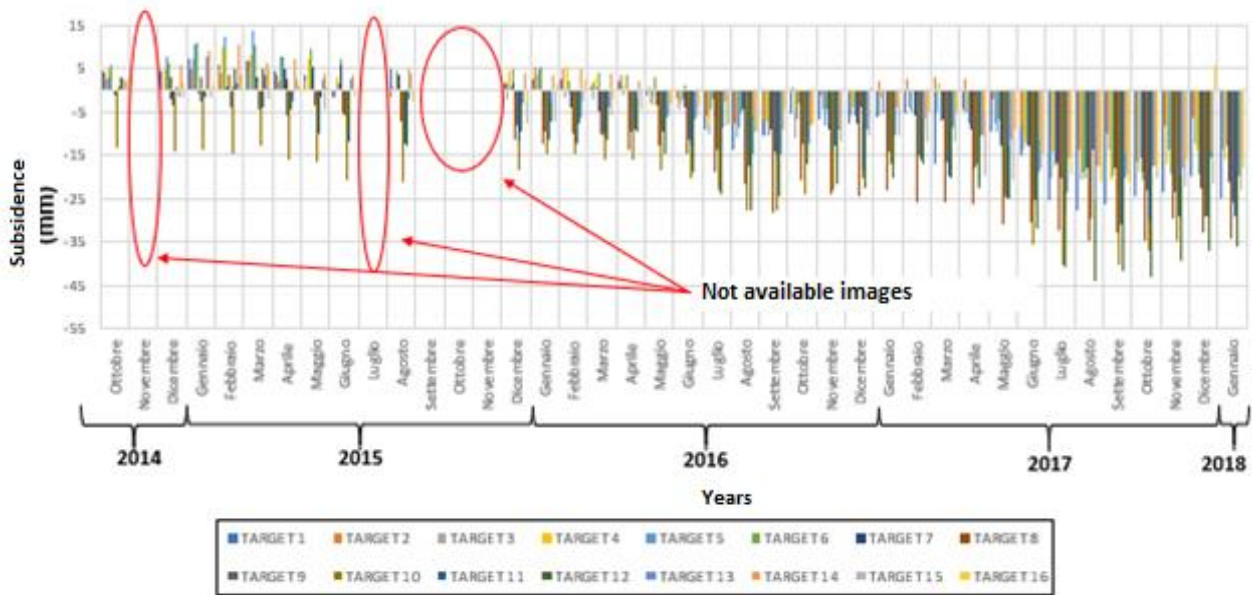


Figure 15 - Subsidence trend for the 16 selected targets (2014-2018 period).

Subsequently, a validation of the results obtained by satellite interferometry was performed. The validation was carried out through a territorial photographic analysis in the areas affected by more important subsidence, photographing evident signs of subsidence (Figure 16).

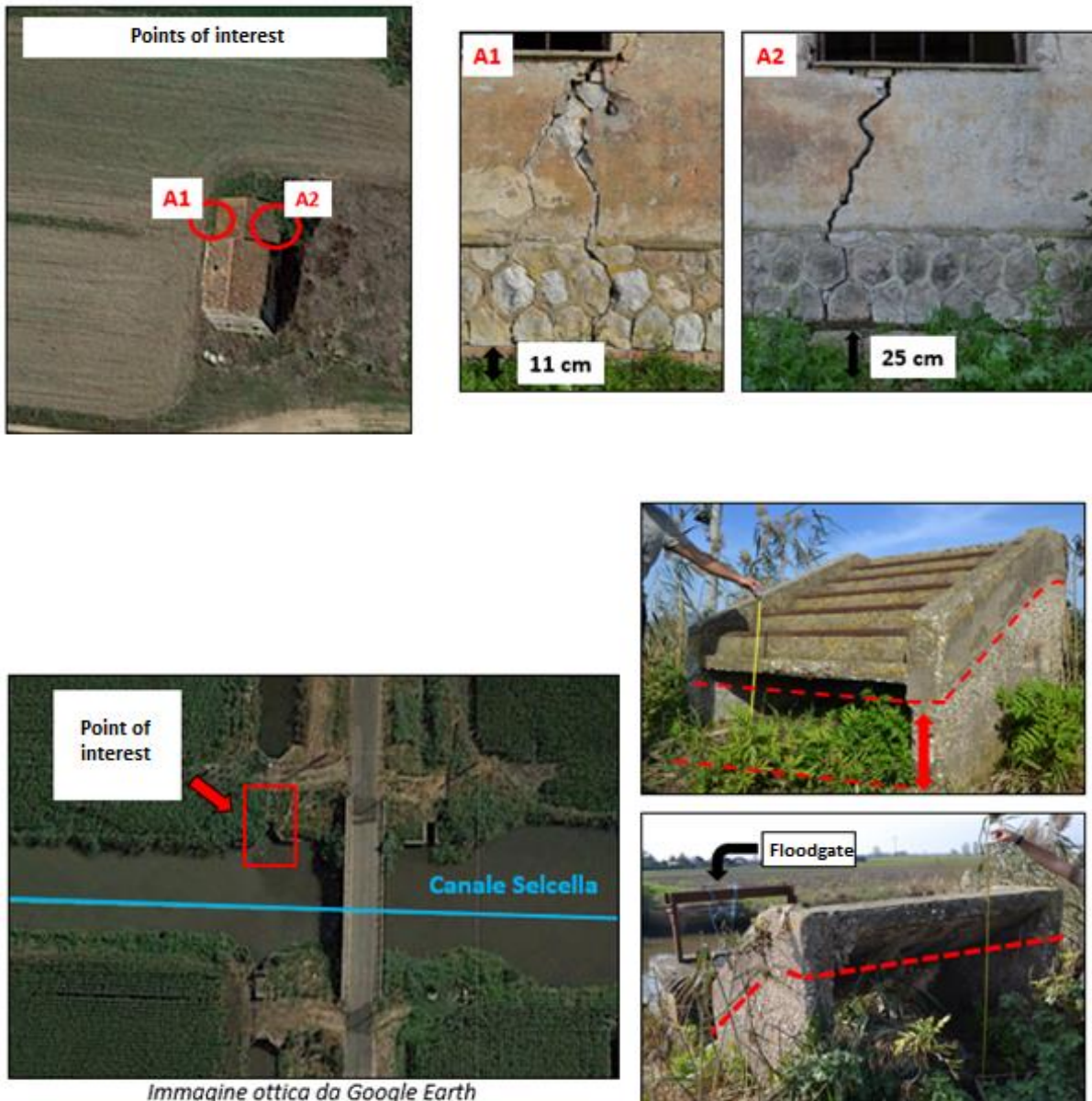


Figure 16 - Examples of photographs for the 10 and 12 targets that allowed to view the presence or absence of subsidence.

It was possible to deduce from this analysis how the targets identified by remote sensing were able to capture the phenomenon of subsidence, whose effects were clearly captured by the different photographs.

In the third analysis, groundwater collection works (wells) were identified, from which it was possible to spatially identify the position of each of them and see if there was a sort of relationship, based on proximity, with the most important subsidence zones (Figure 17).

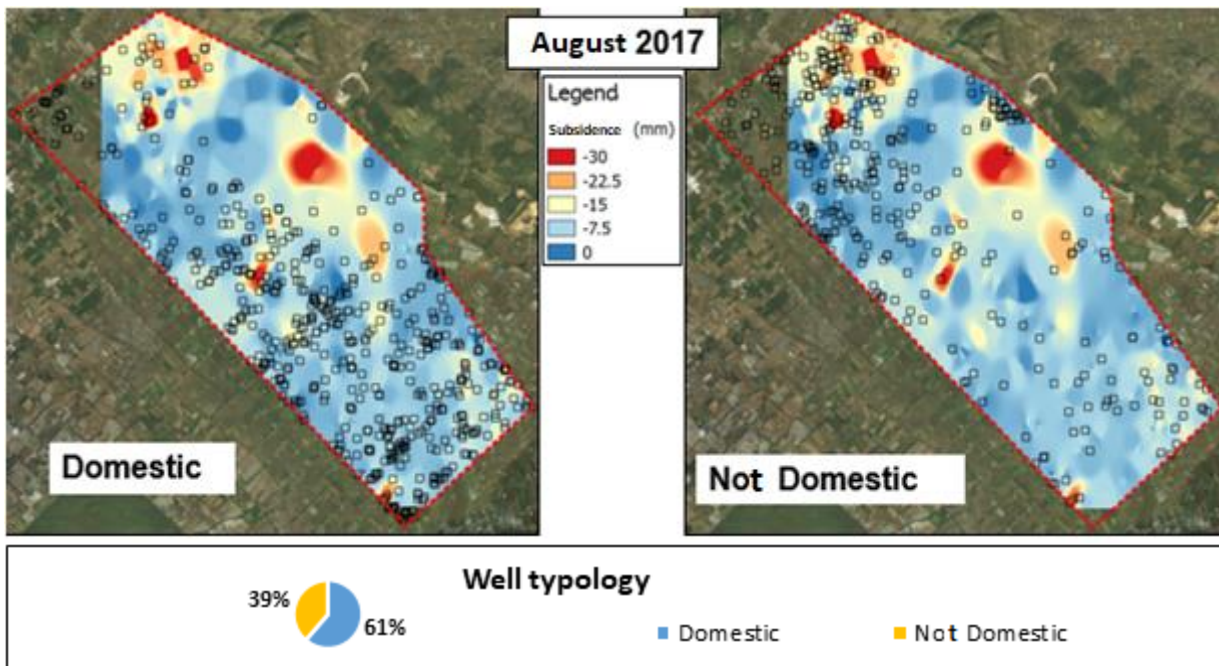


Figure 17 - Location and typologies of wells presents in Aoi

The results show that the relevant areas of subsidence were found near mainly non-domestic wells (irrigation, industrial, etc.) and this suggests a possible over-exploitation of aquifers in conditions of severe dry events. The quantities, in terms of percentages, relating to the two types of use of wells in the area of interest have shown that for 61% there are domestic wells, with a greater concentration located in the South, the remaining 39% represent non-domestic wells located mostly north-west of the study area.

In support of the analysis, it should be emphasized that obviously the reported value constitutes a decidedly underestimated value since the declared values to the authority are generally lower than those actually captured.

The fourth analysis, through a comparison based on the overlapping of the layers inherent to subsidence and land use, has allowed us to ascertain that most of the most "critical" subsidence was found on agricultural lands characterized by intensive cultivation with a prevalence of vegetables and protected crops. These types of crops require a considerable water requirement. The analysis was carried out using various photographs of the study area in addition to the land cover made available by the Lazio Region.

To verify if there was a sort of spatial coherence of the subsidence phenomenon, the PCA method was applied on all interferometric data falling within the study area, so as to calculate the first main component (PC1 = 70% of variance). Principal component analysis (PCA) is a multivariate statistical method that is very effective in compressing a series of correlated data and extracting the most relevant information describing the systematic variability of the data.

What we try to see, doing this kind of correlation, is whether the study area has undergone a collective subsidence over the whole territory or only in an isolated manner.

After obtaining the correlation value for each target it was possible to create a correlation map, using the IDW interpolation method, to further facilitate the representation of the data on the entire area of interest (Figure 18).

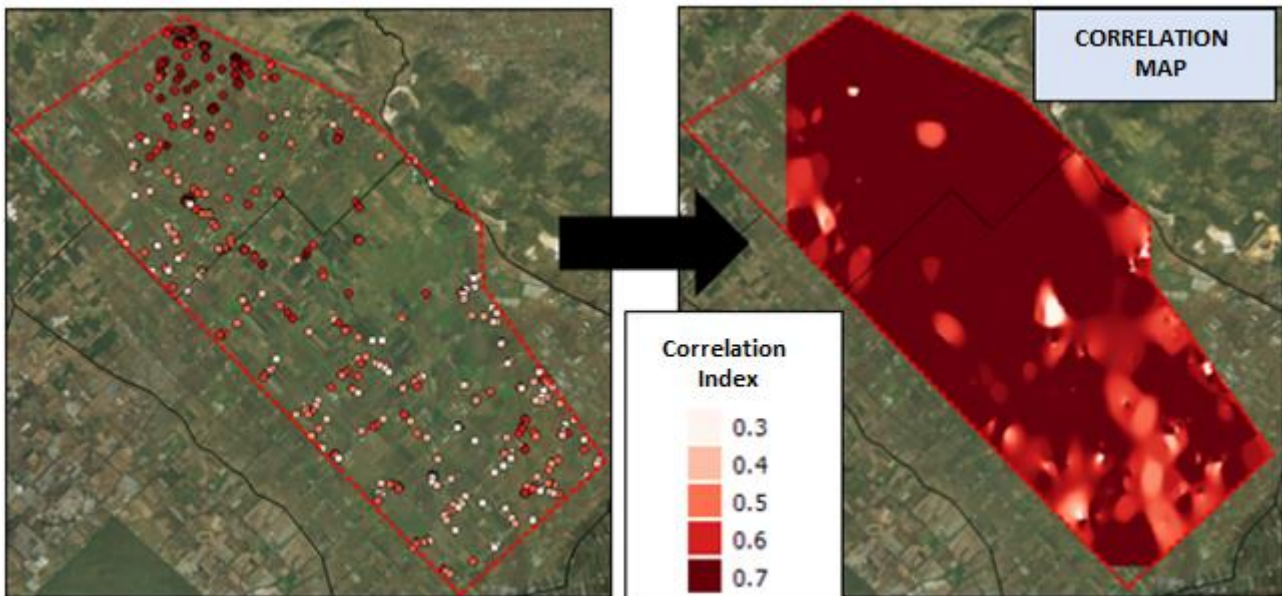


Figure 18 - Results of the correlation between PCA and Target (individual data of each target in the image on the left. Correlation map in the image on the right).

The result of the correlation shows a sort of global spatial coherence of the subsidence phenomenon trend, in which the areas in which there is a more marked correlation show that they have a collective lowering of the ground level. This means that almost the whole area has suffered a lowering of the ground, for some points more drastic while for some less relevant. That said, we proceeded with two other types of correlation.

The first refers to the correlation between the various rain gauge stations with each individual PS. Through the representation of the subsidence trend of each single target, together with the pluviometric trend of the stations, it was possible to have a first direct comparison, even if qualitative, between the ground deformations and the different local meteorological contributions of each station to single gauge. In this phase, the intent is to be able to detect a sort of analogy and correlation between the two phenomena.

This operational phase is aimed at a better understanding of the phenomena and their spatial characterization and temporal evolution, limited to the period in which the available data overlap. What we have been able to find, first of all, with this comparison, is that based on the monthly amount of rain, a response is given to a certain lowering or raising of the subsidence value. For example, from Figure 19 it can be seen that in the summer season of 2017, in which a strong water crisis occurred, due to low rainfall, the

level of subsidence has increased dramatically and this allows a sort of reasoning on the potential link that can exist between the two phenomena.

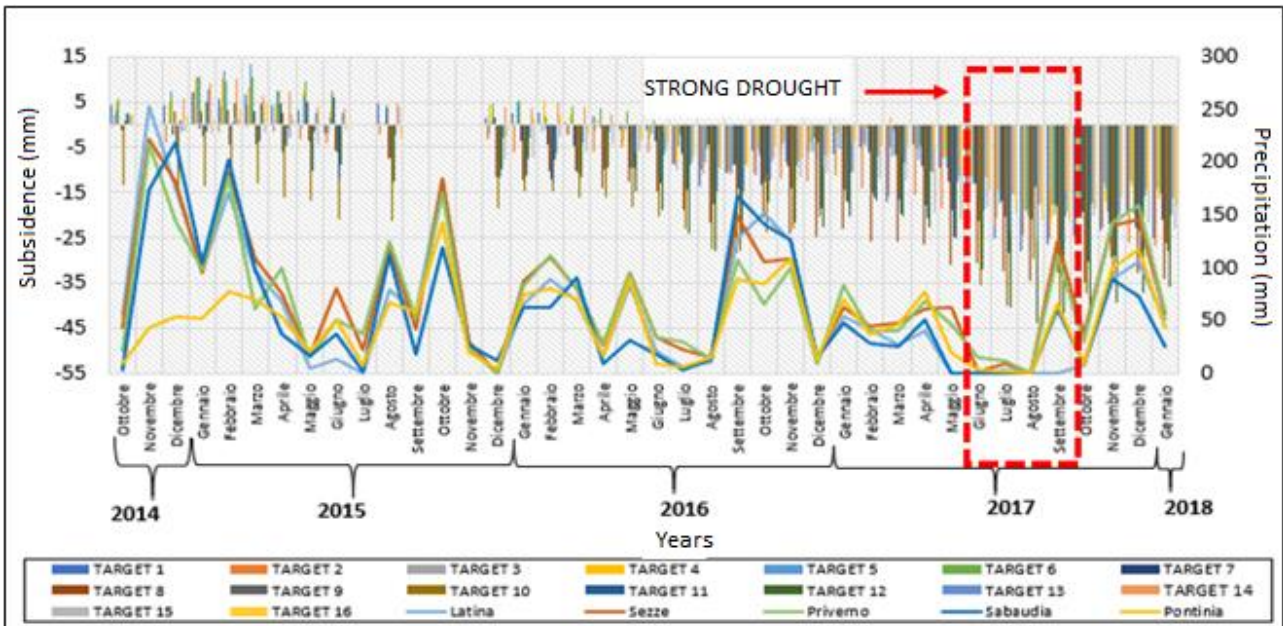


Figure 19- Precipitation and subsidence trends inherent to the 16 selected targets.

Finally, the last correlation achieved concerned the drought values with the individual PS. The graphical representation of the progress of the two measurements is shown in Figure 20.

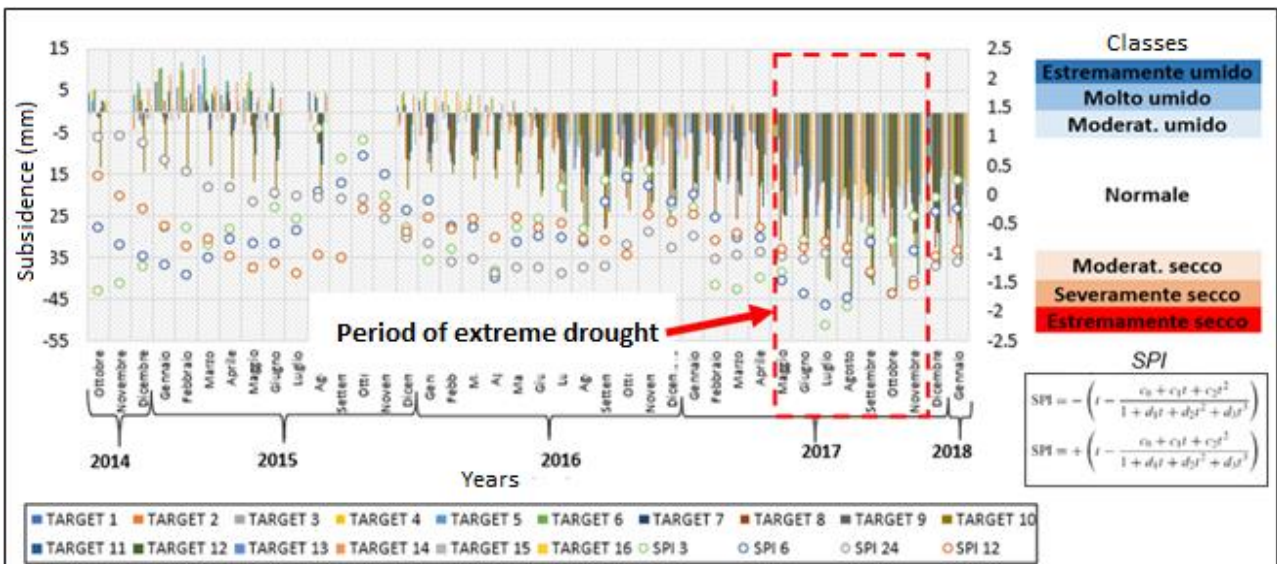


Figure 20 - SPI index values and subsidence trend inherent to the 16 selected targets.

By applying the Pearson correlation index it is possible to obtain 4 correlation maps based on the correlation between subsidence measurements and the SPI index inherent to the 4 time scales (Figure 21).

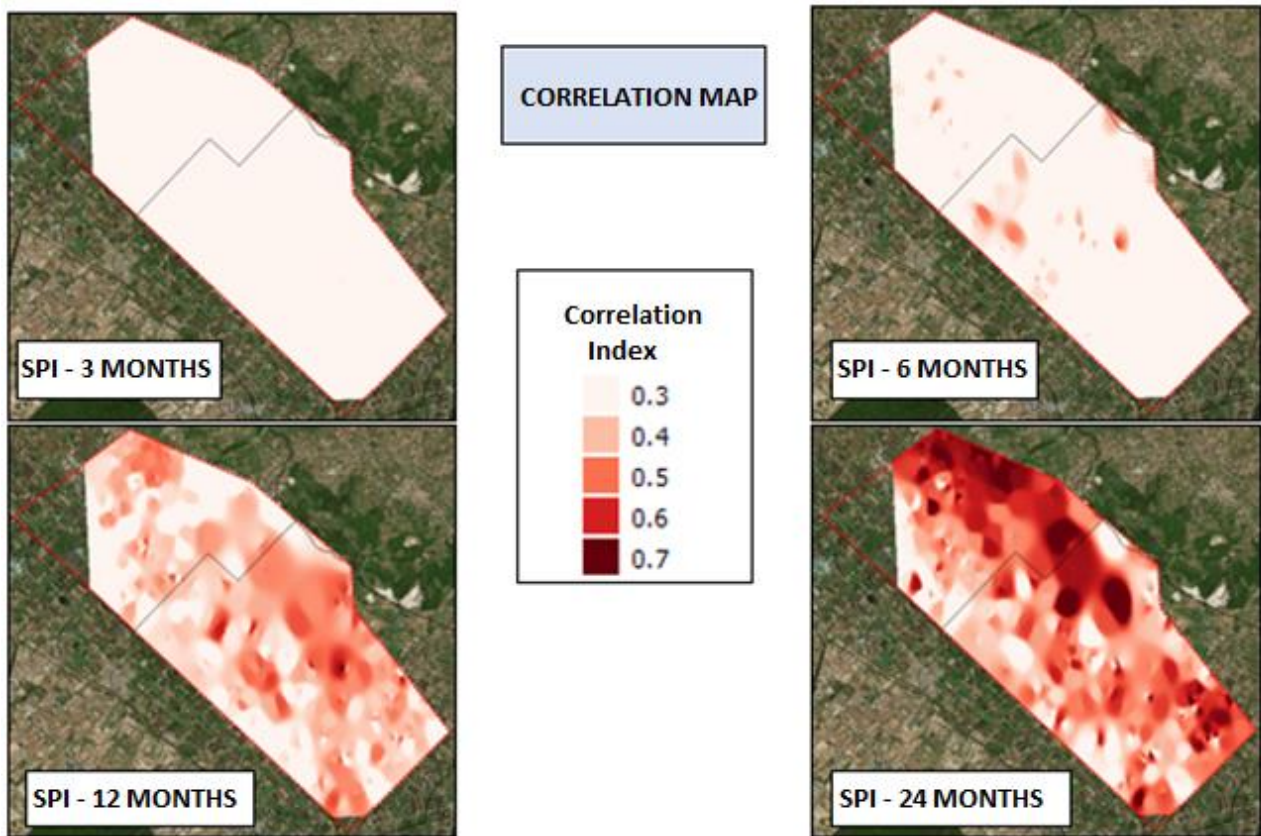


Figure 21 - Subsidence - Drought Correlation (SPI elaborated by the pluviometric data of the Pontinia station).

The objective was to identify which time scale, in relation to the SPI index, represented greater coherence with the trend of subsidence. The results show that there is a fairly important correlation on the territorial area located to the east of the study area, in particular near the Monti Lepini, inherent to the 24-month time scale. This scale, with greater correlation, provides such clear results due to the summer season of 2017 led to a serious water crisis and which led to a strong agricultural and hydrogeological drought. We can imagine this correlation as a kind of connection between the levels of piezometric groundwater variation with the subsidence phenomena found in the area.

The work carried out, consisting of targeted analyzes in the area, allowed to easily frame the environmental conditions of the investigated area of the Pontine territory. From the totality of the results emerged that in this area the phenomenon of subsidence depends essentially on two main factors: the overdrawing pumping from wells in conditions of strong agricultural and the drought phenomena, accentuated by a significant lowering of the soil during the summer months of 2017.

The InSAR satellite remote sensing technique is now a new and very effective tool for high precision monitoring of earth surface deformation phenomena. The ability to remotely cover large areas of the earth's

surface, without the need for instrumentation installation, makes it a tool with great potential for application in the area of land monitoring and control.

3.2 INTEGRATION OF SATELLITE INFORMATION (SAR) WITH HYDRAULIC MODELING: CASE STUDY OF THE STRYMON BASIN

This application allowed to understand how remote sensing from satellite can be integrated with hydraulic modelling. In particular, the possibility to exploit the information concerning the extension, to a certain time instant, obtained by satellite sensing as a calibration element of hydraulic modeling was investigated.

The Strymon basin was chosen as a study area (Figure 22). Strymon/Struma is a transboundary river with a catchment of 18,078 km² (290 km and 10,797 km² in southwest Bulgaria; 110 km and 7,281 km² in northern Greece), its tributaries even extending into four countries (small parts are in Serbia & Montenegro and FYR Macedonia). It has a mean runoff of 2,500 million m³/year (Greek border) and is of great importance for the irrigation of the Serres plain (100,000 ha) in Greece.

The course of the Strymon River through Greek territory is 26 km until it reaches the Kerkini Lake, the river stretch downstream up to the coast is 110 km long. Kerkini reservoir (109 km²) was built in 1933 at a former swamp for regulating the Strymon river discharges, irrigation and flooding protection (new dam in 1982).

According to Vouvalidis (1994), the Strymon River, as well as the rest of the hydrographic network in the area, was formed during the second phase of the Graben evolution (Quaternary up to the beginning of the last century), while during the third phase (from the beginning of the last century), flood control prevention, drainage, and irrigation projects were conducted. This last period was characterized by the creation of a “man-made hydrography.” Changes in bedding, and meander formation were also common.

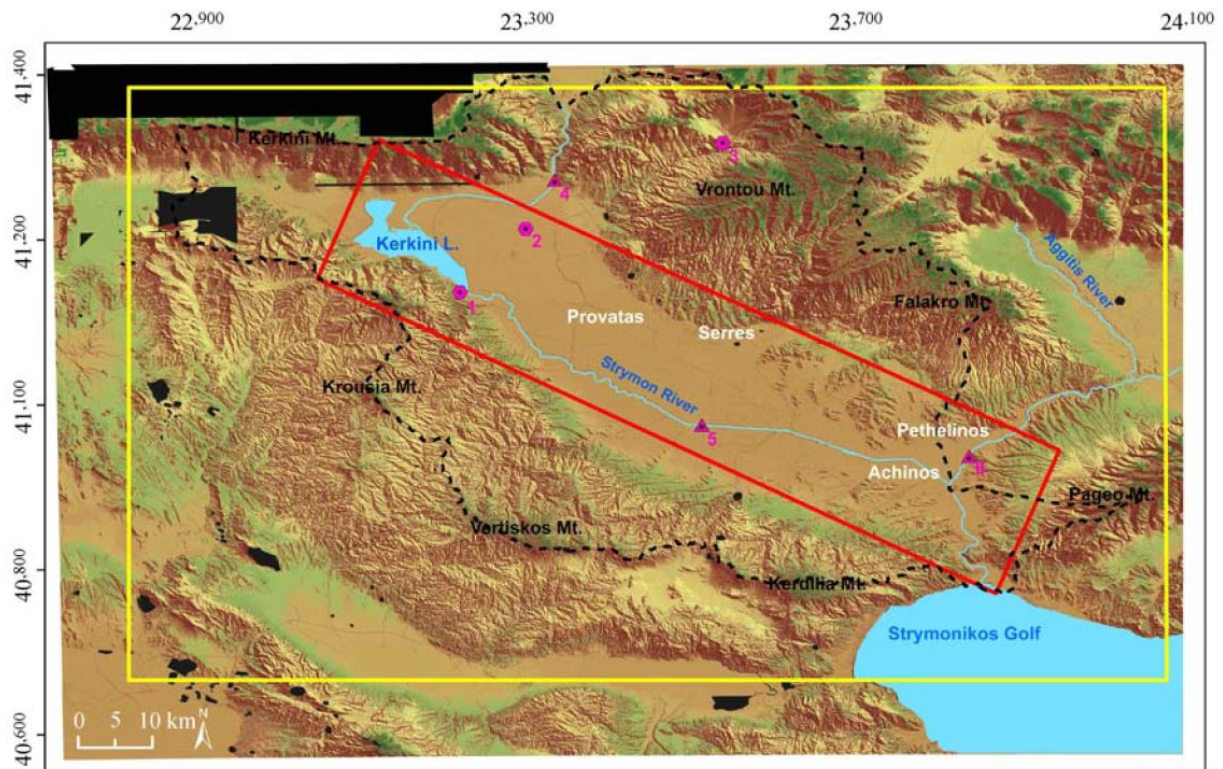


Figure 22 - Location map. Yellow frame refers to the SAR subset processed image; the black dashed frame represents the Serres basin; finally pink polygons represent the meteo-stations (hexagons): 1- Lithotopos, 2- Koimissi Serron, 3- Achladochori and the water level telemetry stations (triangles): 4- Trimeristis, 5- Nigrita, 6- Aggitis.

The water level in the lake is controlled by the incoming flow of the Strymon River, which is controlled downstream through the Lithotopos dam. After the 1983 construction of the dam the lake was characterized by seasonal changes of approximately 5 m in the water level (Jerrentzup, 1992) which decreased potential flood risk downstream. The dam, furthermore, affects the stratification conditions in the mouth of the Strymon River during spring and early summer (April to June) (Sylaios et al., 2010). The silting of the lake with debris from the Strymon River, causes in the Kerkini lake the reduction of the total volume of the water. The retention of sediment, in fact, essentially reduces the effective water reservoir volume which in turn decreases the amount of water that can be stored, and may even defuse flood benefits.

The Serres basin, one of the most important sedimentary basins in northern Greece, is located in the southernmost part of an on-shore, intra-mountainous graben, part of the broader Strymon basin which is located in eastern Macedonia. Its area of 3.970 km² constitutes 23% of the total area of the catchment basin of Strymon. The basin is the final recipient of natural water throughout the Strymon's catchment located both within and outside Greece (Psilovikos et al., 1994). The present form of a river network within the Serres basin is primarily considered as natural, yet has been negatively impacted by human activities over the last few decades in the form of construction using hydraulics. The boundaries of the basin are defined by the following mountains: Kerkini (north) Kerdilia, Krousia, (west), and Falakro, Lekani, and Pageo (south-east).

The total thickness of the Neogene and Quaternary sediments at the center of the basin is approximately 4000 m (Syrides, 2000). The sediments found in the area of Achinos consist of basal conglomerates, limestone, sandstone, marl, silt, and clay with a total thickness ranging from a few meters to 1000 m (Karydakis et al., 2005).

About 63% of the Serres basin is covered by marshes, lakes, ponds, and periodically by flooded land. Only 37% of the area was not threatened by floods. The large projects carried out in the area resulted in drainage of the ponds and marshes. The rehabilitation of several thousand acres were given to local population for cultivation (Perrou et al., 2018). Among the improvement projects, including the drying of Achinos Lake, was the arrangement of the Strymon River bed and the remaking of the old Lake Kerkititis, known today as Kerkini.

The images used refer to those obtained from the Sentinel-1 satellite. The Sentinel-1A, the first of the twin satellites, was launched in April 2014 by ESA, and was equipped with a C-band sensor, image swath of 250 km with the Interferometric Wide swath (IW) acquisition mode, spatial resolution of 5 m in range and 20 in azimuth, and a repeat time of 12 days. In April 2016, the Sentinel-1B was also placed successfully into orbit, decreasing the temporal resolution to 6 days.

Level 1 Ground Range Detected (GRD) Sentinel 1A C- band scenes were collected for this study from the Copernicus open Access Hub (<https://scihub.copernicus.eu>) on ESA's website. Level 1 GRD products concern SAR data detected, multi-looked, and projected to ground range using an earth Ellipsoid Model, with an approximate square pixel resolution.

A total number of 14 GRD SAR scenes, in descending and one in ascending Interferometric Wide (IW) swath mode, with polarization VV and VH, were collected spanning the period from October 2014 to October 2015 (Table 2). These data were processed and analyzed to create binary water/non-water products as well as SAR multitemporal products based on the contrast of the surface variations of land and water showing different back-scattering signatures.

Date	Orbit	Mode	Track/slice
2014/10/18	2879	Descending	7/5
2014/11/11	3229	Descending	7/5
2014/12/5	3579	Descending	7/5
2015/1/10	4104	Descending	7/5
2015/2/3	4454	Descending	7/5
2015/2/15	4629	Descending	7/5
2015/3/5	4899	Ascending	102/7
2015/3/11	4979	Descending	7/18
2015/4/16	5504	Descending	7/18
2015/5/22	6029	Descending	7/18
2015/6/27	6554	Descending	7/18
2015/7/21	6904	Descending	7/18
2015/8/26	7429	Descending	7/11
2015/9/7	7604	Descending	7/11
2015/10/25	8304	Descending	7/11

Table 2 - Catalogue of Sentinel-1 SAR scenes used

The satellite images were implemented through the SNAP software and with the process that can be derived from the diagram in figure 2.2.2. The detail description of the methodology applied for the implements of SAR images, can be found in the paper by Perrou et al., 2018. It was not been descript this methodology here, because we want focused on the possibility to obtain a flooding map with good accuracy using information from satellite flooding footprint and hydraulic modeling.

The hydraulic modelling HEC-RAS was used for the case study. The 2D hydraulic model, used in the analysis, refers to the USACE Hydrologic Engineering Center's River Analysis System (HEC-RAS 5.0.7). Such Hydraulic Numerical Models is a public domain software that meets the minimum requirements of National Flood Insurance Program as required by FEMA (<https://www.fema.gov/hydraulic-numerical-models-meeting-minimum-requirement-national-flood-insurance-program>). Recent FEMA report (<https://www.fema.gov/media-library-data/1561469561757-6fed6a4fd077673f684920b9ad5a0e53/RapidResponseFloodModelingFinalReport.pdf>) shows that such model produces results with highest precision (standard deviation) and predictive value (correlation) than other models.

The code, whose details can be found in HEC-RAS, River Analysis System Hydraulic Reference Manual, solves either the 2D shallow water equations (with optional momentum additions for turbulence and Coriolis effects) or the 2D Diffusion Wave equations. In the case study, full momentum equations were used. The equations in HEC-RAS are solved with an implicit Finite Volume algorithm. This algorithm allows the use of a structured or unstructured computational mesh. Local thickening of computational mesh can be applied by breaklines, added along levees, buildings, roads, and in abrupt slope change.

In HEC-RAS 2D modelling the mesh size can be arbitrarily chosen. Generally, to limit the computational time, especially for large integration domains, computational mesh sizes coarser than the spatial DEM resolution

are used. This would result in a rough representation of the domain geometry especially in building areas or in the presence of abrupt ground level changes. However, to take into account the details of the underlying terrain, the subgrid approach proposed by Casulli (2008) is integrated in the algorithm.

Such approach consists in calculating the volume and mass/momentum fluxes through the cell faces at the coarser scale by the modification of the continuity and momentum equations, expressed in integral form, to account the variability of the ground level and the presence of obstructions as represented at finer DEM scale. To this purpose, using the DEM, suitable relationships, describing the variation of the wet volume and area of the faces as a function of water elevation, are preliminary calculated for each cell. With this approach it is possible to exploit the high topographic information resolution obtainable from DEM and, at the same time, to use calculation cells with a size coarser than the resolution of the input data.

The HEC-RAS code simulates wet and dry conditions and allows the direct application of the precipitation. Neither spatial variation of precipitation nor losses and infiltrations are currently able to be computed within HEC-RAS. In the cases in which pluvial contributions and their spatial and temporal variability play a determinant role in producing flooding, these limitations could represent a serious drawback.

Through HEC-RAS, and through its combination with the flooding delineation obtained from satellite, a reconstruction of Struma river inundation were conducted. At the beginning, because of no discharge data of the rivers involved in the inundation were available, a hydrological study was done using another USACE software, HEC-HMS.

Through this software, applying a runoff method, the discharge data was calculate using the following gauge stations: Lithotopos (1), Koimissi Serron (2), and Achladochori Trimeristis (3). For the Aggitis river, tributary of Struma river present in the south of the area of interest, instead, the flow hydrograph was available. Both the typology of the station measurements, gauge and water levels, provided data every 15 minutes.

For the analysis, the hydrographs used as input of the hydraulic modeling were converted to a monthly average. This operation was necessary for the huge temporal permanence of the inundation in the area of interest. The boundary conditions of discharge of the upstream flow of the Struma and Aggitis rivers were applied to the hydraulic model. Downstream, instead, the sea level measurements (obtained from the website: <http://www.ioc-sealevelmonitoring.org/map.php>) have been inserted.

Because HEC-RAS does not allow the application of spatial precipitation distribution and infiltration, the calibration of the model was crucial for the right replication of the inundation emerged from satellite.

To overcome the above limitations, numerical model was calibrated using a saturation factor that allowed to obtain, the flooding areas detected from satellite for each temporal instants.

The saturation factor k as defined by Şen (2008) was assumed as calibration parameter

$$\frac{dR}{dP} = (1 - e^{-kP}) \quad (1)$$

Where $\frac{dR}{dP}$ is the runoff rate, being R the runoff and P the precipitation amount. Typically, the value of k ranges between 0.1 to 0.5 (inches⁻¹) in dependence on the land cover and of hydrologic soil group. In the present study case uniform values of k were assumed for the entire integration domain. To calibrate the model, the saturation rate k was varied within the above mentioned range. In this case study the k= 0.3 allowed to replicate well the inundation event.

In order to quantify, for the different values of k, the fitting between the flooding areas detected by satellite images A_{obs} and those obtained by mathematical simulations A_{sim} , the following index was used:

$$I(k) = \frac{A_{obs} \cap A_{sim}(k)}{A_{obs} \cup A_{sim}(k)} \quad (2)$$

The best fitting simulation is identified by the value of saturation factor k corresponding to the maximum value of $I(k)$. In Eq. (2) A_{obs} refers only to the flooding areas which are supposed to be detected by satellite.

The delineation of flooding derived from the SAR images and used for the calibration of the hydraulic model are shown in Figure 23.

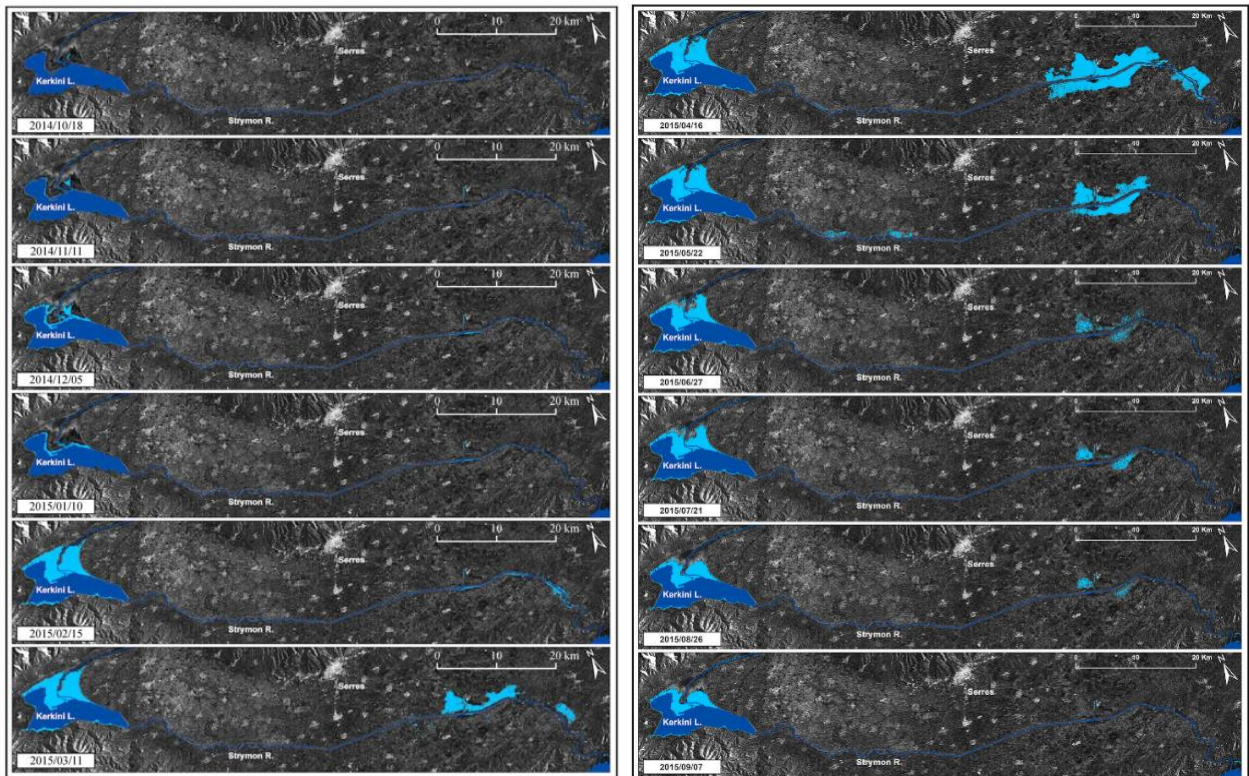


Figure 23 - Water/non-water. Binary images water/non-water from October 2014 to March 2015.

The other input data used in the hydraulic model, in addition to the discharge of the Struma and Aggitis rivers and the sea level, refers to:

- Digital Elevation Model (DEM) in the WGS84 ellipsoid, with a very high resolution of 5 m / pixel, derived from airborne photogrammetry, provided by the National Catasto and Mapping Agency SA of Greece;
- Use of soil by Corine Land Cover 2012 with 100 m spatial resolution;
- Size of the calculation cell set to 15x15 m with a calculation time of 0.5 seconds.

Flooding maps referred to the same temporal moment of the SAR images, implemented for the flooding delineation, are shown in Figure 24.

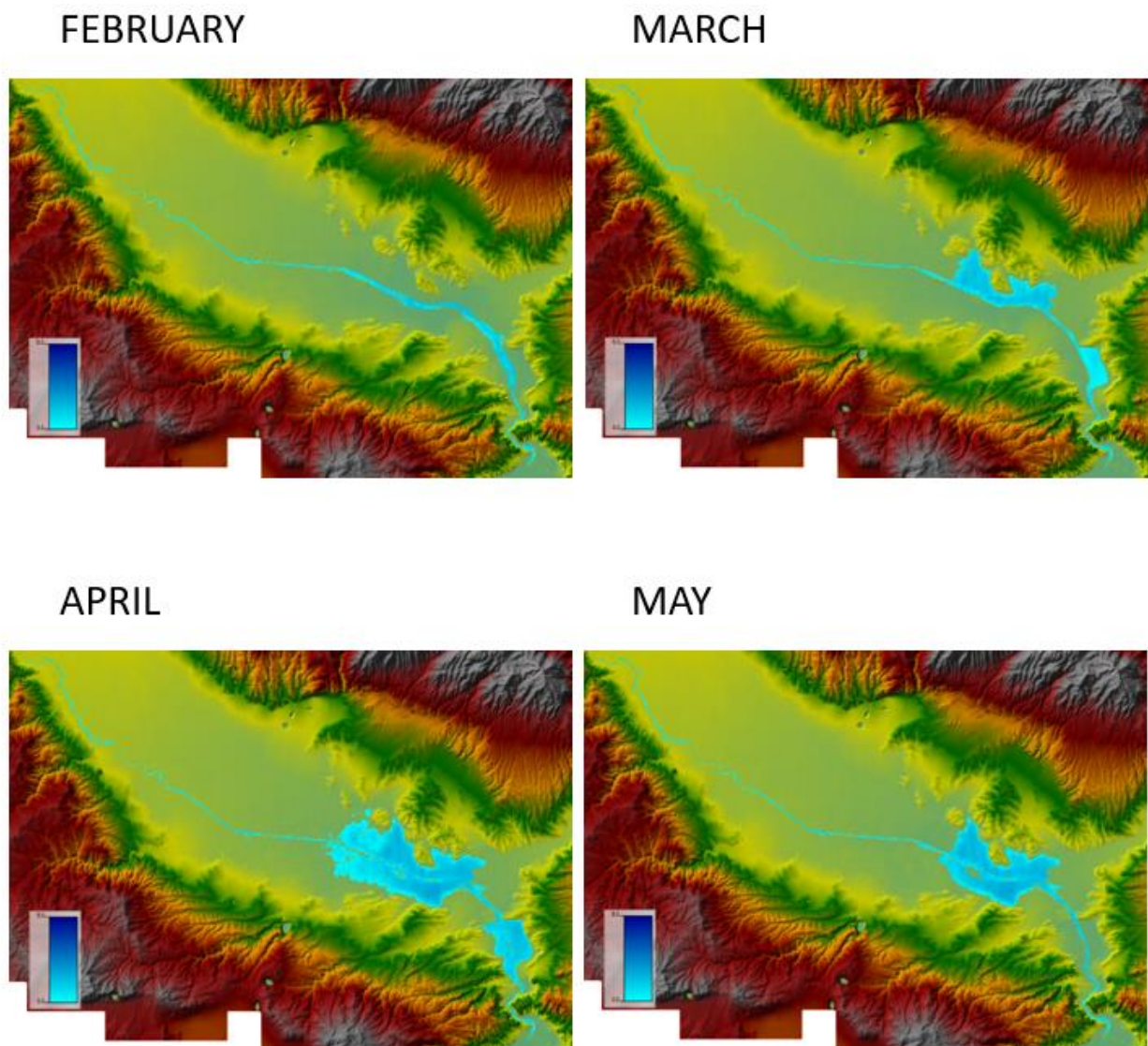


Figure 24 - Flooding maps obtained from Hydraulic modelling

Figure 24 shows the maps for those months, as shown on satellite, where the flooding was most evident in the area of interest. For all the months considered for the simulations, the values of the fitting index (Eq. 2) ranges from 0.80 to 0.95 were obtained.

Through this methodology it was possible to reconstruct a flooding map which also allowed to show, given the different scenes on different dates, the total evolution of the event.

This application, carried out in collaboration with Prof. Parcharidis and his team in Athens, has allowed us to understand how remote sensing is an excellent tool for monitoring the flooding in those favorable areas, such as the suburban area of the study area, and for the calibration of the hydraulic model in order to reconstruct flooding maps of good accuracy.

3.3 RECONSTRUCTION OF FLOODING MAP IN INSTRUMENTED AREA (CASE STUDY: HARVEY HURRICANE, HOUSTON)

In the previous case study, remote sensing was combined with hydraulic modelling to determine the flood extension of the Strymon river after an extreme alluvial event by using SAR images. The methodology employed was based on the comparison between the extension of flooding obtained from hydraulic modelling and that detected from satellite.

It must be said, however, that the output of hydraulic modelling is not only the extension of flooding but also its depth and velocity. The methodology used for the Strymon river inundation case study doesn't allow to understand if the depth and velocity parameters are correctly reproduced from the hydraulic modelling.

The main goal of the study is to explore the possibility to obtain an accurate post-event flooding map integrating data extracted by satellite images, social markers and hydraulic numerical model simulations.

In particular we are interested in obtaining as accurate as possible reconstruction of flow characteristics (depth and velocity) within urban areas, which, as underlined in the introduction, are not detected by satellite images and difficult to calculate by numerical models.

The idea, to overcome the above limitations, is to calibrate numerical model using the flooding areas detected in suburban or rural areas, where the satellite images provide reliable records of flooding, and then to infer the flow depth and velocity within the urban areas from the hydraulic simulations by the calibrated model. As in the previous case study of Struma river, the saturation factor k as defined by Şen (2008) as calibration parameter (Eq. 1) and the index (Eq. 2) for the fitting between the flooding areas detected by satellite images A_{obs} and those obtained by mathematical simulations A_{sim} were assumed.

The best fitting simulation is identified by the value of saturation factor k corresponding to the maximum value of $I(k)$. Also in this case study, in Eq. (2) A_{obs} refers only to the flooding areas which are supposed to be detected by satellite. We select such flooded areas on the basis of land-cover types. Specifically, we remove from the totality of simulated flooding areas those belonging to urban and forest land cover types.

To validate model simulations within the urban areas, we use flow depths obtained by social markers which provide photographs or records of the flooding event at specific location and time.

In order to verify the reliability of the proposed approach, as well as, to gain a more in-depth insight about its advantages and drawbacks, we apply such methodology to the case study focused on the reconstruction of the serious flooding occurred in Houston region due to the Harvey hurricane.

Harvey hurricane of category 4, hit the South-eastern Texas between August 25th and 31st of 2017, with catastrophic rains, which caused major flooding in Houston and its low-lying surrounding areas. Harvey Hurricane generated the largest rainfall of any US hurricane on record. Heavy rains scattered over the territory with a 1270 mm total rainfall amount.. On August 27th, a maximum daily rainfall amount of 760 mm was observed. The highest rainfall amount was recorded at Galveston Bay, Houston, with over 1016 mm of rain in 48 hours (NWS 2017). Over 20,000 people were forced to seek emergency shelter during the event and an estimated 120,000 structures were affected by flooding. Emanuel (2017) estimated a return period of Hurricane Harvey's rainfall around a once in 2,000 y event in the late 20th century. The same author, using climatic projections from general circulation models (GCM), has shown as the return period of the same event (storm total rainfall greater than 500 mm) reduce to a once in 100 y by the end of this century. The increasing probability of occurrence of such extreme rainfall events - also highlighted by others authors (e.g. Van Oldenborgh et al. (2017) - suggests the importance of carrying out accurate post-event flooding maps to identify and design measures and infrastructures to mitigate future more frequent extreme floods.

A further motivation for the choose of such case study, beyond the underlined exceptionality of the hydrological event, is that Houston is equipped with a large number of monitoring rainfall and streamflow stations, which provide further data for the validation of the proposed approach.

Hydraulic simulation of the event, as in the Struma river inundation case study, was carried out by 2D hydraulic model from the USACE Hydrologic Engineering Center's River Analysis System (HEC-RAS 5.0.7), which is one of the model that meets the minimum requirements of National Flood Insurance Program as required by FEMA.

On the basis of the case study results, we show the effectiveness of the proposed approach. Moreover, we argue about the possible sources of inaccuracy and bias, which could affect an accurate reconstruction of the post event flooding map, especially in urban areas.

In particular, in such areas, we explore how the spatial resolution of the mesh affects the accuracy of model simulations.

The precipitation products used in the study refer to those provided by the Harris County flooding warning system. The Harris County Flooding Control District's Flooding Warning System measures rainfall amounts and monitors water levels in bayous and major streams on a real-time. The system relies on 163 gage stations strategically placed throughout Harris County bayous and their tributaries.

The rainfall data were downloaded from the website www.harriscountyfws.org and were recorded in the time interval 20/08 - 01/09 with a time resolution of 15 minutes. Given the distribution of precipitation that occurred during the days of the event, and since it uniformly covered the whole area involved, the precipitation used in the reconstruction of the flooding map refers to the average of the values recorded by all the stations present in the study area. Because the hydraulic model used does not take into account the phenomena of evapotranspiration and the presence of sewers, a runoff coefficient is calculated.

In general, data from the Harris County Flooding Control District's Flooding Warning System played a key role in both the input of the hydraulic model used, the precipitation, and both the calibration phase. In fact, thanks to the hydrometric levels recorded by the ground stations it was possible to make a comparison with those obtained with the hydraulic model and to understand if this respected the flooding times of the various bayou present in the area of interest.

Satellite SAR images were downloaded from the Copernicus website (<http://emergency.copernicus.eu>) and are the result of the Change Detection (CD) technique applied on high-resolution X-band images (from 1 to 4 m) of the Italian COSMO-SkyMed constellation (Chini et al., 2012). "Change detection" refers to the process of identifying changes in an object or a phenomenon that occur in a particular time frame. A fundamental assumption of the change detection analysis performed with remote sensing data is that a change in ground or surface coverage observed by a sensor corresponds to a change in radiometric spectral response, and that this spectral change is significantly more relevant than changes due to other factors such as weather conditions at the time of acquisitions, or soil moisture or differences in the conditions for acquisition of remote sensing data.

Flooding mapping is performed using SAR images and is based on the physical response of water bodies when illuminated by the radar signal. The sensor detects stagnant water, generally all flat surfaces, with a low backscatter intensity due to the specular reflection of the incident SAR rays. This type of phenomenon is represented in SAR intensity images with dark colors (Richards A. et al., 1987). This processing of SAR images in case of flooding generates information related to (a) extension of the flooding and (b) flooding height in case an accurate model of digital elevation is available interpolating the heights points of the DEM terrain with those of the flooding (Cian et al., 2018; Cian et al., 2018). The images used for the study are referred to

the days 28, 30 and 31 August 2018 and are respectively shown in figure 25 a, b c where the flooding is clearly visible in blue.

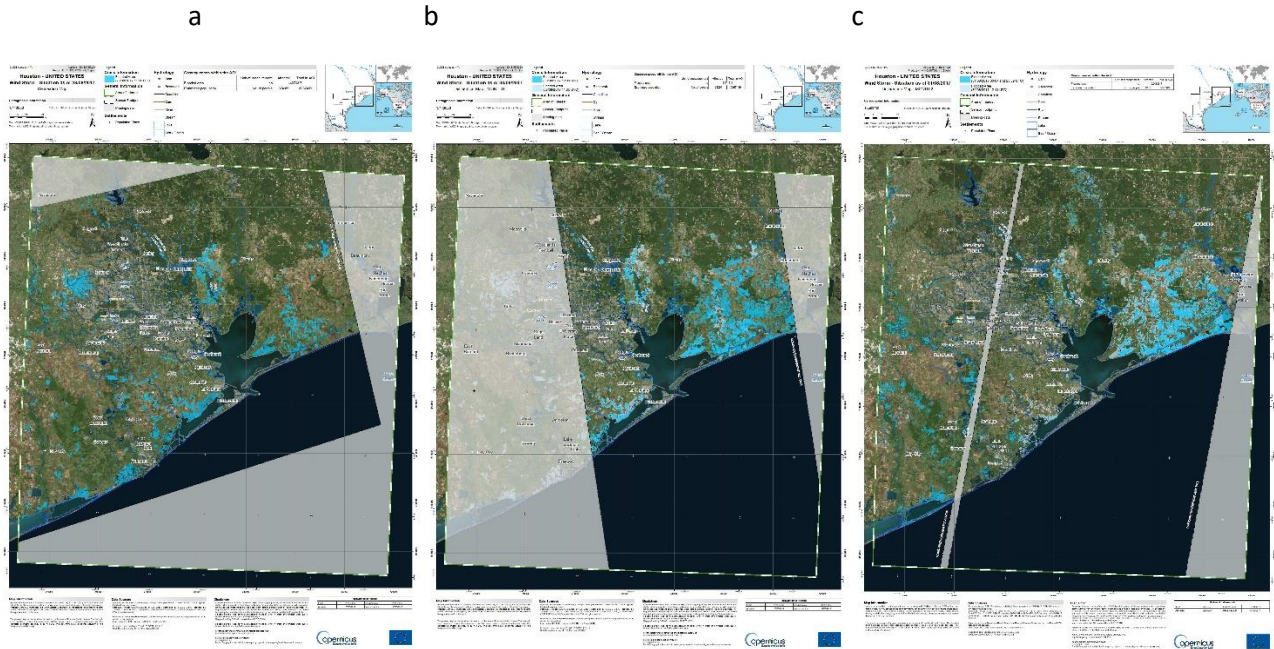
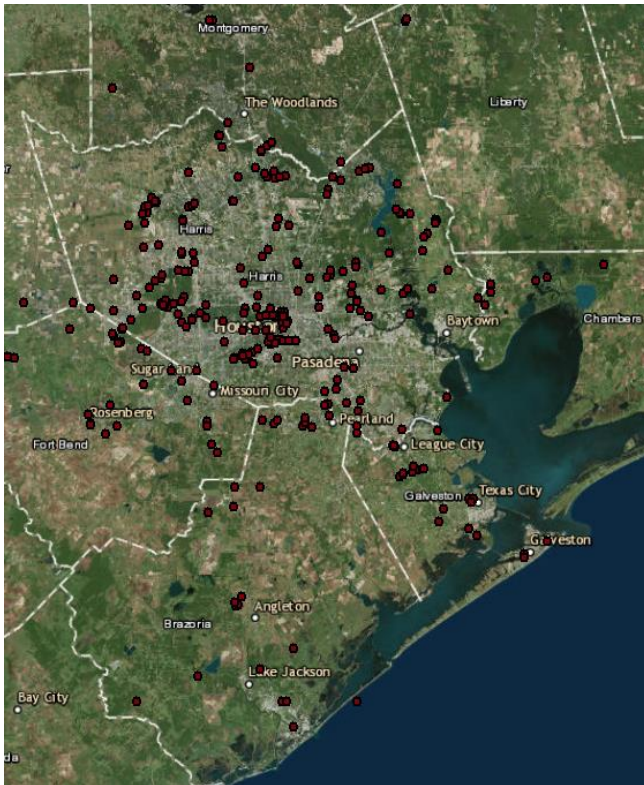


Figure 25 - Flooding hazard maps of Harvey Hurricane of a) 28/08/2017, b) 30/08/2017 and c) 31/08/2018

These maps were useful to calibrate the hydraulic model by establishing a runoff coefficient such that the flooding evoked by the model, in terms of extension, would be the same as that emerging from the SAR satellite. This comparison was made by comparing, for the same temporal instance, the extension of flooding deduced from hydraulic modelling in all those areas favourable to the satellite.

The social media markers used in the study were provided by the Evolution of the Emergency Copernicus database (E2mC) owned by Copernicus (Scalia et al., 2017). The markers obtained from this research project refer to the same dates as the satellite images described above. This service is mainly based on the integration of information derived from remote sensing, spatial analysis algorithms, social media and crowdsourcing. All these data are collected by remote digital volunteers and local journalists. For a detailed description of how the posts are extracted, geolocated and made available, see Havas et al., 2017. The markers used for the Harvey extreme event, given the strong activity on the social networks of the inhabitants of Houston especially during the days of the extreme event, were in a number that allowed to have a total coverage of the city and therefore to have a lot of useful information to describe the event and validate the results of the hydraulic model, in particular, where also the satellite is unable to give any description. In figure 26 a, the spatial distribution of the markers obtained for the days of the extreme event are shown. An example of photograph used in the analysis is shown in figure 26 b.

a



b



Figure 26 - Location of social media marker in Houston and b) example of photo used for the validation of hydraulic modelling (obtained from E2mC).

The validation of the results obtained from the hydraulic simulation was carried out comparing the simulated water depths with those estimated from social media markers. Such estimation was carried out through photographs and comments extracted by the social media markers, which provide, especially in the urban areas, location and time of the water depths during the event, where neither satellite images nor ground based stations are able to provide such data.

In fact, the downloaded social media markers contain very important information for the validation of the results of the model, such as the location (geographical coordinates and name of the road of interest), date and time, the comment of the author of the post and above all photographs that are explanatory of what really occurred. The image in Figure 26, refers to a part of the social markers detected on 28/08/2017. Such social markers refer to the urban context which is the most problematic to simulate, due to the presence of numerous elements such as houses, roads, bridges and parks only partially represented by the DEM.

The estimates of the depth values obtained from social markers have been qualitatively based on comparison to elements present in the image and eights (e.i. road sign, sidewalk, river bank, etc.) which are known with certainty. These qualitative estimates have an uncertainty of ± 0.10 m.

The 2 D hydraulic model, used in the analysis, refers to the USACE Hydrologic Engineering Center's River Analysis System (HEC-RAS 5.0.7). The time step obtained and used for the simulation is 5 seconds.

In the case study the integration domain, delimited by the watershed ridge shown in figure 27, was selected. In this way there was no surface runoff from the external regions, and the flooding within the domain was due only to rainfall and/or to storm surge along the coast. Thus, the calculation of flow entering in the domain by rainfall-runoff hydrological models, which requires a preliminary very complex model parameter identification, was avoided. A 5m of DEM resolution was obtained from USGS (United States Geological Survey, link: <https://viewer.nationalmap.gov/basic/>). Due to the very large size of the domain, a nominal grid resolution (250x 250 m) was selected and the computational mesh constructed by the HEC-RAS tools. In the zones where a major resolution was required, breaklines were introduced to obtain a resolution up to 5 m.

In figure 27 is shown the land cover map extracted from Copernicus images related to the period of the flood (August 2017).

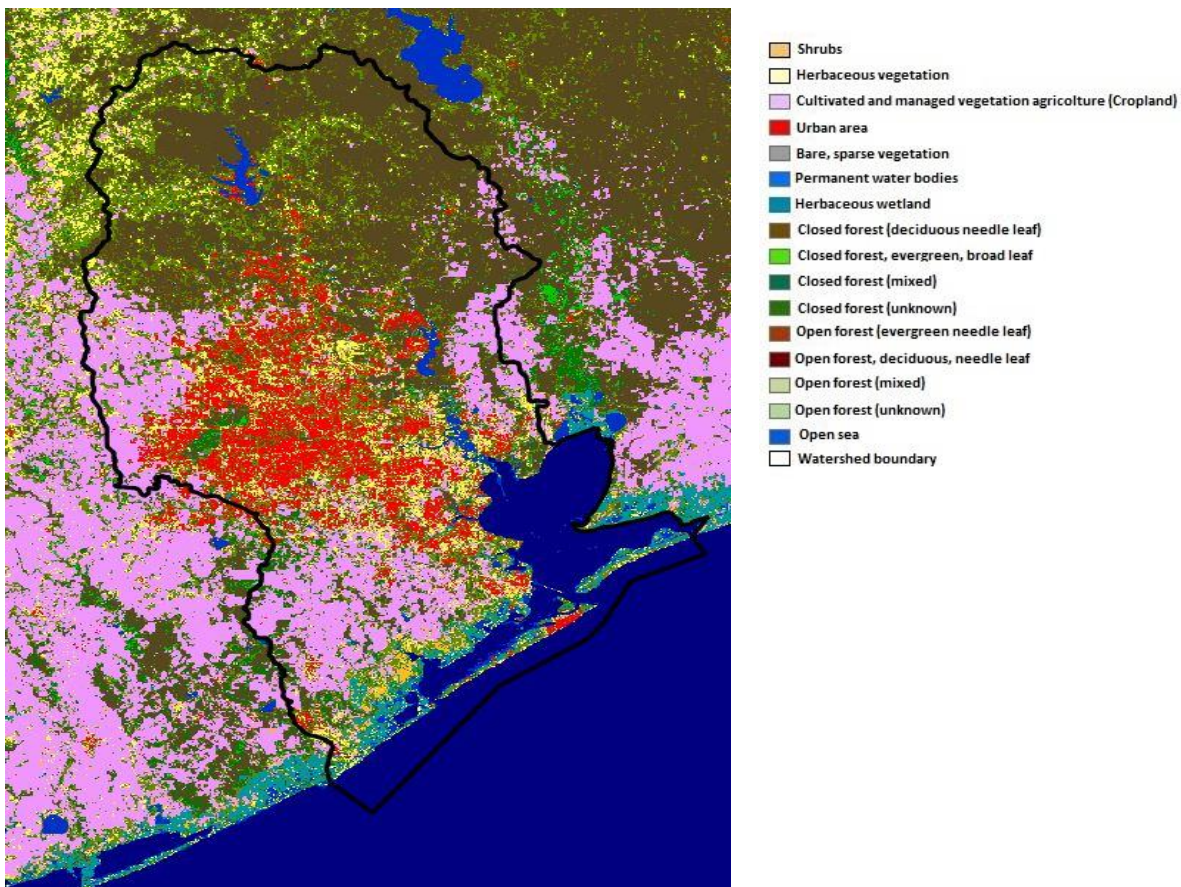


Figure 27 - Land cover by supervised classification algorithm on Copernicus images

As figure 27 shown, most of the territory within the domain boundaries is covered by forest or urban areas. The values of Manning resistance coefficient were deduced, in each point of integration domain, as a function of the Land Use classification, according to table 3.

Land Cover Type	Default Manning Valued [$m^{1/3} s^{-1}$]
Natural Vegetation, shrubs and cropland	0.04
Herbaceous Vegetation	0.045
Developed (urban area)	0.25
Main channel	0.022
Barren land rock/sand/clay	0.04
Permanent water bodies	0.035
Mixed and evergreen forest	0.08
Bare, sparse vegetation	0.02
Herbaceous wetland	0.16
Sea	0.03

Table 3 - Spatial variability roughness used in the hydraulic model

Unfortunately, as previously underlined, neither spatial variation of precipitation nor losses and infiltration can be taken into account in HEC-RAS. However, in the present case study, due to the exceptionality of the hydrological event, precipitation was rather spatially uniform. Therefore a precipitation spatial average over the integration domain was applied. Furthermore, the rainfall amount was so exceptionally high that the soils, independently from their nature, resulted completely saturated in short time. This is evidenced in figure 28 where the temporal variation of the instantaneous runoff coefficient (Eq.1) is shown as function of the precipitation trend. The figure refers to typical values of saturation coefficient k (Table 1 in Şen (2008)) that are characteristic of different land cover types. To further confirm the high level of soil saturation, NASA analysed the soil moisture in south-eastern Texas before and after Harvey landing using data from NASA's Soil Moisture Active Passive (SMAP) satellite. SMAP observations from August 2017 21st and 22nd showed that soil surface conditions were already very wet a few days before the hurricane made landfall, with 20% to 40% moisture levels (<https://phys.org/news/2017-08-nasa-harvey-saturated-areas-texas.html>).

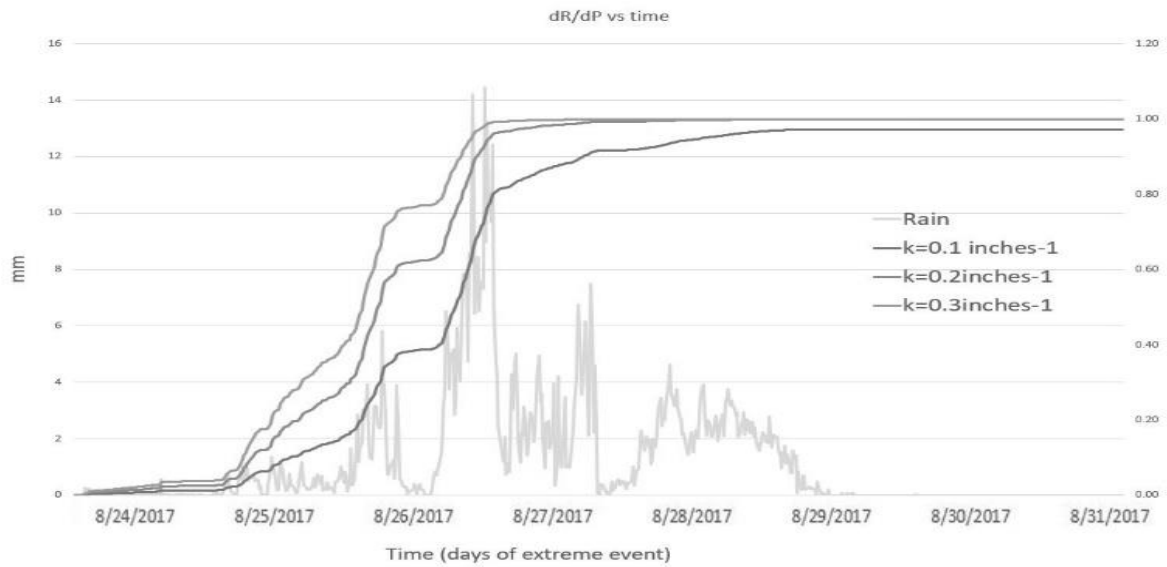


Figure 28 - Rainfall amount (right) and runoff rate dR/dP for different values of k (left)

The sea level trend, due to the storm surge, and recorded during the extreme event along the coastal, was applied as boundary condition (www.u-surge.net/hurricane-harvey.html).

First, several simulations were carried out for different values of the saturation factor k appearing in Eq. 1. Then for each model simulation, the fitting index $I(k)$, defined by Eq. 2, was calculated. Simulated flooding areas A_{sim} belonging to urban and forest land cover types were excluded from the calculations of $I(k)$.

Figure 29 shows the flooding map - referred to August 28th at 11 AM - obtained from the hydraulic simulation for $k=0.1 \text{ inches}^{-1}$, at which corresponds the highest fitting index value.

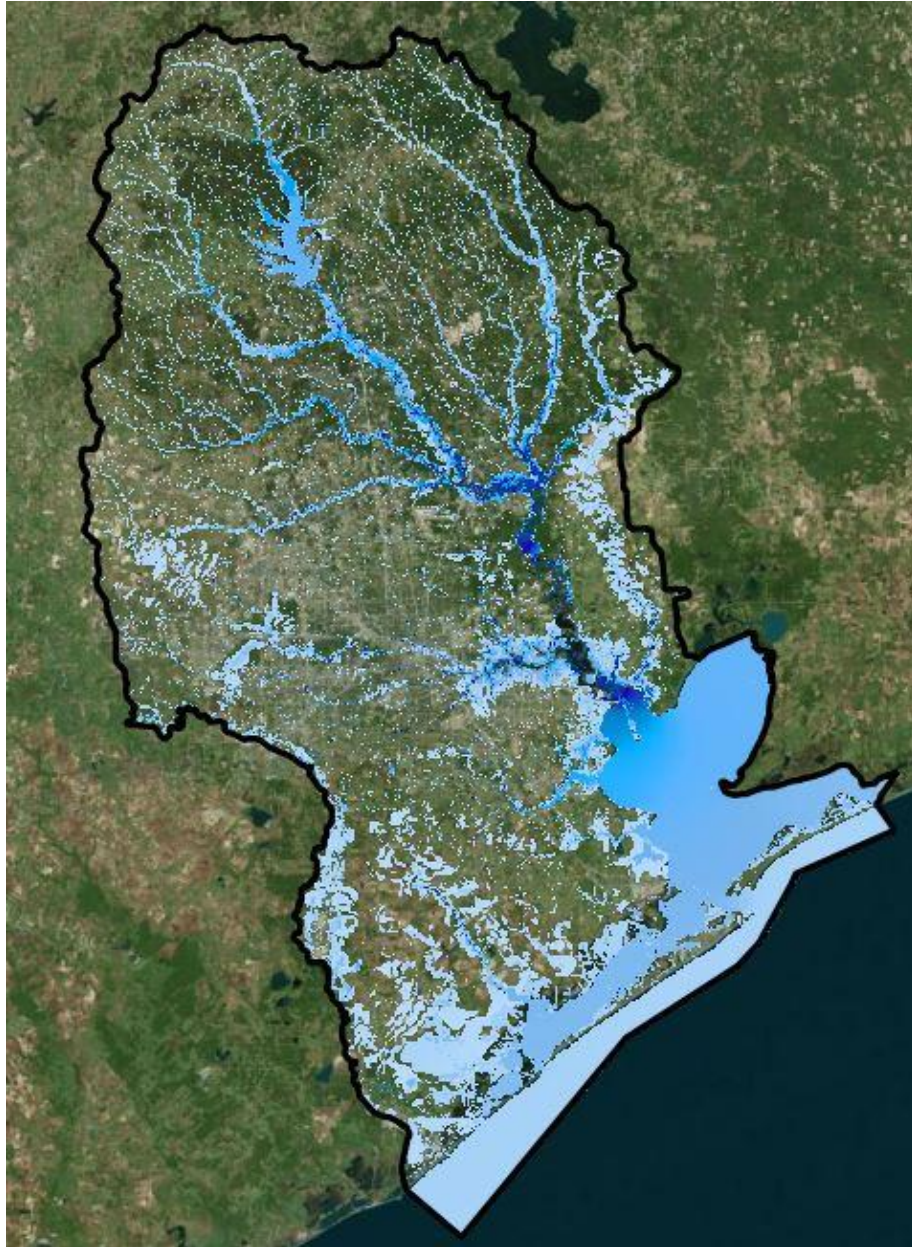


Figure 29 - Flooding map obtained from hydraulic modelling ($k=0.1$)

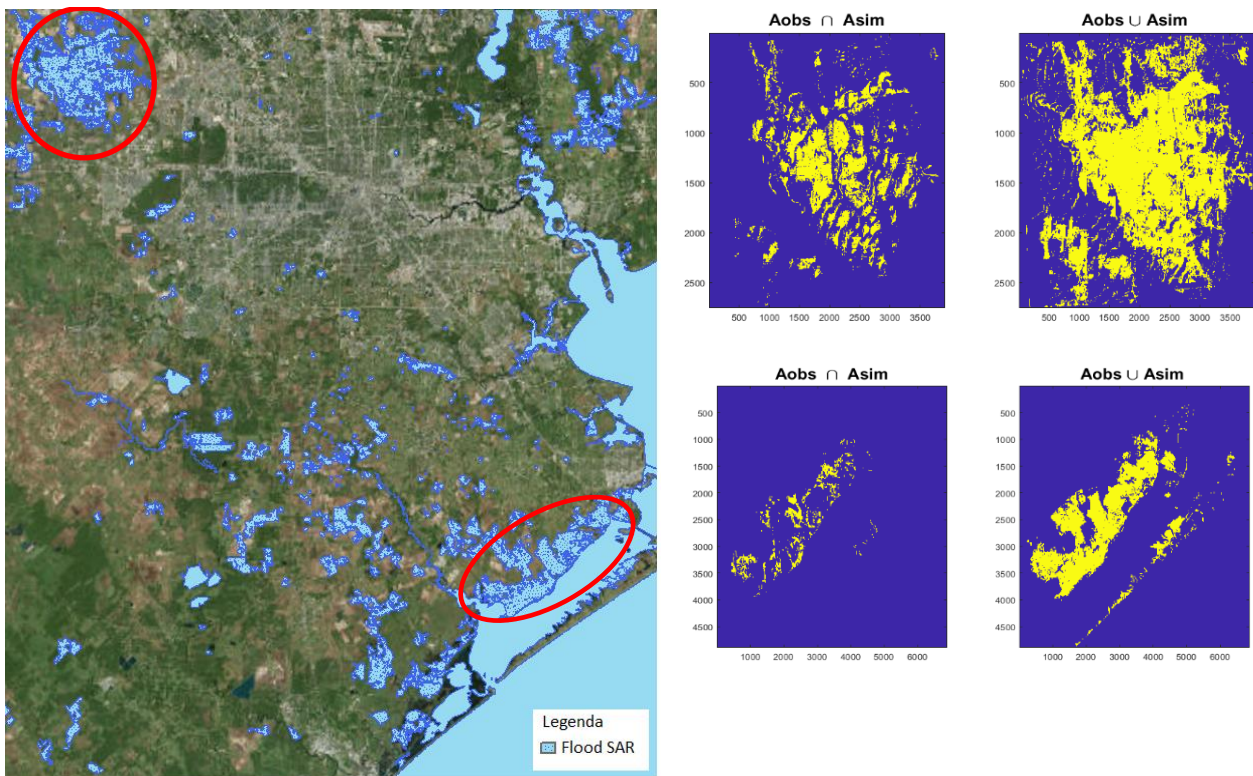


Figure 30 - Correspondence between the flooding areas obtained by hydraulic simulation and SAR satellite

Comparing the inundation map in Figure 29, with that obtained by satellite image (shown at the left side of figure 30), clearly emerges how in urban and forest land cover areas the flooding is not recognized by satellite, despite the evidence in figure 5 of large inundated areas.

However, as figure 30 shows (right side), in rural areas, location and extension of flooding areas - simulated and detected by satellite images – fit satisfactory. Values of the fitting index ranges from 0.60 to 0.80 were obtained for the rural flooding areas selected.

To confirm the goodness of the calibration procedure, in figure 31 (right side) the simulated and measured time series of free surface level in correspondence of some hydrometric gauges (figure 31 left side), homogeneously distributed in the areas of interest, are compared. As shown in figure 31 (right side) the simulated free surface trends at the different locations satisfactorily fits the actual trend of observed values.

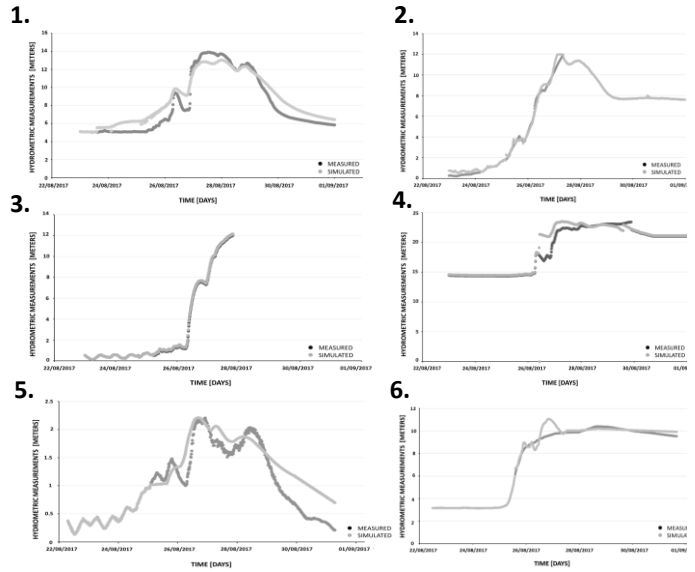
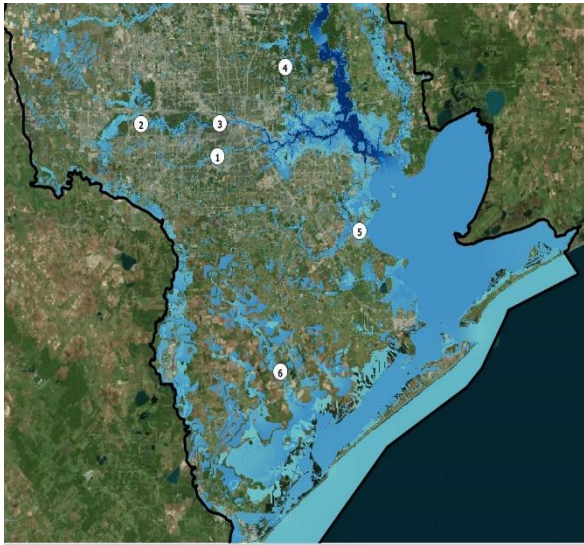
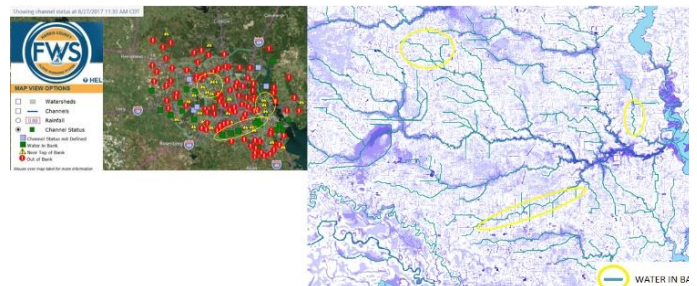
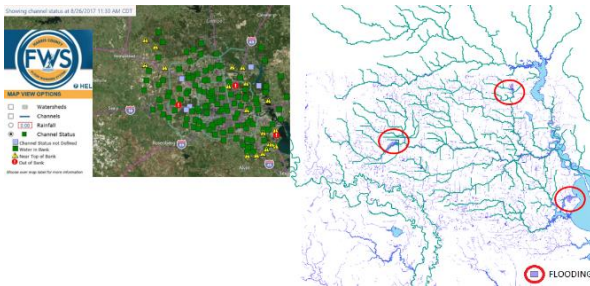


Figure 31 - Location of measurement stations of the levels considered and hydrometric levels detected during the extreme event.

Furthermore, the timing of the simulated and observed overflowing, in different cross sections of bayous passing through the urban Houston area, was compared. The network of the alert stations presents in the Houston area and owned by the HCFCD was used. In the Harris maps (shown in the left side of figure 32), the red symbols indicate the locations where the water level exceeds the top of the bank, the yellow where the level is near the top of the bank and the green when the water flows inside the bank. All the maps are referred to the same hour, for all the days considered, at 11.30 a.m. The comparison, shown in figure 32, demonstrates that the hydraulic model simulation followed the temporal trend of the floods during the days of the extreme rainfall event.

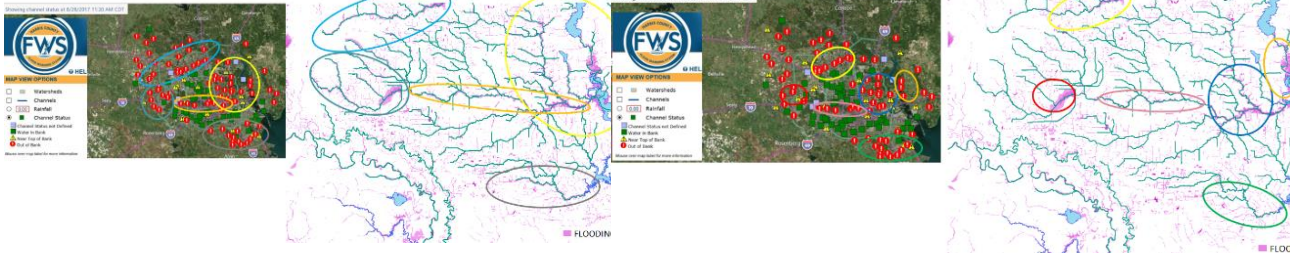
26/8/2017 11:30 AM

27/8/2017 11:30 AM



28/8/2017 11:30 AM

29/8/2017 11:30 AM



30/8/2017 11:30 AM

31/8/2017 11:30 AM

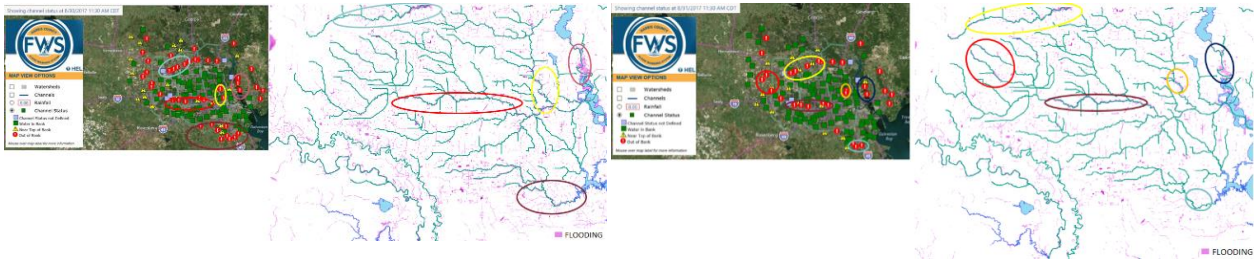


Figure 32 - Temporal trend of the floods in Houston during Hurricane Harvey from 26/08 to 31/08. Red symbols indicate the locations where the water level exceeds the top of the bank, the yellow where the level is near the top of the bank and the green when the water flows inside the bank.

The comparison between the simulated water depths with those estimated by the photographs at the same location and time, adds an additional element of judgement, in particular in urban areas where satellite is not able to recognize the flooding (Figure 33).

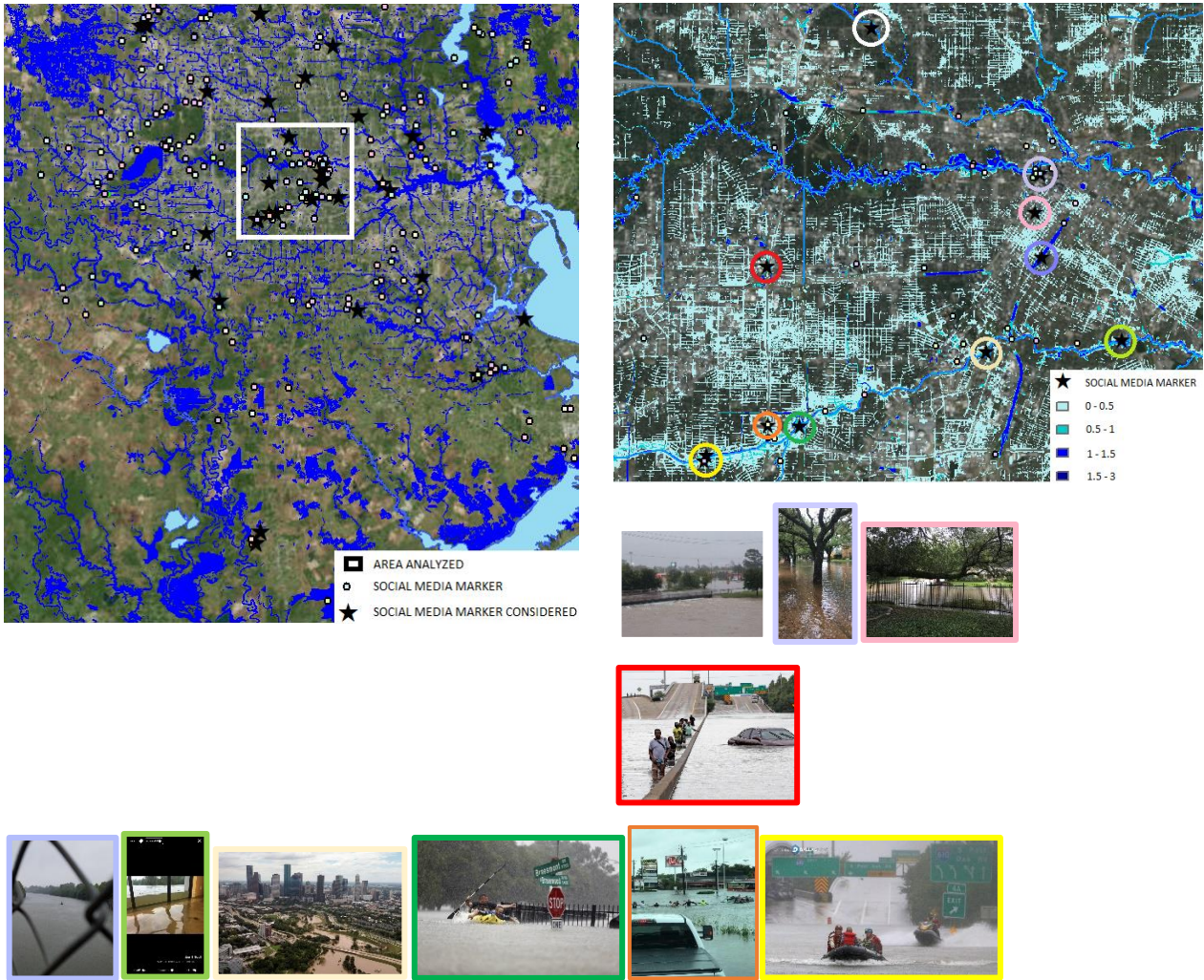


Figure 33 - Social media marker referred at the same day of the flooding maps (28/08/2017) used for the validation of the results.

In table 4, the water depth estimated by social marker and simulated at the locations of figure 33 are shown.

IDENTIFICATION COLOUR	DEPTH BY HYDRAULIC MODELING [m]	DEPHT ESTIMATED BY SOCIAL MEDIA MARKER [m]
WHITE	2	2 ± 0.10
PURPLE	0.4	0.5 ± 0.10
PINK	0.35	0.3 ± 0.10
RED	0.5	0.5 ± 0.10
VIOLET	2.7	2.5 ± 0.10
LIGHT GREEN	0.4	0.5 ± 0.10
LIGHT YELLOW	bayou 7 other 1.5	bayou 5 ± 0.1 other 1 ± 0.1
DARK GREEN	1.8	1.5 ± 0.10
ORANGE	0.56	0.5 ± 0.10
YELLOW	0.8	1 ± 0.10

Table 4 - Comparison between water depth [m] estimated by social marker and simulated by hydraulic model

The comparison of table 4 demonstrates, despite the uncertainties in deducing the water depth from the photographs, that the proposed approach was satisfactory for the quantification of flow depth and velocity, as well as inundation timing, in urban areas where such flow characteristics are more challenging to detect.

The results obtained clearly show that approach proposed aimed to carry out post-event flooding maps by integrating satellite images, hydraulic model simulations and social markers. Inundation areas detected by satellite images was used to calibrate the hydraulic numerical model, whose simulations were validated by information extracted by the social markers.

The application to the case study – addressed to the inundation of Houston area produced by the Harvey Hurricane - has shown that this approach allows a credible reconstruction of the main flooding characteristics as flow depth and velocity, as well as flooding timing, which are relevant information for a correct post-event damage evaluation or to plan future flood defense systems.

Specifically, the approach has shown to be reliable in flooding reconstruction in urban areas where the detection of inundate areas by satellite images is still challenging. In fact, it has been shown that in the presence of buildings, roads, shadows, rough terrain, dense vegetation, and detection methods based on SAR fail to recognize flooding areas. Hydraulic model simulations allow to overcome such limitation, but in order to reduce the computational time by using mesh with a resolution coarser than the DEM resolution, we need to use a sub-grid approach, which could be a further source of inaccuracies. In this context model validation in the urban areas by social markers assures on the reliability of the flooding reconstruction.

Social markers could be very effective for the reconstruction of the flooding event since they provide spatial and temporal very well-defined data. Despite this, photographs are not taken in systematic way and are affected by randomness, because people shoot photographs without a predefined plan. Thus, there is not possibility to a realistic reconstruction of the flooding map using only social markers. Despite this, we show that social markers are a very useful tool for hydrodynamic model validation as the present study demonstrates.

The use of social marker, however, due to the very detailed spatial and temporal resolution, imposes the use of hydrodynamic model able to represent with notable accuracy the free surface level and velocity fields within the complex morphology of urban context. In this study we used HEC-RAS which is one of the model suggested from FEMA to simulate flooding phenomena. Such model uses to simulate flow in urban areas a subgrid approach proposed by Casulli (2008). Although, the approach seems to be effective for simulating flooding in domains not particularly large, where the size of the mesh can be chosen of the same order of magnitude of the DEM mesh, in the cases where very large regions have to be analyzed the approach seems to fail. In fact, the analysis conducted for Houston has shown that the hydraulic model used, HEC-RAS, has a strong sensitivity when using computational cell sizes much larger than those of the DEM. From the tests

conducted it was shown how increasing the computational grid size the hydraulic model simulations have significant errors for the calculated velocity and considerable loss of information in terms of extension of flooding. The error in water depth are minor (67% at maximum) but still significant for flow velocities, however, errors were as large as 400 % for dimensions of computational cells much greater than the DEM accuracy. This fact suggests that more efforts should be directed towards improving subgrid modelling, particularly for simulating free surface flows in urban areas.

3.4 RECONSTRUCTION OF FLOODING MAP IN A NON-INSTRUMENTED AREA, CASE STUDY OF THE DIAMREY TYPHOON IN QUANG NGAI (VIETNAM)

This analysis, referred to an area of interest in which there are no hydrological measurements from ground stations and a DEM with good accuracy, allowed to understand if it is possible or not the rebuilding of a post event flooding map with an acceptable accuracy. In addition, also in this case the HEC-RAS 5.0.3 software was used for the hydraulic simulations.

The study area refers to Quang Ngai, in Vietnam, and the event that generated the flooding is the typhoon Diamrey. Typhoon Damrey, known in the Philippines as Severe Tropical Storm Ramil, was a strong tropical cyclone that affected Vietnam during early November 2017. Damrey first originated as a tropical depression over the Philippine archipelago of Visayas on October 31. Emerging to the South China Sea few days later, the system strengthened into the second deadliest and twenty-third named storm of the 2017 Pacific typhoon season. Rapidly intensifying, Damrey strengthened into the tenth typhoon on November 3, reaching its peak strength as a Category 2 in the same day. Damrey made landfall over Khánh Hoà, Vietnam during the next day as it rapidly weakened, and fully dissipated on November 5. Damrey was the strongest typhoon to strike South-Central Vietnam since 2001's Typhoon Lingling.

Figure 34 shows the track of typhoon. Strong winds, heavy rainfall and result severe flooding in Central Vietnam by the typhoon killed 142 people and total damage reached over US\$1 billion.

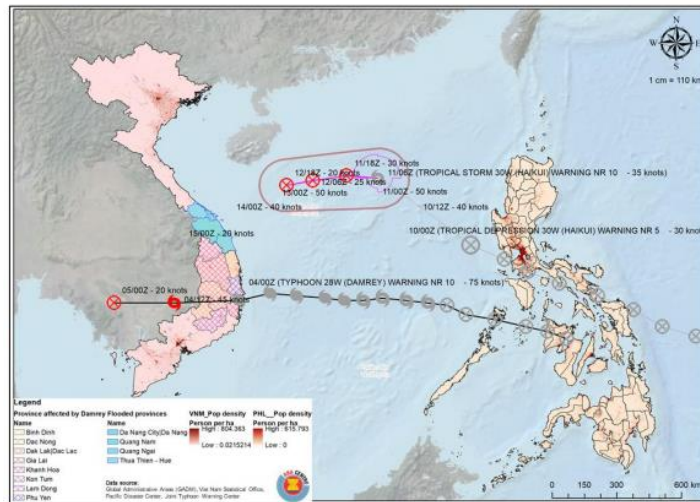


Figure 34 - Track of Diamrey Typhoon

For this application a terrain elevation model of the SRTM (Shuttle Radar Topography Mission) was used, provided by NASA for global coverage and obtained by processing RADAR images with interferometric techniques. The spatial resolution of the DEM is 30 meters.

The study area, not being equipped with precipitation monitoring stations with accessible datasets, was analyzed using the precipitation data estimated by the TRMM 3B42RT satellite.

Concerning the precipitation data from remote sensing, no satellite yet exists that can reliably identify rainfall and accurately estimate the rainfall rate in all circumstances (Dinku et al., 2018). The data were downloaded from the website www.giovanni.gsfc.nasa.gov and this dataset is the output from the TMPA (TRMM Multi-satellite Precipitation) Algorithm, and provides precipitation estimates in the TRMM regions that have the (nearly-zero) bias of the "TRMM Combined Instrument" precipitation estimate and the sampling of high-quality microwave data with fill-in using three-hourly combined microwave-IR estimates (with gauge adjustment).

Satellite precipitation is largely underestimated compared to reality. The error, in general, is due to signal saturation problems affecting the sensors on board the TRMM satellite. This fact led to the use of a multiplying coefficient in the calibration phase of the hydraulic modelling. Through this value it was possible to increase the rainfall detected in order to obtain an extension of the flooding that was the closest to that detected by the satellite.

The problem inherent in the underestimation of precipitation by satellites will be discussed in more detail in the next chapter.

In figure 35 it is possible to see on the left the final result obtained by hydraulic modeling and on the right the flooding extracted by the technique of Change Detection applied to the SAR images. The satellite images used for the analysis refer to the 2/11/2017 and 11/14/2017 as a post event while for the pre that of

08/22/2017. The images were downloaded from the ESA Copernicus portal at the following link <https://scihub.copernicus.eu/> and are from Sentinel 1 sensors.

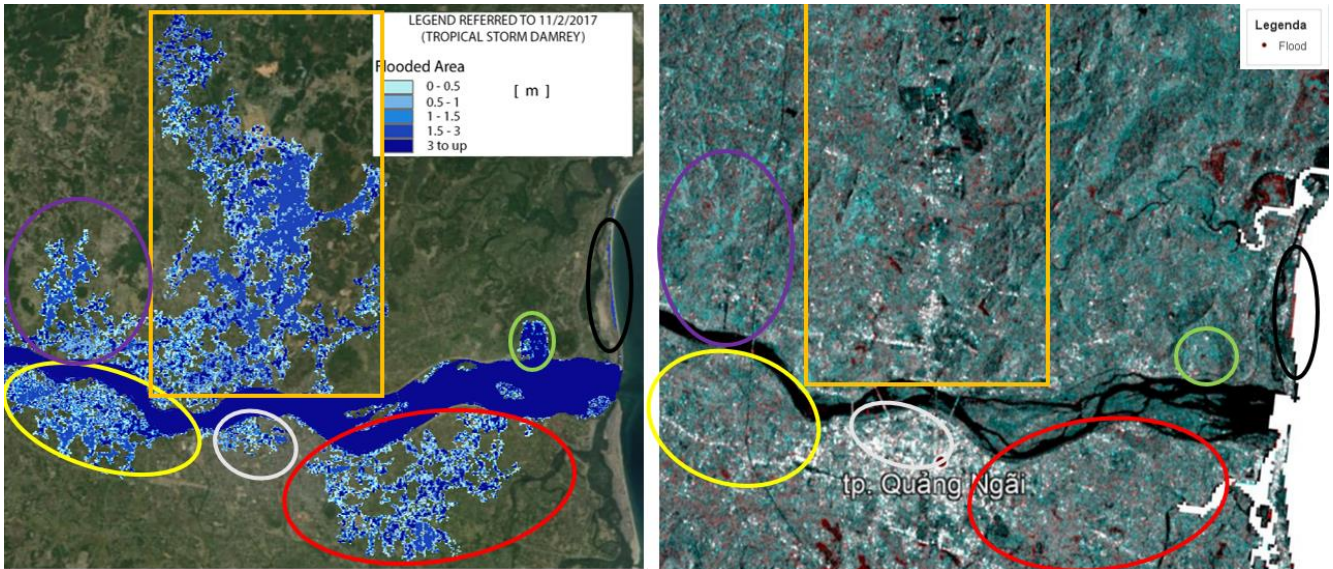


Figure 35 - Result of the hydraulic modeling is shown on the left and the result of the Change Detection technique applied to Sentinel images 1 on the right.

As input, in addition to the DEM and to the precipitations described above, the land cover deriving from the Chinese product GLC 30 (Global Land Cover 3) was used, with a spatial resolution of 30 meters, and a spatial and temporal discretization of the computational cells respectively of 50 meters and 1 second.

As in the Houston case study, also for this application the hydraulic modelling results were calibrated using the remote sensing information and validated with social media marker and pictures found on the web.

The results obtained (shown on the left of figure 35) from the simulation showed that we were able to reproduce the same extension of flooding detected from satellite, but with not in term of depth and velocity of flooding flow. This issue is due to the low resolution of the DEM (see figure 36) which presents numerous occlusions. The occlusions are incorrect representation of the elements present in the study area (for example roads, buildings, bridges, etc.) that doesn't allow the right runoff of flooding.

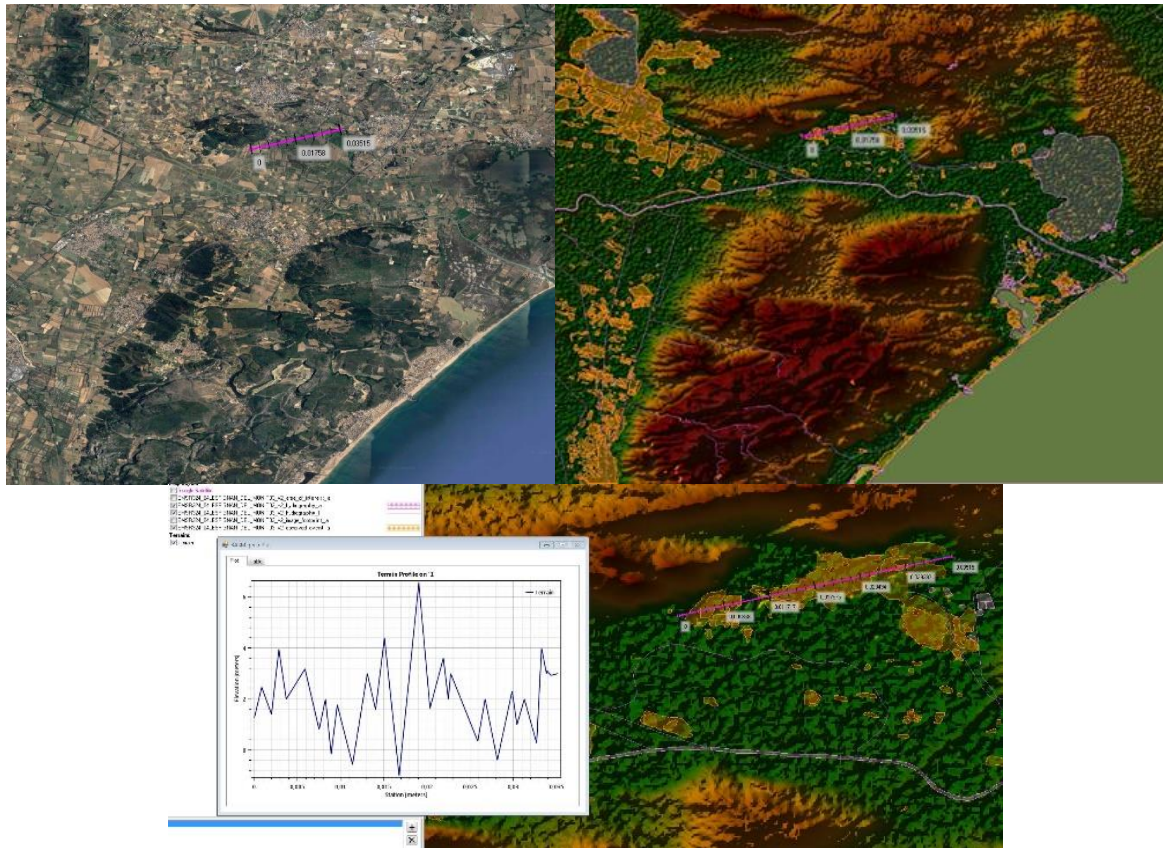


Figure 36 - Zoom showing the occlusions presents on DEM used as input of hydraulic modelling for the rebuild of post event flooding map

For this reason, in order to replicate the same flooding area detected from satellite with hydraulic modelling a multiplying coefficient was used in the precipitation data. The rainfall, in this case study, was incremented of 60% with respect to the original. This fact has allowed us to fill the occlusions presents on the DEM with flooding and to reproduce the same inundation detected from satellite.

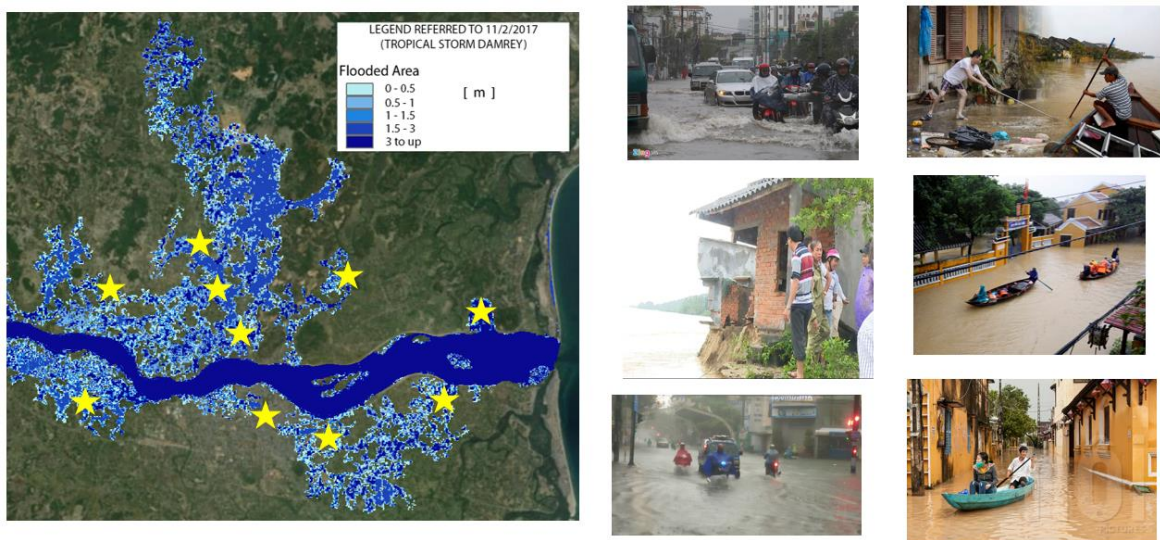


Figure 37 - Validation of hydraulic modeling results with pictures of the AoI

Once completed the calibration phase, the validation was conducted. We must consider for that phase that the occlusions present on the DEM used in this application, in some cases, shows heights up to 4 meters.

The qualitative depth values obtained from hydraulic modelling with that of social media marker revealed a strong overestimation. This fact confirms that without a robust input data, especially concerning the DEM, it is impossible to realize a post event flooding map useful for the flooding risk assessment. In the figure 37, almost all of the pictures used for the validation phase are shown.

3.5 ANALYSIS OF PRECIPITATION DATASET ALWAYS AVAILABLE AS INPUT OF HYDRAULIC MODELING IN A NOT INSTRUMENTED AREA

Rain gauges present several problems, firstly the lack of global coverage of the territory (for example in oceanic or sparsely populated areas). To overcome this problem one possibility is to use satellite data, able to provide global coverage and distributed more evenly (through IR and MW observations).

As a further improvement in the accuracy of the measurements, products have been developed that combine those of satellites and rain gauges, in order to maximize the benefits brought by each type of data.

An example is the GPCP (Global Precipitation Climatology Project), which combines the observations of the rain gauge with the data of satellites in low orbit (therefore MW sensors) and geosynchronous (therefore IR sensors). These different types of data have allowed to quantify the trend of climate change and also, thanks to high resolution satellite products, to monitor phenomena such as drought and floods. The data on rainfall, therefore, are of fundamental importance in the role that assumes as input in hydrological and hydraulic models.

Although today there is an increase in the availability of data sets with ever better spatial and temporal resolution, their are not entirely consistent (due to the lack of data sources and the generation of individual products). Several studies have been developed for their comparison, but most focus on comparing some data sets; it is difficult to find those that offer a global view of all the existing ones.

The data collected by rain gauges are handled by national meteorological agencies, with the aim of creating a global database, useful for research purposes and climate studies. Due to the irregular distribution of rain gauges, data grids are required for many climatic applications. For this purpose, several data sets have been created over the years, shown in Table 5.

Summary of Global Gauge-Based Products						
Data set	Resolution	Frequency	Coverage	Period	Source	Reference
CRU	0.5° × 0.5°	Monthly	Global land	1901–2015	The CRU of the University of East Anglia	(Harris et al., 2014; New et al., 2000)
GHCN-M	5° × 5°	Monthly	Global land	1900–present	National Climatic Data Center	(Peterson & Vose, 1997)
GPCC	0.5° × 0.5°, 1.0° × 1.0°, 2.5° × 2.5°	Monthly	Global land	1901–2013	GPCC	(Rudolf et al., 2009)
GPCC-daily	1.0° × 1.0°	Daily	Global land	1988–2013	GPCC	(Schamm et al., 2014)
PRECL	0.5° × 0.5°, 1.0° × 1.0°, 2.5° × 2.5°	Monthly	Global land	1948–2012.1(0.5°) 1948–present	NCEP/NOAA	(Chen et al., 2002)
UDEL	0.5° × 0.5°	Monthly	Global land	1900–2014	University of Delaware	(Willmott & Matsuura, 1995)
CPC-Global	0.5° × 0.5°	Daily	Global land	1979–2005	CPC	(Xie et al., 2010)

Table 5 - Summary of Global Gauge-Based Products

An important issue concerning the use of rain gauges as a source of data is shown in figure 38, in which we can appreciate a decrease in the instrument number used in the different years (decrease due to a series of factors such as the increase in costs, the migration with consequent abandonment of the sites, etc.), a worrying fact, which could seriously compromise the ability to follow the changes in precipitation.

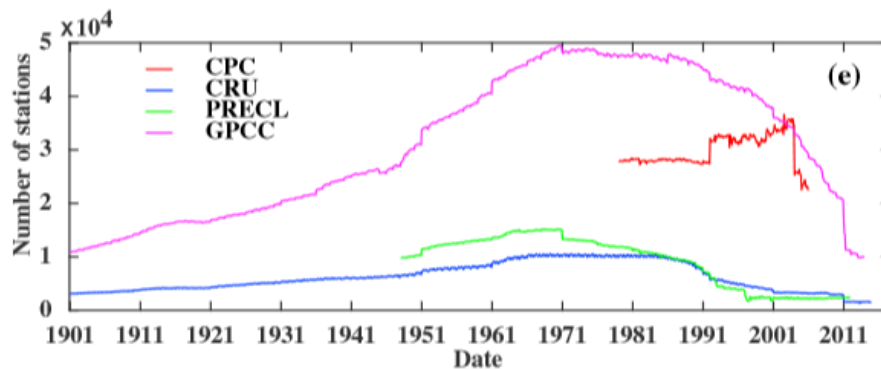


Figure 38 - Number of gauge stations used in different databases in operation over time (Sun et al. 2018)

The satellite is the only technology that allows to perform homogeneous and global precipitation measurements, at regular time intervals. In April 1960, the first satellite capable of reproducing cloud images was launched into orbit: the TIROS (TV and IR observation satellite). On this type of satellite we have 3 categories of sensors:

- Visible / IR (VIS / IR), on satellites in GEO and low earth observation (LEO) orbit;
- Passive microwaves (PMW) on satellites in LEO orbit;
- Microwaves active on satellites in LEO orbit.

Corresponding to the type of sensor, different methods have been developed for the derivation of precipitation, based on VIS/IR methods, on active and passive MW techniques, approaches based on a fusion between VIS/IR and MW, the so-called "united" products" (Kidd & Levizzani, 2011). Here are some references to these types of sensors:

- VIS / IR methods: the operating principle of these methods essentially concerns the link between the temperature of the cloud surface and the probability/intensity of precipitation; the lower this temperature is, the greater the vertical development of the cloud (so it contains more rain). They provide good coverage at tropical latitudes, with good temporal and spatial resolution. However, not all clouds form precipitation, due to the fact that the correlation between surface temperature and precipitation is indirect.

There are several VIS / IR algorithms used for these acquisitions:

- Griffith-Woodley (Griffith et al., 1978);
 - GEO Operational Environmental Satellite (GOES) precipitation index (GES) (Arkin 1979; Arkin and Meisner 1987);
 - The convective / stratiform technique (CST) (Adler & Negri, 1988).
- PMW methods: the era of PMW observations began in 1987, with the launch of the first SSM / I (Special Sensor Microwave / Imager). In contrast to the IR, relatively low frequency passive microwave (PMW) signals (10–37 GHz) sense the thermal emission of raindrops while higher frequencies (85 GHz and higher) sense the scattering of upwelling radiation from the earth to space due to ice particles in the rain layer and tops of convective systems (Joyce R. J. et al., 2004).

Other MW missions:

- TRMM: launched in 1997, it contained the TMI (PMW TRMM MW Imager) and represents the turning point in the field of representation and analysis of tropical precipitation (it was the first mission in which MW active sensors were used, allowing thus the capture of the three-dimensional structure of the rain);
- MW sounding unit (MSU), launched in 1998 on board the NOAA 15: provided information at higher frequencies, between 23.8 GHz and 190 GHz, useful for deriving precipitation products which, combined with those derived from the DMSP (US Satellite Meteorological Satellite Program) SSM / I, allow for a more global observation;
- AMSR-E (Advanced Radiometer Scanning MW for the Observation Earth), developed in 2002, as a multi-channel PMW radiometer, deals with measurements of geophysical parameters related to water, with a spatial resolution twice as high as the PMW radiometer and multi-channel scanning to the SSM / I data;
- GPM (Global Precipitation Measurement), designed to provide new standards in rainfall measurement (liquid and solid), to offer a global product characterized by more accurate instantaneous measurements and acquisitions from a unified constellation of microwave radiometers (see Figure 39).

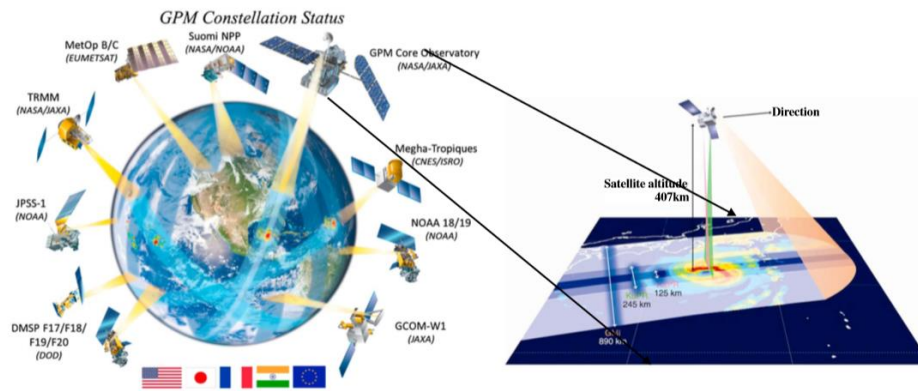


Figure 39 - GPM Constellation, Hou et al.(2014)

Table 6 shows the different sets of data from satellite current available and to follow a relative description (Sun et al. 2018).

Summary of Major Satellite-Related Precipitation Products Currently Available									
Data set	Adjusted	Res.	Freq.	Coverage	Period	Data source	Algorithm	Reference	
GPCP	GPCC, GHCN	2.5°	Monthly	Global	1979–present	GPI, OPI, SSM/I scattering, SSM/I emission, TDVS		(Adler et al., 2003)	
GPCP 1cd	GPCC, GHCN	1.0°	Daily	Global	1996–present	SSM/I-TNPI, TDVS		(Huffman & Bolvin, 2013)	
GPCP_PEN_v2.2	GPCC, GHCN	2.5°	5-daily	Global	1979–2014	OPI, SSM/I, GPI, MSU		(Xie et al., 2003)	
CMPF	GPCC, GHCN	2.5°	Monthly	Global	1979–present	GPI, OPI, SSM/I scattering, SSM/I emission, MSU, NCEP–NCAR		(Xie & Arkin, 1997)	
CPC-Global	GTS, CDOF, NMAs	0.5°	Daily	Global land	2006–present	GTS, CDOF, NMAs		(Xie et al., 2010)	
TRMM 3B43	GPCC	0.25°	Monthly	50°S–50°N	1998–present	TMI, TRMM Combined Instrument, SSM/I, SSMIS, AMSR-E, AMSU-B, MHS, and GEO IR	Probability Matching	(Huffman et al., 2007)	
TRMM 3B42	X	0.25°	3 h/Daily	30°S–30°N	1998–present	TMI, TRMM Combined Instrument, SSM/I, SSMIS, AMSR-E, AMSU-B, MHS, and GEO IR	Probability Matching	(Huffman et al., 2007)	
GSMaP	X	0.1°	1 h/daily	60°S–60°N	2002–2012	TMI, AMSR-E, AMSR-E, SSM/I, multifunctional transport satellites (MTSAT), Meteosat-7/8, GOES 11/12	Kalman filter model	(Ushio et al., 2009)	
PERSIANN-CCS	X	0.04°	30 min/3, 6 h	60°S–60°N	2003–present	Meteosat, GOES, GMS, SSM/I, polar/near polar precipitation radar, TMI, AMSR	Artificial Neural Networks	(Sorooshian et al., 2000)	
PERSIANN-CDR	GPCP	0.25°	3, 6 h/Daily	60°S–60°N	1983–present	GOES 8, GOES 10, GMS-5, Meteosat-6, and Meteosat-7, TRMM, NOAA 15, 16, 17, DMSP F13, F14, F15	Artificial Neural Networks	(Ashouri et al., 2015)	
CMORPH	X	0.25°/8 km	30 min/3 h/Daily	60°S–60°N	2002–present	TMI, SSM/I, AMSR-E/AMSU-B, Meteosat, GOES, MTSAT	Propagation & Morphing	(Joyce et al., 2004)	
GPM		0.1°	30 min/3 h/daily	60°S–60°N	2015–present	GHI, AMSR-2, SSMIS, Maderas, MHS, Advanced Technology Microwave Sounder	IMERG	(Hou et al., 2008, 2014)	
MSWEP	CPC, GPCP	0.1°/0.5°	3 h/daily	Global	1979–present	CPC, GPCP, CMORPH, GSMaP-MVK, TMPA, ERA-Interim, JRA-55		(Beck et al., 2017)	

Table 6 - Summary of Major Satellite-Related Precipitation Products currently available

- CMPORH: half-hour frequency, with a resolution grid of 8 km (entirely due to the acquisitions of the MW sensors), uses only the IR data to reproduce the rainfall characteristics when the data from the PMW are not available. A linear interpolation timeline to modify the form and intensity of precipitation between one scan (PMW) and the other, to guarantee temporal and spatial continuity in the estimation of rainfall, CMPORH recovers the precipitation estimates from NOAA, DMSP 13 satellites, 14 and 15, and from NASA Aqua and TRMM Satellites, IR images are provided by GOES 8, GOES 10, Meteosat-5, Meteosat-7, GEO meteorological Satellite-5 (GM-5).

- PERSIANN-CCS (Global PERSIAN Cloud Ranking System) estimates the distribution of precipitation with a better resolution scale (0.4 ° every 30 minutes) through the brightness temperature read by the IR sensors (GEO satellites) and uses the PMW measurements from the LEO satellites to update its parameters. The algorithm estimates the characteristics of some cloud "pieces", then divides them into different groups,

depending on the similarities between the selected features, subsequently obtaining a precipitation map for each cloud grouping. Finally, PERSIANN's high-resolution estimates are supplemented by GPCP data, with a resolution of 2.5 °, for error reduction.

- TRMM: the first sensors present in the constellation of the TRMM mission, included the TMI (Precipitation Radar) and the VIS / IR Radiometer. Through these sensors, a set of precipitation products was obtained, available at 3 levels (level 3 presents the data in a more uniform space-time grid). The most commonly used are 3B42 and 3B43, which combine observation data from different satellites (Liu et al., 2012). The 3B43, for example, combines the 3B42 data with the GPC rain gauge analysis. The TMPA algorithm estimates precipitation by combining high quality PMW observations with data from IR sensors on geostationary satellites. Microwave (MW) precipitation estimates are calibrated and combined with data from different sources: from the TMI present on the TRMM satellites, from the SSM / I on the DMSP satellites, from the AMSR-E present on AQUA, from the AMSU-B on NOAA Satellites, from the MW Humidity Sounders (MHS) on the latest NOAA satellites and from the European operational meteorological satellite.

- GSMaP (Global Satellite Mapping of Precipitation): is a project sponsored by the Japanese science and technology agency, between 2002-2007, with the aim of developing global precipitation maps and specific algorithms for MW radiometers. It collects data from TMI, ASMR-E, SSM / I, AMSU-B microwave radiometers and data from IR sensors from all satellites in GEO orbit, creating high-resolution precipitation maps (1, 1 h).

- GPCP: based on a combination of MW, IR and rain gauge data. In the period from 1987 to the present (it was SSM / I), the MW measurements from SSM / I and SSMIS, calibrate the GPI between 40 ° S and 40 ° N, combined with the estimates based on TOVS (TIROS Operational Vertical Sounder) and IR Atmospher Sounder, thus obtaining a global product entirely based on satellite estimation (the calibration took place differently in the pre-SSM / I era, before 1987). Subsequently, these analyzes are combined with the data of the rain gauges on the ground, used to correct the "multi-satellite" estimates.

- CMAP (CPC Merged Analysis of Precipitation): data input similar to those of GPCP, but different data fusion techniques. The CMAP is built in 2 steps, combining the data of seven independent data sets with different characteristics:

1. The data sets are combined in a linear way using a "maximum probability" method in which the weighting coefficients are inversely proportional to the square of the individual random error. Land and ocean errors are determined by comparing the GPCP and rain gauge measurements.

2. The outputs of the first step are combined with the measurements of the rain gauges on the ground using the variational mixing method, to remove any errors.

However, CMAP and GPCP are generally consistent, with only some minor differences due to the discrepancy in the data source and in the data fusion technique.

- TRMM 3B43: it is built by combining multi-satellite observations and rain gauges;
- GPCP 1dd (GPCP 1 ° daily analysis of precipitation), is issued to meet the initialization requirements of numerical methods, to develop models of the earth's surface, to validate forecasting models. Its TMP (Threshold Matched Precipitation Index) algorithm, used to obtain instantaneous precipitations, is based on a fusion of data sets constructed with IR data from GEO satellites (ie brightness temperature readings) and TOVS precipitation estimates at multiple latitudes high. NB: all the "united" data sets are based on the assumption that the precipitation distribution estimated by the combined observations between the satellites is optimal and that the measurements of the rain gauges on the ground are not affected by errors.
- MSWEP (Multi-Source Weighted-Ensemble Precipitation): it is a set of data that provides a 3-hour and spatial time resolution of 0.25 °, combining the best sources of precipitation data available depending on the time scale and position. Use a combination of rain gauge measurements, satellite observations and estimates from atmospheric models. Each observation is assigned a weight, which determines a temporal variability in each MSWEP data grid.

As can be seen, some of the products presented are derived from rain gauges and satellites, but the reanalysis data for estimating precipitation is also used. The idea behind the reanalysis methods is to combine observations and irregular models containing different physical and dynamic models, in order to obtain a synthesized estimate of the state of the system through a uniform grid, homogeneous in space, continuous over time and with a multidimensional hierarchy. Many of the output variables obtained from the reanalysis systems still maintain a physical structure and can be obtained after a short calculation period. A reanalysis system is essentially composed of a forecasting model and a routine of assimilation of data: as we read in Bosilovich et al., 2008 ", the assimilated observations in a system of reanalysis, the parametrizations of the model and the interactions between the model and the observations influence all the subsequent

precipitation forecasts generated by the system ". Among the various reanalysis systems, the best known are:

- NCEP 1 and NCEP2, the last of which was developed to improve human error in the first NCEP version through better vertical resolution;
- ERA-40, it had problems of overestimation of precipitation on tropical ocean regions, due to errors in the moisture analysis scheme and error correction (bias);
- ERA-Interim performs a four-dimensional variational assimilation of data, uses a completely automated system for distortion calibration (bias) in satellite radiance observations and performs changes in cloud models, leading to greater atmospheric stability, with an underestimation of the rainfall.
- 20CRv2, CFSR and MERRA, are reanalysis systems with better spatial resolution, which use advanced numerical models and assimilation schemes that combine observations from different sources.

Once a summary of the currently available data sets has been made, for the various technologies, some considerations are reported on the limits that afflict them and that are found in the literature.

Microwave sensors have problems in real time, due to their low sampling rate (being in LEO orbit, they can do a maximum of a couple of passes a day at a given point), which is why we decided to sacrifice the accuracy of the measurements using a fusion with the data coming from the IR sensors, less precise but certainly more frequent.

The GPM has introduced a multiplicity of high frequency channels which have considerably increased its sensitivity compared to the TRMM, obtaining a better identification of light and snowfall. The operating principle is based on the fusion of data (from microwaves and infrared) coming from an entire constellation of satellites.

Speaking of measures in the strict sense:

- VIS sensors are based on the identification of the brightest cloud spectrum (with respect to the bottom surface). In general, brighter clouds are thicker clouds and thicker clouds indicate a greater probability of rain. However, this connection between brightness / thickness and rain probability is a weak connection, so the errors that occur are important. Based on what has been said, it is explained why the measurements above the ocean are significantly better than those on the earth's surface, since the emissivity of the latter can go to mask that of the clouds (as opposed to a "watery" surface) which is clearly more in contrast with the clouds);

- IR sensors instead measure thermal emissions: the colder the clouds are, the greater the probability of rain (measurement of the brightness temperature of the clouds). Also in this case, the relationship between the measured data and the probability of rain is of an indirect nature, therefore inevitably influenced by errors;

- The MW sensors instead "go" to listen to the radiation emitted naturally by the earth and clouds, identifying the latter. They have difficulty in measuring rainfall near the earth's surface, as they identify the hydrometeors at a certain height above the ground, so for the estimation of rainfall on the ground an average time is needed that includes the time necessary for the raindrop to reach the ground. Furthermore, the emissivity of the earth's surface masks the precipitation emissions (based on back scattering, better revision and addition).

Therefore, the advantage in terms of accuracy of MW measurements compared to VIS, VIS / IR, is lost on long-term scales, due to the bad temporal sampling of LEO satellites.

One of the reasons behind the underestimation of satellite measurements, which emerged above all during the TRMM mission, is the fact that the satellite "mediates" the measurements (to compensate for the bad temporal sampling), so for example it can go to spatially mediate an area where there is a strong precipitation with a surrounding area in which the precipitation is absent; the result of this operation will be an underestimation of precipitation.

In tropical areas a better combination of rain gauges and satellites has been achieved. Different discourse for those areas of high latitude, where the satellites were certainly in difficulty (mainly due to systematic errors); there is a deterioration in the performance of IR sensors, which have difficulty recognizing light and snow. There is also an increase in the discrepancy with rainfall data in arid / semi-arid areas.

Another factor that influences accuracy and performance is the orography. The orographic rains are in fact problematic for satellite acquisitions (in particular for the IR sensors that tend to underestimate them heavily), which are in difficulty even in the presence of convective rains and of short duration (rapid temporal phenomena). In flat areas, with simple orography, satellite estimates show good agreement with precipitation estimates, contrary to what happens in areas with complex topography.

In order to quantify the systematic errors existing between some of the pluviometric data sets found in the literature, for the Houston area, comparisons have been made between these and those deriving from earth stations. In the case of Hurricane Harvey hitting Houston we first compared the rainfall temporal and spatial distribution obtainable from ground-based station measurements and from TRMM satellite data induced by the Harvey Hurricane. Then we compared the heavy daily rainfall amount – identified by 95th , 99th and 99.9th percentile - of time series of wet days obtained by different sources of remote sensing precipitation datasets, and from an ensemble of rain gauges in a more restricted area of Houston.

Houston was chosen as a case study, due to the strong presence of monitoring stations, for the homogeneous distribution of these and because in 2017 Hurricane Harvey hit the city, of which many measurements are available.

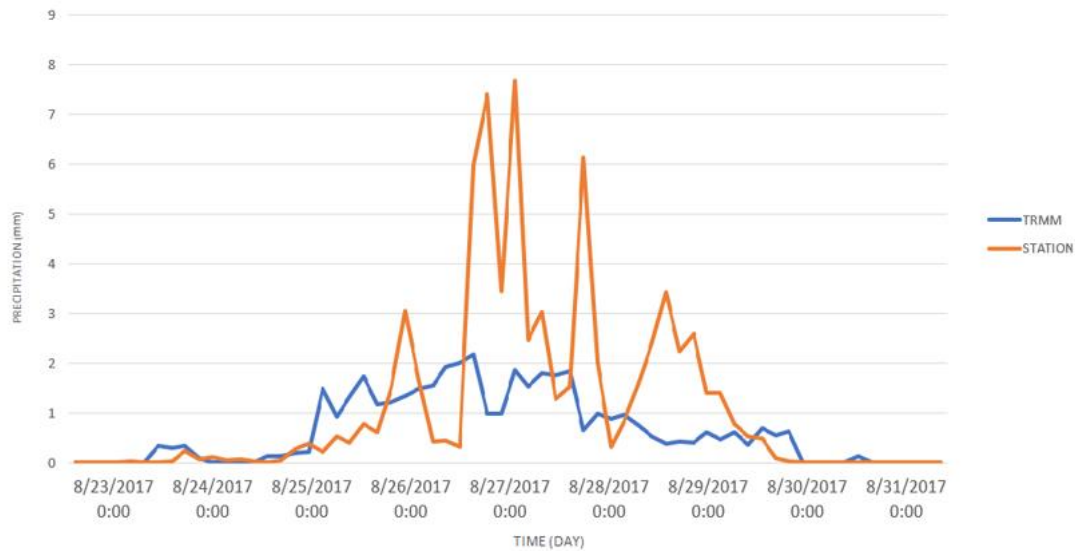


Figure 40 - Comparison between the amount of rain detected on the ground with that from satellite (TRMM); the rainfall from rain gauges are averaged for the stations, indicated in green square, in the figure on the left.

The graph in figure 40 shows the time series of area-averaged precipitation from the ensemble of ground measurement stations (orange) and from TRMM (blue). The figure shows an underestimation of both peak and volume of rainfall amount obtained by satellite.

For the second analysis, a more restricted area of Houston was taken into account, i.e. $0.1^\circ \times 0.1^\circ$ square in Houston city where rainfall can be assumed spatially homogenous. In order to characterize heavy rainfall amount, we calculated the 95th, 99th and 99.9 percentile of daily rainfall amount averaged for all the rain gauges within such area. The time series from the year 2003 to the year 2017 were used. The GPM (Global Precipitation Measurement), being launched in orbit after the other technologies considered in the study, was considered from 2014 and compared for the period 2014 - 2017. To select remote sensing dataset we referred to the papers of Sun et al., 2018, Tan M. L. & Santo H., 2018, Omranian E. & Sharif H.O., 2018 and Beck H.E. et al., 2017. These studies, depending on the data sources treated, have the main purpose of showing the bias existing in the estimate of the precipitation obtained from satellite, reanalysis or radar. The technologies that have been taken into consideration in this work are those that have presented a better return of precipitation compared with those of ground station in the previously cited papers. The comparison

between the heavy rainfall from ground-based and remote sensing records was based on the following error indices:

$$MBE = \frac{\sum_{i=1}^{Ni} (Mi - Si)^2}{\frac{1}{Ni} \sum_{i=1}^{Ni} Mi} \quad (3)$$

$$CV(RMSE) = \frac{\sqrt{\frac{\sum_{i=1}^{Ni} [(Mi - Si)^2]}{Ni}}}{\frac{1}{Ni} \sum_{i=1}^{Ni} Mi} \quad (4)$$

Where Mi and Si are respective measured and simulated data at instant i , and Ni is the count of the number of values used in the calculation.

The MBE (Mean Bias Error) indicates the average quadratic discrepancy between the values of precipitation from ground-based stations and the estimated values from remote sensing. However, this index may be affected by compensation errors. Therefore, as an additional index, the CV (RMSE) (Cross-validated root mean square error) is used, which represents the coefficient of variation of the average standard deviation, ie the ratio between the average square deviation of a certain period and the mean value of the data measured in the same period (Royapoor, M. & Roskilly, T., (2015)).

Table 7 shows the datasets used and their MBE and CV(RMSE) errors for each data set.

DATA SET	95 percentile		99 percentile		99.9 percentile	
	MBE	CV(RMSE)	MBE	CV(RMSE)	MBE	CV(RMSE)
TRMM-3B42	0.18179	0.78394	0.2792	0.60023	0.327316	0.40898
CHIRPS	0.37345	0.79004	0.45149	0.72057	0.690627	0.764733
NCEP-CPC	0.396979	0.98555	0.34326	0.63134	0.536868	0.539435
NCEP-GOB	0.48376	0.8927	0.38653	0.80616	0.30597	0.359693
GPM	0.23598	0.60905	0.31589	0.5756	0.205597	0.215769

Table 7 - Values of MBE e CV(RMSE) referred to 95, 99 e 99.9 percentile

From Table 7 we can observe that the errors are rather large, resulting in each case in an underestimation of the effective heavy rainfall amount. The best dataset seems to be the GPM, but also in this case errors are large. This analysis suggests that the use of remote sensing datasets as input of hydraulic simulations should be made carefully, taking into account of the existence of such bias. It also suggests that more research efforts should be made to overcome this drawback.

Another aspect that this study has highlighted is inherent to the precipitation obtainable from the satellite. The integrated approach we proposed has demonstrated its reliability if applied to well-instrumented areas. The issue remains open how to improve flooding detection in non-instrumented areas, since measurements of extreme or heavy precipitation by satellite are affected by significant inaccuracies. The study has shown that such precipitations are strongly underestimated (circa 50%).

Given the importance of the availability of satellite data for precipitation measurements, which are essential especially in areas without ground-based instrumentation, it would be appropriate to focus the research on methods to correct such bias, both improving the calibration techniques of satellite data and exploring the capability to overcome such drawback of the new satellites, such as GPM, sent in orbit for this type of survey.

3.6 DISCUSSION ABOUT THE MAIN DRAWBACKS AS ARISE FROM THE CASE STUDIES

As mentioned at the beginning of this chapter, analyses of the capability of remote sensing useful in the post-event flooding risk assessment were carried out by applying it to a real case. The analyses were performed respectively on the study of flooding risk as subsidence, flooding area extension, spatial and temporal distribution of rainfall fields.

In the first application, the subsidence phenomena in a coastal area (Mazzocchio (LT)) was studied. The analysis revealed that the DInSAR technique is very useful for the detection of subsidence phenomena. However, this methodology exhibits some limitations: a) the temporal and geometric decorrelations that influence the phase noise component (Hanssen, 2001); b) the phase unwrapping that concerns the estimation of the residual topographic error components (Ghiglia and Pritt, 1998); and c) the atmospheric component (Zebker et al., 1997). All these errors, hence, require a validation of the obtained results from the analyses conducted. However, the information required for the validation are often not available. In detail, documents such as a land cover map update at the date of the analysis, wells map, pictures of the damages, and all the information useful for a complete evaluation of the phenomena in action are not always available.

After that, other techniques were integrated with remote sensing from satellite and exploited to rebuild post event flooding maps.

For the case studies of Strymon river, Quang Ngai and Houston, different technologies were integrated, namely, remote sensing from satellite, hydraulic modelling, social media marker and ground based measurements in order to understand if each of them, separately investigated, is able to rebuild a post event flooding map with high accuracy. In detail, the Strymon river case study revealed that the combination of hydraulic modelling with only the remote sensing results is not exhaustive. For this reason, also social media

markers were considered for the applications of Harvey hurricane (Houston) and Diamrey Typhoon (Quang Ngai).

Houston case study allows to gain more information than those obtained from the Strymon case. This information come also from the ground stations measurements, which enable to understand the goodness of the accuracy of the flooding map. The second case study, instead, taking into account that Quang Ngai is a totally un-instrumented area from the point of view of the rain gauge stations and not provided with an accurate DEM (Digital Elevation Model), revealed that the accuracy of the input data is of the primary importance and that both precipitation from satellite and DEM with low resolution (30 meters) don't allow to rebuilt a map able to show the real depth and velocities verified during the typhoon.

After this study, an analysis was carried out on the precipitation datasets available in the literature – specifically those deriving from satellite, reanalysis and ground radar - to understand if and which of them can be useful as input of hydraulic modeling in areas not provided with gauge stations. From this comparison emerged that all these datasets lead to a significantly underestimation of the extreme event peaks. These typologies of data, to date, are still not useful as input of the hydraulic modelling and require to be further investigate in the future.

4 THE TWO-DIMENSIONAL MODEL FHM 2D

4.1 THE NECESSITY OF A MORE ACCURATE HYDRAULIC MODEL

The open source hydraulic model used in the previously described case studies presents some limitations:

- 1) Does not allow a direct application of a spatially distributed rainfall;
- 2) Use a dissipative numerical technique which is not accurate in steep morphology or in presence of abrupt slope changes or discontinuities which generally produce change in flow conditions from supercritical to subcritical ones;
- 3) It has long computation times when high spatial resolution DEM are used.

With reference to the last of the listed points it should be underlined that the most 2D flow modeling programs require that the computational mesh cell size is the same as the resolution of the terrain model used. However, this implies high computational times, especially in the case of high resolution DEM (ie Lidar data, etc). Several numerical codes, as HEC-RAS, in order to overcome this issue use the subgrid approach (Casulli et al., 2008).

An example useful for the evaluation of the goodness of this approach is Houston, described in chapter 2.3. In fact, for this application a DEM with high accuracy, a large domain of computation (about 12000 km²) and a mesh with dimension bigger (150x150m) than the one of the previous DEM (5 m) were used. Furthermore, considering that the area under investigation includes complex geometries, most of these are urban, we have questioned the effectiveness of the hydraulic model used in reporting the information of velocity, depth and extension of flooding.

HEC-RAS, the software used in the study, takes into account such geometries through Casulli's sub-grid approach (Casulli 2008). The fundamental goal of this sub-grid model is to reduce these high computational costs without losing the accuracy in the modeling.

Casulli solves the two-dimensional shallow water equations in the particular case that only one vertical layer is specified. In this scheme, the water surface elevation in the momentum equations and the velocity in the vertically integrated continuity equation, are discretized by the theta method (the discretization was shown in Casulli, 2000). Additionally, the bottom friction terms are discretized implicitly for stability purpose. The solution of shallow water equations, according to the Casulli method, is solved through a semi-implicit method of finite volumes. The discretization of the equations can be seen in (Casulli, 2009).

It must be remembered that the subgrid approach comes into play only when computational meshes are used for a hydraulic simulation with a size that is larger than that of the DEM cells.

The computational mesh generated for the reconstruction of the flooding map of Houston in this study has been the subject of a refinement. As mentioned above, this operation was possible by using the breakline option present in HEC-RAS. Such breaklines have been used in correspondence of the complex geometries present in the study area such as buildings, sudden slope changes, etc. The refinement operation of the computational mesh at the same size of the DEM (5 m) performed, allowed to reconstruct with a good accuracy the flooding map. This procedure, due to the big extent and the complexity of the area of interest, required a very long times for the construction of the breaklines and for the cell computation.

The mesh was reinforced by imposing, at the breaklines, computational cells with a size of 5 m.

In order to test the effect of the mesh size on the accuracy of the hydraulic simulation in urban areas we performed a number of simulations on a structured computational grid with mesh size: 5x5 m; 10x10 m; 25x25 m; 50x50 m; 100x100 m; 250x250 m and 500x500m. The simulations refers to a integration domain which covers an urban portion of Houston city (see Figure 41).

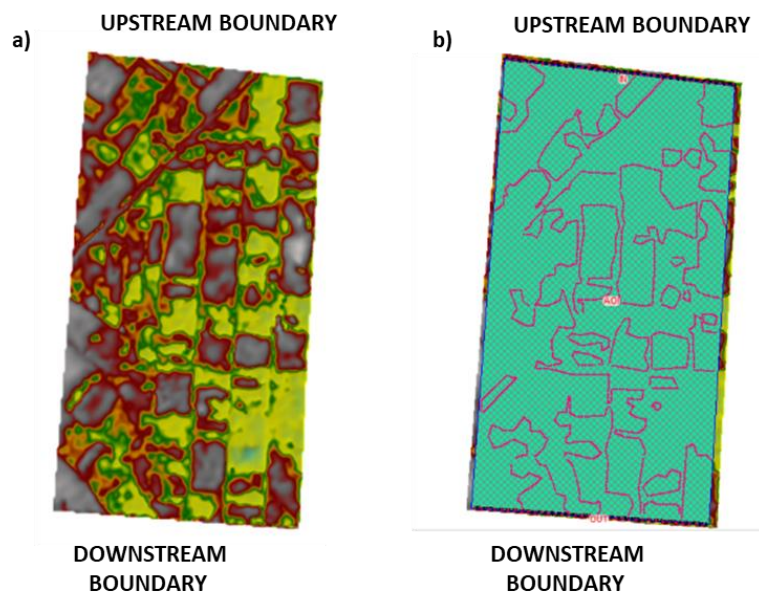


Figure 41 - a) DEM used for the tests; b) computational mesh with breaklines (visible as pink lines).

The boundary conditions for all the tests are the followings: a) at the upstream boundary of the domain the hydrograph of Figure 42 was applied; b) at downstream boundary normal flow condition was applied. The simulation period was long enough to allow steady flow conditions to be established.

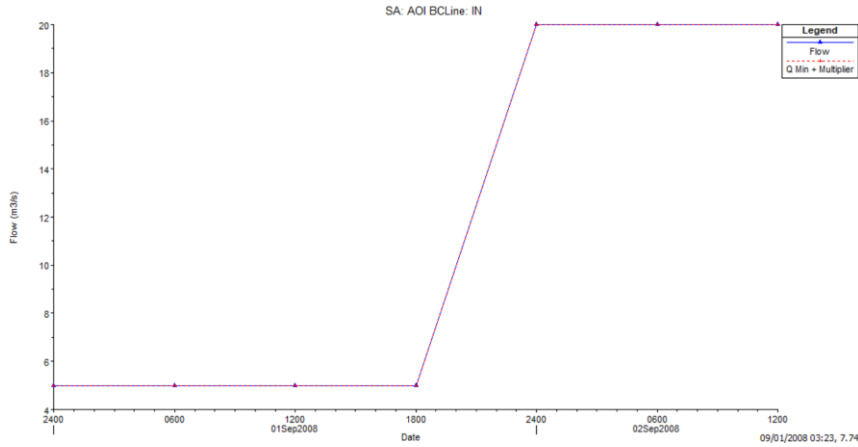


Figure 42 - Flow hydrograph used how input for the analysis

The time step was set equal to 0.5 seconds. The following errors were defined, pixel by pixel in the area of interest (see figure 41), to estimate the effect of the different mesh sizes on the simulated depth and velocity

$$h_{err} = \frac{h_{5X5} - h_{DIM>5X5}}{h_{5X5}} \quad (5)$$

$$v_{err} = \frac{v_{5X5} - v_{DIM>5X5}}{v_{5X5}} \quad (6)$$

In figure 43, the errors obtained by equations are shown for the case no breaklines are inserted, of the depth and velocity evaluation, with the mesh sizes of 10x10, 100x100 and 500x500 m respectively, while in table 8 are reported the max value of MBE (Mean Bias Error) obtained for each of mesh size examined.

	5x5 vs 10x10	5x5 vs 25x25	5x5 vs 50x50	5x5 vs 100x100	5x5 vs 250x250	5x5 vs 500x500
DEPHT	-0.0174	0.0399	0.0607	0.168	0.45775	0.67
VELOCITY	0.2015	-0.53	-1.02	-1.25	-1.45	-2.77

Table 8 - MBE (Mean Bias Error) for each of mesh size examined

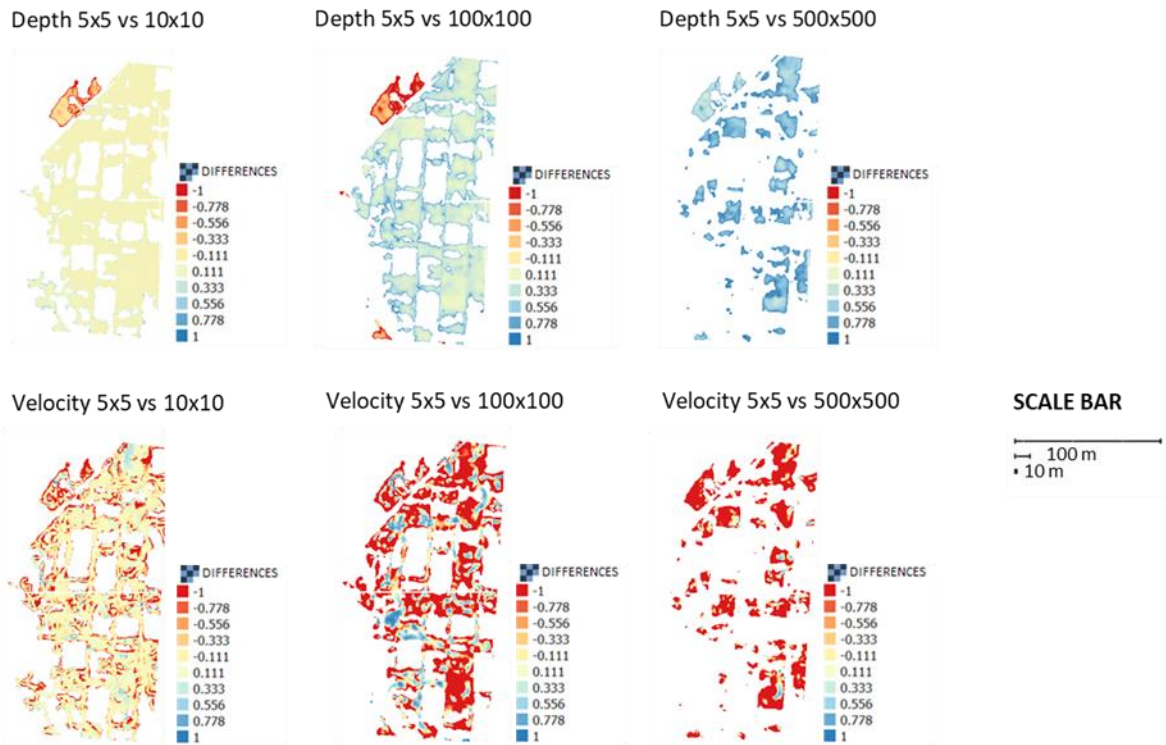


Figure 43 - Hydraulic simulation results for the depth and velocity at the mesh size 5x5 vs 10x10, 100x100 and 500x500.

	5x5 vs 10x10	5x5 vs 25x25	5x5 vs 50x50	5x5 vs 100x100	5x5 vs 250x250	5x5 vs 500x500
A ref (5X5)/A subgrid	0.958	0.877	0.879	1.048	1.649	2.165

Table 9 - Ratio of extension of reference area (mesh size 5x5 m) with extension area with subgrid approach (10x10, 25x25, 50x50, 100x100, 250x250, 500x500)

The analysis showed that the errors grow as the mesh size increases. This fact is particularly evident in the case where a structured square mesh is used, i.e. without the insertion of the breaklines. Through the calculation of the MBE it was possible to demonstrate, moreover, how in the case of depths there are errors of underestimation of values while, on the contrary, in the case of velocities there are heavy overestimations in the values of the pixels obtained. It must be considered that all the parameters of depth and velocity typical of numerical instability were neglected in the analyses.

As shown in Table 8, the errors obtained are both positive and negative. The positive ones, identifying the underestimation of the considered parameter, occur when the values of the pixels obtained using meshes with large dimensions (with subgrid approach) are smaller than those of the reference dimension, in our case those of the mesh 5x5 m. Instead, if the error is negative, identifying an overestimation, it indicates that the values of the pixels obtained using the 5x5 mesh are smaller than those obtained with subgrid approach.

For the depth there was a maximum value of MBE of 0.67 in the case of the 500x500 m cell. For the velocity, always for the same size of cell, equal to 2.77. This means that the depth, when using a very large computational mesh such as 500x500 m, is affected by an underestimation error of the order of 67 %. In the case of velocity, again for the same mesh size, it even has an overestimation of 277 % compared to the ideal case.

Table 9, on the other hand, shows the results concerning the comparison between the extensions of the flooding obtained using the different sizes of the cells. The comparison was made through a ratio between the area found in the ideal case (5x5 m) and that of any extension of the flooding obtained with greater computational meshes. It has emerged that as the size of the calculation cells increases, there is a considerable loss of information (see Fig. 43). In the worst case, the one with a 500x500 m cell, a ratio of 2.16 was calculated. This means that there is a loss of information equal to twice the ideal case.

This test has made it possible to understand the effectiveness of the Casulli subgrid approach, in the software used, in the return of depth and velocity values in case no breaklines are used. For the reconstruction of the flooding map of Houston presented in this study, as already mentioned above, the breaklines for all buildings have been reported in the urban context. Performing this operation requires very high operator work and computational times. For this reason, with this study, we tried to understand if the hydraulic model used allowed to bypass the use of breaklines. From the analysis it emerged that this is impossible given that we would get restitutions of depth, velocity and extent of the flooding untrue. Therefore, it is necessary to develop subgrid schemes that are more accurate than those currently used in order to reduce operator work and calculation times.

Taking into the account the errors found in the previous test and the fact that the HEC-RAS software, used in the various simulations, is a non-modifiable code, a new code was developed. The equations presents in the code were taken using as reference the papers of: (Audusse et al., 2004) for the governing equations, for the Lax-Friedrichs first order of flux discretization, and finally for the first and second order extension of the source discretization; (Hou, J. et al., 2015) for the TVD MUSCL second order flux discretization; (Jameson A. et al., 1981) and (Marqués, J. M. F., 2000), respectively, for the Runge-Kutta 4th order and Forward Euler explicit scheme for the discretization of the time derivative. Finally, for the precipitation and infiltration parameters the works of (Cea, L. et al., 2010) and (Chow et al. 1988) were used respectively.

The proposed code overcomes the limitations listed at the beginning of the paragraph and in detail: 1) it is a parallel code that significantly reduces the calculation times for equal spatial resolution; 2) it solves the presence of discontinuities and regime changes in the flow; 3) it allows an arbitrary distribution of the rainfall.

Furthermore, in this code developed in this thesis not was considerate the subgrid approach considering the limitation that still present. The numerical model created and called FHM-2D is two-dimensional and solves

the shallow water equations at the same resolution of the DEM. Below a description of the numerical applied to the model is shown.

4.2 GOVERNING EQUATIONS

The two-dimensional depth-integrated shallow water equations (SWE) are obtained by integrating the Navier–Stokes equations over the flow depth with the following assumptions: uniform velocity distribution in the vertical direction, incompressible fluid, hydrostatic pressure distribution, and small bottom slope. The continuity and momentum equations are:

$$\begin{cases} h_t + (hu)_x + (hv)_y = 0 \\ (hu)_t + \left(hu^2 + \frac{1}{2}gh^2\right)_x + (huv)_y = -ghz_x \\ (hv)_t + (huv)_x + \left(hv^2 + \frac{1}{2}gh^2\right)_y = -ghz_y \end{cases} \quad (7)$$

It is possible to write this system in the conservative form:

$$q_t + F(q)_x + G(q)_y = q_t + \text{div}(\mathbf{F}(q)) = S(x, y, q) \quad (8)$$

Where:

$$q = \begin{bmatrix} h \\ hu \\ hv \end{bmatrix}, F(q) = \begin{bmatrix} hu \\ hu^2 + \frac{1}{2}gh^2 \\ huv \end{bmatrix}, G(q) = \begin{bmatrix} huv \\ hv^2 + \frac{1}{2}gh^2 \end{bmatrix}$$

$$s(x, y, q) = S_z + S_f = \begin{bmatrix} 0 \\ -ghz_x(x, y) \\ -ghz_y(x, y) \end{bmatrix} + \begin{bmatrix} 0 \\ ghS_{fx} \\ ghS_{fy} \end{bmatrix}, \mathbf{F} = [F \ G]$$

Where q is the cell-centered vector of discrete unknowns; $F(q)$ and $G(q)$ are the numerical fluxes; u and v are the velocity components in the x and y directions, respectively; h is the water depth; g is the acceleration due to gravity; $z_x(x, y)$ and $z_y(x, y)$ are the bed slopes in the x and y directions, S_{fx} and S_{fy} are the friction slopes in the x and y directions, respectively. In the model, the friction slopes are estimated by using the Manning formula

$$S_{fx} = \frac{n^2 u \sqrt{u^2 + v^2}}{h^{4/3}}$$

$$S_{fy} = \frac{n^2 v \sqrt{u^2 + v^2}}{h^{4/3}}$$

where n is the Manning's roughness coefficient. In general, the influence of bottom roughness prevails over the turbulent shear stress between cells. Therefore, the effective stress terms were neglected in the computation.

4.3 NUMERICAL MODEL

A cell-centered finite volume method is formulated for the equation (8) over a rectangular control volume, where the dependent variables of the system are stored at the center of the cell and represented as piecewise constants. Integrating the eq. (8) over the area of the i -th control volume, one obtains

$$\int_{A_i} \frac{\partial \bar{q}_{ij}}{\partial t} d\Delta + \int_{A_i} \nabla \cdot E dA = \int_{A_i} S dA \quad (9)$$

where $E = F(q)_i + G(q)_i$ and A_i is the area of the control volume. Using the divergence theorem, the second integral on the lefthand side of the equation 9 can be replaced by a line integral around the control volume

$$\int_{A_i} \frac{\partial \bar{q}_{ij}}{\partial t} d\Delta + \oint_{\Gamma_i} \nabla \cdot E dA = \int_{A_i} S dA \quad (10)$$

where Γ_i is the boundary of the i -th control volume and n is the unit outward vector normal to the boundary. Approximating the line integral by a midpoint quadrature rule, Eq. (10) can be written as

$$\frac{\partial \bar{q}_{ij}}{\partial t} = -\frac{1}{A_i} \sum_{j=1}^4 E * n_{ij} \Delta \Gamma_{ij} + S_{ij} \quad (11)$$

where i and j denote the i -th cell and the j -th edge of the cell, respectively; q_{ij} and S_{ij} are the average quantities stored at the center of the i -th cell; n_{ij} is the unit outward normal vector at the j -th edge; $\Delta \Gamma_{ij}$ is the length of the j th edge; and E is the numerical flux through the edge which is computed by an exact or approximate Riemann solver.

Thus, evaluating fluxes at the cell edges and applying the FVM and the theorem of divergence we get the following semi-discrete scheme:

$$\Delta x \Delta y \frac{\partial \bar{q}_{ij}}{\partial t} + (\vec{F}_{i+1/2,j} - \vec{F}_{i-1/2,j}) + (\vec{G}_{i,j+1/2} - \vec{G}_{i,j-1/2}) = \Delta x \Delta y \vec{S}_{ij} \quad (12)$$

where Δx and Δy denotes a possibly variable mesh size $\Delta x = x_{i+1/2} - x_{i-1/2}$ and $\Delta y = y_{i+1/2} - y_{i-1/2}$.

The aim of this study is to develop a Nonlinear shallow water Cartesian solver that allows for:

- ✓ Arbitrary topography from DEM input → structural grid fitted on DEM grid

- ✓ Well-balanced formulation for discrete lake-at-rest preservation --> source term discretization
- ✓ Automatic wet/dry transition capability → FVM with approximated Riemann solver
- ✓ Automatic capturing of hydraulic jumps → FVM with approximated Riemann solver
- ✓ Implicit treatment of friction terms with spatially varying Manning coefficient → specific treatment of bottom friction term
- ✓ Arbitrary space-and-time precipitation
- ✓ Fully parallel MPI implementation
- ✓ Runs in matter of hours

The shallow water equations are a nonlinear hyperbolic system of conservation laws (with a source term due to the topography). For such a problem, where shocks can form in the solution, finite volume methods have proved to be very effective.

The model developed allow to solve the shallow water equations by an implicit finite volume method with time discretization by 4 order Runge-kutta method and first order forward Euler explicit scheme method. The fluxes, instead, are discretized, for the first order of accuracy, with an approximate Riemann solver - Lax friedrichs (LF) and, for the second order, with MUSCL - TVD scheme (Total Variation Diminishing).

4.4 TIME INTEGRATION

Runge Kutta 4th order

Higher order schemes of time integration are needed when the numerical flux is approximated by higher order schemes. One of the higher order schemes is fourth-order Runge-Kutta method (RK4). The RK4 method has the fourth-order of accuracy. It means that the error per step is of the order $O(\Delta t^5)$ while the total accumulated error has order $O(\Delta t^4)$. The higher accuracy of RK4 is redeemed by high computational demands.

$$\Delta x \Delta y \frac{\partial \vec{q}_{ij}}{\partial t} + (\vec{F}_{i+1/2,j} - \vec{F}_{i-1/2,j}) + (\vec{G}_{i,j+1/2} - \vec{G}_{i,j-1/2}) = \Delta x \Delta y \vec{S}_{ij}$$

if we considerate

$$RHS_i = - \left[\left(\vec{F}_{i+\frac{1}{2},j} - \vec{F}_{i-\frac{1}{2},j} \right) + \left(\vec{G}_{i,j+\frac{1}{2}} - \vec{G}_{i,j-\frac{1}{2}} \right) \right] + \Delta x \Delta y \vec{S}_{ij}$$

We can write

$$\frac{\partial \vec{q}_{ij}^n}{\partial t} = RHS_i(\vec{q}_{ij}^n)$$

where n means the time level.

The solution of the equation $\frac{\partial \vec{q}_{ij}}{\partial t}$ at the $n + 1$ th time level is

$$\vec{q}_{ij}^{n+1} = \vec{q}_{ij}^n + \frac{\Delta t}{6} (k_1 + 2k_2 + 2k_3 + k_4)$$

$$k_1 = RHS_i(\vec{q}_{ij}^n)$$

$$k_2 = RHS_i(\vec{q}_{ij}^{n+1*})$$

$$\vec{q}_{ij}^{n+1*} = \vec{q}_{ij}^n + \frac{\Delta t}{2} k_1$$

$$k_3 = RHS_i(\vec{q}_{ij}^{n+1**})$$

$$\vec{q}_{ij}^{n+1**} = \vec{q}_{ij}^n + \frac{\Delta t}{2} k_2$$

$$k_4 = RHS_i(\vec{q}_{ij}^{n+1***})$$

$$\vec{q}_{ij}^{n+1***} = \vec{q}_{ij}^n + \Delta t k_3$$

Forward Euler explicit scheme method

As mentioned before, in addition to the scheme of RK4, here it was applied the first order forward Euler temporal discretization method. In this section, it was explained the scheme adopted.

If we considerate the equation (11)

$$\frac{\partial \vec{q}_{ij}}{\partial t} = - \frac{1}{A_i} \sum_{j=1}^4 E * n_{ij} \Delta \Gamma_{ij} + S_{ij}$$

Different discretizations for this equation can be obtained from the Taylor series expansion. For example, if i is the spatial index and n the time index,

$$q_{ij}^{n+1} = q_{ij}^n + \left. \frac{\partial q}{\partial t} \right|_i^n \Delta t + \frac{1}{2} \left. \frac{\partial^2 q}{\partial t^2} \right|_i^n \Delta t^2 + O(\Delta t^3)$$

and the time derivative can be approximated as

$$\left. \frac{\partial q}{\partial t} \right|_i^n = \frac{q^{n+1} - q^n}{\Delta t} - \frac{1}{2} \left. \frac{\partial^2 q}{\partial t^2} \right|_i^n \Delta t + O(\Delta t^2)$$

which is a first order forward discretization. Also

$$F(q_{ij}^n)_{i+1} = F(q_{ij}^n) + \left. \frac{\partial F(q)}{\partial x} \right|_i^n \Delta x + \frac{1}{2} \left. \frac{\partial^2 F(q)}{\partial x^2} \right|_i^n \Delta x^2 + \frac{1}{6} \left. \frac{\partial^3 F(q)}{\partial x^3} \right|_i^n \Delta x^3 + O(\Delta x^4)$$

$$F(q_{ij}^n)_{i-1} = F(q_{ij}^n) - \left. \frac{\partial F(q)}{\partial x} \right|_i^n \Delta x + \frac{1}{2} \left. \frac{\partial^2 F(q)}{\partial x^2} \right|_i^n \Delta x^2 - \frac{1}{6} \left. \frac{\partial^3 F(q)}{\partial x^3} \right|_i^n \Delta x^3 + O(\Delta x^4)$$

$$G(q_{ij}^n)_{j+1} = G(q_{ij}^n) + \left. \frac{\partial G(q)}{\partial y} \right|_i^n \Delta y + \frac{1}{2} \left. \frac{\partial^2 G(q)}{\partial y^2} \right|_i^n \Delta y^2 + \frac{1}{6} \left. \frac{\partial^3 G(q)}{\partial y^3} \right|_i^n \Delta y^3 + O(\Delta y^4)$$

$$G(q_{ij}^n)_{j-1} = G(q_{ij}^n) - \left. \frac{\partial G(q)}{\partial y} \right|_i^n \Delta y + \frac{1}{2} \left. \frac{\partial^2 G(q)}{\partial y^2} \right|_i^n \Delta y^2 - \frac{1}{6} \left. \frac{\partial^3 G(q)}{\partial y^3} \right|_i^n \Delta y^3 + O(\Delta y^4)$$

and subtracting the two equations, respectively for F and G, we obtain a space centered second order discretization

$$\left. \frac{\partial F(q_{ij}^n)}{\partial x} \right|_i^n = \frac{F(q_{ij}^n)_{i+1} - F(q_{ij}^n)_{i-1}}{2\Delta x} - \frac{1}{6} \left. \frac{\partial^3 F(q_{ij}^n)}{\partial x^3} \right|_i^n \Delta x^2 + O(\Delta x^3)$$

$$\left. \frac{\partial G(q_{ij}^n)}{\partial y} \right|_i^n = \frac{G(q_{ij}^n)_{j+1} - G(q_{ij}^n)_{j-1}}{2\Delta y} - \frac{1}{6} \left. \frac{\partial^3 G(q_{ij}^n)}{\partial y^3} \right|_i^n \Delta y^2 + O(\Delta y^3)$$

Then equation (5) can be written in discretized form as

$$\frac{q_{ij}^{n+1} - q_{ij}^n}{\Delta t} + \frac{F(q_{ij}^n)_{i+1} - F(q_{ij}^n)_{i-1}}{2\Delta x} + \frac{G(q_{ij}^n)_{j+1} - G(q_{ij}^n)_{j-1}}{2\Delta y} = \vec{S}_{ij}$$

from which the following numerical algorithm results

$$q_{ij}^{n+1} = q_{ij}^n + \frac{1}{2} \frac{\Delta t}{\Delta x \Delta y} \left(F(q_{ij}^n)_{i+1} - F(q_{ij}^n)_{i-1} \right) + \left(G(q_{ij}^n)_{j+1} - G(q_{ij}^n)_{j-1} \right) + \vec{S}_{ij}$$

This scheme, first order in time and second in space, is called Euler explicit scheme.

4.5 DISCRETIZATION OF NUMERICAL FLUXES

Lax Friedrichs - Approximate Riemann solver

Generally, a robust and well-balanced scheme for shallow water equations should satisfy some mathematical properties such as preserve the no negativity of water height h , well-balanced, i.e. it preserves the discrete steady state, consistent with the shallow water equations and satisfy a discrete entropy inequality.

In the code the SWE for first-order accurate scheme, all the unknowns of the system are approximated on the same mesh and the numerical fluxes are computed with a Lax Friedrichs approximate Riemann solver. This method is conservative and first order accurate, hence quite dissipative. This method is explicit and first order accurate in time and first order accurate in space $O(\Delta t) + O\left(\frac{\Delta x^2}{\Delta t}\right)$. Under these conditions, the method is stable if and only if the following condition is satisfied:

$$\left| \frac{\Delta t}{\Delta x} \right| \leq 1$$

Lax–Friedrichs method is classified as having second-order dissipation and third order dispersion (Chu et al., 1978). For functions that have discontinuities, the scheme displays strong dissipation and dispersion (Thomas et al., 1995).

If we take the equation (12)

$$\Delta x \Delta y \frac{\partial \vec{q}_{ij}}{\partial t} + (\vec{F}_{i+1/2,j} - \vec{F}_{i-1/2,j}) + (\vec{G}_{i,j+1/2} - \vec{G}_{i,j-1/2}) = \Delta x \Delta y \vec{S}_{ij}$$

where $\vec{F}_{i+1/2,j}, \vec{F}_{i-1/2,j}, \vec{G}_{i,j+1/2}, \vec{G}_{i,j-1/2}$ are the momentum fluxes presents at the faces of the cell (figure 44).

Here we want show how it was discretized the flux in the one dimensional case.

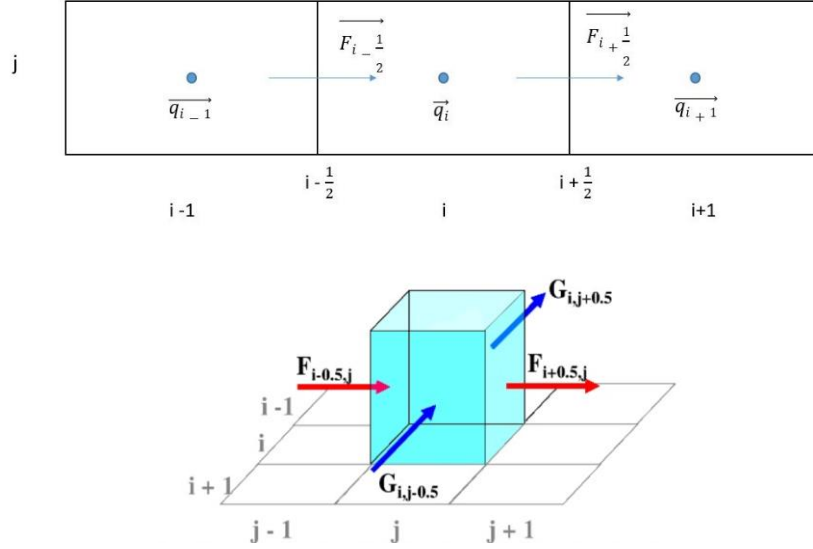


Figure 44 - Momentum numerical fluxes through the face of the cells

The numerical flux function is defined as

$$\vec{F}_{i+\frac{1}{2}} = \vec{F}(\vec{q}_{i-1}^-; \vec{q}_{i+1}^+)$$

$\vec{q}_{i-1}^-; \vec{q}_{i+1}^+$ are the interfaces values and are derived from a local hydrostatic reconstruction. The numerical fluxes $\vec{F}_{i\pm 1/2,j}$ correspond to a nonlinear combination of first and second-order approximations to the continuous flux function

$$\vec{F}_{i+1/2,j} = \vec{F}^+(\vec{q}_i, \alpha) + \vec{F}^-(\vec{q}_{i+1}, \alpha)$$

where the terms of the equation are respectively

$$\vec{F}^+(q_i, \alpha) = \frac{1}{2}(\vec{F}(\vec{q}_i) + \alpha \vec{q}_i)$$

$$\vec{F}^-(\vec{q}_{i+1}, \alpha) = \frac{1}{2}(\vec{F}(\vec{q}_{i+1}) + \alpha \vec{q}_{i+1})$$

where $\vec{F}(q_i) = hu$ and $\alpha = \max(|u_i| + \sqrt{gh_i}, |u_{i+1}| + \sqrt{gh_{i+1}})$.

This discretization was used for demonstrate that the scheme is able to robustly captures dry regions where $h_i = 0$. If $h_i = 0$, we have that $h_{i+\frac{1}{2}}^- = 0$ and $h_{i-\frac{1}{2}}^+ = 0$. If these terms are zero also the fluxes are

$\vec{F}_{i+1/2}^- = 0$ and $\vec{F}_{i-1/2}^+ = 0$. Before to study the nonnegativity of h we have to define $\frac{dh_i}{dt}$ the variaton of h

in the time.
$$\frac{dh_i}{dt} = -\frac{1}{h} \left[\vec{F}_{i+\frac{1}{2},j} - \vec{F}_{i-\frac{1}{2},j} \right]$$

$$\begin{aligned}
\frac{\partial h_i}{\partial t} &= -\frac{1}{h} \left[(uh)_{i+\frac{1}{2}} + (uh)_{i-\frac{1}{2}} \right] \\
&= -\frac{1}{h} \left[\frac{1}{2} \left((h_{i+\frac{1}{2}} u_{i+\frac{1}{2}} + \alpha h_{i+\frac{1}{2}}) + (h_i u_i + \alpha h_i) \right) \right. \\
&\quad \left. + \frac{1}{2} \left((h_{i-\frac{1}{2}} u_{i-\frac{1}{2}} + \alpha h_{i-\frac{1}{2}}) + (h_i u_i + \alpha h_i) \right) \right] = \\
&= -\frac{1}{h} \left[\frac{1}{2} \left((h_{i+\frac{1}{2}} u_{i+\frac{1}{2}} + \alpha h_{i+\frac{1}{2}}) \right) + \frac{1}{2} \left((h_{i-\frac{1}{2}} u_{i-\frac{1}{2}} + \alpha h_{i-\frac{1}{2}}) \right) \right] \\
&= \frac{1}{h} \left[\frac{1}{2} (h_{i+1/2} (-u_{i+1/2} + \alpha) + h_{i-1/2} (u_{i-1/2} + \alpha)) \right]
\end{aligned}$$

The positivity of h requires that $\frac{\partial h_i}{\partial t} \geq 0$, consequently we have $h^-_{i+1/2} \geq 0$ and $h^+_{i-1/2} \geq 0$. We can

write that

$$\begin{aligned}
\frac{1}{h} \left[\frac{1}{2} \left(h_{i+\frac{1}{2}} (-u_{i+\frac{1}{2}} + \alpha) + h_{i-\frac{1}{2}} (u_{i-\frac{1}{2}} + \alpha) \right) \right] &\geq 0 \\
\frac{1}{2} \left(-h_{i+\frac{1}{2}} u_{i+\frac{1}{2}} - \alpha h_{i+\frac{1}{2}} + h_{i-\frac{1}{2}} u_{i-\frac{1}{2}} + \alpha h_{i-\frac{1}{2}} \right) &\geq 0
\end{aligned}$$

If $h^-_{i+1/2} \geq 0$ $h^+_{i-1/2} \geq 0$ we can exclude from the previous equation and we have

$$\frac{1}{2} (-u_{i+1/2} - \alpha + u_{i-1/2} + \alpha) \geq 0$$

We can write
$$\begin{cases} \alpha - u_{i+1/2} \geq 0 \\ \alpha + u_{i-1/2} \geq 0 \end{cases}$$

We have nonnegativity of h when α is defined how

$$\alpha = \max(|u_{i+1/2}|, |u_{i-1/2}|)$$

DEMONSTRATION

Hyperbolicity is the property that represents the central point concerning the aim of solving the 2D shallow water equations numerically. On the one hand, it is known that hyperbolic systems of conservation laws can develop discontinuities in the solution after finite time even for smooth initial conditions, and that thus

solutions can only be understood in the weak sense. On the other hand, hyperbolicity allows to determine the solution of a special discontinuous initial value problem, the Riemann problem. If we take the (12)

$$\Delta x \Delta y \frac{\partial \vec{q}_{ij}}{\partial t} + (\vec{F}_{i+1/2,j} - \vec{F}_{i-1/2,j}) + (\vec{G}_{i,j+1/2} - \vec{G}_{i,j-1/2}) = \Delta x \Delta y \vec{S}_{ij}$$

Is possible to write in the nonlinear form

$$\frac{\partial \vec{q}_{ij}}{\partial t} + (A, B) \nabla (\vec{q}_{ij}) = \vec{S}_{ij}(\vec{q}_{ij})$$

The Jacobian matrix A^\pm are

$$A = \frac{\partial F^\pm}{\partial q} = \begin{bmatrix} 0 & 1 & 0 \\ c^2 - u^2 & 2u & 0 \\ -uv & v & u \end{bmatrix}$$

$$B = \frac{\partial G^\pm}{\partial q} = \begin{bmatrix} 0 & 1 & 0 \\ -uv & v & u \\ c^2 - v^2 & 0 & 2v \end{bmatrix}$$

There are three unknowns, water depth and two velocity components, and therefore three equations are required. The information used to find the solution in first order of approximation travels through the world line and two selected bicharacteristic curves. In the first order upwind scheme, the eigenvalues play a role similar to that of the bicharacteristic curves, and that of the world line but computed at every cell edge and contributing to the discretization of the three conservation equations (mass and momentum).

Depending on the dimensionless normal Froude number, the characteristic cone has a different shape. At a given cell, a characteristic cone can be defined and the value of the three unknowns at the cell can be updated using information carried by the ingoing characteristic lines.

If we considerate the eq. (5) is possible to write the Jacobian matrix J_n of the normal flux ($E * n$) in the follow mode

$$\frac{\partial \vec{q}_{ij}}{\partial t} = -\frac{1}{A_i} \sum_{j=1}^4 (E * n_{ij}) \Delta \Gamma_{ij} + S_{ij} \quad (5)$$

$$J_n = \frac{\partial E * n}{\partial \vec{q}_{ij}} = \frac{\partial F}{\partial \vec{q}_{ij}} n_x + \frac{\partial G}{\partial \vec{q}_{ij}} n_y$$

and can be expressed as

$$J_n = \begin{bmatrix} 0 & n_x & n_y \\ \left(gh - \frac{P_x^2}{h^2}\right) n_x - \frac{P_x P_y}{h^2} n_y & \frac{P_y}{h} n_y + \frac{2P_x}{h} n_x & \frac{P_x}{h} n_y \\ \left(gh - \frac{P_y^2}{h^2}\right) n_y - \frac{P_x P_y}{h^2} n_x & \frac{P_y}{h} n_x & \frac{P_x}{h} n_x + \frac{2P_y}{h} n_y \end{bmatrix}$$

where $P_x = hu$ and $P_y = hv$. The eigenvalues of J_n are a representation of the characteristic speeds a^l

$$a1 = unx + vny + c,$$

$$a2 = unx + vny,$$

$$a3 = unx + vny - c.$$

The corresponding eigenvectors are

$$e^1 = \begin{bmatrix} 1 \\ u + cn_x \\ v + cn_y \end{bmatrix} \quad e^2 = \begin{bmatrix} 0 \\ -cn_y \\ cn_x \end{bmatrix} \quad e^3 = \begin{bmatrix} 1 \\ u - cn_x \\ v - cn_y \end{bmatrix}$$

Considering the characteristic speeds $e^1 = e^2 = e^3 = e$, for allow the nonnegativity of the height inside the cell we have that

$$J_n^+ \rightarrow a \geq 0$$

$$J_n^- \rightarrow a \leq 0$$

$$J_n^+ \rightarrow a^+ = u + e \pm c \geq 0 \text{ is } a \geq |u \pm c|$$

$$J_n^- \rightarrow a^- = u + e \pm c \leq 0 \text{ is } a \leq |u \pm c|$$

Flux discretization with TVD scheme

Second order spatial accuracy can be achieved by introducing more upwind points or cells in the schemes. The method used for the generation of second order upwind schemes based on variable extrapolation is often referred to in the literature as the MUSCL (“Monotone Upstreamcentered Schemes for Conservation Laws”) approach. The use of nonlinear limiters in such procedure, with the intention of restricting the amplitude of the gradients appearing in the solution, avoiding thus the formation of new extrema, allows that first order upwind schemes be transformed in TVD high resolution schemes with the appropriate definition of such nonlinear limiters, assuring monotone preserving and total variation diminishing methods.

The expressions to calculate de fluxes following a MUSCL procedure and the nonlinear flux limiter definitions employed in this work, which incorporates TVD properties, are defined as follows.

The conserved variables at the interface $(i+\frac{1}{2},j)$ can be considered as resulting from a combination of backward and forward extrapolations. To a linear one-sided extrapolation at the interface between the averaged values at the two upstream cells (i,j) and $(i-1,j)$, one has:

$$\vec{q}_{i+\frac{1}{2},j}^L = \vec{q}_{i,j} + \frac{\varepsilon}{2}(\vec{q}_{i,j} - \vec{q}_{i-1,j}^L), \text{ cell } (i,j) \quad (7)$$

$$\vec{q}_{i+\frac{1}{2},j}^R = \vec{q}_{i,j} - \frac{\varepsilon}{2}(\vec{q}_{i+2,j} - \vec{q}_{i+1,j}^R), \text{ cell } (i+1,j) \quad (8)$$

leading to a second order fully one-sided scheme. If the first order scheme is defined by the numerical flux

$$\vec{F}_{i+\frac{1}{2},j} = \vec{F}(\vec{q}_{i,j}; \vec{q}_{i+1,j})$$

the second order space accurate numerical flux is obtained from

$$\overrightarrow{F^{(2)}}_{i+\frac{1}{2},j} = \vec{F}(\vec{q}_{i+\frac{1}{2},j}^L; \vec{q}_{i+\frac{1}{2},j}^R)$$

Higher order flux vector splitting or flux difference splitting methods, are obtained from:

$$\overrightarrow{F^{(2)}}_{i+\frac{1}{2},j} = \vec{F}^+(\vec{q}_{i+\frac{1}{2},j}^L) + \vec{F}^-(\vec{q}_{i+\frac{1}{2},j}^R)$$

All second order upwind schemes necessarily involve at least five mesh points or cells. To reach high order solutions without oscillations around discontinuities, nonlinear limiters are employed, replacing the term ε in Eqs. (7-8) by these limiters at the left and at the right states of the flux interface. To define such limiters, it is necessary to calculate the ratio of consecutive variations of the conserved variables. These ratios are defined as follows:

$$r_{i+\frac{1}{2},j}^+ = (\vec{q}_{i+1,j} - \vec{q}_{i,j}) / (\vec{q}_{i,j} - \vec{q}_{i+1,j})$$

and

$$r_{i+\frac{1}{2},j}^- = (\vec{q}_{i+2,j} - \vec{q}_{i+1,j}) / (\vec{q}_{i+1,j} - \vec{q}_{i,j})$$

where the nonlinear limiters at the left and at the right states of the flux interface are defined by

$$\psi^L = \psi(r_{i+\frac{1}{2},j}^+)$$

$$\psi^R = \psi(1/r_{i+\frac{1}{2},j}^-)$$

In this work, two options of nonlinear limiters were considered to the numerical experiments. These limiters are defined as follows:

$$\psi^{VL}(r_l) = \frac{r_l + |r_l|}{1 + r_l} \text{ Van Leer limiter}$$

and

$$\psi^{MIN}(r_l) = \text{signal}_l \text{Max}(0, \text{MIN}(|r_l|, \text{signal}_l)) \text{ minmod limiter.}$$

with “ l ” varying from 1 to 4 (two-dimensional space), $signal_l$ being equal to 1 if $r_l \geq 0$ and -1 otherwise, r_l is the ratio of consecutive variations of the l th conserved variable.

4.6 SOURCE TERM DISCRETIZATION

- *first order*

In conditions of the steady state of a lake at rest we have $H + z = Cost, u = 0$

$$\Delta x \frac{\partial \vec{q}_i}{\partial t} + (\vec{F}_{i+1/2} - \vec{F}_{i-1/2}) = \Delta x \vec{S}_i$$

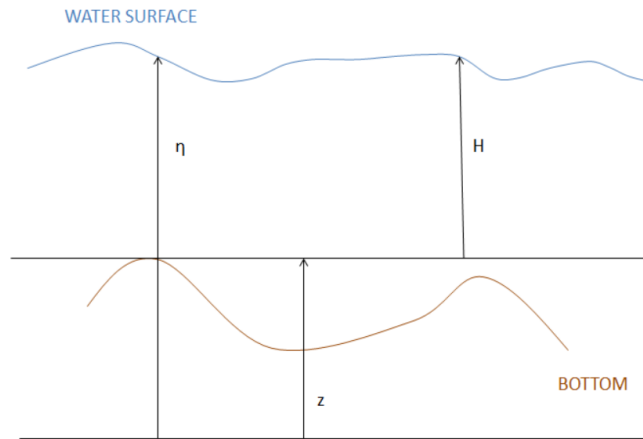


Figure 45 - Shallow domain

where $\eta = H + z$

$$S_i = \begin{pmatrix} 0 \\ -gHB \end{pmatrix} \text{ where } B = \nabla z$$

$$S_i = \begin{pmatrix} 0 \\ -gH\nabla z \end{pmatrix}$$

For the i -th grid cell we have this approximation of the source term

$$-\int_{x_{i-1/2}}^{x_{i+1/2}} gh\nabla z = \left(\frac{g}{2} H^2_{i+1/2^-} - \frac{g}{2} H^2_{i-1/2^+} \right)$$

At this point we can write

$$S_i = \begin{pmatrix} 0 \\ \frac{g^2}{2} H_{i+\frac{1}{2}}^- - \frac{g^2}{2} H_{i-\frac{1}{2}}^+ \end{pmatrix}$$

For balance of momentum flux and momentum source terms we can write

$$\frac{\partial}{\partial x} \left(\frac{gh^2}{2} \right) = -hg \frac{\partial z}{\partial x}$$

$$F_{i+\frac{1}{2}} - F_{i-\frac{1}{2}} = S_{i+\frac{1}{2}} - S_{i-\frac{1}{2}}$$

where $S_{i+\frac{1}{2}}$ and $S_{i-\frac{1}{2}}$ are

$$S_{i+\frac{1}{2}} = \frac{g}{2} H_{i+\frac{1}{2}}^2 -$$

$$S_{i-\frac{1}{2}} = \frac{g}{2} H_{i-\frac{1}{2}}^2 +$$

At this point we must define the heights $H_{i+1/2}^-$ and $H_{i+1/2}^+$. $F_{i+1/2}$ and $F_{i-1/2}$ will show in the follow section. For $z+H=cost$ and $u=0$ for the lake at rest conditions we have followed hydrostatic balance

$$\frac{dH}{dx} = - \frac{dz_i}{dx}$$

$$H_{i+\frac{1}{2}}^- = H_i - \frac{\Delta x_i}{2} \left(\frac{z_{i+\frac{1}{2}} - z_i}{\frac{\Delta x_i}{2}} \right) = H_i - z_{i+\frac{1}{2}} + z_i$$

$$H_{i+\frac{1}{2}}^+ = H_{i+1} - \frac{\Delta x_{i+1}}{2} \left(\frac{z_{i+1} - z_{i+\frac{1}{2}}}{\frac{\Delta x_i}{2}} \right) = H_{i+1} + z_{i+1} - z_{i+\frac{1}{2}}$$

$$H_{i+1/2}^- = \max \left(0, H_i + z_i - z_{i+\frac{1}{2}} \right) \text{ and } H_{i+1/2}^+ = \max \left(0, H_{i+1} + z_{i+1} - z_{i+\frac{1}{2}} \right)$$

With heights of topography defined how

$$z_{i+\frac{1}{2}} = \max \left(0, H_i + z_i - z_{i+\frac{1}{2}} \right)$$

- **second order extension**

Starting from a given first-order method, a common way to obtain a second-order extension is, for a hydrostatic reconstruction, to compute the fluxes from limited reconstructed values on both sides of each interface rather than cell-centered values. This gives the second-order well-balanced scheme:

$$\Delta x \frac{\partial \vec{q}_i}{\partial t} + \left(\vec{F}_{i+\frac{1}{2}} - \vec{F}_{i-\frac{1}{2}} \right) = \Delta x (\vec{S}_i + \vec{S}_{ci})$$

where

$$\vec{F}_{i+\frac{1}{2}} = \vec{F}(\vec{q}_{i-1}^-; \vec{q}_{i+1}^+)$$

$$\vec{q}_{i-1}^- = \begin{bmatrix} h_{i+\frac{1}{2}}^- \\ h_{i+\frac{1}{2}}^- u_{i,dx} \end{bmatrix}$$

$$\vec{q}_{i+1}^+ = \begin{bmatrix} h_{i+\frac{1}{2}}^+ \\ h_{i+\frac{1}{2}}^+ u_{i+1,lf} \end{bmatrix}$$

For $z+H=cost$ and $u=0$ for the lake at rest conditions we have follow hydrostatic balance

$$\frac{dH}{dx} = -\frac{dz_i}{dx}$$

$$H_{i+\frac{1}{2}}^- = H_{i,dx} - \frac{\Delta x_i}{2} \left(\frac{z_{i+\frac{1}{2},dx} - z_i}{\frac{\Delta x_i}{2}} \right) = H_{i,dx} - z_{i+\frac{1}{2},dx} + z_i$$

$$H_{i+\frac{1}{2}}^+ = H_{i+1,lf} - \frac{\Delta x_{i+1}}{2} \left(\frac{z_{i+1} - z_{i+\frac{1}{2},lf}}{\frac{\Delta x_i}{2}} \right) = H_{i+1,lf} + z_{i+1} - z_{i+\frac{1}{2},lf}$$

$$H_{i+\frac{1}{2}}^- = \max\left(0, H_{i,dx} - z_{i+\frac{1}{2},dx} + z_i\right) \text{ and } H_{i+\frac{1}{2}}^+ = \max\left(0, H_{i+1,lf} + z_{i+1} - z_{i+\frac{1}{2},lf}\right)$$

with heights of topography defined how

$$z_{i+\frac{1}{2}} = \max\left(0, H_i + z_{i,dx} - z_{i+\frac{1}{2},lf}\right)$$

Precipitation and infiltration term in the SWE 2D

If we consider the SWE 2D (1)

$$\begin{cases} h_t + (hu)_x + (hv)_y = 0 \\ (hu)_t + \left(hu^2 + \frac{1}{2}gh^2\right)_x + (huv)_y = -ghz_x + ghS_{fx} \\ (hv)_t + (huv)_x + \left(hv^2 + \frac{1}{2}gh^2\right)_y = -ghz_y + ghS_{fy} \end{cases}$$

In this case for add the precipitation in the model we modified the SWE 2D in the following mode

$$\begin{cases} h_t + (q)_x + (q)_y = R - f \\ (q_x)_t + \left(\frac{q_x^2}{h} + \frac{1}{2}gh^2\right)_x + \left(\frac{q_x q_y}{h}\right)_y = -ghz_x - \frac{\tau_{b,x}}{\rho} + \frac{\partial h\tau_{xx}^e}{\partial x} + \frac{\partial h\tau_{xy}^e}{\partial y} + RV_x - fu_x \\ (q_y)_t + (huv)_x + \left(hv^2 + \frac{1}{2}gh^2\right)_y = -ghz_y - \frac{\tau_{b,y}}{\rho} + \frac{\partial h\tau_{xy}^e}{\partial x} + \frac{\partial h\tau_{yy}^e}{\partial y} + RV_y - fv_y \end{cases}$$

Where, over at the terms describe already above, (q_x, q_y) are the two components of the unit discharge and R is the rainfall intensity, $\tau_{xx}^e, \tau_{xy}^e, \tau_{yy}^e$ are the turbulent shear stresses and at the end V_x, V_y are the 2 horizontal components of the rain velocity and f is the infiltration rate. The rainfall intensity R is imposed directly at each spatial point, contributing to the surface runoff. In overland flows the water depth is very small and turbulence is mainly produced by bed friction. In this situation, the effects of turbulent stresses can be neglected and therefore, they have not been included in the computations.

The infiltration rate is computed at each spatial point using the formulation of Green-Ampt (Chow et al. 1988) (Figure 46). The potential infiltration rate is then computed as:

$$f(x, t) = k_s \left(1 + \frac{(h(x, t) + \varphi(x)\Delta\theta)}{F(x, t)} \right)$$

$$F(x, t) = \int_0^t f(x, t) dt$$

$$L(x, t) = \frac{F(x, t)}{\Delta\theta}$$

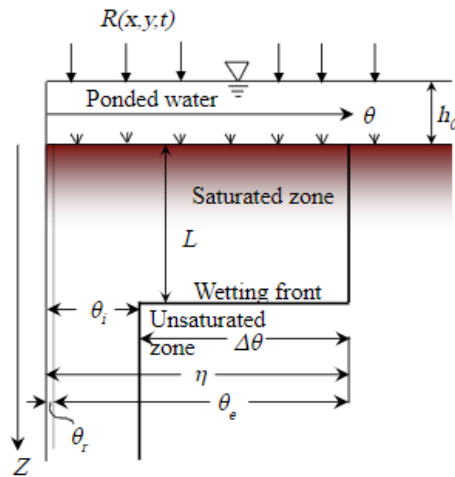


Figure 46 - Schematization of Infiltration variables definition in the Green Ampt method variables used in FHM-2D

where k_s is the saturated hydraulic conductivity of the soil, h is the water depth over the bed surface, ϕ is the suction in the non-saturated region of the soil, $\Delta\theta = \phi - \theta_i$ is the change in moisture content of the soil as the saturation front advances, θ_i is the initial moisture content of the soil, ϕ is the soil porosity, and L is the width of the saturated region in the soil. The actual infiltration rate is equal to the potential infiltration rate except when the water depth is too small and there is not enough water to infiltrate, in which case the infiltration is computed from the available water depth. Evapotranspiration is not considered, since it is negligible in urban storm events.

Wet/Dry Interface Treatment

Computations of the numerical flux near the wet/dry interface needs special attention. Basic problem is computation of velocity when water depth h approaches zero value. The velocity is computed from the vector of conservative variables $W = [h, hu]^T$ as $u = (h, hu)$. Due to numerical inaccuracy of the computers the velocity can reach non-physically large values when $h \rightarrow 0$.

The simplest method dealing with this problem is to set some limit ϵ which is small but larger than the numerical accuracy of the computer. This tolerance defines whether a finite volume is flooded or not. All values of the vector of conservative variables are considered to be zero when water depth is smaller than this constant. According to small changes of this value do not affect numerical results a lot, when computing frictionless cases. But the model becomes more sensitive to changes in ϵ for problems with bed friction parametrized by the Manning expression. This is because the Manning formula requires division by h , which can result in an unrealistically large prediction of the shear stress in shallow regions near wet/dry boundaries. Another way how to cope with this phenomenon is to set the celerity of the flow to zero in the finite volume which abuts wet/dry interface. But this can hypothetically cause problems when there is no wet/dry interface

in the computational domain and this domain is covered by the tiny layer of water. The last way mentioned in this code is to use following relation

$$u = \frac{h(hu)}{h^2 + \epsilon_v}$$

where ϵ_v is small positive constant. This relation is simple and computationally undemanding, but for computations when $h > \epsilon_v$ the velocity is computed with error depending on ratio of h^2 and ϵ_v .

Boundary conditions

The boundaries of the two-dimensional domain in which a numerical solution of the overland flow problem is sought are the different parts of the external contour line of the field. As in any other boundary problem in computational fluid dynamics, there is first a question concerning the number of physical boundary conditions required at every boundary point. To help, the theory of characteristics in 2D tells us that, depending on both the value of the normal velocity through the boundary

$$U^* n = u n_x + v n_y$$

and the local Froude number $Fr = u^*n/c$, the possibilities are

- Supercritical inflow: $u^*n \leq -c$, \Rightarrow all the variables must be imposed.
- Subcritical inflow: $-c < u^*n \leq 0$, \Rightarrow two variables must be imposed.
- Supercritical outflow: $u^*n > c$, \Rightarrow none of the variables must be imposed.
- Subcritical outflow: $0 < u^*n \leq c$, \Rightarrow one variable must be imposed.

4.7 NUMERICAL TESTS

In order to understand if the numerical code was robust and able to provide correct results, various benchmarking tests, from literature, were conducted. Below are the cases analyzed with the respective results obtained.

1) Oscillating lake

This benchmarking test found in (Audusse et al., 2004), is indicative of the robustness of a solver as it involves wet-dry conditions. We are interested in the case of an oscillating lake with a nonflat bottom and nonvertical shores. The lake is initially at rest, but a small sinusoidal perturbation affects the free surface:

$$z(x) = 0.5(1 - 0.5(\cos(\pi(x - 0.5)/0.5) + 1))$$

$$h(0, x) = \max(0, 0.4 - z(x) + 0.04 \sin((x - 0.5)/0.25) - \max(0, -0.4 + z(x))).$$

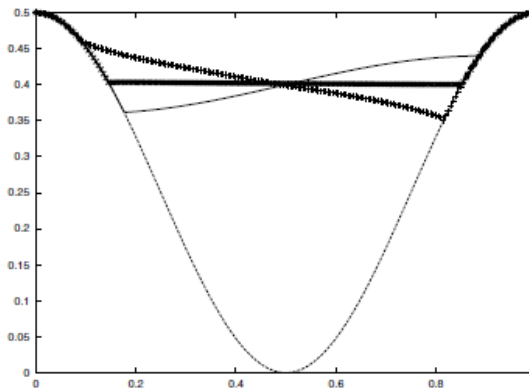


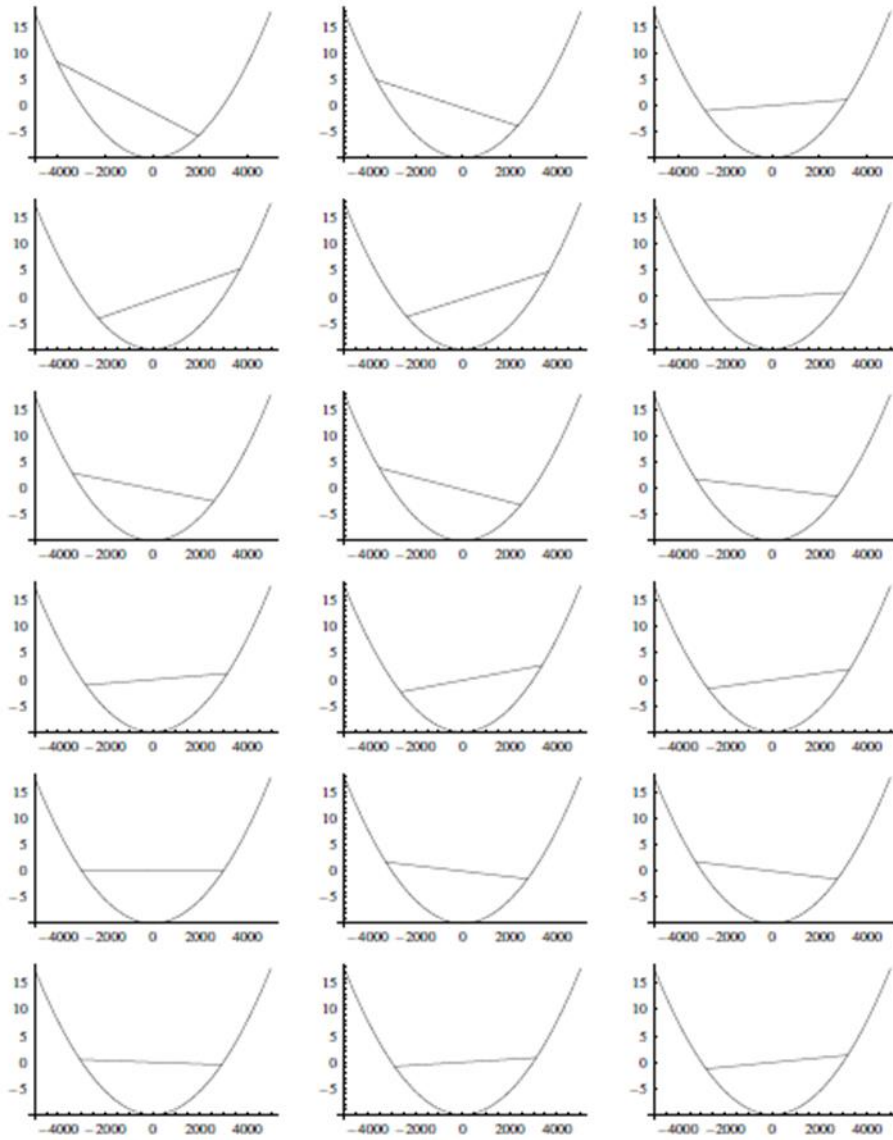
Figure 47 - Oscillating lake: well-balanced scheme. First-order scheme (times crosses). Second order scheme (plus crosses). Initial solution and bottom topography (solid and dotted lines).

This analysis is very important because it allows us to show that the flow oscillates with each timestep and that therefore the code is able to treat an interface between a wet cell and a dry cell on each shore of the lake. Figure 47 shows the results obtained with the well balanced scheme with 200 points at $t = 19.87$ s. This time has been identified because it corresponds to that in which the flow reaches its highest level on the left bank. Both the well-balanced schemes of the first and second orders are robust, but the scheme of the first order dampens the oscillations much more quickly. As also happens in the Audusse test, the FHM-2D has reproduced fifty oscillations to return to rest. On the other hand, the well-balanced second order scheme maintains the periodic regime up to the accuracy of the machine.

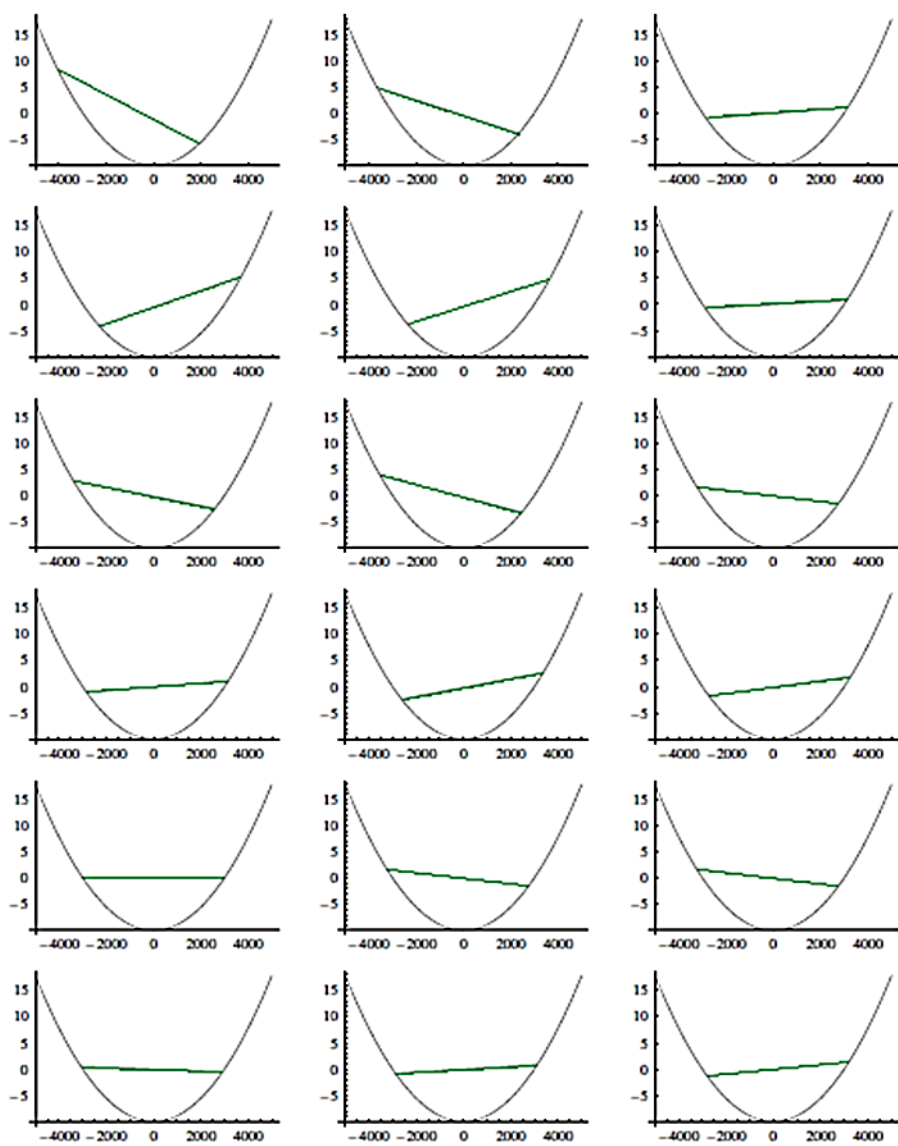
2) Oscillating lake with drag

This benchmarking test was found in the document (Sampson et al., 2004) and the movement of the fluid in a parabolic channel is represented in which a drag $\tau = 0.001 \text{ s}^{-1}$ is applied to the walls. The results shown in Figure 48, refer to those ranging from $t = 0$ s to $t = 3400$ s, in increments of 200 s. The FHM-2D reports the same results for each time found in the article taken as reference from the literature, demonstrating also in this case a good accuracy. Also in this case, however, the well-balanced second order scheme proved to be more robust considering that the first order reproduced slightly faster oscillations.

a)



b)



c)

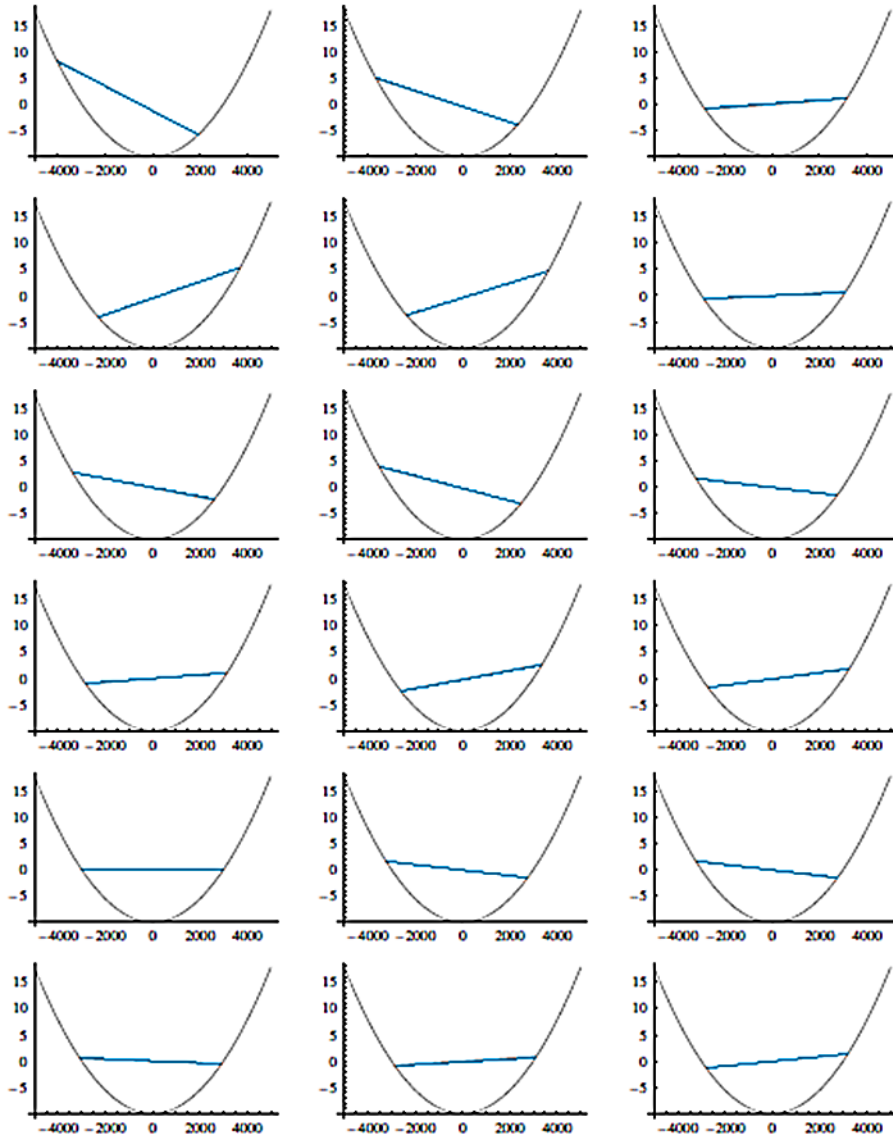


Figure 48 - Oscillating lake with drag; well-balanced scheme. In a) is shown the analytical solution and bottom topography (black line), obtained in (Sampson et al., 2004); in b) the first-order scheme (times crosses) (light blue line) and in c) the second order scheme (plus crosses) obtained from FHM-2D (green line).

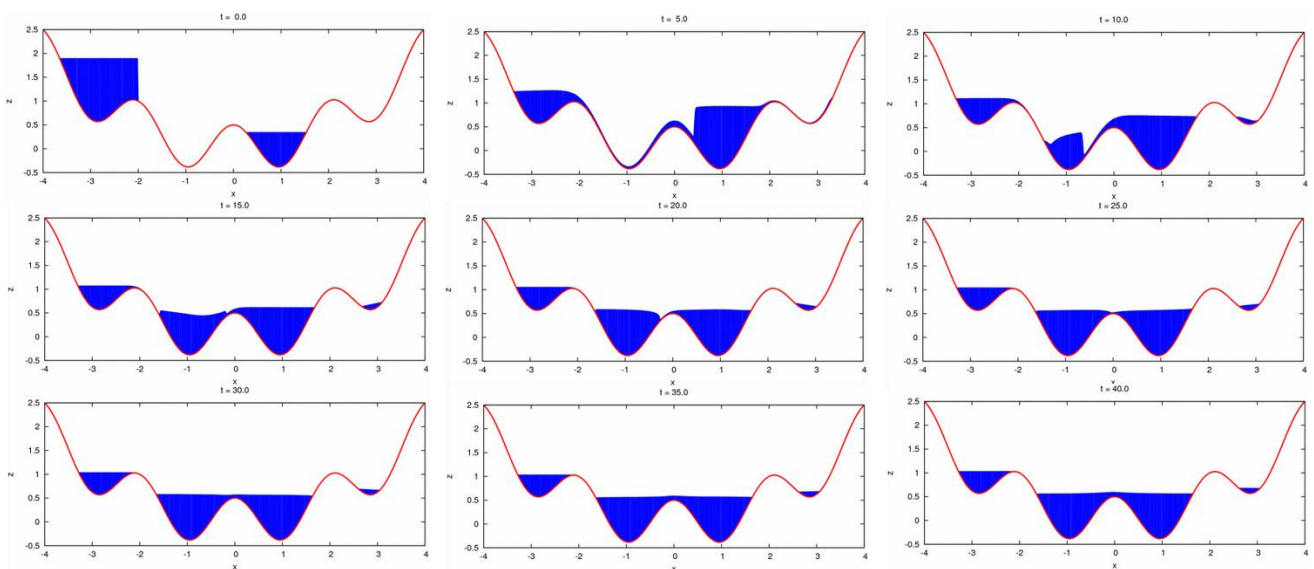
3) Dam break

The dam break is a reference test for the validation of theoretical models. Numerous Finite Volume schemes have been applied to the resolution of dam break problems (Zoppou and Roberts, 1999; Wan et al., 2002; Lai et al., 2005). However, the resolution of the Riemann problem required by the application of the classical bracing methods, widely used as the most accurate in the approach to Finite Volumes (Roe, 1981; Toro, 2016; LeVeque, 2002), is generally quite complicated, for the complexity of the self-structure, in all the problems of multi-phase currents, where the number of conservation equations is greater than two (Altinakar et al., 2010).

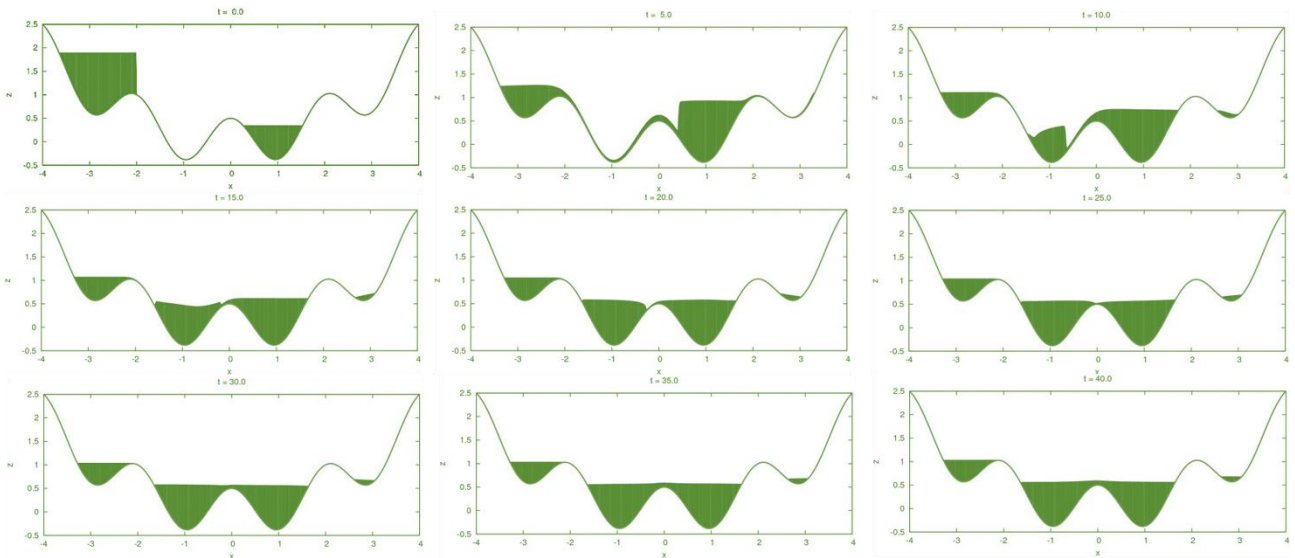
Therefore, after describing the importance in conducting this test, we show the results obtained using the test proposed in the Gerris examples (Version 1.3.2) at the following link: <http://gerris.dalembert.upmc.fr/gerris/examples/examples/dam.html#htoc23>. In this example all the equations useful for the reconstruction of the complex geometry, all the boundary conditions and finally all the time frames useful for the understanding of the goodness of the results obtained with FHM-2D were described.

The test was performed for both the first order accuracy with Lax-Friedrichs and second order accuracy with the TVD-MUSCL, presents in the FHM-2D. As reported in the web link the duration of the simulation was 40 seconds. Here in figure 49 a is shown, at different time steps, the solution obtained from the author for the case study proposed in their example, and in b and c, the results obtained with FHM-2D, respectively for the first and second order.

a)



b)



c)

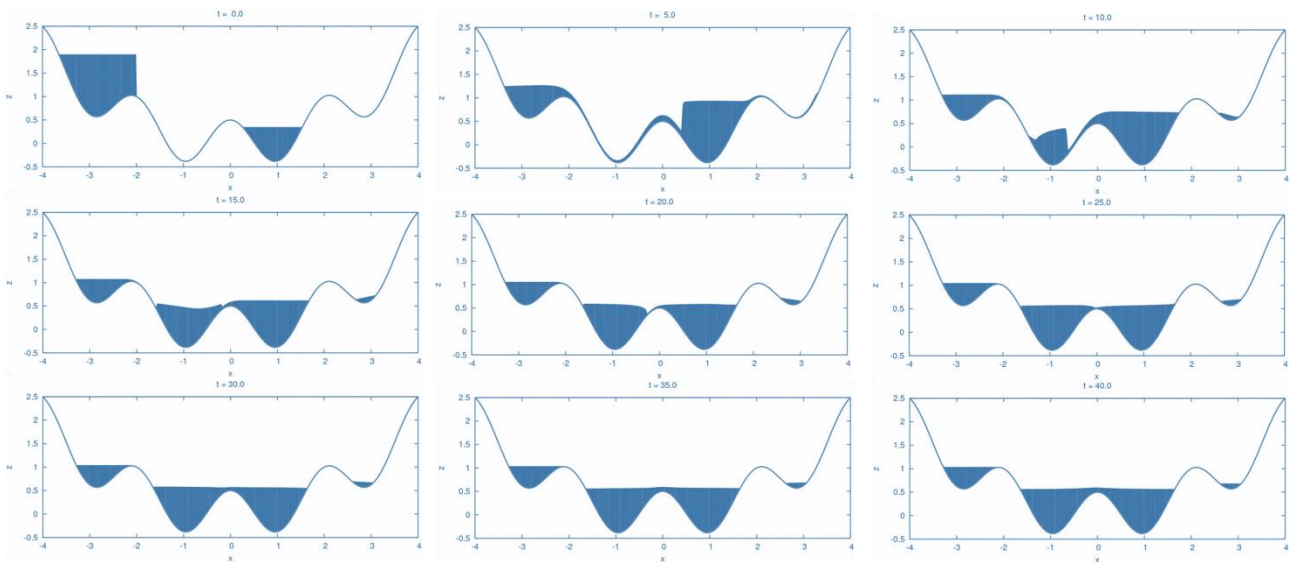


Figure 49 – Dam break test: a) analytical solution; b) with first order extension; and c) with second order extension.

For both orders of accuracy, FHM-2D has shown an excellent behavior, having been able to reproduce the same trend found in the case study founded on web in every time instant.

4) The Steady Flow over a Bump in a Rectangular Channel

The purpose of this problem is to calculate the steady flow over a bump in a rectangular channel with constant breadth. The breadth of the channel is constant, $B(x) = 1$ m, the length is $L = 25$ m and the bottom topography is given by:

$$z(x) = \begin{cases} (0.2 - 0.05(x - 10))^2 & \text{if } 8 < x < 12, \\ 0 & \text{otherwise} \end{cases}$$

According to the boundary and initial conditions, the flow may be transcritical with and without a steady shock, or supercritical. All case studies were taken from (Vazquez-Cendón, 1999) and are conducted for both the first and the second order of accuracy. The graphs referred to the analysis shown in a is reported the analytical solution, while in b with green that obtained from first order and, finally, in c with blue that from second order of accuracy.

- Transcritical flow without shock (Figure 50):

—Downstream. The water level $h = 0.66$ m is imposed only when the flow is subcritical.

—Upstream. The discharge is imposed $Q = 1.53$ m³/s.

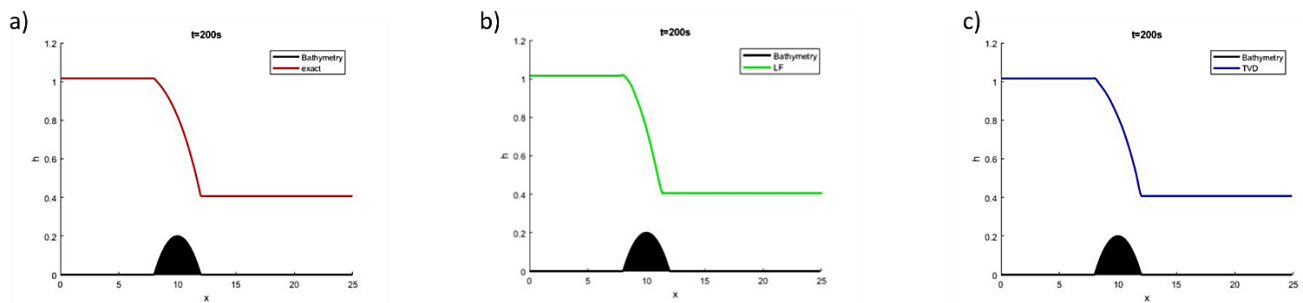


Figure 50 - $Z(x)$, $h(x, t) + Z(x)$ transcritical flow without shock. In a is represented the analytical solution; in b that obtained from first order and in c that from second order extension.

- Transcritical flow with shock (Figure 51):

—Downstream. The water level $h = 0.33$ m is imposed.

—Upstream. The discharge $Q = 0.18$ m³/s is imposed.

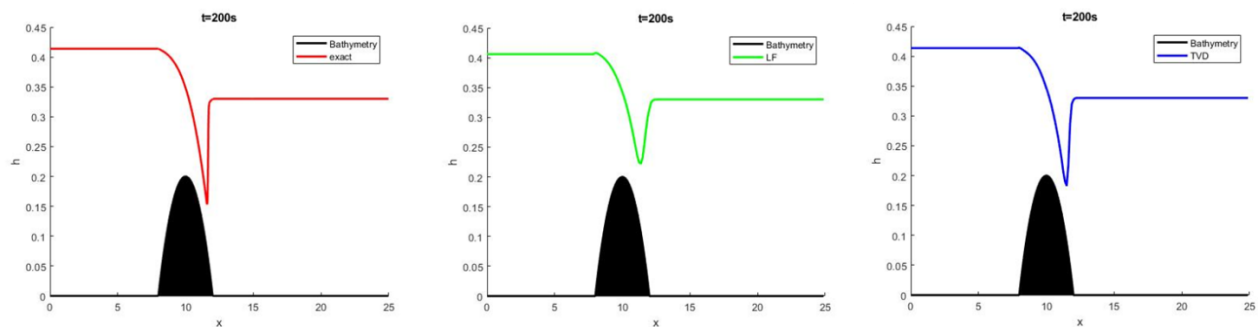


Figure 51 - $Z(x)$, $h(x, t) + Z(x)$ Transcritical flow with shock. In a is represented the analytical solution; in b that obtained from first order and in c that from second order extension.

- Subcritical flow (Figure 52):

—Downstream. The water level $h = 2$ m is imposed.

—Upstream. The discharge $Q = 4.42$ m³/s is imposed.

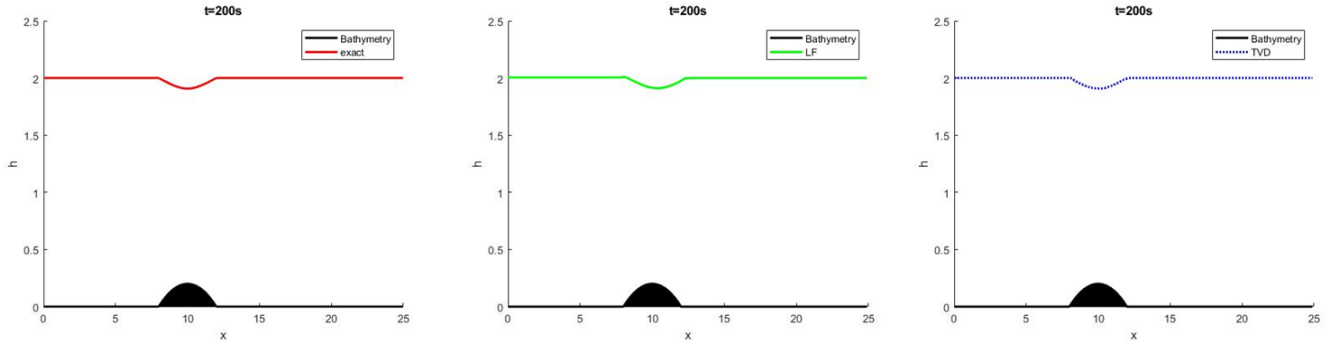


Figure 52 - $Z(x)$, $h(x, t) + Z(x)$ subcritical flow. In *a* is represented the analytical solution; in *b* that obtained from first order and in *c* that from second order extension.

In the three cases as initial conditions, we took a constant water level equal to the level imposed downstream and the discharge equal to zero.

The comparison of the results with the associated analytical solutions illustrates the improved performance of the discretization in critical situations. The level of the water was chosen to show the numerical results because it is more relevant than the discharge, as it is zero for the three cases. We take $CFL = 1$, $\Delta x = 0.25$ m, $t = 200$ s, where the steady state is reached.

This election of Δx is sufficient to compute the solutions in Figure 50 and in Figure 52 properly. In Figure 51 the shock can be obtained with more accuracy if the number of nodes is increased.

The bump test has also been reproduced in 2D (Figure 54) and the test was resumed, in order to have a comparison in terms of results obtained, from (Le Veque et al., 1998). The two-dimensional bump used was represented from the Eq. 9, which has a maximum height of 0.8 at the center of the unit square.

$$B(x,y) = 0.8 \exp(-50((x-0.5)^2 + (y-0.5)^2)) \quad (9)$$

The depth was set as $h(x,y) = 1 - B(x,y)$ corresponding to a flat surface and the initial velocity is zero so that the surface should remain undisturbed. The domain used for the test case is the same of the one used in (LeVeque, 1998) that is a rectangular domain of $[0,2] \times [0,1]$ dimensions as represented in figure 53.

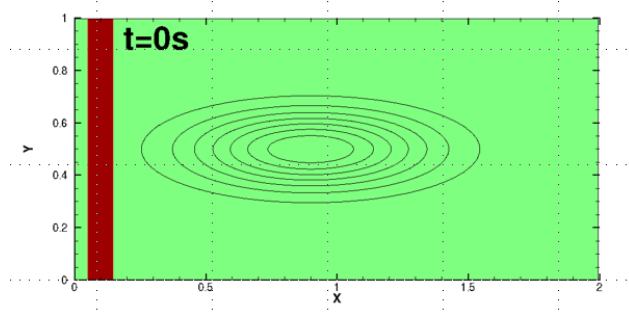


Figure 53 - Elliptical hump used for the test case. The lowest contour level is at 0.01 and the bump has height 0.8.

The boundary conditions were equal to those chosen by (LeVeque, 1998) and in general, the zero-order extrapolation on the entire boundary domain was imposed. The duration of test case was fixed to $t=1.8$ s. In figure 54, are shown on the left the analytical solutions obtained in LeVeque and on the right, the ones obtained from FHM-2D, respectively for the first and second order of accuracy. From the figure is possible to understand how the FHM-2D was able to reproduce, instant by instant, for both the orders of the accuracy, the same solution obtained from the LeVeque paper.

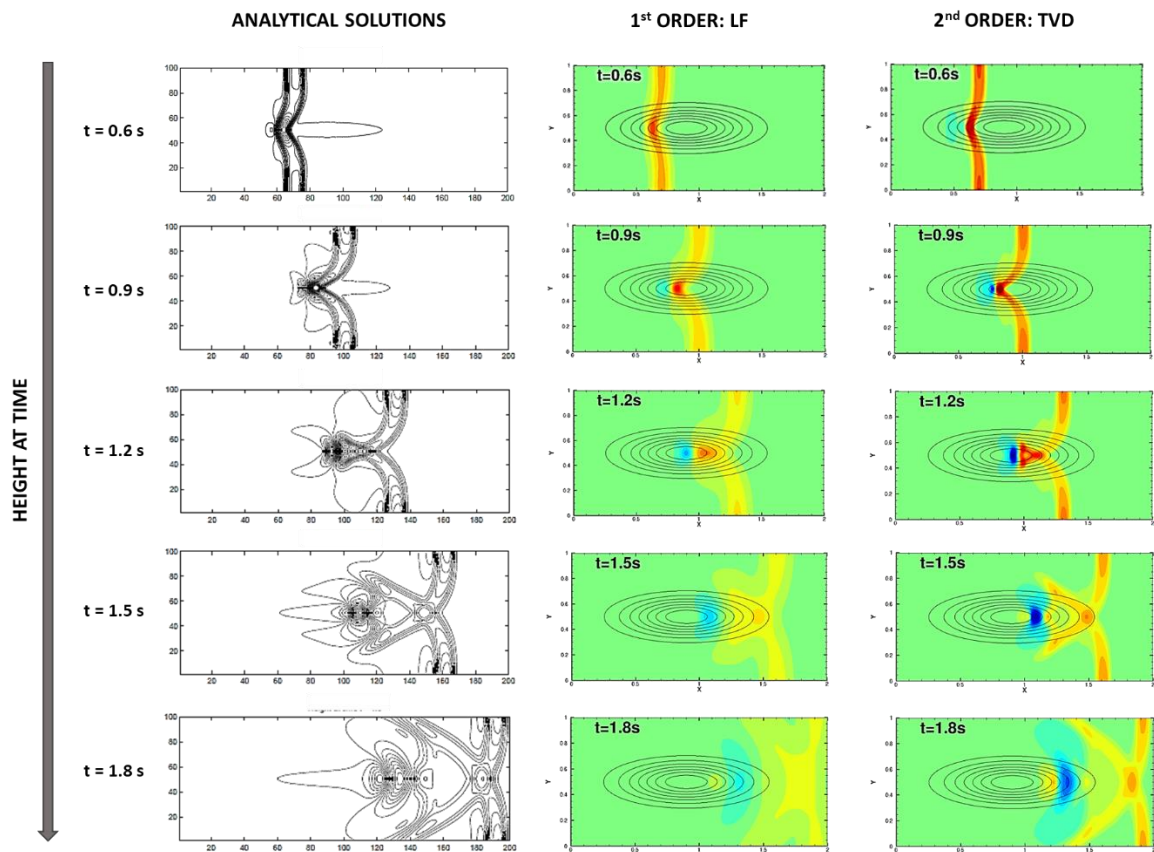


Figure 54 - Bump test results in 2D

5) Runoff test

The test concerning the outflow was carried out taking as reference that carried out by (Cea et al., 2010). The analysis saw the application of a precipitation in a rectangular tank with dimensions 2 x 2.5 m formed by three floors with an approximate slope of 5% (Figure 55).

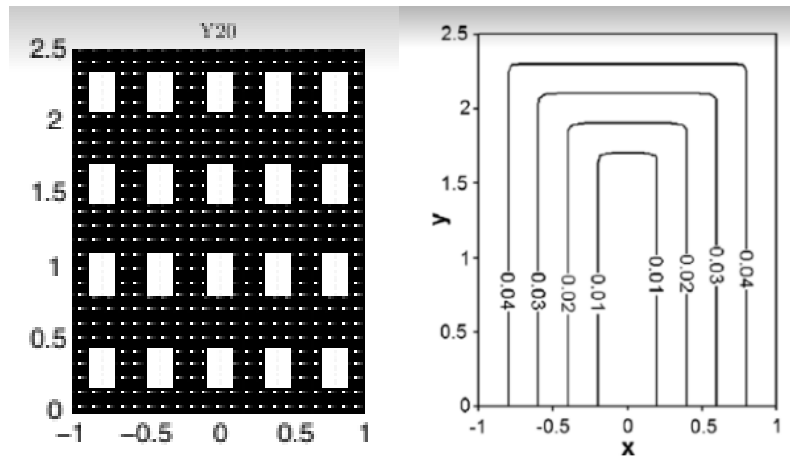


Figure 55 - Detailed topography of the catchment (from Cea et al., 2010)

The bed surface is impervious and therefore the infiltration does not need to be considered. Rainfall was simulated with a grid of 100 nozzles distributed evenly over the basin. The only variable measured in the experiments was the discharge hydrograph generated at the outlet of the basin.

At the outlet boundary a free outflow boundary condition was used. The wet-dry tolerance parameter was set to 10^{-6} m. The numerical mesh for each configuration must be fine enough in order to adequately resolve the flow around the buildings. The Manning coefficient used for the test was $0.016 \text{ s/m}^{1/3}$. In Figure 56 and in Figure 57, are represented the results obtained for both the orders of accuracy.

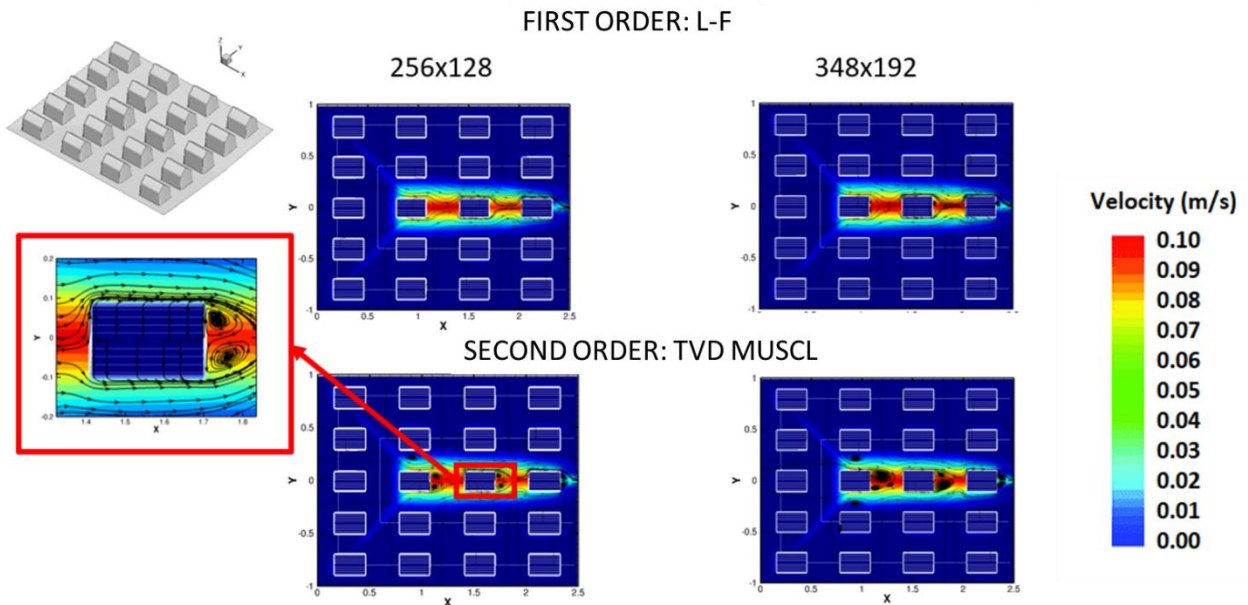


Figure 56 - Velocity fields computed at time $t = 20$ s in runoff test with slope

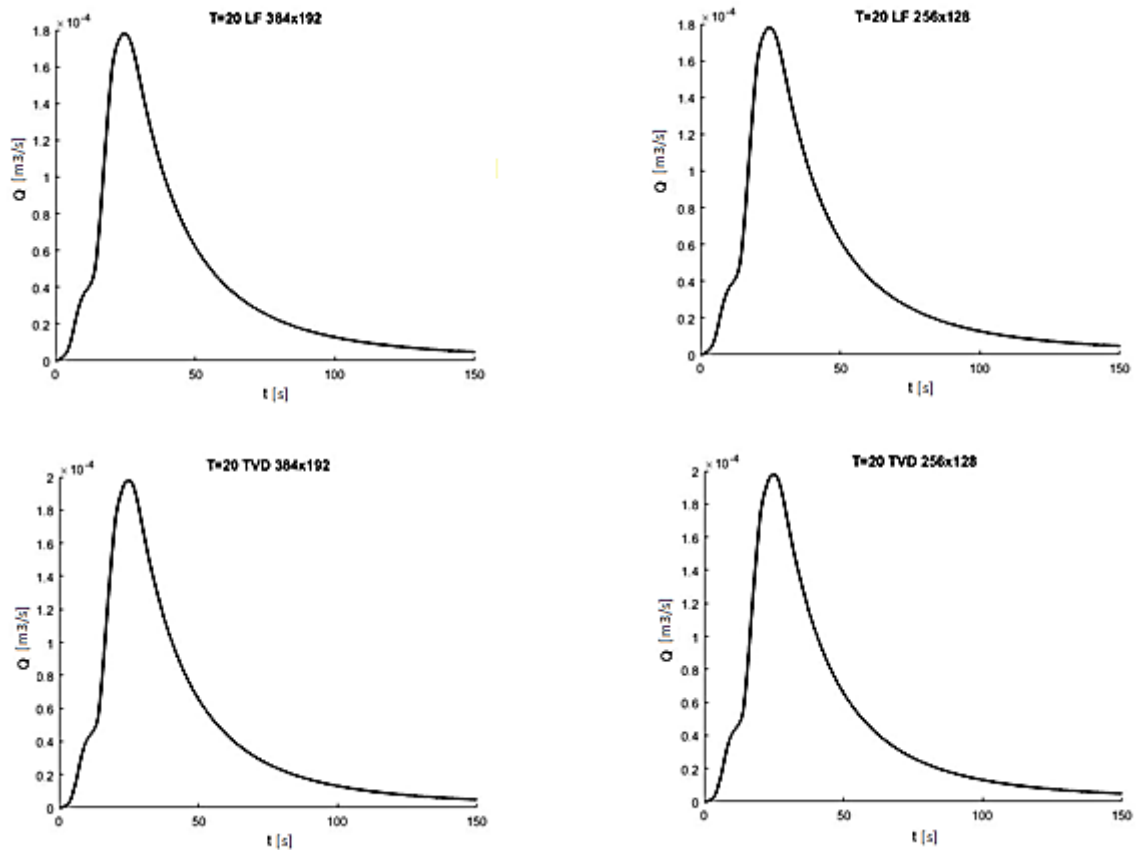
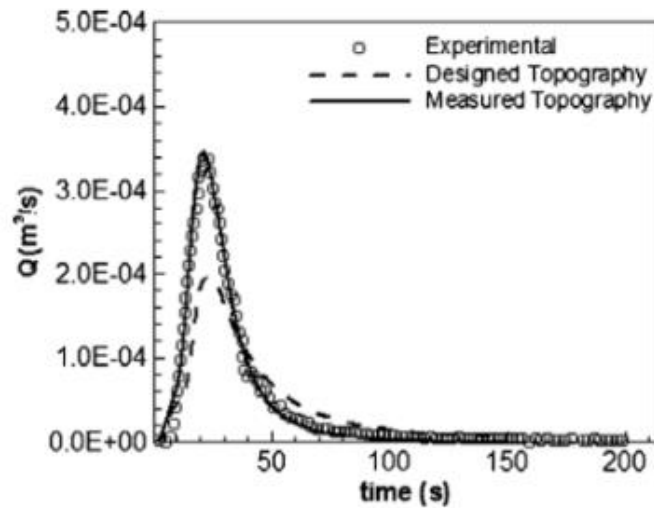


Figure 57 – Outlet hyetograph obtained from FHM-2D using the first and second order of accuracy for different number of cell computation 348x192 and 256x128.

The discharge obtained and compared with those taken as reference in (Cea et al., 2010), shown in Figure 58, give very close values independently of the order of accuracy and cell discretization used. In the case of the first order there is a slight underestimation of the flow rate calculated with FHM-2D.



(a) Geometry Y20. Hyetography Q25T20.

Figure 58 - Outlet hyetograph obtained in Cea et al, 2010 used for the comparison with the FHM-2D results.

Finally, another test was conducted to understand the behavior of the numeric code at a slope (Figure 59).

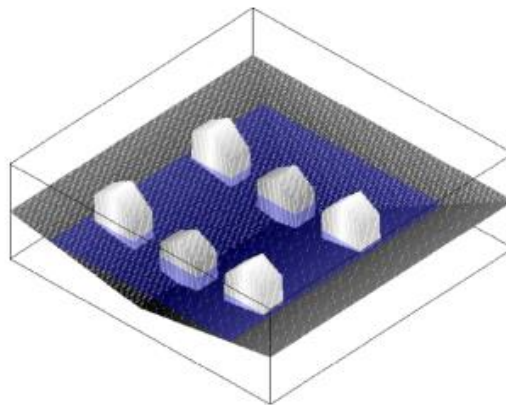


Figure 59 - The bottom setting of numerical examples. The figure illustrates the case of urban draining with obstacles like houses.

In all of the examples in the succeeding texts, the gravitation constant $g = 9.8 \text{ m/s}^2$ and the minmod parameter $\theta=1.3$. In this example, a Manning crew coefficient of $0.002 \text{ s/m}^{1/3}$ and a slope of 0.05 has been applied.

In Figure 60, was reported the analytical solution obtained in (Chertock et al., 2015) that was replicated, in the test case with FHM-2D, for different grid sizes precisely 100, 200, 400 and 800 m and for both the orders of accuracy .

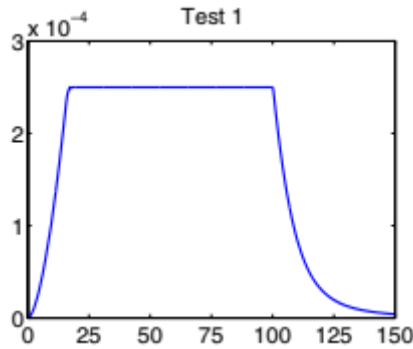


Figure 60 - Outlet discharge as a function of time obtained from (Chertock et al., 2015). On x-axis was reported the time in seconds and in y-axis the discharge.

In figure 61, are shown the plots of the first component of the numerical flux at the right edge of the computational domain as a function of time. Notice that this is an approximation of the outlet discharge, which is a measurable quantity in experimental settings. The simulations were performed in the 2-D domain of the width 0.2, so that all of the discharge values in Figure 61 are to be multiplied by the factor of 0.2 in order to be compared with those of Chertock’s paper.

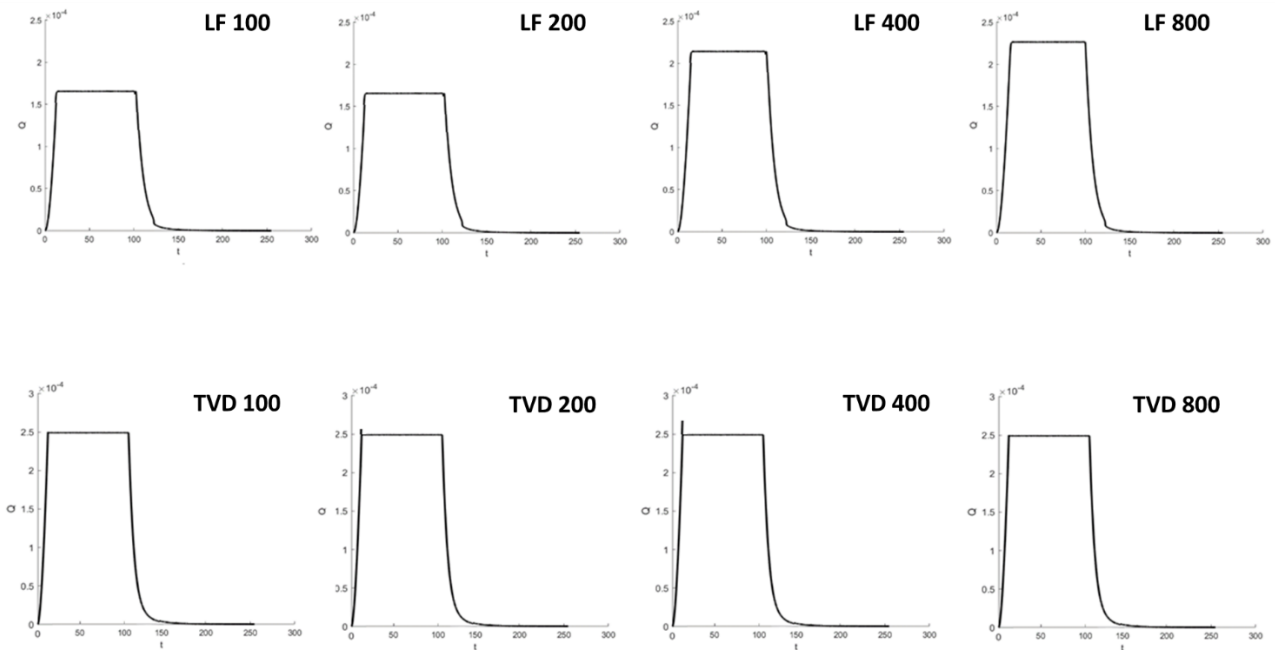


Figure 61 - Outlet discharge as a function of time obtained with FHM-2D: figure a, b, c, d are referred at first order of accuracy and respectively at 100, 200, 400 and 800 m of computational grid size; e, f, g, h are referred at second order of accuracy and respectively at 100, 200, 400 and 800 m of computational grid size.

In this test case were observed that , for the first order Lax Friedrichs, the maximum value of the discharge for the cell size of 100 and 200 m was underestimate, while for the 400 and 800 were the same reported in Chertock’s paper. For the second order TVD –MUSCL, instead, in all the cases analyzed the outlet discharge were the same of that obtained in the reference. This fact is due at robustness of TVD MUSCL method compared to that of Lax Friedrichs.

4.8 APPLICATION FHM-2D TO A REAL CASE STUDY

Once all the benchmarking tests that allowed us to understand the robustness of FHM-2D model have been performed, we proceeded by applying it to a real case study. The area of interest considerate for the analysis was Saint Lucia, an island located in the Caribbean, where 12 extreme events happened in the past (Figure 62).

The capital of Santa Lucia is Castries, where 32.4% of the population lives. Other major cities include Gros Islet, Soufrière and Vieux Fort. The population tends to concentrate around the coast, with the interior more sparsely populated.

The local climate is tropical, moderated by the north-eastern trade winds. The average daytime temperatures are around 30 ° C and average night temperatures are around 24 ° C. The temperature does not fluctuate much between winter and summer. Average annual rainfall ranges from 1300 mm on the coast to 3810 mm in mountain rainforests.

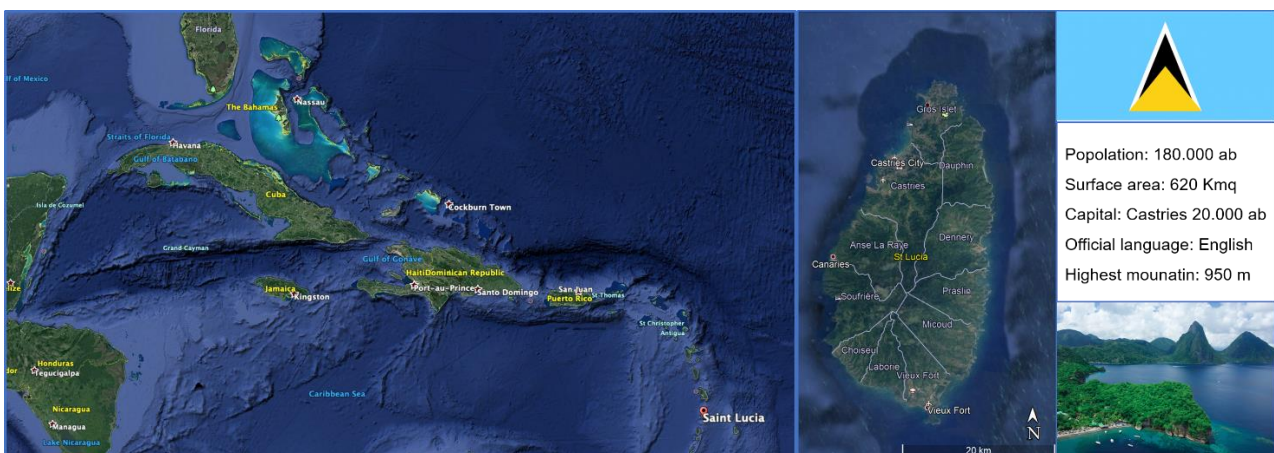


Figure 62 - Area of Interest: Saint Lucia Island

This area has been selected thanks to its strategic position. In fact, especially in the recent years considering the ongoing climate changes, heavy rains are increasingly frequent on the island due to hurricanes and / or

tropical storms. These extreme atmospheric phenomena, as shown in Figure 63, present traces that are very close or cross the area of interest.

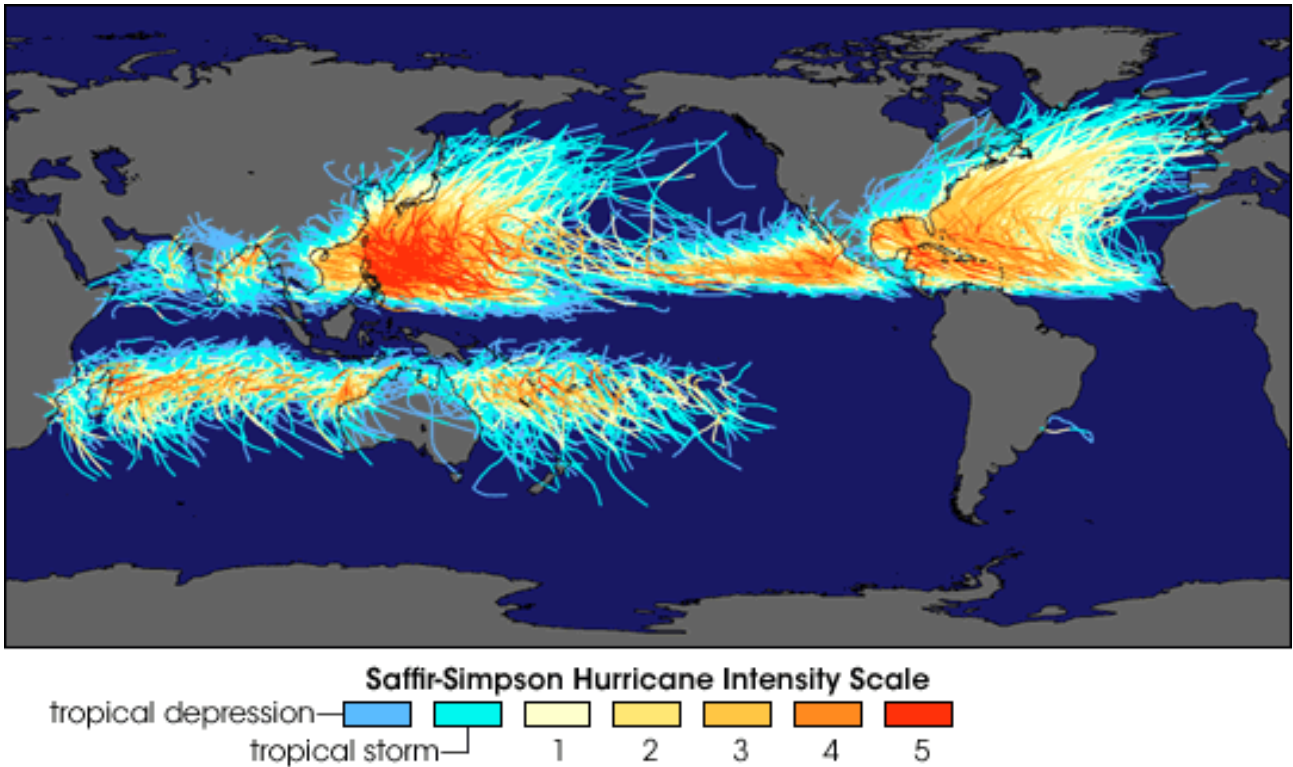


Figure 63 - Tracks of nearly 150 years of tropical cyclones weave across the globe

Moreover, even the hydro-geological conformation, which divides the island into many very small basins, has made possible to analyze deeply the results obtained by FHM-2D.

For the hydraulic simulations, the precipitation data used as input have been provided directly by the competent local authority. The rainfall data of the simulated extreme events were recorded from the gauge stations of the SLUMET (Saint Lucia Meteorological Services) and of the WRMA (Water Risk Management Association). In the test case only the precipitation data recorded from WRMA were used. This choice was due to the better completeness of the dataset in correspondence of the extreme events of interest (see Figure 64).

SLUMET

#	Name	WGS84_E	WGS84_N
1	Anse La Raye_1	711276.7127	1541526.059
2	Anse La Raye_2	715472.401	1538852.765
3	Errard	724190.6715	1537685.295
4	Barre De L'Isle	720711.2681	1540713.907
5	Grace	719620.2495	1524224.891
6	Canaries	710508.477	1536401.425
7	Mahaut	720852.4003	1531244.055
8	Forestierre	719822.3563	1546337.9
9	Millet	716802.928	1537745.018
10	Blanchard	722027.2581	1527340.874
11	Soucis	716121.3466	1547366.917
12	Moule-A-Chique	722599.0241	1516683.535
13	Bocage	719350.2564	1548882.217
14	Derraches	713934.5277	1532393.968
15	Debarras	725812.0722	1547951.902
16	Rodney Bay	723110.2745	1557164.543
17	Monchy	724838.4738	1553519.94

Stations position

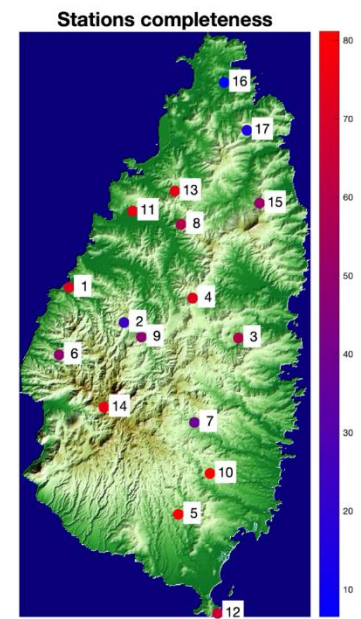
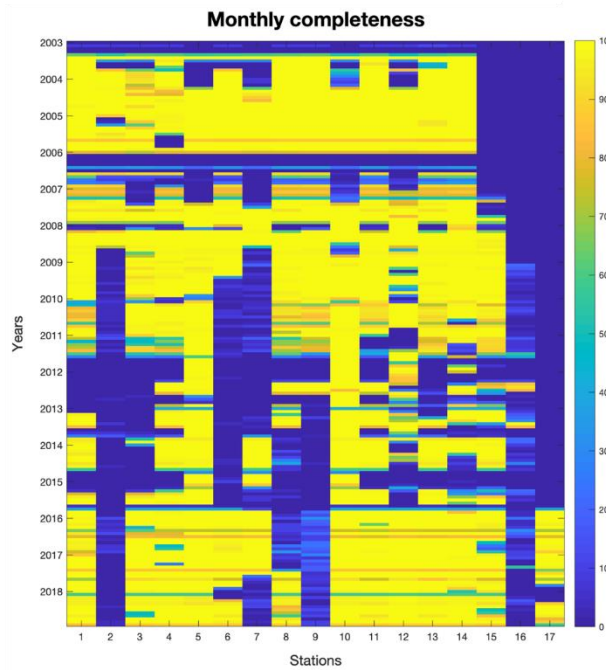


WRMA

#	Name	WGS84_E	WGS84_N	Height
1	Anse La Raye	711259.894	1541526.659	92.964
2	Barre De Lisle	720628.13	1540604.987	279
3	Barthe Nursery	712511.69	1528559.72	372.21
4	Blanchard	722061.152	1527312.022	183.08
5	Cap Estate	722741.02	1559373.22	31.84
6	CARDI	724583.17	1542738.21	27.32
7	Desraches	713552.3989	1533568.107	\
8	Errard (Estate)	723255.8423	1536748.807	\
9	George V Park	717475.67	1549983.64	15.56
10	Government House	716291.95	1549245.2	135.12
11	Grace	719632.4908	1524198.312	\
12	Hewanorra (Climate)	721519	1519573	6.1
13	Mahaut	720945.36	1531145.82	\
14	Marquis Babonneau	724439.26	1549305.27	64.01
15	Millet	716751.98	1537615.8	0
16	Rodney Bay	723083	1557139	\
17	Roseau	713910.16	1543819.91	22.16
18	Saltibus	714737.44	1527042.99	292.55
19	Soucis	716166.62	1547392.67	39.6
20	Soufriere	710121.45	1532897.16	32.92
21	Troumassee (Estate)	726582.6	1528172.39	40.6
22	Trouya	718870.64	1555633.49	30.67
23	Union Vale (Estate)	710140.87	1527719.64	254.42
24	Union (Agri Station)	720253.77	1551079.57	18
25	Vigie (Airport Rain Gauge)	716690.51	1550887	7

SLUMET data

Number	17 stations
Acquisition range	hourly
Time Window	from 2003 to 2018



WRMA data

Number	25 stations
Acquisition range	daily
Time Window	from 1955 to 2018

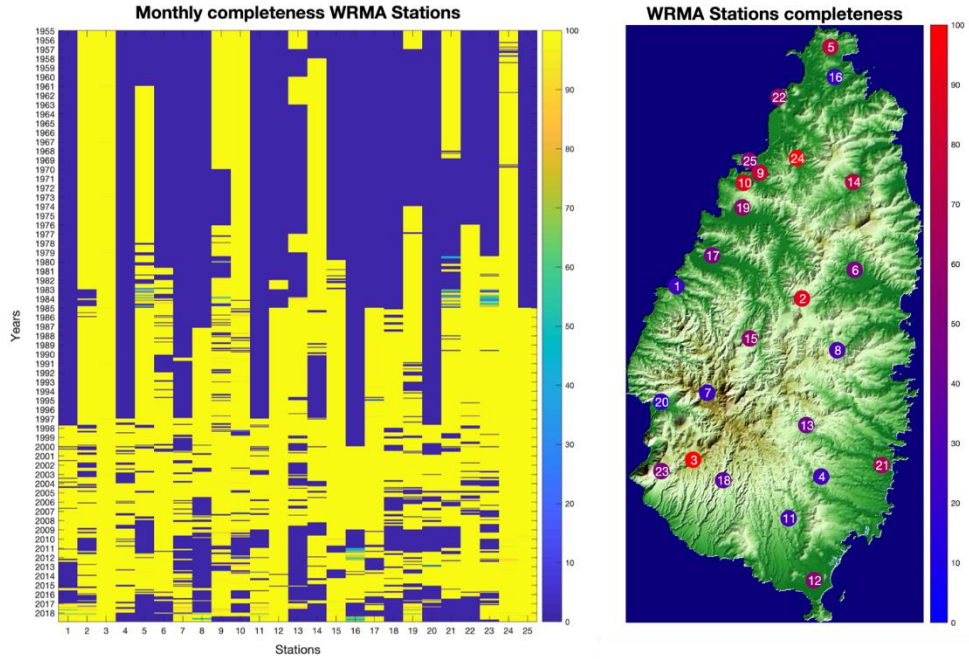


Figure 64 - Rain gauge stations presents in Saint Lucia island and status of completeness of rainfall data in SLUMET and WRMA stations

The 12 extreme events were chosen considering: a) presence and completeness of rainfall data recorded during the event; b) the huge hazard and the importance of the damages that happened; c) the number of social media marker and info from web useful for the validation of the model results.

In Figure 65 the extreme alluvial events simulated with FHM-2D as test case are highlighted in yellow.

List of extreme climatic events in Saint Lucia in the last 40 years

#	DATE	EVENT NAME
1	9/11/1988	Tropical Storm Gilbert
2	11/6/1990	Landslides
3	11/29/1992	Landslides
4	8/15/1993	Tropical Storm Cindy
5	10/9/1994	Tropical Storm Debby
6	9/7/1995	Hurricane Iris
7	8/18/2001	Tropical Storm Chantal
8	10/4/2001	Tropical Storm Jerry
9	10/9/2001	Hurricane Iris
10	7/7/2003	Tropical Wave/ hurricane Claudette
11	8/3/2004	Tropical Storm Bonnie
12	9/9/2004	Hurricane Ivan
13	7/1/2005	Heavy rain, Landslide Windjammer landing beach resort
14	8/17/2007	Hurricane Dean
15	10/30/2010	Hurricane Tomas
16	4/28/2011	Heavy rain - 4 days long
17	8/3/2012	Tropical depression
18	8/10/2012	Tropical depression
19	7/9/2013	Hurricane Chantal
20	12/24/2013	Christmas Eve event
21	8/1/2014	Hurricane Bertha
22	9/28/2016	Hurricane Matthew
23	9/5/2017	Hurricane Irma
24	9/18/2017	Hurricane Maria
25	7/5/2018	Moderate to heavy rain next 12/24h (MET Office)
26	9/13/2018	Hurricane Isaac
27	9/27/2018	Hurricane Kirk
28	10/19/2018	Montoute says Desrameaux road closed, flooding
29	10/23/2018	Trinidad et Tobago flooding
30	11/11/2018	Heavy rain - flooding

Sources:
www.charim.net
www.stlucianewsonline
www.nhc.noaa.gov
<http://nemo.gov.lc>

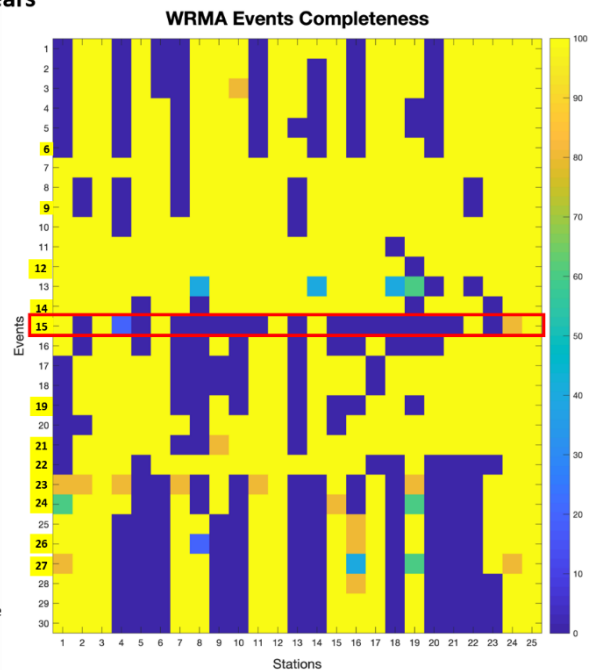


Figure 65 - In yellow are shown the 12 extreme climatics events simulated and the sources where it were founded the social marker used for the validation of results.

For the hydraulic simulation, a DEM with a spatial resolution of 5 m was reconstructed ad hoc, performing different pre-processing (Figure 66). A DEM available online was handled, deriving from the Aster RADAR satellite, with a spatial resolution of 25 m.

The preprocessing has seen the following operations:

- Creation and/or rebuilding of the non-existent river network;
- Addition of existing buildings using the footprints made available by Openstreetmap dataset;
- Reconstruction of marine bathymetry, using the contour lines present in some nautical charts, fundamental for the right representation of the storm surge phenomenon, always present during the extreme events that hit the area of interest;
- Resampling of the initial DEM, with the addition of the new elements, with a resolution of 5 m.

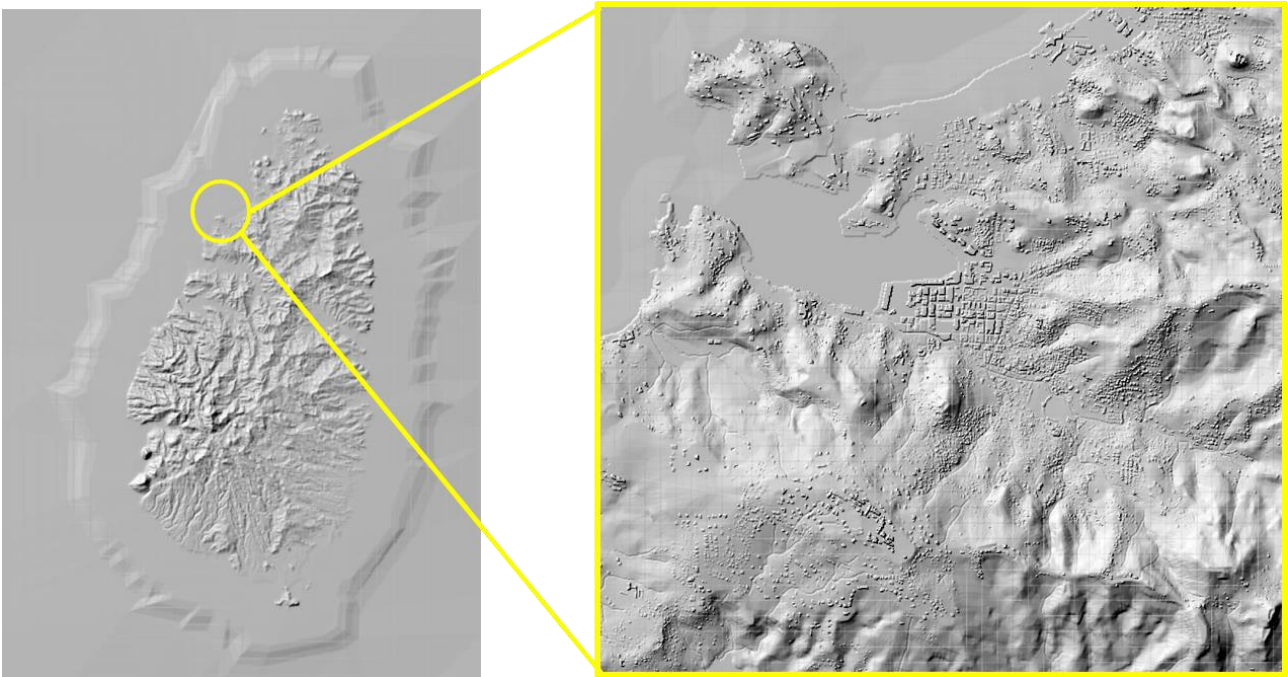


Figure 66 - DEM of Saint Lucia island rebuilt for the simulation and zoom of urban area where is possible to see the good accuracy in the reproduction of the elements (houses, rivers, etc.)

As input of the hydraulic modelling have been used:

- precipitation data obtained from WRMA gauge stations;
- sea level measurements recorded during the days of the event by the website (<http://www.ioc-sealevelmonitoring.org/map.php>);
- Land use deriving from the Chinese product GLC30 with a spatial resolution of 30 m.

The spatial discretization of the mesh imposed in the FHM-2D was 5 m, the same of the DEM. This choice was justified by the fact that in the hydraulic modelling developed, any subgrid approach was considered.

Among the 12 events simulated that have been rebuilt with FHM-2D, only the post event flooding map related to the depth max of the Tomas hurricane was selected and shown in Figure 67. Such event was chosen since it was the most dangerous extreme event.

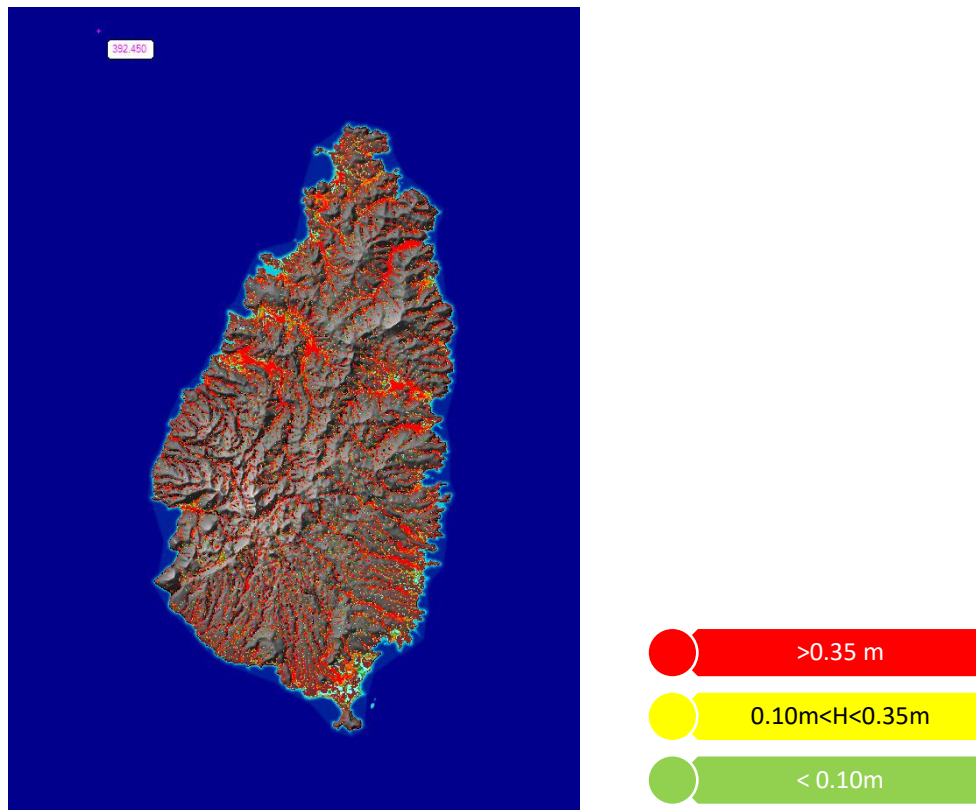


Figure 67 - FHM-2D result of Tomas hurricane

In Figure 68 the post event flooding map of Thomas hurricane and some zoom of the flooding in the main city of the island were shown.

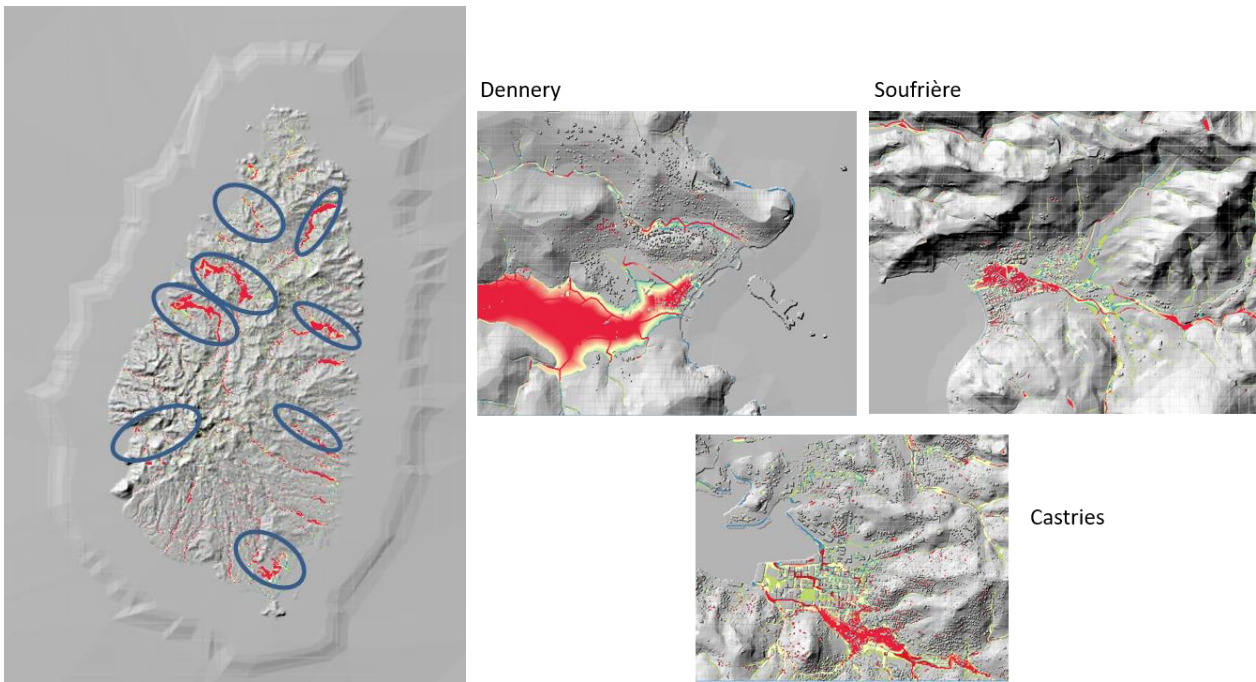


Figure 68 - FHM-2D result of Tomas hurricane and zoom on three urban areas present on the island of Saint Lucia

The validation of the results obtained with FHM-2D, was based first of all on the comparisons between the flooding extension and location obtained from the hydraulic modelling and those of the maps shown on the various reports found online. The second step of the validation process was made with the various social marker related the extreme event days. Also in this case, as for Houston case study, the social media marker allowed to understand the goodness of the depth results obtained with FHM-2D and to confirm the real presence of the flooding.

Figure 69 shows the map of the damages found during Hurricane Tomas on the CHARIM website (Caribbean Handbook on Risk Information Management). For this extreme event, thanks to this map, the goodness of the hydraulic modelling results in terms of location of the flooding was understood. In Figure 70 a zoom, as an example, of the comparison between the two maps is shown.

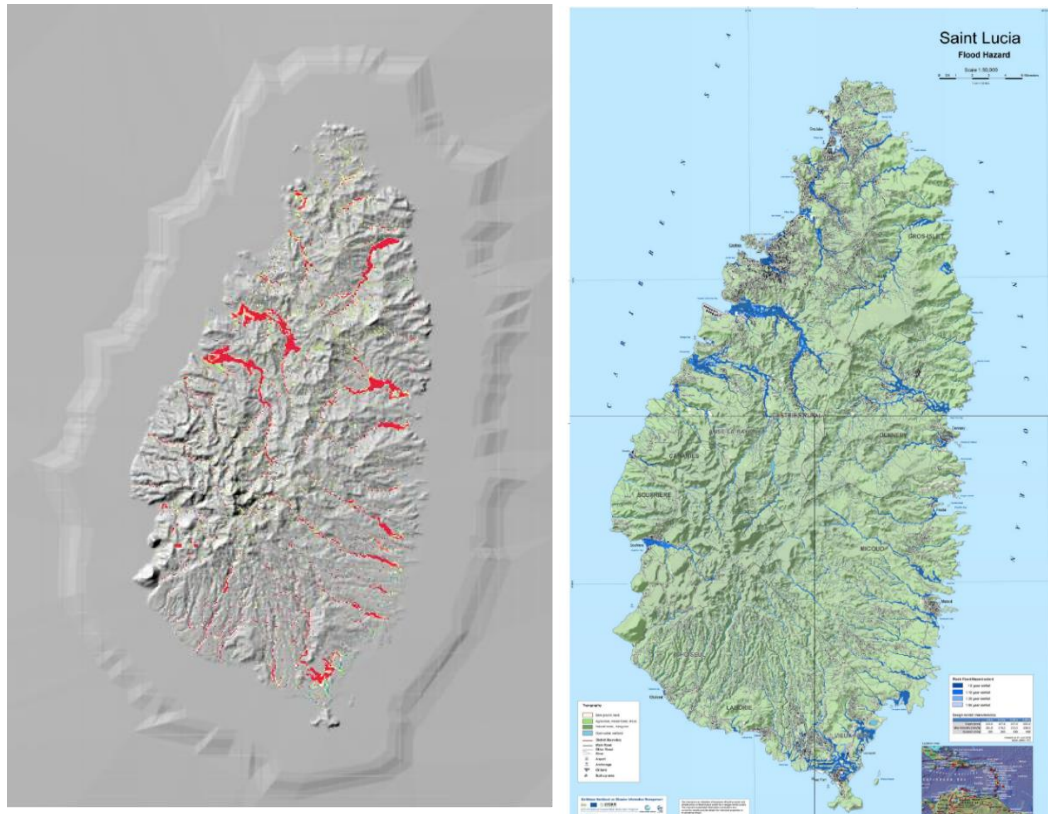


Figure 69 - FHM-2D result of Tomas hurricane and map showing the damage that emerged during the extreme flooding event

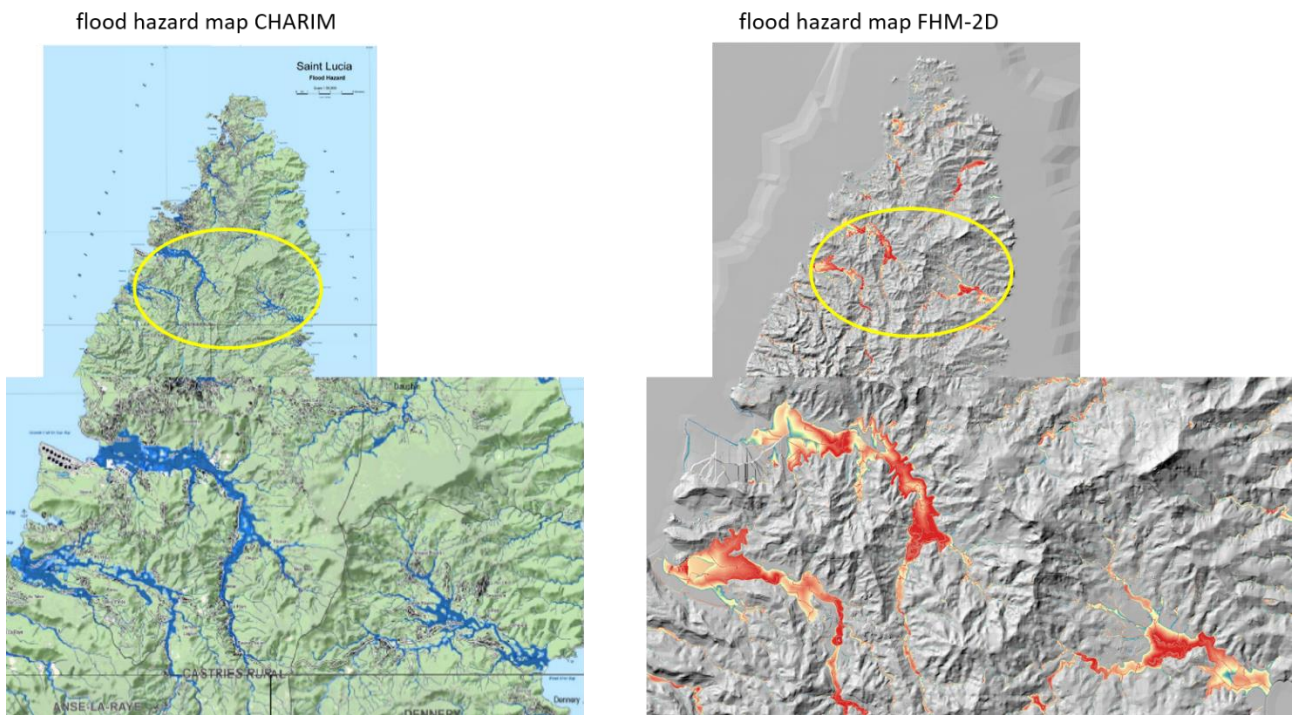


Figure 70 - zoom of a part of the island flooded in the CHARIM map and in the hydraulic model map

In Figure 71 some pictures used for the validation of depth results and obtained from modelling were shown.

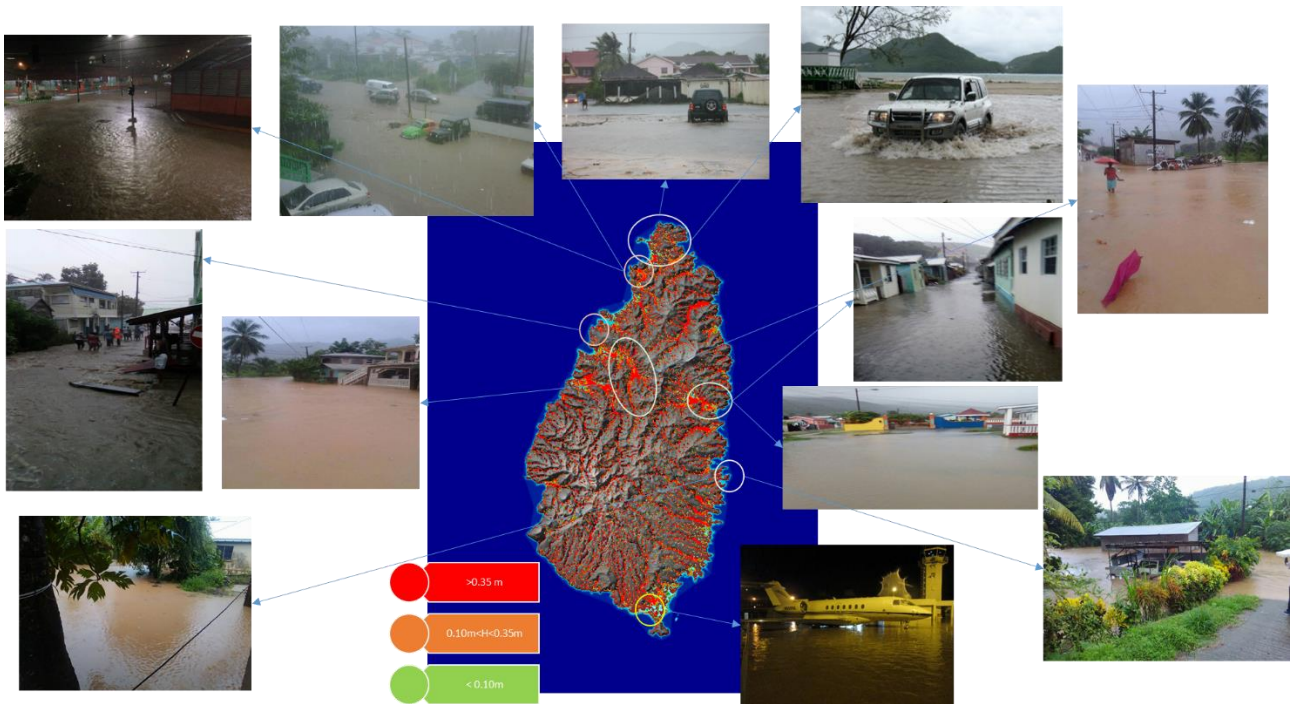


Figure 71 - social markers used in the validation of the results obtained by FHM-2D

The analyses carried out allowed us to understand that the FHM-2D returns very accuracy results in terms of extension, location, depth and velocity of the flooding flow. Furthermore, the FHM-2D was provided with the capability to work in parallel with no much longer simulation time. In this way it was possible to calibrate the results in reasonable times. The results obtained were computed with a super computer with 512 CPUs. Despite the huge size of the interest area, a numerical simulation, referred to 5 days extreme event with a grid discretization of the 5 m, was carried out taking about 12 hours for the complete hydraulic computation. On the contrary, when HEC-RAS was used for the same case study, it was not able to perform the simulation. This allowed us to confute also the robustness of the model developed.

5 FLOOD RISK ASSESSMENT IN NOWCASTING PHASE

5.1 THE NOWCASTING PHASE

The World Meteorological Organization defines now casting as “That phase that comprises the detailed description of the current weather along with forecasts obtained by extrapolation for a period of 0 to 4 hours ahead. In this time range it is possible to forecast small features such as individual storms with reasonable accuracy”. To cope extreme events in nowcasting, Civil Protection needs tools that are able to return maps of hydraulic hazard in a very short time.

The information used in the nowcasting of hydrological extreme events are the spatial distributions of the rainfall intensity at given time, obtained by radar, satellite and rain gauge data.

Usually nowcasting is mainly aimed to the short time forecast of rainfall intensity. The levels of warning are identified by the exceedance of prefixed rainfall amount thresholds, e.g. 100 mm/24h. Hazard flooding maps, preliminarily constructed in relation to a given rainfall amount, can thus be used to identify the most dangerous areas for people and goods.

Here we use a novel approach which directly provides the extension of the inundated areas and the associated risk levels (as a function of local value of flow depth and velocity), carried out by a real time surrogate model which transforms the temporal and spatial distribution of rainfall intensity, measured by radar, runoff characteristics over the domain. The idea, described in the following section, is to implement a surrogate model, based on an artificial intelligent approach, which is trained by a lot of input-output time series obtained by high detailed hydraulic simulations and that mimics the physical link between rainfall and runoff, as it is represented by 2D shallow water models.

5.2 A REAL TIME FLOOD SURROGATE MODEL

High spatial resolution hydraulic simulations by shallow water models usually have long computational time, not compatible with the nowcasting, in which the forecast needs to be performed on a temporal scale from one to few hours. Moreover, these simulations cannot be used in the flash flooding mainly because these phenomena happen in a very short time. Therefore, there is the need to model the flooding processes in order to have a real time response. However, such models have to maintain the capability to: a) manage the temporal and spatial complex distribution of the rainfall (as that from radar measurement); b) provide an accurate calculation of the flow characteristics in all the regions interested by the rainfall event i.e. to return a result very close to the result provided by the numerical integration of the shallow water equations. Last

but not least, the model should be very easy to maintain and/or implemented to allow its accessibility to non-expert users.

In order to construct such model, in the framework of Artificial Intelligent approaches, a nonlinear regression problem between input and output data have to be solved. This is a very complex problem since we need of an algorithm that transform a time varying input map (having a not regular spatial distribution of the input variable) in an output map. Several kinds of these algorithms are available and there is an increasing interest in developing new ones.

Each algorithm has its own properties; therefore, several driving factors should be considered during the choice of an algorithm. Some of them have high accuracy but low memory and others have high memory but low accuracy; some are linear, others are non-linear.

Accurate forecasting of rainfall/runoff processes is one of the most important issues in hydrological research. Since such forecasting involves a rather complex nonlinear data pattern, there are several approaches that could be applied. Recurrently, artificial neural networks (RNNS) (Yen M. H. et al., 2019), as well as, models based on fuzzy theory and neural network have shown to be very effective on dealing with nonlinear system (Yen M. H. et al., 2019). Furthermore, the need to manage a large amount of data, as these coming from hydraulic simulations, have to be taken into account.

The key features that we considered here to develop an algorithm, able to provide an answer to the issues above remarked, are: a structure based on multi-core CPU, control of accuracy, non-linear modelling of the link between inputs and outputs that are reduced by technique of image processing. A neural network was selected as starting algorithm. Input data are the temporal evolution of spatially distributed rainfall similarly to those obtainable by radar measurements. The outputs were constructed using the flow velocity and depth fields obtained by high resolution hydraulic simulations. To simplify the problem the two fields of flow velocity and depth, were converted in a unique field by introducing a discrete variable (with values 1,..,4) each value of which, defined as 'flag', represents the potential level of dangerous associated to a given combination of flow velocity and depth (see figure 79). A time delay neural network (TDNNs) was thus developed to model the link between time series of the input and the output fields. The TDNN results have lower computational costs than RNNs techniques. The TDNN was trained by the input and output fields obtained by a number of hydraulic simulations carried out by the 2D shallow water model previously described.

The algorithm, presented here, is based on a sequence of rainfall fields as input data and return accurate forecasted flag maps, as those obtained from FHM-2D, as output data. With the aim to further reduce the computational cost, principal component analysis (PCA) of the input and output fields was applied.

As we assume that inputs and outputs coming from the shallow water equations can be considered as images, in which each point of the grid represent a pixel and each image has a resolution of 9984 x 6112 pixels, corresponding to the number of the cells of the grid considered for the shallow water simulation, the

need to apply PCA is fundamental. As a consequence, the resolution of each image is extremely high: it corresponds to more than 61 mln cells. Therefore, each moment of the simulation, if saved, occupies 220 Mb. In our study, the number of simulations available was 12 and the amount of data available was 2 TB: thus keeping low computational cost for this project was a challenge. Moreover it should be taken into account that the most of the computational cells are useless to our intents because of the flag value that is ~ 0 or because some of them don't change from one simulation to the following (they are not involved in the flooding event). In addition, outliers could happen and is not possible to control all them manually because of the high number of pixels (61mln) for each instant of the simulation. Finally, it is mandatory to keep the computational costs as low as possible, without sacrificing the accuracy.

PCA is a technique based on the dimensional reduction extremely common in the field of big data, but very innovative in the field of image processing where it starts to be used from 1990. PCA seeks to represent observations in a form that enhances the mutual independence of contributory components. The PCA technique considers a multidimensional space and reduces this space creating a new coordinate system where the variance of the points is maximized. For example, if we consider a bidimensional space of observation (X_1, X_2) , PCA technique is able to create a novel coordinate system for this 2D image in which the greatest variance lies on the first coordinate, the second greatest variance on the second coordinate and so on (it means for each axes that we are considering). Each coordinate is also called principal component. In detail, each image can be considered as a matrix in which every computational cell constitutes a "pixel" of the image. In each cell the actual value of a field is the same as the brightness of the pixel. This methodology is commonly used in face recognition (Turk, Pentland, 1991) (Figure 72).

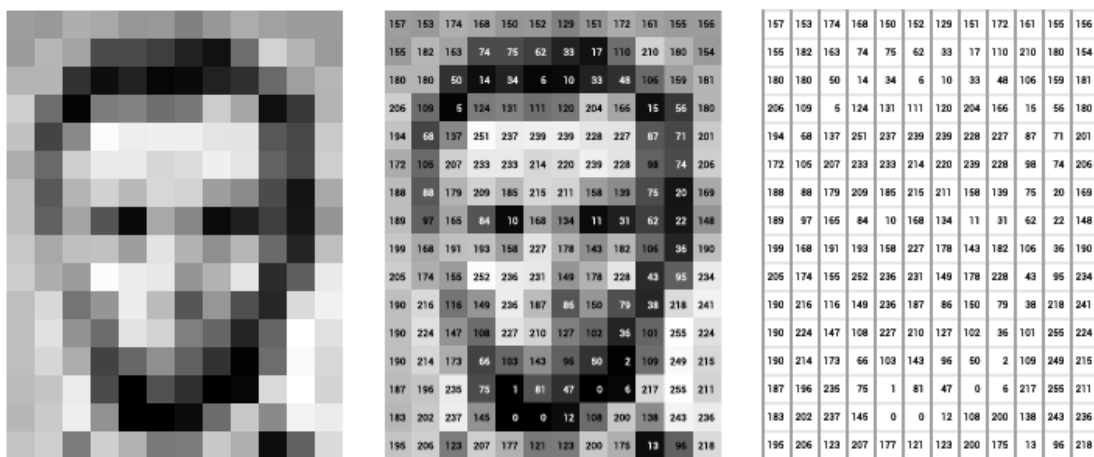


Figure 72 - face recognition technique

Hereafter, the letter N was used to denote the total number of solutions in the database.

The goal was the reduction of a matrix of $[N \times n \text{ pixel}]$ to something computationally cheaper of shape $[N \times M]$, with $M \ll n$. Each matrix (solution) here is technically called "unrolled", because it generates a single array in which the dimension (size) of the array (vector) will be $[n_x \times n_y]$, where n_x and n_y are the number of

cells in each direction. In our situation, each array will be ~ 60 mln of cells. Each of these values will correspond to the starting value of the brightness. The intensity variation is assumed in each pixel of the image. This process is repeated for every solution of the shallow water model. As a consequence, if each simulation is composed of N temporal moments, the matrix dimension will be $[N \times n \text{ pixel}]$, where $n \text{ pixel}$, as previously reported is $\sim 60 \times 10^6$. The covariance matrix is computed and the PCA are derived. In order to effectuate the PCA analysis, all the available simulations should be considered. Therefore, because 12 simulations are available and each simulation is $\sim 20\text{-}30$ Giga, the computer should be able to process all of this amount of data. To reach this goal it was necessary to reduce the resolution of the shallow water simulation to $\frac{1}{4}$. Therefore the solutions reported here have a resolution of $20\text{m} \times 20\text{m}$.

Through PCA analysis, we are able to obtain autovectors and autoimages from each matrix. Depending on the number of the axes present in the coordinate system chosen, the explained variance could be higher or lower; usually, this is called eigen images in which the number of the ideal components is chosen to explain more than 95% of the variance.

To achieve this goal, every row of the observation matrix is projected into the new frame of reference, leading to a new matrix that is $[N \times L]$, where L is the number of principal components. All the starting datasets are therefore divided into a score matrix whose dimension is the number of components \times starting examples and some fixed matrices whose dimension will be $[M \times \text{total pixel}]$ (where M is the number of components). In this way, as dataset we can consider only the training dataset. In this way, we will have $[N \text{ solution} \times N \text{ of components}]$ instead of $[N \text{ solution} \times 61\text{mln}]$ and the whole dataset can be managed by any computer.

Let's focus on how we studied our input data: we have a hyetograph for all the simulations through with we know all the flags of each time step (Figure 73).

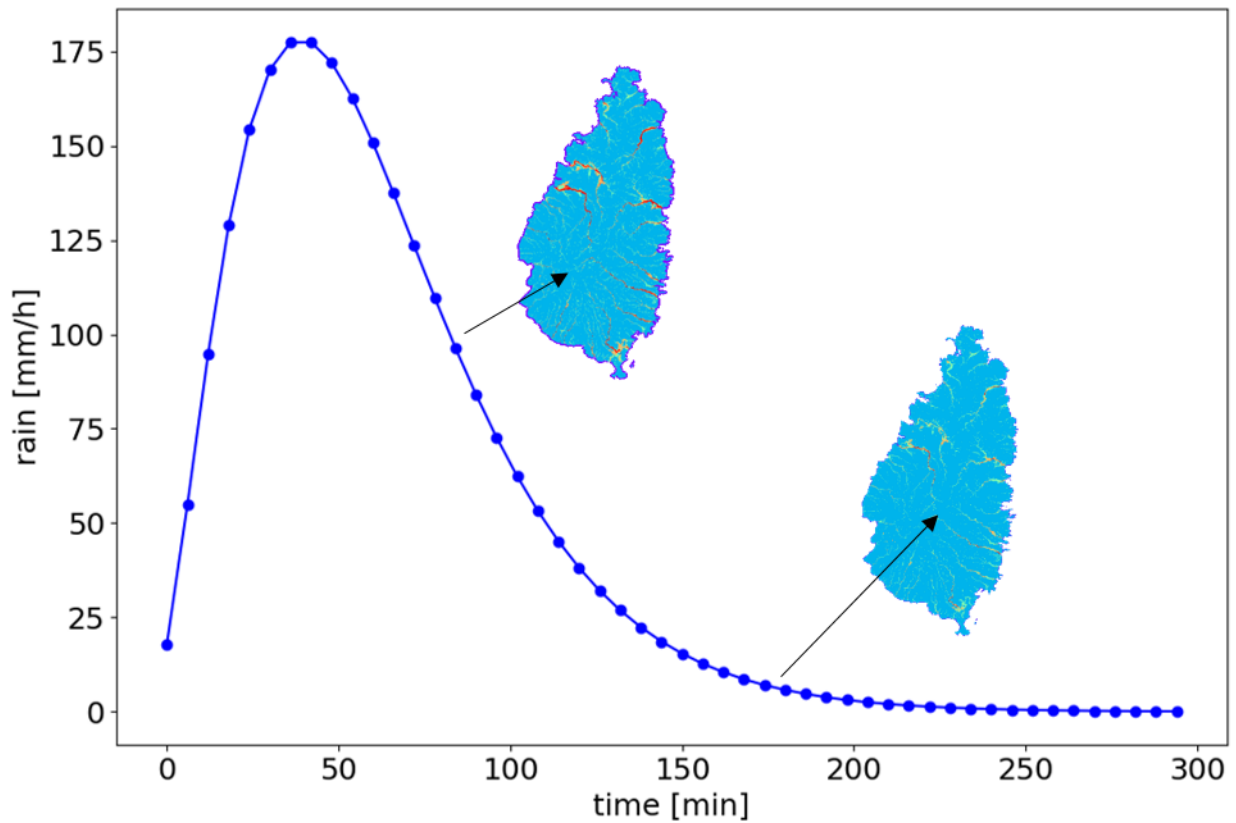


Figure 73 - Hyetograph of a rainfall with 10 years return period

In order to create the input data, we took into account the rain sequences, e.g. t_0 corresponds to $rain_0$; t_1 to $rain_1$ and so on. All of these events are introduced in a sequence (r_1, r_2, r_3, r_4, r_5 and so on) (see figure 74). In order to properly replicate water runoff, we also included the cumulated rain to the input features (feature added). Each of these rain sequences is related to the forecast flag: it means that we can shift from few temporal moments to have a forecast. For example, if we are interested in the first rain sequence (from r_1 to r_5) we can shift from 10 temporal moments and we knew that the first temporal sequence corresponded to a certain flag forecast. In this way we can get the complete raining database of our algorithm. Each rain sequence is associated with autovectors of the corresponding flag.

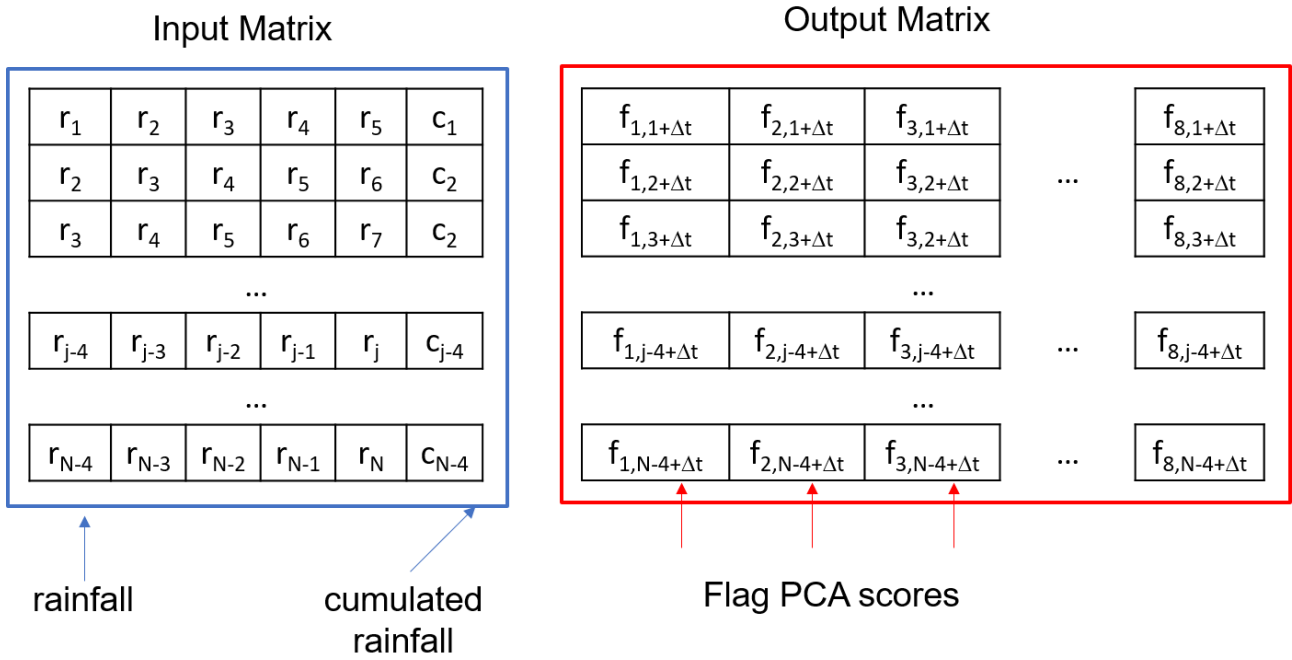


Figure 74 - Input and output features of matrix

The code has been performed in an open-source environment and the framework is based on Python 3.6.x; moreover, for the training of the network we used Tenton-pro that is a platform of artificial intelligence. Figure 75 shows how the operative framework works hour by hour: the database is split into train database and test database.

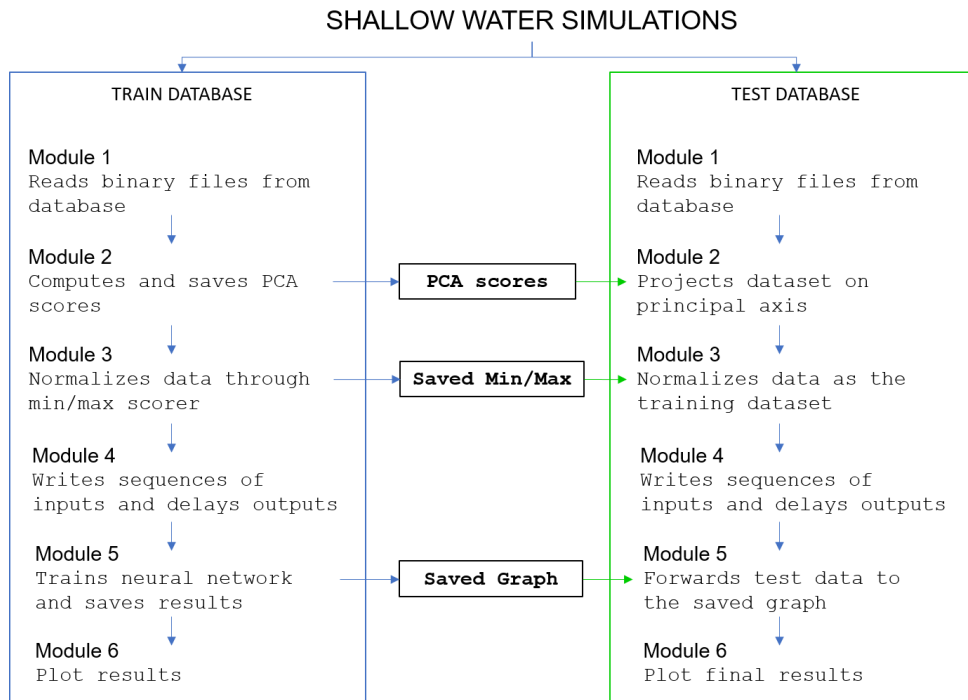


Figure 75 - Operative frameworks of the algorithm

The train database is used for the training of the algorithm, while the test is used to test the algorithm to be sure that it can be generalized. Most of the moduli are similar in both cases, only in three cases they differ from each other.

In detail the data from shallow water equations are rapidly read, PCA were calculated and data were normalized and processed in order to write sequences of input and delayed outputs. Finally neural network is trained and the results were saved and plotted. In order to ensure that the model is reproducible and can be generalized, a test is performed: in detail, all the data provided were processed according to the train database and, hence, project dataset on principal axis, was normalized as the training dataset and finally forwarded to the saved graph.

5.3 PRELIMINARY RESULTS

For PCA analysis and image processing fifteen simulations are currently available, with more going on. Twelve simulations are taken as train dataset. Each simulation is distinguished by a different hyetograph and return time; nine of them train the algorithm, while the remaining three are kept apart and exploited as test dataset. Looking at the PCA scores, eight principal components are sufficient to explain 95% of the variance. Figure 76 shows the PCA of the shallow water model: each shallow water solution can be considered as a summation of some coefficients for each of these images. Each image explains a percentage of the variance: figure 76 shows the maximum explained variance and so on.

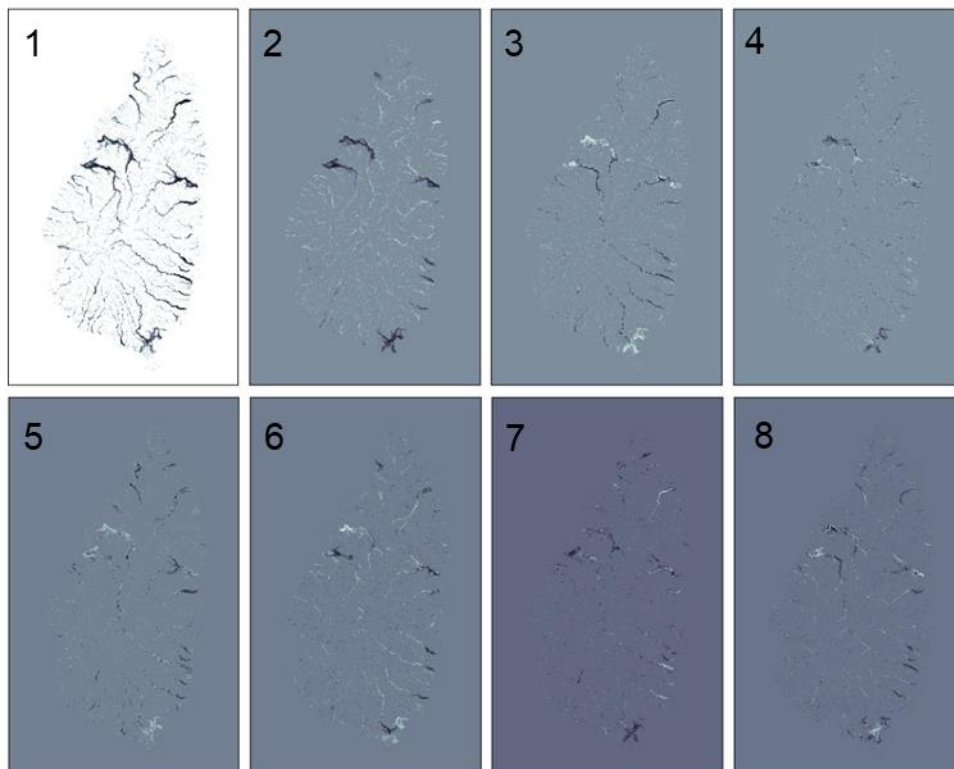


Figure 76 - The eight eigen-values derived from PCA transformation of training dataset

Interestingly there are some points of the island in which the flooding pattern is not relevant and hence they are redundant in the train of an artificial intelligence.

All the hyperparameters have been tuned heuristically to grant the faster training speed/accuracy. Different techniques have been used to avoid the model overfitting and to confirm that the model can work also for other training database (we need to demonstrate that is generalizable). It should be emphasised that this is the major limit of the algorithms reported in literature: they work exclusively for a single database being not reproducible.

Figure 77 reports the training. The accuracy of the algorithm is relatively high even after 3000 or 4000 epochs. However, these plots are not very significative because of the accuracy depends also on the way in which the training is developed.

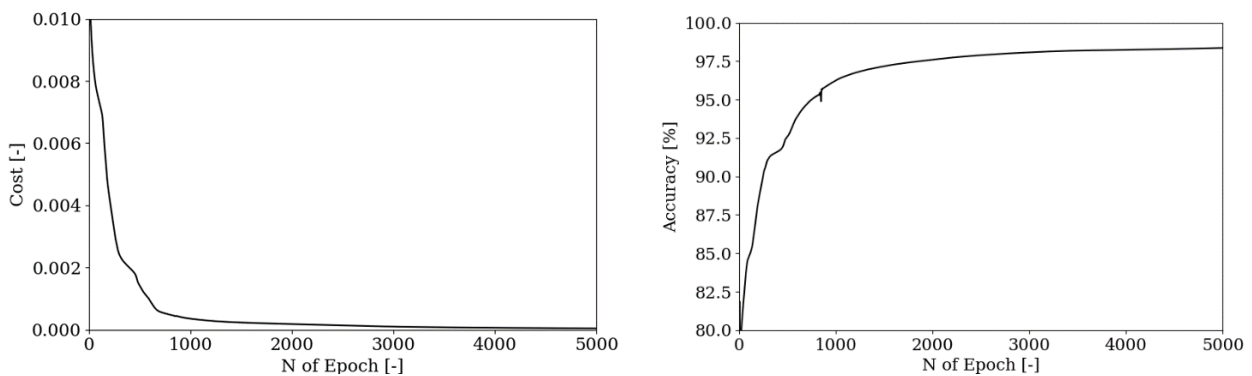


Figure 77 - cost of the validation dataset as a function of the number of epochs (left) and accuracy of the validation dataset as a function of the number of epochs (right)

The training is completed in approximately 10 mins on a standard CPU. 20% of the train dataset was kept as validation dataset, to monitor the absence of overfitting and the convergence of the algorithm.

In Figure 78 some results, obtained using Tomas and Dean hurricanes as test cases, are shown. In detail, figure shows, for different temporal instances, the maps obtained from FHM-2D (visible in figure as REAL) and those obtained with the surrogate model (visible in figure as PRED).

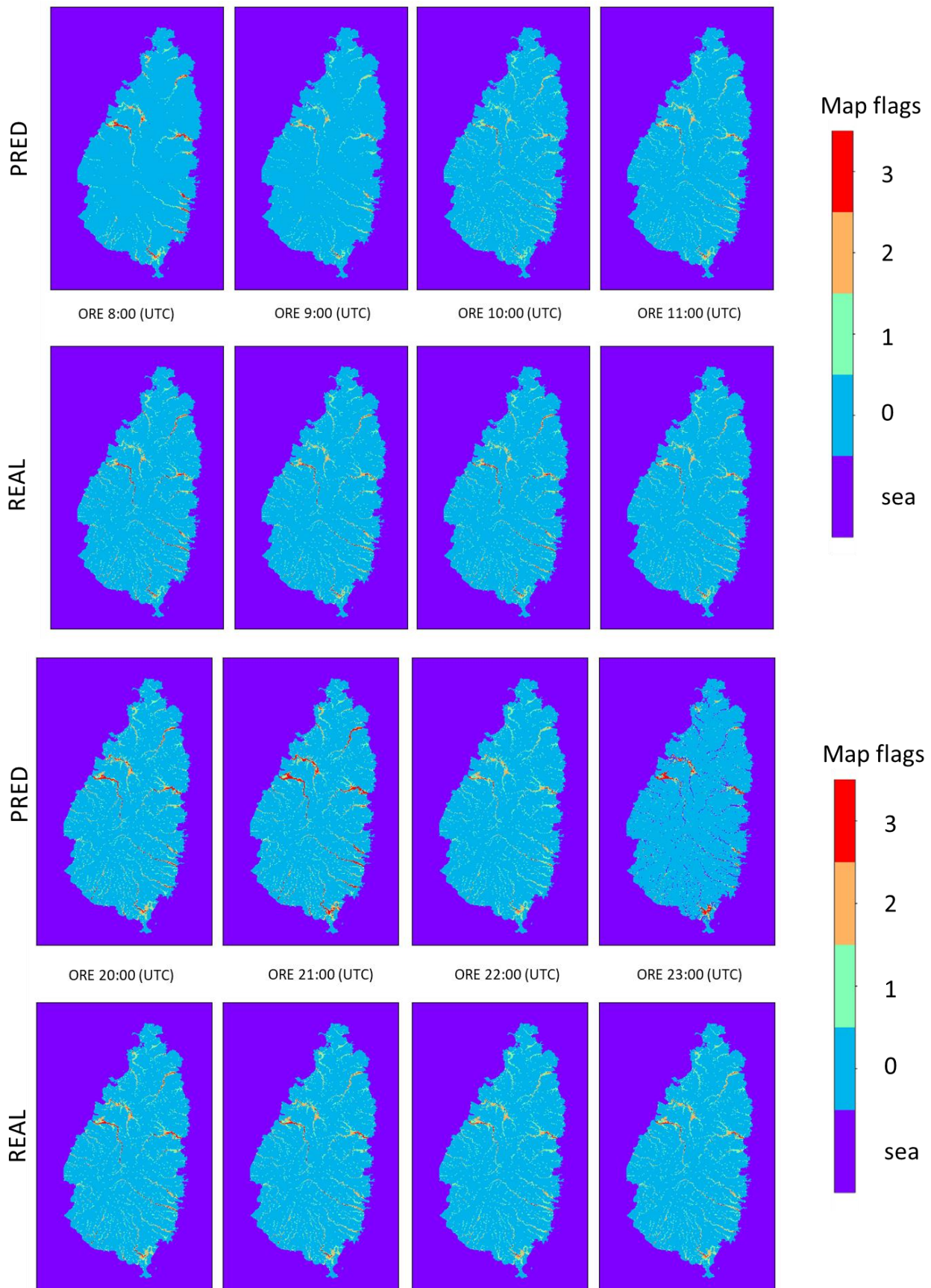


Figure 78 - Results obtained from the algorithm for a) 10 years, b) 20 year and c) 50 year of return time

From these images is possible to obtain a flag value forward in time. The flag values are based on a flow depth and velocity relationship and the thresholds are represented in figure 79. In figure 78 the “low” flag is represented in green and identified as 1 in the legend. The “medium” flag, is identified in orange and reported in the legend with the value 2, and finally, the “high” flag is reported with 3 in the legend and identified in red. The classes are referred to the dangerousness of the flooding at a certain relationship of depth and velocity values.

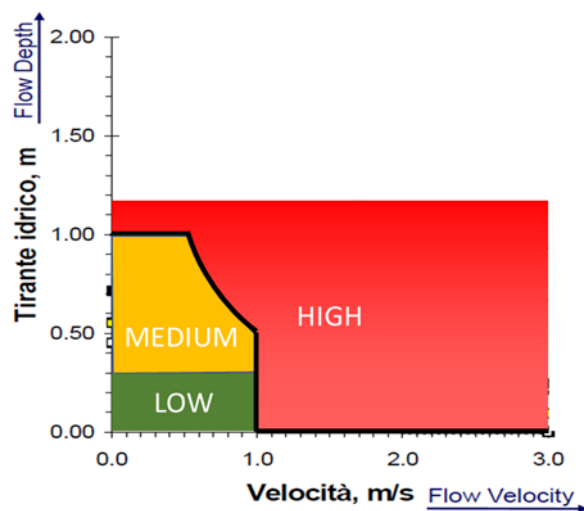


Figure 79 - Flag classification classification obtained from the flow depth and velocity relationship

The first results obtained with the surrogate model, for the case study adopted, showed a high confidence. In fact, the maps predicted with the AI are the same as those obtained from FHM-2D for each temporal instance. However, the problem is that the simulations did not take into account the run-off because they are too short. As a consequence, the model works well only when it is supposed to predict the flooding in the future. If we are interesting, instead, in understanding how the watershed of the island will be drained once that the rains stop, the model developed here doesn't work well yet. However, even in this last situation we have already the solution: it's necessary only increase the time of the simulations in order to allow the right runoff of the flooding present in the area of interest.

5.4 CONCLUSIONS AND ONGOING DEVELOPMENTS

The surrogate model proposed and described above is resulted effective in reproducing the link between input (rainfall) and output (flooding) similarly to that simulated by 2D hydraulic model, within the spectrum of simulations used to train the model. However, the result obtained have to be considered as preliminary, and further model validations have to be performed to confirm the goodness of the approach, in a larger range of rainfall temporal and spatial variations.

However, there are some issues that require to be further investigated. The use of not spatially uniform rainfall requires to be investigated in more details. Not spatially uniform rainfalls differ from spatially uniform rains because they require a PCA analysis on the input data. In this scenario, all the input data have to be analysed and the PCA analyses realized; in this way the input features will increase, but this allows a more general and flexible application of the proposed methodology. Rainfall distribution from radar data can be used as input to the surrogate model, in way to generate a short forecast.

6 SUMMARY AND PERSPECTIVES

6.1 SUMMARY

This thesis was addressed to explore how remote sensing technologies could be effectively used in the assessment of hydraulic risk due to extreme hydrological extreme as floods. In this context different methodologies - separately and/or among them combined were investigated- the most part of the work has been focused on the flood risk assessment referred at the two phases of post event analysis and the nowcasting respectively.

In detail, for the post event phase three different approaches have been used and combined to rebuild post event flooding maps: remote sensing, hydraulic modelling and social media marker. The remote sensing from satellite resulted a very useful tool for the assessment of the flooding risk due to its numerous advantages (i.e. huge number of information due to the global coverage; capability to obtain information during the night and/or in extreme weather condition, high spatial resolution of most sensors, etc.). Furthermore, the ever wider spatial coverage and the launch new missions with boarding sensors with increasing resolution make these tools fundamental in the flood risk analysis. Hydraulic modelling has been widely used to generate inundation maps and is expected an increase of its performance. At the date, however both the approaches exhibit some shortcomings that require to be overcome. Remote sensing from satellite is not able to carefully monitor the alluvial extreme event in particular areas, as urban or vegetated ones. In such area the complexity of geometry and the need of high spatial resolution limits the applicability of the hydraulic modelling too. To overcome this problems, the combination of these techniques and the further use of others tools, as e.g. the social marker, has been investigated in this thesis. Concerning the nowcating phase, the long computational times required by hydraulic models prevents their use, therefore other approaches have to be developed. In this thesis, the potentiality of the machine learning algorithm was exploited in order to overcome the main limitation of the hydraulic modelling, that is the high computational time. Even if for preliminary results the possibility to obtain flooding maps in real time was proved.

Chapter 1 provides an introduction on the importance of having useful tools for the assessment of all the phases of an extreme rainfall event (prevention, prevision, monitoring, nowcasting and post-event). Particular attention is given to the remote sensing from satellite in the assessment of the flooding risk thanks to its ability to give information for all the above mentioned phases and also to the hydraulic modelling for the post-event investigation. Moreover, other emerging techniques has been investigated including social media marker and machine learning for their promising utility in the post-event and nowcasting phases, respectively. In detail, the importance of combining some of these techniques (remote sensing from satellite, hydraulic modelling and social media marker) was highlighted for their capability to rebuild very accurate

post event flooding maps. Finally, the aim and the outlines of this thesis are presented: the whole discussion is finalized to the identification of new tools for the development of very accurate post event flooding maps and for the significant reduction of computational times in the nowcasting phases.

The aim of **Chapter 2** was to explore how the satellite data are useful for the monitoring of phenomena that contribute to the hydraulic risk and how the accuracy of the satellite instrument could be improved in relation to the context in which the floodings occur (urban, suburban, dense vegetation, etc.). Moreover, also the ability of the social media markers to visualize or not the elements blind to the satellites and to evaluate, therefore with greater resolution, the damages produced by the flooding was investigated. In this contest, data from hydraulic simulations and satellite maps were used to reconstruct the flooding map of Strymon river after an extreme rainfall event. Because of the remote sensing from satellite didn't allow to estimate the flooding depth of the event, social media marker were also used and combined to the other previous reported techniques. In detail, two different case studies were investigated: hurricane Harvey in Houston (USA) and Diamrey typhoon in Quang Ngai (Vietnam). Harvey initially developed as a low-pressure system becoming soon a tropical cyclone. The highest record in terms of rain recordings occurred at Cedar Bayou, also in Houston, with 1318 mm of rain that fell during the storm (NWS 2017). Over 20,000 people were forced to seek emergency shelter during the event and an estimated 120,000 structures were affected by flooding. This extreme event and the area were chosen for four main reasons: 1) this event has gone down in history, due to recorded damage and record rainfall, as one of the five major historical events in the United States; 2) Houston was one of the cities most affected by Hurricane Harvey; 3) the particularity of the morphological and geographical characteristics of the region which makes it vulnerable to flooding; 4) the area is particularly well monitored and this makes the analysis possible. The second case study was the Typhoon Damrey that first originated as a tropical depression becoming then a strong tropical cyclone and causing 142 casualties and a total damage over US\$1 billion. This area was chosen because of the lack of ground gauge stations as well as high accuracy DEM. In the first case study, a flooding map with significant accuracy was obtained by using remote sensing from satellite and ground station information for the calibration of the hydraulic modelling results and social media marker for the validation. The same techniques were also used for the calibration and validation of the hydraulic modelling results of Diamrey typhoon. However, in this case, not good flooding map was obtained because of the low accuracy of inputs data (DEM and precipitation data from satellite). Taking into account this limit, further investigations, performed on radar, satellite and reanalysis datasets, highlighted that all of these tools underestimate the event peaks.

In **Chapter 3**, starting from the promising results of the Houston case study, further tests were carried out on the data provided by the HEC-RAS software in order to understand if the approach of Casulli sub-grids allows to have results in terms of extension, depth and speed without mistake. The obtained results revealed a high number of mistakes for all these three parameters. As a consequence, a new finite volume calculation

code for the integration of motion equations mediated along the depth, called FHM-2D, was developed. The equations presents in the code were taken using as reference the papers of: (Audusse et al., 2004) for the governing equations, for the Lax-Friedrichs first order of flux discretization, and at least for the first and second order extension of the source discretization; (Hou, J. et al., 2015) for the TVD MUSCL second order flux discretization; (Jameson A. et al., 1981) and (Marqués, J. M. F., 2000), respectively, for the Runge-Kutta 4th order and Forward Euler explicit scheme for the discretization of the time derivative. Finally, for the precipitation and infiltration was used respectively, (Cea, L. et al., 2010) and (Chow et al. 1988). This model exhibits the ability to overcome all the limitations of the commercial codes currently available and allow to do simulations in parallel. In this way, more accurate results at the DEM resolution scale and in urban contexts were obtained. Finally, the code was validated by bench tests and through its application to real case studies happened in Saint Lucia Island after tropical cyclones and hurricanes. For all the investigated cases data related to past flooding events were used as input. These findings reveal that the hydraulic modeling appears to be an excellent tool for the post-event but not for the nowcasting phase because of the long computational times. To overcome this limit, a surrogate model through machine learning was developed.

Chapter 4 describes, therefore, the development of a surrogate hydraulic model, based on the use of Artificial Neural Network techniques, specifically, Time Delay Neural Network (TDNN). A supervised algorithm was used to train the algorithm using known input (precipitation fields) and output (flooding maps) data derived from radar and FHM-2D, respectively. After the training, the surrogate model was validated. With this approach flooding maps, related to a specific atmospheric condition emerged from the radar, were obtained in a very short time with a consequently significant reduction of the computational costs.

6.2 PERSPECTIVES

The main topic of this thesis is the development of new methodologies and the improvement of the existing ones in the rebuilding of post event flooding maps with high accuracy and the significant reduction of the computational times during the nowcasting phase of flooding risk assessment. In detail, remote sensing from satellite, hydraulic modelling and social media marker were used in combination to obtain post event maps with increased accuracy (Chapters 2 and 3), while machine learning approach was used to reduce the computational costs in the nowcasting phase (Chapter 4). The results obtained in this applications could be a very useful in the development of innovative tools for the assessment of the hydraulic risk, which assumes particularly relevance due to the expected increases of frequency and intensity of extremes in ongoing climate changings. In fact, the possibility to have very accurate flooding maps allows to plan actions to reduce flooding risk in the most vulnerable areas, as well as, to organize better emergency plans.

However, some issues require further investigation and some improvements. In detail, in non-instrumented areas, the reconstruction of accurate flooding maps is actually an open issue even if remote sensing from satellite, hydraulic modelling and social media marker were combined (Chapter 2). This is mainly due to an intrinsic limit of the remote sensing that is the underestimation of the precipitation peaks and because of precise DEM usually are not available and/or free. To overcome these limits, GPM constellation should be considered and exploited since some preliminary studies have shown its ability to reduce the uncertainties compared to the other well-known techniques reported in literature.

Concerning social media marker, the main problem is related to the interpretation of the water depth from the pictures available, that in this first scenario was based on the subjected interpretation of the operator. In this contest, artificial intelligence represents a valid alternative, which deserves further investigation. . In fact, there are some shortcomings that require to be overcome, such as the difficulty of the training of the algorithm (because of the huge number of different elements that could be in a picture) and the issue in the establishment of the relationship between the picture prospective and the corresponding flooding depth.

Concerning the machine learning approach developed in Chapter 4 further tests have to be performed for better training the algorithm. In detail, in this thesis the training algorithm was based on twelve extreme event pictures (obtained from FHM-2D developed in Chapter 3); however, higher precision could be obtained providing the model with more pictures (collected from other alluvial extreme events). Moreover, after an extensive training of the algorithm in a specific area of the extreme event, there will be the chance to get information not only in the nowcasting but also in the forecast phase, and in the optimization planning where a huge number of simulations are necessary.

It can be concluded that the techniques investigated in this thesis, due to their unique and promising properties, are attractive candidates for a wide range of social, environmental and industrial applications. I believe that such methodologies, especially when combined to each other, can find practical applications not only in the nowcasting and post event analysis, but in the more general framework of flooding risk assessment.

ACKNOWLEDGEMENTS

I ringraziamenti, in contrasto con quanto fatto per la stesura della tesi, li farò in lingua italiana così da poter esibire tutta la mia capacità nello scrivere in modo “barocco”, come tanto piace al mio PROF.

Ecco, la prima persona a cui vorrei dire un gigantesco grazie è proprio lui, IL MIO PROF, il CIOFFONE NAZIONALE o, solo per i pochi intimi, IL GENTILUOMO DI SALERNO. IL MIO PROF ha saputo capirmi in ogni situazione, sostenermi nei momenti bui, invogliarmi a fare sempre meglio, farmi ridere nei momenti felici ed in quelli più duri, realizzare il sogno della mia vita (andare a NY non da turista ma da lavoratore) e soprattutto sempre trovare quelle parole giuste al momento giusto. Posso dire davvero di essere fortunato, perché in questo viaggio che molti chiamano semplicemente “Dottorato di Ricerca”, io ho trovato un grande uomo oltre che un grande maestro. Dovrei scrivere un'altra tesi solo per descrivere tutti gli attimi che abbiamo condiviso insieme quotidianamente, ma spero che queste poche righe ti portino a capire quanto ti voglia bene MIO PROF, che in molti momenti sei stato come un secondo papà, e che soprattutto sei e sarai sempre un gran punto di riferimento per la mia vita professionale e non.

Vorrei ringraziare una persona che, purtroppo non sono riuscito mai a conoscere, la Prof.ssa Silvia Macchi. A Lei devo la nascita di questo fantastico percorso del Dottorato svolto in collaborazione con e-GEOS e che mi ha portato oggi ad essere assunto.

Ringrazio i Prof. Parcharidis e Ceccato per avermi dato la possibilità, prima ad Atene e poi a New York, di collaborare con loro ed imparare tantissime cose e di conoscere tanti colleghi, ormai amici, meravigliosi.

Ringrazio il grandissimo Prof. Sergio Pirozzoli per avermi insegnato un mondo di cose in pochissimo tempo e permesso di fare cose impensabili. Senza il suo aiuto non ce l'avrei mai fatta. Il nostro Frankenstein model è la nostra bestia e rimarrà sempre tale! Ringrazio anche Simone che ha assistito a tutte le nostre diatribe durante la costruzione del codice.

Vorrei dire grazie a Federica Mastracci, Domenico Grandoni, Dino Quattrococchi, Lucia Luzietti e tutti i miei cari colleghi di e-GEOS per avermi reso questo percorso aziendale-universitario molto stimolante ed avvincente. Tutti siete stati sempre disponibili e molto comprensivi con me e questo mi porta a dirvi sempre più grazie ad ognuno di voi!

Ora è il suo momento, il mio amore che ho fatto tanto soffrire e tribolare in questo ultimo anno. Nicolina grazie per l'amore che mi hai sempre regalato e dimostrato senza mai chiedermi niente. Grazie per il sostegno che già dalle superiori mi hai sempre dato e per avermi fatto capire che nella vita sarei potuto essere qualcuno e non la persona mediocre che sarei diventato senza te. Grazie piccola soprattutto per quelle mille correzioni o torture fai tu, tra l'inglese e l'italiano a cui ti ho costretta tante volte. Amore finire questo percorso insieme è praticamente ciò che ho sempre desiderato. Essere allo stesso punto della nostra vita ci permette di poter

iniziare insieme un'altra tipologia di cammino e quindi ti chiedo, come hai sempre voluto tu, in maniera inaspettata e riservata (:P), **MI VUOI SPOSARE???** (la proposta è quella vera, quindi non morire ti prego e limitati solo a guardare davanti a te ed a dire **SI!**)

Vorrei ringraziare ora la mia famiglia (Papi, Mami, il Magico e la Wuagliona) che amo e che tante volte bistratto. Sono ben conscio di avere un caratteraccio ma vi voglio bene e devo tutto ai vostri sacrifici se oggi sono arrivato ad un livello tale da potermi permettere di costruire una famiglia, comprare una macchina e casa ed in generale avere tutto il desiderabile. Vi voglio bene non dimenticatelo mai e vi sarò riconoscente per sempre.

Ringrazio i miei suoceri Alfeo, Anna GIS e Ciccio, la mia seconda famiglia. Anche a loro ho fatto passare dei brutti momenti che ora però sono e devono essere sepolti perché non riemergeranno mai più. Sono stati molto importanti in questo periodo di Dottorato per il sostegno datomi. Pensandoci, non oso immaginare la reazione dei suoceri alla lettura della proposta di matrimonio fatta a Nicolina ahahahahah (...secondo me Anna che se la ride di gusto ed Alfeo completamente gelato o col fucile in braccio... ahahahha). Cercherò di essere il genero SEMPRE Più PREFERITO!

Ringrazio ora gli amici di sempre che mi hanno visto gioire, soffrire e bestemmiare durante questo percorso...beh le analisi vanno bene come possono non andare e la blasfemia è sempre presente in questi casi... ahahahahha. Ringrazio tra tutti il mio Mariuzz con cui ho condiviso anche delle nottate di simulazioni e tutto ciò che fanno i veri amici, i cessi di Sesso, Satana e Chappy, il mio amore Luchino, Daria, Elisa e poi tutto il resto del cucuzzaro (non sentitevi offesi se non leggerete il vostro nome ma mi sono già sforzato per i ringraziamenti scritti fino ad ora e fate come se il vostro nome fosse scritto) e sappiate che vi voglio bene tutti.

PS IO MI SONO DOTTORATO E QUINDI MI CHIEDO, CONSIDERANDO CHE TUTTO E' POSSIBILE A QUESTO PUNTO, MA IL NAPOLI LO VINCERA' MAI LO SCUDETTO???

FORZA NAPOLI E JUVE MERDA SEMPRE <3

7 REFERENCES

- Abbot, J., & Marohasy, J. (2014). Input selection and optimisation for monthly rainfall forecasting in Queensland, Australia, using artificial neural networks. *Atmospheric Research*, 138, 166-178.
- Abrahart, R.J. and Kneale, P.E. (1997) "Exploring neural network rainfall-runoff modelling", Proceedings of the Sixth National Hydrology Symposium, University of Salford, 9.35-9.44.
- Adler, R. F., & Negri, A. J. (1988). A satellite infrared technique to estimate tropical convective and stratiform rainfall. *Journal of Applied Meteorology*, 27(1), 30-51.
- Aires, F., Aznay, O., Prigent, C., Paul, M., Bernardo, F., (2012), Synergistic multi-wavelength remote sensing versus a posteriori combination of retrieved products: Application for the retrieval of atmospheric profiles using MetOp-A. *J. Geophys. Res.: Atmosphere* 117(D18).
- Alcrudo F. and Garcia-Navarro P., (1993). A high-resolution Godunov type scheme in finite volumes for the 2D shallow water equations. *Int. J. Num. Meth. Fluids*, 16: 489-505.
- Altinakar, M. S., McGrath, M. Z., Ramalingam, V. P., & Omari, H. (2010). 2D modeling of big bay dam failure in mississippi: Comparison with Field Data and 1D Model Results. In *River Flow* (Vol. 2010, pp. 547-554).
- Anastasiou K. and Chan C. T., (1997). Solution of the 2D shallow water equations using the finite volume method on unstructured triangular meshes. *Int. J. Num. Meth. Fluids*, 24: 1225- 1245.
- Anusha, N., & Bharathi, B. (2019). Flood detection and flood mapping using multi-temporal synthetic aperture radar and optical data. *The Egyptian Journal of Remote Sensing and Space Science*.
- Aronica G.T. & Lanza L.G., (2005) Drainage efficiency in urban areas: a case study. *Hydrol Process*, 19, 1105–1119. doi: 10.1002/hyp.5648.
- Arnaud, A., Adam, N., Hanssen, R., Inglada, J., Duro, J., Closa, J. And Eineder, M. (2003), ASAR ERS interferometric phase continuity. *Geoscience and Remote Sensing Symposium*, 2003. IGARSS '03. Proceedings. 2003 IEEE International, 2, pp.1133-1135, 21-25 July 2003.
- Arkin, P. A., (1979): The relationship between fractional coverage of high cloud and rainfall accumulations during GATE over the B-array. *Mon. Wea. Rev.*, 107, 1 382- 1387.
- Arkin, P. A., and B. Meisner, (1987): The relationship between large-scale convective rainfall and cold cloud over the Western Hemisphere during 1982 - 1 984. *Mon. Wea. Rev.* , 115, 5 1-74.

Asare-Kyei, D, Forkuor, G & Venus, V (2015), 'Modeling Flood Hazard Zones at the Sub-District Level with the Rational Model Integrated with GIS and Remote Sensing Approaches', *Water*, vol. 7, pp. 3531-3564.

Atlas, D.; Thiele, O.W., (1981), *Precipitation Measurements from Space: Workshop Report. An Element of the Climate Observing System Study*; NASA Tech. Memo. NASA-TM-85329431; NASA Goddard Space Flight Center: Greenbelt, MD, USA.

Audusse, E., Bouchut, F., Bristeau, M. O., Klein, R., & Perthame, B. T. (2004). A fast and stable well-balanced scheme with hydrostatic reconstruction for shallow water flows. *SIAM Journal on Scientific Computing*, 25(6), 2050-2065.

Auynirundronkool, K., Chen, N., Peng, C., Yang, C., Gong, J., & Silapathong, C., (2012). Flood detection and mapping of the Thailand Central plain using RADARSAT and MODIS under a sensor web environment. *International Journal of Applied Earth Observation and Geoinformation*, 14(1), 245-255.

Aziz, K.; Rahman, A.; Fang, G.; Shrestha, S., (2014). Application of artificial neural networks in regional flood frequency analysis: A case study for australia. *Stoch. Environ. Res. Risk Assess.*, 28, 541–554.

Bagan H, Yamagata Y. (2012), Landsat analysis of urban growth: how Tokyo became the world's largest megacity during the last 40 years. *Remote Sensing Environ.* 127:210-222

Bales, J.D., Wagner, C.R., (2009). Sources of uncertainty in flood inundation maps. *J. Flood Risk Manag.* 2, 137e147.

Barrett, E.C.; Martin, D.W., (1981), *Use of Satellite Data in Rainfall Monitoring*; Academic Press: Cambridge, MA, USA,.

Bates, P., Hervouet, J., (1999). A new method for moving-boundary hydrodynamic problems in shallow water. *Proc. R. Soc. London A* 455, 3107–3128. <http://dx.doi.org/10.1098/rspa.1999.0442> .

Bates, P., Horritt, M., Fewtrell, T., (2010). A simple inertial formulation of the shallow water equations for efficient two-dimensional flood inundation modelling. *J. Hydrol.* 387, 33–45. <http://dx.doi.org/10.1016/j.jhydrol.2010.03.027> . Bear, J. , 1972. *Dynamic of Fluids in Porous Media*. Dover, New York .

Bapulu, G.V. and Sinha, R., (2005). *GIS in Flood Hazard Mapping: a case study of Kosi River Basin, India*. Noida: GIS Development. Available from: http://home.iitk.ac.in/~rsinha/PDF's/2006_FloodGISdevelopment.pdf [Accessed: 21/07/10].

Beck, H. E., Vergopolan, N., Pan, M., Levizzani, V., van Dijk, A. I., Weedon, G. P., ... & Wood, E. F. (2017). Global-scale evaluation of 22 precipitation datasets using gauge observations and hydrological modeling. *Hydrology and Earth System Sciences*, 21(12), 6201-6217.

Behrang, A.; Hsu, K.L.; Imam, B.; Sorooshian, S.; Kuligowski, R.J., (2009), Evaluating the utility of multispectral information in delineating the areal extent of precipitation. *J. Hydrometeorol.*, 10, 684–700.

BLANCO-SANCHEZ, P., MALLORQUÍ, J.J., DUQUE, S. AND MONELLS, D. (2008), The Coherent Pixels Technique (CPT): An Advanced DInSAR Technique for Nonlinear Deformation Monitoring, *Pure Appl. Geophys.*, 165, pp. 1167-1194.

Byun, Y, Han, Y & Chae, TB, (2015), 'Image Fusion-Based Change Detection for Flood Extent Extraction Using Bi-Temporal Very High-Resolution Satellite Images', *Remote Sensing*, vol. 7, pp. 10347-10363. DOI:10.3390/rs70810347.

Branney M J, (1995), Downsag and extension at calderas: new perspectives on collapse geometries from icemelt, mining, and volcanic subsidence. *Bulletin of Volcanology*, Vol. 57, Issue 5, 303- 318.

Brivio, P. A., Colombo, R., Maggi, M., & Tomasoni, R. (2002). Integration of remote sensing data and GIS for accurate mapping of flooded areas. *International Journal of Remote Sensing*, 23(3), 429-441.

Balzano, A., (1998). Evaluation of methods for numerical simulation of wetting and drying in shallow water flow models. *Coastal Eng.* 34, 83–107. [http://dx.doi.org/10.1016/S0378-3839\(98\)00015-5](http://dx.doi.org/10.1016/S0378-3839(98)00015-5).

Berardino, P., Fornaro, G., Lanari, R. And Sansosti, E., (2002), A new algorithm for surface deformation monitoring based on small baseline differential interferograms. *Geoscience and Remote Sensing, IEEE Transactions*, 40, no.11, pp.2375-2383.

Boushaki, F.I.; Hsu, K.L.; Sorooshian, S.; Park, G.H.; Mahani, S.; Shi, W. Bias, (2008), adjustment of satellite precipitation estimation using ground-based measurement: A case study evaluation over the southwestern united states. *J. Hydrometeorol.*, 10, 1231–1242.

Campolo, M., Soldati, A., & Andreussi, P. (2003). Artificial neural network approach to flood forecasting in the River Arno. *Hydrological Sciences Journal*, 48(3), 381-398.

Carincotte, C., Derrode, S., & Bourennane, S., (2006). Unsupervised change detection on SAR images using fuzzy hidden Markov chains. *IEEE Transactions on Geoscience and Remote Sensing*, 44(2), 432-441.

Casas, A., Lane, S., Yu, D., Benito, G., (2010). A method for parameterising roughness and topographic sub-grid scale effects in hydraulic modelling from LiDAR data. *Hydrol. Earth Syst. Sci.* 14, 1567–1579. <http://dx.doi.org/10.5194/hess-14-1567-2010>.

Castelletti, A., Galelli, S., Ratto, M., Soncini-Sessa, R., Young, P.C., (2012). A general framework for Dynamic Emulation Modelling in environmental problems. *Environ. Model. Software* 34, 5–18. <https://doi.org/10.1016/j.envsoft.2012.01.002>.

- Castro-Gama, M.E., Popescu, I., Li, S., Mynett, A., van Dam, A., (2014). Flood inference simulation using surrogate modelling for the Yellow River multiple reservoir system. *Environ. Model. Software* 55, 250–265. <https://doi.org/10.1016/j.envsoft.2014.02.002>.
- Casulli, V., & Walters, R. A., (2000). An unstructured grid, three-dimensional model based on the shallow water equations. *International journal for numerical methods in fluids*, 32(3), 331-348.
- Casulli, V., (2008). A high-resolution wetting and drying algorithm for free-surface hydrodynamics. (August 2008):391–408.
- Casulli, V., (2009). A high-resolution wetting and drying algorithm for free-surface hydrodynamics. *Int. J. Numer. Methods Fluids* 60, 391–408. <http://dx.doi.org/10.1002/flid.1896> .
- Cea, L., Garrido, M., & Puertas, J. (2010). Experimental validation of two-dimensional depth-averaged models for forecasting rainfall–runoff from precipitation data in urban areas. *Journal of Hydrology*, 382(1-4), 88-102.
- Chau, K. (2006). A review on the integration of artificial intelligence into coastal modeling. *Journal of environmental management*, 80(1), 47-57.
- Chertock, A., Cui, S., Kurganov, A., & Wu, T. (2015). Well-balanced positivity preserving central-upwind scheme for the shallow water system with friction terms. *International Journal for numerical methods in fluids*, 78(6), 355-383.
- N. Chen, X. Zhang (2004), Dynamic observation capability index for quantitatively pre-evaluating diverse optical imaging satellite sensors. *IEEE J. Select. Top. Appl. Earth Obs. Remote Sens.*, 7 (2), pp. 515-530.
- Chen, A. S., Evans, B., Djordjevic, S. & Savic, D. A. (2012a). A coarse-grid approach to representing building blockage effects in 2D urban flood modelling. *Journal of Hydrology* 426–427, 1–16.
- Chen, A. S., Evans, B., Djordjevic, S. & Savic, D. A. (2012b) Multi-layered coarse grid modelling in 2D urban flood simulations. *Journal of Hydrology* 470–471, 1–11.
- Cheng, M. Y., Tsai, H. C., & Sudjono, E. (2010). Conceptual cost estimates using evolutionary fuzzy hybrid neural network for projects in construction industry. *Expert Systems with Applications*, 37(6), 4224-4231.
- Chini, M., Pulvirenti, L., & Pierdicca, N., (2012). Analysis and interpretation of the COSMO-SkyMed observations of the 2011 Japan tsunami. *IEEE Geoscience and Remote Sensing Letters*, 9(3), 467-471.
- Chini, M., Papastergios, A., Pulvirenti, L., Pierdicca, N., Matgen, P., & Parcharidis, I., (2016, July). SAR coherence and polarimetric information for improving flood mapping. In *Geoscience and Remote Sensing Symposium (IGARSS), 2016 IEEE International* (pp. 7577-7580). IEEE.

Chow V. T., Maidment D. R., and Mays L.W., (1988), Applied Hydrology. McGraw- HillBook Co., New York. 1988. 572 PP.

Christelis, V., Bellos, V., & Tsakiris, G. (2016, July). Employing surrogate modelling for the calibration of a 2D flood simulation model. In *Sustainable Hydraulics in the Era of Global Change, Proceedings of 4th IAHR Congress, Liege, Belgium* (pp. 27-29).

Chuvieco, E., Aguado, I., Yebra, M., Nieto, H., Salas, J., Martín, M. P., ... & De La Riva, J. (2010). Development of a framework for fire risk assessment using remote sensing and geographic information system technologies. *Ecological Modelling*, 221(1), 46-58.

Cian, F., Marconcini, M., & Ceccato, P. (2018). Normalized Difference Flood Index for rapid flood mapping: Taking advantage of EO big data. *Remote sensing of environment*, 209, 712-730. Chuvieco, E., Aguado, I., Yebra, M., Nieto, H., Salas, J., Martín, M. P., ... & De La Riva, J., (2010). Development of a framework for fire risk assessment using remote sensing and geographic information system technologies. *Ecological Modelling*, 221(1), 46-58.

Cian, F., Marconcini, M., Ceccato, P., & Giupponi, C. (2018). Flood depth estimation by means of high-resolution SAR images and lidar data. *Natural Hazards & Earth System Sciences*, 18(11).

Coates, A., & Ng, A. Y. (2011). The importance of encoding versus training with sparse coding and vector quantization. In *Proceedings of the 28th international conference on machine learning (ICML-11)* (pp. 921-928).

Conesa García, C., Espín Sánchez, D., García Lorenzo, R., & Ruiz Álvarez, V. (2017). Las lluvias torrenciales e inundaciones de los días 17 y 18 de diciembre de 2016 en la Región de Murcia con particular incidencia en el área vertiente del Mar Menor. *Ingeniería del agua*, 21(4), 213-229.

Costabile, P.; Costanzo, C.; Macchione, F., (2012). Comparative analysis of overland flow models using finite volume schemes. *J. Hydroinform.*, 14, 122.

Cognard, A.-L., Loumagne, C., Normand, M., Olivier, P., Otle', C., Vidal- Madjar, D., Louahala, S. And Vidal, A., (1995), Evaluation of the ERS1/ Synthetic Aperture Radar capacity to estimate surface soil moisture: two year results over the Naizin watershed. *Water Resource Research*, 31, pp. 975–982.

Cunge, J., Holly, F.M. and Verwey, A., (1980). *Practical Aspects of Computational River Hydraulics*. Pitman Advanced Publishing Program, London, 420 pp.

D'Addabbo, A., Refice, A., Lovergine, F. P., & Pasquariello, G., (2017). DAFNE: A Matlab toolbox for Bayesian multi-source remote sensing and ancillary data fusion, with application to flood mapping. *Computers & Geosciences*.

de Almeida G.A.M., Bates P.D., Freer J. & Souvignet M., (2012). Improving the stability of a simple formulation of the shallow water equations for 2D flood modeling. *Water Resour Res*, 48. doi: 10.1029/2011WR011570.

de Almeida, G. A., Bates, P., & Ozdemir, H., (2018). Modelling urban floods at submetre resolution: challenges or opportunities for flood risk management. *Journal of Flood Risk Management*, 11, S855-S865.

Debbarma, S., Choudhury, P., Roy, P., & Kumar, R. (2019). Analysis of Precipitation Variability using Memory Based Artificial Neural Networks. *International Journal of Applied Metaheuristic Computing (IJAMC)*, 10(1), 29-42.

Defina, A., (2000). Two dimensional shallow flow equations for partially dry areas. *Water Resour. Res.* 36, 3251–3264. <http://dx.doi.org/10.1029/2000WR900167> .

Dewan AM, Yamaguchi Y., (2009). Land use and land cover change in Greater Dhaka, Bangladesh: using remote sensing to promote sustainable urbanization. *Appl Geogr.* 29:390401.

de Bruijn, J. A., de Moel, H., Jongman, B., Wagemaker, J., & Aerts, J. C., (2018). TAGGS: Grouping tweets to improve global geoparsing for disaster response. *Journal of Geovisualization and Spatial Analysis*, 2(1), 2.

De Zan, F., et. al., 2014. *IEEE Transactions on Geoscience and Remote Sensing*, 52, 418–425.

DHI, MIKE by DHI (2012b). MIKE 21 Flow Model, Hydrodynamic Module, Scientific Documentation. DHI, Denmark.

Di Baldassarre, G., Montanari, A., (2009). Uncertainty in river discharge observations: a quantitative analysis. *Hydrol. Earth Syst. Sci.* 13, 913e921.

Di Baldassarre, G., Schumann, G., Bates, P.D., Freer, J.E., Beven, K.J., (2010). Flood-plain mapping: a critical discussion of deterministic and probabilistic approaches. *Hydrol. Sci. J.* 55 (3), 364e376.

Dinku, T., Funk, C., Peterson, P., Maidment, R., Tadesse, T., Gadain, H., & Ceccato, P. (2018). Validation of the CHIRPS satellite rainfall estimates over eastern Africa. *Quarterly Journal of the Royal Meteorological Society*, 144, 292-312.

Dubois, P.C., Van Zyl, J. and Engman, T., (1995), Measuring soil moisture with imaging radars. *IEEE Transactions on Geoscience and Remote Sensing*, 33, pp. 915–926.

Domeneghetti, A., Vorogushyn, S., Castellarin, A., Merz, B., Brath, A., (2013). Probabilistic flood hazard mapping: effects of uncertain boundary conditions. *Hydrol. Earth Syst. Sci.* 17, 3127e3140.

- Dottori, F. & Todini, E. (2011). Developments of a flood inundation model based on the cellular automata approach: testing different methods to improve model performance. *Physics and Chemistry of the Earth* 36, 266–280.
- Dottori, F. & Todini, E. (2012). Testing a simple 2D hydraulic model in an urban flood experiment. *Hydrological Processes*. doi:10. 1002/hyp.9370.
- Dottori, F., Di Baldassarre, G., Todini, E., (2013). Detailed data is welcome, but with a pinch of salt: accuracy, precision, and uncertainty in flood inundation modeling. *Water Resour. Res.* 49, 6079e6085.
- Dorigo, W.A., Wanger, W., Roland, H., Sebastian, H., Christoph, P., Matthias, D., Mecklenburg, S., Peter, V.O., Robock, A., Tj, J., (2011). The International Soil Moisture Network: A data hosting facility for global in situ soil moisture measurements. *Hydrol. Earth Syst. Sci.* 15(5), 1675e1698.
- Dorigo, W.A., Gruber, A., De Jeu, R.A.M., Wanger, W., Stacke, T., Loew, A., Albergel, C., Brocca, L., Chung, D., Parinussa, R.M., et al., (2015). Evaluation of the ESA CCI soil moisture product using ground-based observations. *Remote Sens. Environ.* 162, 380e395.
- Dokka R K, (2006). Modern-day tectonic subsidence in coastal Louisiana. *Geology*, v.34, 281-284.
- Du, J.Y., Kimball, J.S., Jones, L.A., (2016). Passive microwave remote sensing of soil moisture based on dynamic vegetation scattering properties for AMSR-E. *IEEE Trans. Geosci. Remote Sens.* 54(1), 597e608.
- Entekhabi, D., Njoku, E.G., O'Neill, P.E., Kellogg, K.H., Crow, W.T., Edelstein, W.N., Entin, J.K., Goodman, S.D., Jackson, T.J., Johnson, J., et al., (2010). The soil moisture active passive (SMAP) mission. *Proc. IEEE* 98(5), 704e716.
- Falter, D., Vorogushyn, S., Lhomme, J., Apel, H., Gouldby, B., and Merz, B., (2013). Hydraulic model evaluation for large-scale flood risk assessments, *Hydrol. Process.*, 27, 1331–1340, doi:10.1002/hyp.9553.
- Fang X. & Su D., (2005). An integrated one-dimensional and twodimensional urban stormwater flood simulation model. *J Am Water Resour Assoc*, 42, (3), 713–724.
- Feyisa, G. L., Meilby, H., Fensholt, R., & Proud, S. R. (2014). Automated water extraction index: a new technique for surface water mapping using Landsat imagery. *Remote Sensing of Environment*, 140, 23-35.
- Ferrari A., Viero D.P., Vacondio R., Defina A., Mignosa P., (2019) Flood inundation modeling in urban areas: a mesh-independent anisotropic porosity approach, *Advances in Water Resources* 125 (2019) 98-113.
- Ferretti, A., Prati, C., & Rocca, F., (2001). Permanent scatterers in SAR interferometry. *IEEE Transactions on geoscience and remote sensing*, 39(1), 8-20.

- Ferretti, A., Fumagalli, A., Novali, F., Prati, C., Rocca, F. And Rucci, A., (2011). A New Algorithm for Processing Interferometric Data-Stacks: SqueeSAR. *IEEE T Geo-science and Remote Sensing, IEEE Transactions*, 49 (9), pp.3460-3470
- Fohringer, J., Dransch, D., Kreibich, H., & Schröter, K., (2015). Social media as an information source for rapid flood inundation mapping. *Natural Hazards and Earth System Sciences*, 15(12), 2725-2738.
- Franci F., Mandanici E. & Bitelli G., (2015). Remote sensing analysis for flood risk management in urban sprawl contexts, *Geomatics, Natural Hazards and Risk*, 6:5-7, 583-599, DOI: 10.1080/19475705.2014.913695
- Frazier PS, Page KJ., (2000). Water body detection and delineation with Landsat TM data. *Photogramm Eng Remote Sensing*. 66:1461-1468
- Fung, A.K., (1994), *Microwave Scattering and Emission Models and their Applications* (Norwood, MA: Artech House).
- Fung, A.K., Li, Z. and Chen, K.S., (1992), Backscattering from a randomly rough dielectric surface. *IEEE Transactions on Geoscience and Remote Sensing*, 30, pp. 356–369.
- Gallegos H.A., Schibert J.E. & Sanders B.F., (2009). Two-dimensional, high-resolution modeling of urban dam-break flooding: a case study of Balwin Hills, California. *Adv Water Resour*, 32, 1323–1335.
- Gallien T.W., Schibert J.E. & Sanders B.F., (2011). Predicting tidal flooding of urbanised embayments: a modeling framework and data requirements. *Coast Eng*, 58, 567–577.
- Gama, M.C., Popescu, I., Shengyang, L., Mynett, A., (2014). Modeling the inference between upstream inflow hydrographs and downstream flooded areas in a reservoir driven system. *Procedia - Social and Behavioral Sciences* 108, 207–218. <https://doi.org/10.1016/j.sbspro.2013.12.832>.
- Ghiglia D.C., Pritt. M.D., (1998). *Two-dimensional Phase Unwrapping: Theory, Algorithms, and Software* Wiley, New York .
- Ghimire, B., Chen, A. S., Djordjević, S. & Savić, D. A. (2011). Application of cellular automata approach for fast flood simulation. *CCWI: Computing and Control for the Water Industry*, 5–7 September 2011, University of Exeter, UK, Conference Proceedings.
- Giustarini, L., Hostache, R., Matgen, P., Schumann, G. J. P., Bates, P. D., & Mason, D. C., (2013). A change detection approach to flood mapping in urban areas using TerraSAR-X. *IEEE transactions on Geoscience and Remote Sensing*, 51(4), 2417-2430.
- Griffith, C. G., W. L. Woodley, P. G. Grube, D. W. Martin, J. Stout, and D. N. Sikdar, 1978: Rain estimation from geosynchronous satellite imagery- visible and infrared studies. *Mon. Wea. Rev.*, 106, 1153-1 171.

- Grigg, N. S., & Helweg, O. J. (1975). STATE-OF-THE-ART OF ESTIMATING FLOOD DAMAGE IN URBAN AREAS 1. *JAWRA Journal of the American Water Resources Association*, 11(2), 379-390.
- Grimaldi, S., Petroselli, A., Arcangeletti, E., Nardi, F., (2013). Flood mapping in ungauged basins using fully continuous hydrologic-hydraulic modeling. *J. Hydrol.* 487, 39e47.
- Guinot V., (2011). Multiple porosity shallow water models for macroscopic modelling of urban floods. *Adv Water Resour*, 37, 40–72.
- Haddad, K.; Rahman, A., (2012). Regional flood frequency analysis in eastern australia: Bayesian GLS regression-based methods within fixed region and ROI framework–quantile regression vs. Parameter regression technique. *J. Hydrol.*, 430, 142–161.
- Hayes DJ, Sader SA. (2001). Comparison of change-detection techniques for monitoring tropical forest clearing and vegetation regrowth in a time series. *Photogrammetry Eng Remote Sensing*. 67:10671075.
- Hanssen, R.F., Caro Cuenca, M., Klees, R., van der Marel, H., (2012). Decadal vertical deformation of the Netherlands via the geodetic integration of gravimetry, GNSS, leveling and SAR interferometry. In: AGU Fall Meeting Abstracts.
- Hartnack, J. N., Enggrob, H. G. & Rungø, M. (2009). 2D overland flow modelling using fine scale DEM with manageable runtimes. In: *Flood Risk Management: Research and Practice* (P. Samuels, S. Huntington, W. Allsop & J. Harrop, eds). Taylor & Francis Group, London, p. 30.
- Havas, C., Resch, B., Francalanci, C., Pernici, B., Scalia, G., Fernandez-Marquez, J. L., ... & Kirsch, B., (2017). E2mc: Improving emergency management service practice through social media and crowdsourcing analysis in near real time. *Sensors*, 17(12), 2766.
- Henonin, J., Russo, B., Mark, O., & Gourbesville, P. (2013). Real-time urban flood forecasting and modelling—a state of the art. *Journal of Hydroinformatics*, 15(3), 717-736.
- Ho, LTK, Umitsu, M & Yamaguchi, Y, (2010), 'Flood Hazard Mapping By Satellite Images And Srtm Dem In The Vu Gia - Thu Bon Alluvial Plain, Central Vietnam', *Int. Archives of the Photogrammetry, Remote Sensing and Spatial Information Science*, vol. XXXVIII, part 8, Kyoto Japan.
- Hooper, A. (2008). A multi-temporal Insar method incorporating both persistent scatterer and small baseline approaches. *Geophysical Research Letters*, 35(16), L16302. [HTTP://DX.DOI.ORG/10.1029/2008GL034654](http://dx.doi.org/10.1029/2008GL034654).
- Horritt, M., Bates, P., (2001). Effects of spatial resolution on a raster based model of flood flow. *J. Hydrol.* 253, 239–249. [http://dx.doi.org/10.1016/S0022-1694\(01\)00490-5](http://dx.doi.org/10.1016/S0022-1694(01)00490-5) .

Hou, J., Liang, Q., Zhang, H., & Hinkelmann, R. (2015). An efficient unstructured MUSCL scheme for solving the 2D shallow water equations. *Environmental Modelling & Software*, 66, 131-152.

Howe, J., (2006). The Rise of Crowdsourcing, <http://www.wired.com/wired/archive/14.06/crowds.html>.

Hu, Y, Huang, J, Du, Y, Han, P & Huang, W., (2015), 'Monitoring Spatial and Temporal Dynamics of Flood Regimes and Their Relation to Wetland Landscape Patterns in Dongting Lake from MODIS Time-Series Imagery', *Remote Sensing*, vol. 7, pp. 7494-7520. DOI:10.3390/rs70607494.

Hunter, N. M., Bates, P. D., Neelz, S., Pender, G., Villanueva, I., Wright, N. G., ... & Crossley, A. J., (2008). Benchmarking 2D hydraulic models for urban flood simulations. In *Proceedings of the institution of civil engineers: water management* (Vol. 161, No. 1, pp. 13-30). Thomas Telford (ICE publishing).

Jacks, E., Davidson, J., & Wai, H. G. (2010). *Guidelines on early warning systems and application of nowcasting and warning operations*. World Meteorological Organization.

Jameson, A., Schmidt, W., & Turkel, E. (1981, June). Numerical solution of the Euler equations by finite volume methods using Runge Kutta time stepping schemes. In *14th fluid and plasma dynamics conference* (p. 1259).

Jerrentzup H (1992). The fauna of Lake Kerkini. In: Gerakis P A, ed. Conservation and Management of Greek Wetlands. Proceedings of a Greek Wetlands Workshop, Thessaloniki, Greece, 1989, IUCN, Gland, Switzerland.

Joyce, R.J.; Janowiak, J.E.; Arkin, P.A.; Xie, P. Cmorph, (2003). A method that produces global precipitation estimates from passive microwave and infrared data at high spatial and temporal resolution. *J. Hydrometeorol.* 5, 287–296.

Joyce, R. J., Janowiak, J. E., Arkin, P. A., & Xie, P. (2004). CMORPH: A method that produces global precipitation estimates from passive microwave and infrared data at high spatial and temporal resolution. *Journal of Hydrometeorology*, 5(3), 487-503.

Jung, Y., Merwade, V., (2015). Estimation of uncertainty propagation in flood inundation mapping using a 1-D hydraulic model. *Hydrol. Process.* 29 (4), 624e640.

Kalinga, O.A.; Gan, T.Y., (2010). Estimation of rainfall from infrared-microwave satellite data for basin-scale hydrologic modelling. *Hydrol. Process.* 24, 2068–2086.

Kalteh, A. M., Hjorth, P., & Berndtsson, R. (2008). Review of the self-organizing map (SOM) approach in water resources: Analysis, modelling and application. *Environmental Modelling & Software*, 23(7), 835-845.

Kar, A.K.; Lohani, A.K.; Goel, N.K.; Roy, G.P., (2010). Development of flood forecasting system using statistical and ANN techniques in the downstream catchment of mahanadi basin, india. *J. Water Resour. Prot.* 2, 880.

Karydakakis A, Arvanitis A, Andritsos N, Fytikas M (2005). Low enthalpy geothermal fields in the Strymon Basin (Northern Greece). In: Proceedings World Geothermal Congress 2005 Antalya, Turkey, 24–29 April, 2005

Kerr, Y.H., Waldteufel, P., Richaume, P., Wigneron, J.P., Ferrazzoli, P., Mahmoodi, A., Al, B.A., Cabot, F., Gruhier, C., Juglea, S.E., et al., (2012). The SMOS soil moisture retrieval algorithm. *IEEE Trans. Geosci. Remote Sens.* 50(5), 1384e1403.

Khan I. (2000). Temporal mapping and spatial analysis of land transformation due to urbanization and its impact on surface water system: a case from Dhaka metropolitan area, Bangladesh. *Int Arch Photogrammetry Remote Sensing.* XXXIII:598-605.

Khonder, M.U.H., Wilson, G. and Klinting, A. (1998) “Application of neural networks in real time flash flood forecasting”. In Babovic, V. and Larsen, C.L. (eds.) Proceedings of the Third International Conference on HydroInformatics, A.A.Balkema: Rotterdam, pp. 777-782

Kidd, C.; Kniveton, D.R.; Todd, M.C.; Bellerby, T.J., (2004). Satellite rainfall estimation using combined passive microwave and infrared algorithms. *J. Hydrometeorol.*, 4, 1088.

Kidd, C.; Levizanni, V. Status of satellite precipitation retrievals, (2009). In Proceedings of the Earth Observation and Water Cycle Science, Frascati, Italy, 18–20 November 2009.

Kim, H. I., Keum, H. J., & Han, K. Y. (2019). Real-Time Urban Inundation Prediction Combining Hydraulic and Probabilistic Methods. *Water*, 11(2), 293.

Kim, S. H., & Boukouvala, F. (2019). Machine learning-based surrogate modeling for data-driven optimization: a comparison of subset selection for regression techniques. *Optimization Letters*, 1-22.

Klemas, V. (2014). Remote sensing of floods and flood-prone areas: an overview. *Journal of Coastal Research*, 31(4), 1005-1013.

Klemm H, Quseimi I, Novali F, Ferretti A, Tamburini A, (2010). Monitoring horizontal and vertical surface deformation over a hydrocarbon reservoir by PSInSAR. First break volume 28.

Kneale, P. E., See, L., & Smith, A. (2001, September). Towards defining evaluation measures for neural network forecasting models. In *Proceedings of the Sixth International Conference on GeoComputation, University of Queensland, Australia, available at <http://www.geocomputation.org>.*

Kolassa, J., Gentine, P., Prigent, C., Aires, F., (2016). Soil moisture retrieval from AMSR-E and ASCAT microwave observation synergy, Part 1: Satellite data analysis. *Remote Sens. Environ.* 173, 1e14.

Kolassa, J., Reichle, R.H., Draper, C.S., (2017). Merging active and passive microwave observations in soil moisture data assimilation. *Remote Sens. Environ.* 191, 117 e 130.

- Kotsiantis, S. B., Zaharakis, I., & Pintelas, P. (2007). Supervised machine learning: A review of classification techniques. *Emerging artificial intelligence applications in computer engineering*, 160, 3-24.
- Kroll, C.N.; Vogel, R.M., (2002). Probability distribution of low streamflow series in the united states. *J. Hydrol. Eng.*, 7, 137–146.
- Kubal, C., Haase, D., Meyer, V., & Scheuer, S. (2009). Integrated urban flood risk assessment—adapting a multicriteria approach to a city. *Natural hazards and earth system sciences*, 9(6), 1881-1895.
- Kühnlein, M.; Appelhans, T.; Thies, B.; Nauss, T., (2014). Improving the accuracy of rainfall rates from optical satellite sensors with machine learning—A random forests-based approach applied to msg seviri. *Remote Sens. Environ.* 141, 129–143.
- Irwin, K., Beaulne, D., Braun, A., & Fotopoulos, G., (2017). Fusion of SAR, Optical Imagery and Airborne LiDAR for Surface Water Detection. *Remote Sensing*, 9(9), 890.
- Lai, J. S., Guo, W. D., Lin, G. F., & Tan, Y. C. (2010). A well-balanced upstream flux-splitting finite-volume scheme for shallow-water flow simulations with irregular bed topography. *International journal for numerical methods in fluids*, 62(8), 927-944.
- Leandro, J., Chen, A. S., Djordjević, S., & Savić, D. A., (2009). Comparison of 1D/1D and 1D/2D coupled (sewer/surface) hydraulic models for urban flood simulation. *Journal of hydraulic engineering*, 135(6), 495-504.
- Le Hegrat-Masclé, S., Zribi, M., Alem, F., Weisse, A. And Loumagne, C., (2002), Soil moisture estimation from ERS/SAR data: Toward an operational methodology. *IEEE Transactions on Geoscience and Remote Sensing*, 40, pp. 1–12.
- LeVeque, R. J. (1998). Balancing source terms and flux gradients in high-resolution Godunov methods: the quasi-steady wave-propagation algorithm. *Journal of computational physics*, 146(1), 346-365.
- LeVeque, R. J. (2002). *Finite volume methods for hyperbolic problems* (Vol. 31). Cambridge university press.
- LeVeque, R. J. (2004). Finite volume methods for hyperbolic problems. *Meccanica*, 39(1), 88-89.
- Levizzani, V.; Schmetz, J.; Lutz, H.J.; Kerkmann, J.; Alberoni, P.P.; Cervino, M., (2001). Precipitation estimations from geostationary orbit and prospects for meteosat second generation. *Meteorol. Appl.* **2001**, 8, 23–41.
- Li, J. and Heap, A. D., (2014). Spatial interpolation methods applied in the environmental sciences: a review, *Environ. Modell. Softw.*, 53, 173–189, doi:10.1016/j.envsoft.2013.12.008.

- Li, Z., Wang, C., Emrich, C. T., & Guo, D., (2018). A novel approach to leveraging social media for rapid flood mapping: a case study of the 2015 South Carolina floods. *Cartography and Geographic Information Science*, 45(2), 97-110.
- Li, L.; Xu, H.; Chen, X.; Simonovic, S., (2010). Streamflow forecast and reservoir operation performance assessment under climate change. *Water Resour. Manag.* 2010, 24, 83.
- Liand Q., Borthwick A. G. L. and Stelling G., (2014). Simulation of dam and dyke-break hydrodynamics on dynamically adaptive quadtree grids. *Int. J. Num. Meth. Fluids*, 46: 127-162.
- Lillesand, T., Kiefer, R. W., & Chipman, J., (2014). *Remote sensing and image interpretation*. John Wiley & Sons.
- Lin, C. T., & Lee, I. F. (2009). Artificial intelligence diagnosis algorithm for expanding a precision expert forecasting system. *Expert systems with applications*, 36(4), 8385-8390.
- Lindell, D.B., Long, D.G., (2016). High-resolution soil moisture retrieval with ASCAT. *IEEE Geosci. Remote Sens. Lett.* 13(7), 972e976. <https://doi.org/10.1109/LGRS.2016.2557321>.
- Liu, Y.Y., Dorigo, W.A., Parinussa, R.M., de Jeu, R.A.M., Wagner, W., McCabe, M.F., Evan, J.P., van Dijk, A.I.J.M., (2012). Trend-preserving blending of passive and active microwave soil moisture retrievals. *Remote Sens. Environ.* 123, 280e297.
- Liu, X., Sahli, H., Meng, Y., Huang, Q., & Lin, L., (2017). Flood Inundation Mapping from Optical Satellite Images Using Spatiotemporal Context Learning and Modest AdaBoost. *Remote Sensing*, 9(6), 617.
- Lippmann, R. P., Gold, B., & Malpass, M. L. (1987). *A comparison of Hamming and Hopfield neural nets for pattern classification* (No. TR-769). MASSACHUSETTS INST OF TECH LEXINGTON LINCOLN LAB.
- Malinowski, R, Groom, G, Schwanghart, W & Heckrath, G, (2015), 'Detection and Delineation of Localized Flooding from WorldView-2 Multispectral Data', *Remote Sensing*, vol. 7, pp. 14853-14875. DOI:10.3390/rs71114853.
- Mandlbürger, G., Hauer, C., Höfle, B., Habersack, H., and Pfeifer, N., (2009). Optimisation of LiDAR derived terrain models for river flow modelling, *Hydrol. Earth Syst. Sci.*, 13, 1453–1466, doi:10.5194/hess-13-1453-2009.
- Manunta M, Marsella M, Zeni G, Sciotti M, Atzori S, Lanari R, (2008). Two-scale surface deformation analysis using the SBAS-DInSAR technique: a case study of the city of Rome, Italy. *International Journal of Remote Sensing*, 29, 6,1665-1684.

- Maksimovic C., Prodanovic D., Boonya-Aroonnet S., Leitao J.P., Djordjevic S. & Allitt R., (2009). Overland flow and pathway analysis for modelling of urban pluvial flooding. *J Hydraul Res* 2009, 47, 512–523.
- Maktav D, Erbek FS, Jurgens C., (2005). Remote sensing of urban areas. *Int J Remote Sensing*.
- Marqués, J. M. F., (2000) Introduction to the Finite Volumes Method. Application to the Shallow Water Equations.
- Martinis, S., Fissmer, B., & Rieke, C. (2015, July). Time series analysis of multi-frequency SAR backscatter and bistatic coherence in the context of flood mapping. In *2015 8th International Workshop on the Analysis of Multitemporal Remote Sensing Images (Multi-Temp)* (pp. 1-4). IEEE.
- Mark O., Weesakul S., Apirumanekul C., Boonya-Aroonnet S. & Djordjevic S., (2004). Potential and limitations of 1D modelling of urban flooding. *J Hydrol*, 299, 284–299.
- Massonnet D & Feigl K L, (1998). Radar interferometry and its application to changes in the Earth's surface. *Rev. Geophys.*, 36, 441-500.
- Mazzoleni M., Bacchi B., Barontini S., Di Baldassarre G., Pilotti M., Ranzi R., (2013). Flooding hazard mapping in floodplain areas affected by piping breaches in the Po River, Italy, *Journal of Hydrologic*.
- MacEachren, A. M., Jaiswal, A., Robinson, A. C., Pezanowski, S., Savelyev, A., Mitra, P., Zhang, X., and Blanford, J., (2011). Sense-Place2: GeoTwitter analytics support for situational awareness, in: 2011 IEEE Conference on Visual Analytics Science and Technology (VAST), Providence, Rhode Island, USA, doi:10.1109/VAST.2011.6102456, 181–190.
- Mcfeeters, S.K., (1996). The use of normalized difference water index (NDWI) in the delineation of open water features. *International Journal of Remote Sensing*, 17, pp. 1425
- McMillan, H., Brasington, J., (2007). Reduced complexity strategies for modelling urban floodplain inundation. *Geomorphology* 90, 226–243. <http://dx.doi.org/10.1016/j.geomorph.2006.10.031> .
- Meert, P., Pereira, F., Willems, P., 2016. Computationally efficient modelling of tidal rivers using conceptual reservoir-type models. *Environ. Model. Software* 77, 19–31. <https://doi.org/10.1016/j.envsoft.2015.11.010>.
- Mignot, E., Paquier, A., & Haider, S., (2006). Modeling floods in a dense urban area using 2D shallow water equations. *Journal of Hydrology*, 327(1), 186-199.
- Mingham C. G. and Causon D. M., (1998). A high resolution finite volume method for the shallow water equations. *J. Hydraul. Eng., ASCE*, 124(6): 605-614.
- Minns, A.W. and Hall, M.J. (1996) "Artificial neural networks as rainfall-runoff models", *Hydrological Sciences Journal*, vol. 41, pp. 399-417.

- Mishra, P., Pilli, E. S., Varadharajan, V., & Tupakula, U. (2017). Intrusion detection techniques in cloud environment: A survey. *Journal of Network and Computer Applications*, 77, 18-47.
- Molinaro P., Di Filippo A. & Ferrari F., (1994). Modelling of flood wave propagation over flat dry areas of complex topography in presence of different infrastructures. In: Proceedings of Specialty Conference on Modelling of Flood Propagation over Initially Dry Areas, Milan, 209–225.
- Morstatter, F., Kumar, S., Liu, H., and Maciejewski, R., (2013). Understanding twitter data with TweetXplorer, in: Proceedings of the 19th ACM SIGKDD International Conference on Knowledge Discovery and Data Mining, KDD '13, ACM, New York, NY, USA, 1482–1485, doi:10.1145/2487575.2487703.
- Mukherjee, N. R., & Samuel, C. (2016). ASSESSMENT OF THE TEMPORAL VARIATIONS OF SURFACE WATER BODIES IN AND AROUND CHENNAI USING LANDSAT IMAGERY. *Indian Journal of Science and Technology*, 9(18).
- Neal, J., Odoni, N., Trigg, M., Freer, J., Garcia-Pintado, J., Mason, D., Wood, M., Bates, P., (2015). Efficient incorporation of channel cross-section geometry uncertainty into regional and global scale flood inundation models. *J. Hydrol.* 529, 169–183. <http://dx.doi.org/10.1016/j.jhydrol.2015.07.026> .
- Neal, J., Schumann, G., Bates, P., (2012). A subgrid channel model for simulating river hydraulics and floodplain inundation over large and data sparse areas. *Water Resour. Res.* 48, W11506. <http://dx.doi.org/10.1029/2012WR012514> .
- Njoku, E.G., Li, L., (1999). Retrieval of land surface parameters using passive microwave measurements at 6-18 GHz. *IEEE Trans. Geosci. Remote Sens.* 37(1), 79e93. <https://doi.org/10.1109/36.739125>.
- Njoku, E.G., Jackson, T.J., Lakshmi, V., Chan, T.K., Nghiem, S.V., (2003). Soil moisture retrieval from AMSR-E. *IEEE Trans. Geosci. Remote Sens.* 41(2), 215e229.
- OH, Y., SARABANDI, K. and ULABY, F.T., (1992). An empirical model and an inversion technique for radar scattering from bare soil surfaces. *IEEE Transactions on Geoscience and Remote Sensing*, 30, pp. 370–381.
- Omranian, E., & Sharif, H. O. (2018). Evaluation of the global precipitation measurement (GPM) satellite rainfall products over the lower Colorado River basin, Texas. *JAWRA Journal of the American Water Resources Association*, 54(4), 882-898.
- Paloscia, S., Macelloni, G., Santi, E., Koike, T., (2001). A multifrequency algorithm for the retrieval of soil moisture on a large scale using microwave data from SMMR and SSM/I satellites. *IEEE Trans. Geosci. Remote Sens.* 39(8), 1655e1661.
- Pan, M.; Li, H.; Wood, E., (2010). Assessing the skill of satellite-based precipitation estimates in hydrologic applications. *Water Resour. Res.* 2010, 46, 201–210.

- Parinussa, R.M., Wang, G., Holmes, T.R.H., Liu, Y., Dolman, A.J., de Jeu, R., Jiang, T., Zhang, P., Shi, J., (2014). Global surface soil moisture from the Microwave Radiation Imager onboard the Fengyun-3B satellite. *Int. J. Remote Sens.* 35(19), 7007e7029.
- Parinussa, R.M., Holmes, T.R., Wanders, N., Dorigo, W.A., de Jeu, R.A., (2015). A preliminary study toward consistent soil moisture from AMSR2. *J. Hydrometeorol.* 16(2), 932e947
- Perrou, T., Garioud, A., & Parcharidis, I. (2018). Use of Sentinel-1 imagery for flood management in a reservoir-regulated river basin. *Frontiers of Earth Science*, 12(3), 506-520.
- Piles, M., Petropoulos, G.P., Sanchez, N., Gonzalez-Zamora, A., Ireland, G., (2016). Towards improved spatio-temporal resolution soil moisture retrievals from the synergy of SMOS and MSG SEVIRI spaceborne observations. *Remote Sens. Environ.* 180, 403e417.
- Pinos, J., & Timbe, L. (2019). Performance assessment of two-dimensional hydraulic models for generation of flood inundation maps in mountain river basins. *Water Science and Engineering*, 12(1), 11-18.
- Pluto-Kossakowska, J., Łoś, H., Osińska-Skotak, K., & Beata, W. (2017, September). The concept of SAR satellite data use for flood risk monitoring in Poland. In *2017 Signal Processing Symposium (SPSymposium)* (pp. 1-5). IEEE.
- Poser, K., & Dransch, D., (2010). Volunteered geographic information for disaster management with application to rapid flood damage estimation. *Geomatica*, 64(1), 89-98.
- Prevot, L., Dechambre, M., Taconet, O., Vidal-Madjar, D., Normand, M. And Galle, S., (1993). Estimating the characteristics of vegetation canopies with airborne radar measurements. *International Journal of Remote Sensing*, 14, pp. 2803–2818.
- Prieto, M. S., & Allen, A. R. (2009). Using self-organising maps in the detection and recognition of road signs. *Image and Vision Computing*, 27(6), 673-683.
- Proust, S., Bousmar, D., Riviere, N., Paquier, A., Zech, Y., (2010). Energy losses in compound open channels. *Adv. Water Resour.* 33, 1e16.
- Psilovikos A, Papafilippou-Pennou E, Albanakis K, Vouvalidis K (1994). Bedload transport and deposition in the river Strymon artificial channel before its reach to the Kerkini reservoir. *Bulletin of Geological Society of Greece*, XXX(4): 149–155
- Pulvirenti, L., Chini, M., Pierdicca, N., & Boni, G., (2016). Use of SAR data for detecting floodwater in urban and agricultural areas: The role of the interferometric coherence. *IEEE Transactions on Geoscience and Remote Sensing*, 54(3), 1532-1544.

Quesney, A., Le He´Garat-Masclé, S., Taconet, O., Vidal-Madjar, D., Wigneron, J.P., Loumagne, C. And Normand, M., (2000), Estimation of watershed soil moisture index from ERS/SAR data. *Remote Sensing of Environment*, 72, pp. 290–303.

Raspini, F., Loupasakis, C., Rozos, D., Adam, N. And Moretti, S., (2014) - Ground subsidence phenomena in the Delta municipality region (Northern Greece): Geotechnical modelling and validation with Persistent Scatterer Interferometry. *International Journal of Applied Earth Observation and Geoinformation*, Vol. 28, pp 78-89

Ratto, M., Castelletti, A., Pagano, A., (2012). Emulation techniques for the reduction and sensitivity analysis of complex environmental models. *Environ. Model. Software* 34, 1–4. <https://doi.org/10.1016/j.envsoft.2011.11.003>.

Razavi, S., Tolson, B.A., Burn, D.H., (2012a). Numerical assessment of metamodeling strategies in computationally intensive optimization. *Environ. Model. Software* 34, 67–86. <https://doi.org/10.1016/j.envsoft.2011.09.010>.

Razavi, S., Tolson, B.A., Burn, D.H., (2012b). Review of surrogate modeling in water resources. *Water Resour. Res.* 48, 559. <https://doi.org/10.1029/2011WR011527>.

Refice, A., Capolongo, D., Pasquariello, G., D’Addabbo, A., Bovenga, F., Nutricato, R., ... & Pietranera, L., (2014). SAR and InSAR for flood monitoring: Examples with COSMO-SkyMed data. *IEEE Journal of Selected Topics in Applied Earth Observations and Remote Sensing*, 7(7), 2711-2722.

Reichle, R., De Lannoy, G., Liu, Q., Ardizzone, J., Kimball, J., Koster, R., (2016). SMAP Level 4 surface and root zone soil moisture. In: *Proceedings of the 2016 IEEE International Geoscience and Remote Sensing Symposium (IGARSS)*. IEEE, Beijing, pp. 136e138.

Richards, J. A., Woodgate, P. W., & Skidmore, A. K., (1987). An explanation of enhanced radar backscattering from flooded forests. *International Journal of Remote Sensing*, 8(7), 1093-1100.

Rodríguez-Fernández, N.J., Aires, F., Richaume, P., Kerr, Y.H., Prigent, C., Kolassa, J., Cabot, F., Jimenez, C., Mahmoodi, A., Drusch, M., (2016). Long term global surface soil moisture fields using an SMOS-trained neural network applied to AMSR-E data. *Rem. Sens.* 8(11), 959. <https://doi.org/10.1109/TGRS.2015.2430845>.

Roe, P. L. (1981). Approximate Riemann solvers, parameter vectors, and difference schemes. *Journal of computational physics*, 43(2), 357-372.

- Rogstadius, J., Kostakos, V., and Laredo, J., (2011). Towards real-time emergency response using crowd supported analysis of social media, in: Proceedings of CHI Workshop on Crowdsourcing and Human Computation, Systems, Studies and Platforms, Vancouver, British Columbia, Canada, 1–3.
- Royapoor, M., & Roskilly, T. (2015). Building model calibration using energy and environmental data. *Energy and Buildings*, 94, 109-120.
- Rosen P A, Hensley S, Joughin I R, Li F K, Madsen S N, Rodriguez E, Goldstein R M, (2000). Synthetic aperture radar interferometry. *Proc. I.E.E.E.*, 88 (3), 333-382.
- Rosser, J. F., Leibovici, D. G., & Jackson, M. J., (2017). Rapid flood inundation mapping using social media, remote sensing and topographic data. *Natural Hazards*, 87(1), 103-120.
- Rumelhart, D.E., Hinton, G.E. and Williams, R.J. (1986) "Learning internal representation by error propagation". In D.E. Rumelhart, J.L. McClelland (eds.) *Parallel Distributed Processing: Explorations in the Microstructure of Cognition*, Vol.1. MIT Press: Cambridge MA, pp. 318-362.
- Rujoiu-Mare, M. R., & Mihai, B. A., (2016). Mapping land cover using remote sensing data and GIS techniques: A case study of Prahova Subcarpathians. *Procedia Environmental Sciences*, 32, 244-255.
- Sadeghi, H. R., & Henrich, V. E. (1984). SMSI in Rh/TiO₂ model catalysts: Evidence for oxide migration. *Journal of Catalysis*, 87(1), 279-282.
- Saint-Geours, N., Bailly, J.-S., Grelot, F., Lavergne, C., 2014. Multi-scale spatial sensitivity analysis of a model for economic appraisal of flood risk management policies. *Environ. Model. Software* 60, 153–166. <https://doi.org/10.1016/j.envsoft.2014.06.012>.
- Syrides G (2000). Neogene marine cycles in Strymon basin, Macedonia, Greece. *Geological Society of Greece, Special Publications in: Proceedings Interim Colloquim RCMNS, Patras, Greece, May 1988*, 217–225
- Sommer S, Hill J, Me'gier J (1998). The potential of remote sensing for monitoring rural land use changes and their effects on soil conditions. *Agriculture Ecosystems and Environment*, 67: 197–209
- Sanders B. Integration of a shallow water model with a local time step, (2008). *J Hydraul Res*, 46, (4), 466–475. doi: 10.3826/jhr.2008.3243.
- Sanders, B., Schubert, J., Gallegos, H., (2008). Integral formulation of shallow-water equations with anisotropic porosity for urban flood modeling. *J. Hydrol.* 362, 19–38. <http://dx.doi.org/10.1016/j.jhydrol.2008.08.009>.
- Sanyal, J., & Lu, X. X. (2004). Application of remote sensing in flood management with special reference to monsoon Asia: a review. *Natural Hazards*, 33(2), 283-301.

- Sakaki, T., Okazaki, M., and Matsuo, Y., (2010). Earthquake shakes twitter users: real-time event detection by social sensors, in: Proceedings of the 19th International Conference on World-WideWeb, WWW'10, ACM, New York, NY, USA, 851–860, doi:10.1145/1772690.1772777.
- Scalia, G., (2017). Network-based content geolocation on social media for emergency management.
- Schowengerdt, R. A., (2012). Techniques for image processing and classifications in remote sensing. Academic Press.
- Schumann, G., Bates, P. D., Horritt, M. S., Matgen, P., & Pappenberger, F., (2009). Progress in integration of remote sensing–derived flood extent and stage data and hydraulic models. *Reviews of Geophysics*, 47(4).
- Shaker, A, Yan, WY & El-Ashmawy, N, (2012). 'Panchromatic Satellite Image Classification for Flood Hazard Assessment', *Journal of Applied Research and Technology*, vol. 10, pp. 902-910.
- Shi, J., Wang, J., Hsu, A.Y., O'Neill, P.E. And Engmann, T., (1997). Estimation of bare surface soil moisture and surface roughness parameter using L-band SAR image data. *IEEE Transactions on Geoscience and Remote Sensing*, 35, pp. 1254–1265.
- Scipal, K., Drusch, M., & Wagner, W. (2008). Assimilation of a ERS scatterometer derived soil moisture index in the ECMWF numerical weather prediction system. *Advances in water resources*, 31(8), 1101-1112.
- Singh, A. (1989). Review article digital change detection techniques using remotely-sensed data. *International journal of remote sensing*, 10(6), 989-1003.
- Smith, J. and Eli, R.N. (1995) "Neural network models of rainfall-runoff process", *Journal of Water Resources Planning and Management*, vol.121, pp. 499-509.
- Smith, L., Liang, Q., James, P., & Lin, W., (2017). Assessing the utility of social media as a data source for flood risk management using a real-time modelling framework. *Journal of Flood Risk Management*, 10(3), 370-380.
- Soares-Frazao S., Lhomme J., Guinot V. & Zech Y., (2008). Two dimensional shallow-water model with porosity for urban flood modeling. *J Hydraul Res*, 46, (1), 45–64.
- Song, C., Jia, L., (2016). A method for downscaling FengYun-3B soil moisture based on apparent thermal inertia. *Rem. Sens.* 8(9). <https://doi.org/10.3390/rs8090703>.
- Sowter, A., Bateson, L., Strange, P., Ambrose, K., And Fifik Syafiudin M., (2013). DInSAR estimation of land motion using intermittent coherence with application to the South Derbyshire and Leicestershire coalfields. *Remote Sensing Letters* 4(10): 979-987.

- Stancalie, G., Craciunescu, V., & Irimescu, A. (2007). Contribution of Earth observation data supplied by the new satellite sensors in flood risk mapping. *IAHS PUBLICATION*, 316, 56.
- Shepherd, A.J. (1997) *Second-Order Methods for Neural Networks*. Springer-Verlag Limited: London.
- Stramondo S, Saroli M, Tolomei C, Moro M, Doumaz F, Pesci A, Loddo F, Baldi P, Boschi E, (2007). Surface movements in Bologna (Po Plain — Italy) detected by multitemporal DInSAR. *Remote Sensing of Environment*.
- Stramondo S, Bozzano F, Marra F, Wegmuller U, Cinti F R, Moro M, Saroli M, (2008). Subsidence induced by urbanisation in the city of Rome detected by advanced InSAR technique and geotechnical investigations. *Remote Sensing of Environment*, 112, 3160–3172.
- Solomatine, D. P., & Ostfeld, A. (2008). Data-driven modelling: some past experiences and new approaches. *Journal of hydroinformatics*, 10(1), 3-22.
- Sousa, J. J., Ruiz, A. M., Hanssen, R. F., Bastos, L., Gil, A. J., Galindo-Zaldívar, J., & Sanz De Galdeano, C. (2010). PS-InSAR processing methodologies in the detection of field surface deformation—Study of the Granada basin (Central Betic Cordilleras, southern Spain). *Journal of Geodynamics*, 49(3), 181-189.
- Stephens, G.L.; Vane, D.G.; Tanelli, S.; Im, E.; Durden, S.; Rokey, M.; Reinke, D.; Partain, P.; Mace, G.G., (2008). Austin, R. Cloudsat mission: Performance and early science after the first year of operation. *J. Geophys. Res. Atmos.* 2008, 113, 2036–2044.
- Stenz, R.; Dong, X.; Xi, B.; Feng, Z.; Kuligowski, R.J., (2015). Improving satellite quantitative precipitation estimation using goes-retrieved cloud optical depth. *J. Hydrometeorol.* 2015, 17.
- Sulaiman, J.; Wahab, S.H., (2018). Heavy rainfall forecasting model using artificial neural network for flood prone area. In *It Convergence and Security 2017*; Springer: Singapore, 2018; pp. 68–76.
- Sun, W., Sun, Y., Li, X., Wang, T., Wang, Y., Qiu, Q., & Deng, Z. (2018). Evaluation and Correction of GPM IMERG Precipitation Products over the Capital Circle in Northeast China at Multiple Spatiotemporal Scales. *Advances in Meteorology*, 2018.
- Sylaios G K, Kamidis N, Tsihrintzis V A (2010). Impact of river damming on coastal stratification–mixing processes: the cases of Strymon and Nestos Rivers, N. Greece. *Desalination*, 250(1): 302–312
- Skakun, S., (2012). ‘The Use Of Time-Series Of Satellite Data To Flood Risk Mapping’, *International Journal Information Models and Analyses* vol.1, pp. 260-270.
- Takada Y & Fukushima Y, (2013). Volcanic subsidence triggered by the 2011 Tohoku earthquake in Japan. *Nature Geoscience*, 6, 637–641.

- Tan, M. L., & Santo, H. (2018). Comparison of GPM IMERG, TMPA 3B42 and PERSIANN-CDR satellite precipitation products over Malaysia. *Atmospheric research*, 202, 63-76.
- Tang, L.; Hossain, F., (2012). Investigating the similarity of satellite rainfall error metrics as a function of köppen climate classification. *Atmos. Res.* 2012, 104–105, 182–192.
- Teatini, P., Tosi, L., Strozzi, T., Carbognin, L., Cecconi, G., Rosselli, R., & Libardo, S., (2012). Resolving land subsidence within the Venice lagoon by persistent scatterer SAR interferometry. *Physics and Chemistry of the Earth, Parts A/B/C*, 40, 72-79.
- Thompson, S.A. *Hydrology for Water Management*; CRC Press: Boca Raton, FL, USA, 2017.
- Tomas R, Marquez Y, Lopez-Sanchez J M, Delgado J, Blanco P, Mallorquí J J, Martínez M, Herrera G, Mulas J, (2005). Mapping ground subsidence induced by aquifer overexploitation using advanced Differential SAR Interferometry: Vega Media of the Segura River (SE Spain) case study. *Remote Sensing of Environment*, 98, 269 – 283.
- Tomas, R., Herrera. G., Lopez-Sanchez, J.M., Et Al., (2010). Study of the land subsidence in the Orihuela city (SE Spain) using PSI data: distribution, evolution and correlation with conditioning and triggering factors. *Engineering Geology*, 115, 105–121.
- Topp, G. C., Davis, J. L., & Annan, A. P. (1980). Electromagnetic determination of soil water content: Measurements in coaxial transmission lines. *Water resources research*, 16(3), 574-582.
- Tosi, M., Correa, O. S., Soria, M. A., Vogrig, J. A., Sydorenko, O., & Montecchia, M. S. (2016). Land-use change affects the functionality of soil microbial communities: A chronosequence approach in the Argentinian Yungas. *Applied soil ecology*, 108, 118-127.
- Toro E. F., (2001). *Shock-capturing methods for free-surface shallow flows*. Chichester, John Wiley & Sons.
- Toro, E. F. (2016). The Riemann problem: solvers and numerical fluxes. In *Handbook of Numerical Analysis* (Vol. 17, pp. 19-54). Elsevier.
- Tovey N & Paul M, (2002). Modelling self-weight consolidation in holocene sediments. *Bull. Eng. Geol. Env*, 61, 21-33.
- Tsoukalas, I., Kossieris, P., Efstratiadis, A., Makropoulos, C., 2016. Surrogate-enhanced evolutionary annealing simplex algorithm for effective and efficient optimization of water resources problems on a budget. *Environ. Model. Software* 77, 122–142. <https://doi.org/10.1016/j.envsoft.2015.12.008>.

- Tsoukalas, I., Makropoulos, C., 2015. Multiobjective optimisation on a budget: Exploring surrogate modelling for robust multi-reservoir rules generation under hydrological uncertainty. *Environ. Model. Software* 69, 396–413. <https://doi.org/10.1016/j.envsoft.2014.09.023>.
- Turk, M., & Pentland, A. (1991). Eigenfaces for recognition. *Journal of cognitive neuroscience*, 3(1), 71-86.
- Ulaby, F.T., Aslam, A. and Dobson, M.C., (1982). Effects of vegetation cover on the radar sensitivity to soil moisture. *IEEE Transactions on Geoscience and Remote Sensing*, 20, pp. 476–481.
- Ulaby, F.T., Moore, R.K. and Fung, A.K., (1986), *Microwave Remote Sensing Active and Passive* (Norwood, MA: Artech House).
- Vacondio, R., Dal Palù, A., Mignosa, P., GPU-enhanced Finite Volume Shallow Water solver for fast flood simulations, *Environmental Modelling & Software* (2014), Volume 57, July 2014, Pages 60-75. ISSN:1364-8152. <http://dx.doi.org/10.1016/j.envsoft.2014.02.003>.
- Vacondio R., Dal Palù A., Ferrari A., Mignosa P., Aureli F., Dazzi S., (2017), A non-uniform efficient grid type for GPU-parallel Shallow Water Equations models, *Environmental Modelling & Software* 88.
- Van Asselen S, (2011). The contribution of peat compaction to total basin subsidence: implications for the provision of accommodation space in organic-rich deltas. *Basin Research*, 23, 239–255.
- Van der Schalie, R., De Jeu, R., Parinussa, R., Rodriguez-Fernandez, N., Kerr, Y., Al-Yaari, A., Wigneron, J.-P., Drusch, M., (2018). The effect of three different data fusion approaches on the quality of soil moisture retrievals from multiple passive microwave sensors. *Rem. Sens.* 10(1), 107.
- Vázquez-Cendón, M. E. (1999). Improved treatment of source terms in upwind schemes for the shallow water equations in channels with irregular geometry. *Journal of Computational Physics*, 148(2), 497-526.
- Viero, D., Peruzzo, P., Carniello, L., Defina, A., (2014). Integrated mathematical modeling of hydrological and hydrodynamic response to rainfall events in rural low-land catchments. *Water Resour. Res.* 50, 5941–5957.
- Wagner, W., Lemoine, G., & Rott, H. (1999). A method for estimating soil moisture from ERS scatterometer and soil data. *Remote sensing of environment*, 70(2), 191-207.
- Waibel, A. (1989). "Modular construction of time-delay neural networks for speech recognition", *Neural Computing*, vol.1, pp. 39-36.
- Wan, Z., Zhang, Y., Zhang, Q., & Li, Z. L. (2002). Validation of the land-surface temperature products retrieved from Terra Moderate Resolution Imaging Spectroradiometer data. *Remote sensing of Environment*, 83(1-2), 163-180.

- Wan, L., Zhang, H., Lin, G., & Lin, H. (2019). A small-patched convolutional neural network for mangrove mapping at species level using high-resolution remote-sensing image. *Annals of GIS*, 25(1), 45-55.
- Wang, J., Hsu, A., Shi, J.C., O'Neil, P. and Engman, T., (1997). Estimating surface soil moisture from SIR-C measurements over the Little Washita River watershed. *Remote Sensing of Environment*, 59, pp. 308–320.
- Wang, Y., (2002). Mapping extent of floods: what we have learned and how we can do better, *Nat. Hazards Rev.*, 3, 68–73, doi:10.1061/(ASCE)1527-6988(2002)3:2(68).
- Wang, R. Q., Mao, H., Wang, Y., Rae, C., & Shaw, W., (2018). Hyper-resolution monitoring of urban flooding with social media and crowdsourcing data. *Computers & Geosciences*, 111, 139-147.
- Watts A B, 1982 - Tectonic subsidence, flexure and global changes of sea level. *Nature*, 297, 469 - 474.
- Wigneron, J.-P., Jackson, T.J., Neill, P.O., Lannoy, G.D., de Rosnay, P., Walker, J.P., Ferrazzoli, P., Mironov, V., Bircher, S., Grant, J.P., et al., (2017). Modelling the passive microwave signature from land surfaces: A review of recent results and application to the L-band SMOS &SMAP soil moisture retrieval algorithms. *Remote Sens. Environ.* 192, 238e262.
- Wilheit, T.T.; Chang, A.T.C.; Rao, M.S.V.; Rodgers, E.B.; Theon, J.S., (1977). A satellite technique for quantitatively mapping rainfall rates over the oceans. *J. Appl. Meteorol.* 1977, 16. [CrossRef]
- Wilheit, T.; Kummerow, C.D.; Ferraro, R., (2003). Nadirrainfall algorithms for amsr-e. *IEEE Trans. Geosci. Remote Sens.* 2003, 41, 204–214.
- Weintrit, B., Osińska-Skotak, K., & Pilarska, M. (2018). Feasibility study of flood risk monitoring based on optical satellite data. *Miscellanea Geographica*, 22(3), 172-180.
- Wolfs, V., Meert, P., Willems, P., (2015). Modular conceptual modelling approach and software for river hydraulic simulations. *Environ. Model. Software* 71, 60–77. <https://doi.org/10.1016/j.envsoft.2015.05.010>.
- Wu, C.; Chau, K.-W., (2010). Data-driven models for monthly streamflow time series prediction. *Eng. Appl. Artif. Intell.* 2010, 23, 1350–1367.
- Wu, T., Fu, H., Feng, F., & Bai, H. (2019). A new approach to predict normalized difference vegetation index using time-delay neural network in the arid and semi-arid grassland. *International Journal of Remote Sensing*, 1-14.
- Yao, P.P., Shi, J.C., Zhao, T.J., Lu, H., Al-Yaari, A., (2017). Rebuilding long time series global soil moisture products using the neural network adopting the microwave vegetation index. *Rem. Sens.* 9(1), 35.

- Yazdi, J., Salehi Neyshabouri, S.A.A., (2014). Adaptive surrogate modeling for optimization of flood control detention dams. *Environ. Model. Software* 61, 106–120. <https://doi.org/10.1016/j.envsoft.2014.07.007>.
- Yen, M. H., Liu, D. W., Hsin, Y. C., Lin, C. E., & Chen, C. C. (2019). Application of the deep learning for the prediction of rainfall in Southern Taiwan. *Scientific reports*, 9(1), 1-9.
- Yin, J., Lampert, A., Cameron, M., Robinson, B., and Power, R., (2012). Using social media to enhance emergency situation awareness, *IEEE Intell. Syst.*, 27, 52–59, doi:10.1109/MIS.2012.6.
- Yu, J., Huang, Y. and Feng, X., (2001), Study on water bodies extraction and classification from SPOT image. *Journal of Remote Sensing*, 5, pp. 214–219 [in Chinese].
- Yu, D., Lane, S., (2006). Urban fluvial flood modelling using a two-dimensional diffusion-wave treatment. Part 2: development of a sub-grid-scale treatment. *Hydrol. Process.* 20, 1567–1583. <http://dx.doi.org/10.1002/hyp.5936>.
- Ko, B. C., Kim, H. H., & Nam, J. Y. (2015). CLASSIFICATION OF POTENTIAL WATER BODIES USING LANDSAT 8 OLI AND A COMBINATION OF TWO BOOSTED RANDOM FOREST CLASSIFIERS. *Sensors*, 15(6), 13763-13777
- Zebker H.A., Rosen P.A., S. Hensley, (1997), Atmospheric effects in interferometric synthetic aperture radar surface deformation and topographic maps *J. Geophys. Res.: Solid Earth (1978–2012)*, 102 (B4) (1997), pp. 7547-7563
- Zeng, Q., Wang, Y., Chen, L., Wang, Z., Zhu, H., & Li, B. (2018). Inter-comparison and evaluation of remote sensing precipitation products over China from 2005 to 2013. *Remote Sensing*, 10(2), 168.
- Zhang, K., Chao, L. J., Wang, Q. Q., Huang, Y. C., Liu, R. H., Hong, Y., ... & Ye, J. Y. (2019). Using multi-satellite microwave remote sensing observations for retrieval of daily surface soil moisture across China. *Water Science and Engineering*.
- Zhang, K., Thapa, B., Ross, M., & Gann, D. (2016). REMOTE SENSING OF SEASONAL CHANGES AND DISTURBANCES IN MANGROVE FOREST: A CASE STUDY FROM SOUTH FLORIDA. *Ecosphere*, 7(6).
- Zribi, M. and Dechambre, M., (2003). An new empirical model to retrieve soil moisture and roughness from radar data. *Remote Sensing of Environment*, 84, pp. 42–52.
- Zribi, M., Baghdadi, N., Holah, N. and Fafin, O., (2005). New methodology for soil surface moisture estimation and its application to ENVISAT-ASAR multi-incidence data inversion. *Remote Sensing of Environment*, 96, pp. 485–496.
- Zribi, M., Saux-Picart, S., André, C., Descroix, L., Ottele, C., & Kallel, A. (2007). Soil moisture mapping based on ASAR/ENVISAT radar data over a Sahelian region. *International journal of remote sensing*, 28(16), 3547-3565.

Zoppou, C., & Roberts, S. (1999). Catastrophic collapse of water supply reservoirs in urban areas. *Journal of Hydraulic Engineering*, 125(7), 686-695.